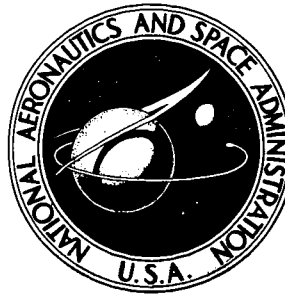


N72-32853

NASA TECHNICAL NOTE



NASA TN D-6820

**CASE FILE
COPY**

NASA TN D-6820

**FLOW-FIELD MEASUREMENTS
AROUND A MARS LANDER MODEL USING
HOT-FILM ANEMOMETERS UNDER
SIMULATED MARS SURFACE CONDITIONS**

*by George C. Greene, Lloyd S. Keafer, Jr.,
Charles G. Marple, and Jerome T. Foughner, Jr.*

*Langley Research Center
Hampton, Va. 23365*

| | | | | | |
|---|--|--|--|---|--|
| 1. Report No. NASA TN D-6820 | | 2. Government Accession No. | | 3. Recipient's Catalog No. | |
| 4. Title and Subtitle FLOW-FIELD MEASUREMENTS AROUND A MARS LANDER MODEL USING HOT-FILM ANEMOMETERS UNDER SIMULATED MARS SURFACE CONDITIONS | | | | 5. Report Date September 1972 | |
| | | | | 6. Performing Organization Code | |
| 7. Author(s) George C. Greene, Lloyd S. Keafer, Jr., Charles G. Marple, and Jerome T. Foughner, Jr. | | | | 8. Performing Organization Report No. L-8134 | |
| | | | | 10. Work Unit No. 815-20-04-06 | |
| 9. Performing Organization Name and Address NASA Langley Research Center Hampton, Va. 23365 | | | | 11. Contract or Grant No. | |
| | | | | 13. Type of Report and Period Covered Technical Note | |
| 12. Sponsoring Agency Name and Address National Aeronautics and Space Administration Washington, D.C. 20546 | | | | 14. Sponsoring Agency Code | |
| | | | | | |
| 15. Supplementary Notes | | | | | |
| 16. Abstract Results are presented from a wind-tunnel investigation of the flow field around a 0.45-scale model of a Mars lander. The tests were conducted in air at values of Reynolds number equivalent to those anticipated on Mars. The effects of Reynolds number, model orientation with respect to the airstream, and the position of a dish-type antenna on the flow field were determined. An appendix is included which describes the calibration and operational characteristics of hot-film anemometers under simulated Mars surface conditions. | | | | | |
| 17. Key Words (Suggested by Author(s)) Flow-field measurements Hot-film anemometers Wind measurements | | | 18. Distribution Statement Unclassified - Unlimited | | |
| 19. Security Classif. (of this report) Unclassified | | 20. Security Classif. (of this page) Unclassified | | 21. No. of Pages 131 | |
| | | | | 22. Price* \$3.00 | |

FLOW-FIELD MEASUREMENTS AROUND A MARS LANDER MODEL
USING HOT-FILM ANEMOMETERS UNDER SIMULATED
MARS SURFACE CONDITIONS

By George C. Greene, Lloyd S. Keafer, Jr., Charles G. Marple,
and Jerome T. Foughner, Jr.
Langley Research Center

SUMMARY

Flow-field surveys were made in the vicinity of a 0.45-scale Mars lander model in the Langley transonic dynamics tunnel in air for values of pressure and velocity representative of expected Mars surface conditions. The influence of the model on the wind speed and wind direction in the near and far fields was determined. The effects of Reynolds number, wind direction, model tilt, and dish-type antenna azimuth and elevation angles were investigated. The data indicated that the flow field around the lander was relatively insensitive to Reynolds number variation over the range anticipated on Mars and that the influence of the model on the flow field decreased rapidly with distance from the model.

INTRODUCTION

The Viking '75 Project is designed to significantly advance the knowledge of the planet Mars by means of observations from orbit and direct measurements in the atmosphere of Mars during entry and on the surface after landing. To accomplish this objective, two spacecraft will be placed in orbit around the planet. These spacecraft will each deploy a lander which will make a soft landing on the surface of Mars.

In addition to imaging, biology, seismology, and organic and inorganic chemical analysis instruments, it is planned that each Viking lander will carry instrumentation to measure the meteorological environment near the surface of the planet. The parameters to be measured are pressure, temperature, wind speed, and wind direction of the atmosphere. The accuracy requirements for these measurements are sufficiently stringent that the question arises as to the interference effects of the lander on the wind and temperature measurements, especially as the wind direction varies with respect to the lander.

In one concept of the meteorology investigation, wind and temperature measurements will be made at the end of a boom deployed from the lander. The length and location

of this boom is to be selected to satisfy accuracy requirements with a minimum of cost and weight. Therefore, the design of a suitable boom requires a knowledge of the flow field around the lander.

Several studies have been made to determine the optimum location and length of booms for mounting wind sensors on towers in the Earth atmosphere. (See refs. 1, 2, and 3.) However, these wind towers are geometrically quite different from Mars lander designs. A preliminary flow-field study with a 1/8-scale model of the Viking lander was performed by the Viking prime contractor. This study was performed in the Colorado State University Meteorological Wind Tunnel at a Reynolds number corresponding to a relatively high wind speed on Mars. Wind speed was measured at several locations around the model for two model positions relative to the wind. Data from these preliminary tests led to the conclusion that it was unnecessary to simulate the Martian atmospheric boundary layer in the present investigation.

This report presents the results of a wind-tunnel investigation which was specifically tailored to determine the effects of the lander on the steady-state measurement of wind speed, wind direction, and temperature as affected by (a) Reynolds number, (b) wind direction with respect to the lander, (c) antenna dish elevation and azimuth angles, (d) radioisotope thermoelectric generator (RTG) operation (heat generation), and (e) lander angle of attack (tilt).

SYMBOLS

The reference system used to locate the flow-field survey points is a standard wind-tunnel axis system with the origin located on the floor of the wind tunnel below the center of the model. (See fig. 1.) Coordinates of the survey probe locations are given with the axis system defined as follows:

x, longitudinal position, measured parallel to the longitudinal axis of the wind tunnel, positive in a downstream direction.

y, lateral position, measured in the horizontal plane, perpendicular to x-direction, positive to the right when facing downstream.

z, vertical position, measured perpendicular to X-Y plane, positive in upward direction.

The reference axis system for angle definition is a body-fixed system designated X_1, Y_1, Z_1 in figure 1. The positive directions of the axes and angles are indicated.

All lineal measurements in the wind-tunnel coordinate system were made in U.S. Customary Units and divided by the model scale (0.45) to represent dimensions consistent with a full-scale lander. These dimensions were then converted to SI Units.

| | |
|-----------------|--|
| A, B, k, m, n | calibration constants for hot-film wind sensors, a subscript is used to designate each of three mutually orthogonal sensors |
| E | bridge voltage of each hot-film sensor |
| M | wind-tunnel Mach number |
| N_{Re} | free-stream Reynolds number |
| p_{st} | free-stream static pressure, newtons per meter ² |
| p_t | free-stream stagnation pressure, newtons per meter ² |
| R_h/R_c | ratio of electrical resistance of hot-film velocity sensor at its operating temperature to its resistance at ambient temperature |
| RTG | radioisotope thermoelectric generator |
| T | temperature, kelvins |
| V | velocity, meters per second |
| X_1, Y_1, Z_1 | designations for model-fixed reference axes |
| x, y, z | coordinates for survey probe location referred to wind-tunnel axis system, adjusted to represent full-scale lander, meters |
| α | angle between resultant velocity vector V_T and axis of wind sensor a , degrees |
| α_L | angle of attack of lander model measured from wind vector to Y_1-Z_1 plane, degrees |
| β | angle between resultant velocity vector V_T and axis of wind sensor b , degrees |
| β_a | azimuth angle of antenna with respect to lander Y_1 -axis, degrees |
| γ | angle between resultant velocity vector V_T and axis of wind sensor c , degrees |

| | |
|----------------|--|
| γ_g | ratio of specific heats of gas |
| δ | elevation angle of antenna with respect to lander Y_1-Z_1 plane, degrees |
| θ, ψ | lander pitch and yaw angles, degrees |
| ρ | mass density, grams per centimeter ³ |
| ϕ | lander roll angle (wind azimuth) measured from wind vector to X_1-Z_1 plane, degrees |

Subscripts:

| | |
|----------|----------------------------------|
| a | wind sensor a |
| b | wind sensor b |
| c | wind sensor c |
| T | resultant of sensors a, b, and c |
| ∞ | free-stream conditions |

TEST APPARATUS

The Langley transonic dynamics tunnel (ref. 4) is a continuous-flow wind tunnel which can operate at Mach numbers from near 0 to 1.2 at pressures from about 900 N/m² to atmospheric pressure. The test section is about 10 meters long and about 5 by 5 meters in cross section. For these tests a remotely operated turntable was installed on the tunnel floor with the center of rotation at the origin of the tunnel axis system. This installation permitted rotating the model to simulate changes in wind direction.

Special instrumentation was installed to measure the wind-tunnel free-stream velocity at the low pressures used for these tests. A brief description of the instrumentation and technique for determining wind-tunnel velocity is given in appendix A.

The model, which was built by the Martin Marietta Corporation, Denver Division, was a 0.45-scale representation of a proposed Viking lander. The major components and dimensions of the full-scale lander are shown in figure 2. The proposed meteorological boom shown in figure 2 was in the stowed position for these tests to facilitate surveying near the model. In addition to the components shown in figure 2, a proposed version of

RTG windshields was installed on the model for these tests. These windshields may be seen in figure 3 which shows the model installation in the wind tunnel including the turntable and flow survey equipment. Additional provisions of the model include (1) capability for electrically heating the RTG's in order to simulate their thermal wake, (2) remote controllability of the elevation angle of the antenna dish, (3) capability for manual adjustment of the antenna azimuth, and (4) capability for changing the tilt angle (or angle of attack) by manually extending or retracting the model legs.

A remotely operated survey device was used to measure wind speed, wind direction, and ambient temperature in the flow field around the lander model. Hot-film-type anemometers were used for the flow-field measurements. The arrangement of the various sensors on the survey probe is shown in figure 4. A detailed description of the sensors and of their operational characteristics is given in appendix B.

TEST CONDITIONS

The parameters considered for simulating the flow field around the lander on Mars were the Mach, Reynolds, and Knudsen numbers. The wind speeds of interest for these tests were sufficiently low that Mach number effects could be ignored. Knudsen number effects, while significant for the small hot-film anemometers, were not important for the overall flow field around the model. Therefore only the Reynolds number was simulated. Test conditions were chosen which would yield Reynolds numbers corresponding to both high and low Mars wind speeds. Because of uncertainties in the values of Mars atmospheric parameters and possible variation in the altitude of the landing site, the zero-altitude conditions of the "most probable atmosphere" of a "Mars Engineering Model" were used. These conditions are as follows:

| | |
|--|-----------------------|
| Ambient pressure, N/m^2 | 600 |
| Ambient temperature, K | 230 |
| Speed of sound, m/sec | 244 |
| Atmospheric density, g/cm^3 | 1.36×10^{-5} |
| Atmospheric viscosity, kg/m-sec | 1.22×10^{-5} |
| Molecular weight, kg/kg-mole | 43.5 |

With the use of these conditions and a reference length of 1.59 meters (length of the top surface of the full-scale lander, measured along the Z_1 -axis, fig. 2), Reynolds numbers were determined for the expected range of wind conditions. Two values of Reynolds number were selected for these tests, 4400 and 97 600.

With the assumed atmospheric parameters for the Mars surface being used, the Reynolds number of 4400 corresponds to a Mars wind velocity of 2.5 m/sec. This Reynolds number represents essentially the minimum practical operating conditions for

the wind tunnel. The only two tests made at $N_{Re} = 4400$ were to determine the effect of Reynolds number on the lander flow interference and the possible effects of RTG operation on the ambient temperature measurement. The wind-tunnel pressure and velocity for a Reynolds number of 4400 were 1000 N/m^2 and 10 m/sec , respectively.

The Reynolds number of 97 600 corresponds to a Mars wind velocity of 55 m/sec . The wind-tunnel pressure and velocity which were selected to yield this Reynolds number were 4100 N/m^2 and 55 m/sec , respectively. The higher values of pressure and velocity at this Reynolds number permitted more accurate wind-tunnel velocity measurements and more repeatable test conditions. The types of tests, test conditions, and model configuration for each test are presented in table I.

Throughout this paper the term "high Reynolds number test conditions" refers to a Reynolds number of 97 600, a velocity of 55 m/sec , and a free-stream static pressure of 4100 N/m^2 , and the term "low Reynolds number test conditions" refers to a Reynolds number of 4400, a velocity of 10 m/sec , and a free-stream static pressure of 1000 N/m^2 .

The effect of Reynolds number on the flow field around the model was evaluated first. This effect was found to be small; therefore, most of the tests were conducted at the higher Reynolds number (97 600) where measurement errors were smaller. These tests to determine the effect of Reynolds number were conducted with model configuration 1. (See table I.) In this configuration, the top and bottom surfaces of the model were parallel with the wind-tunnel floor (no tilt) and the antenna dish was facing upward (90° elevation). The model had a blunt side facing upstream and the corner on which the antenna was mounted facing downstream. The roll angle (angle measured about the X_1 -axis) for this model position was defined to be 0° .

To determine the effect of wind direction on the flow field around the model, the wind-tunnel turntable was used to change the wind direction relative to the model. Flow-field surveys were conducted at model roll angles of 180° , 270° , and 315° .

For the tests to determine the effects of antenna position, the antenna was either faced directly into the wind or 45° off the wind ($\delta = 0^\circ$ and $\beta_a = 90^\circ$ or 45°). It was anticipated that these positions would produce the largest interference effects.

For the tilted-lander tests, the leg nearest the antenna was shortened to tilt the model about 10° . The model was oriented in azimuth such that the short leg was facing downstream.

In checking the effect of the RTG operation, no attempt was made to scale the power and fin temperatures to simulate the thermal conditions which would exist on a full-scale lander on Mars. The purpose of the test was to determine if the RTG's produced a measurable influence on the wind and temperature measurements around the model and, if so, to determine the vertical and lateral extent of the thermal influence. About 900 watts

were applied to each RTG. With the low Reynolds number test conditions, the maximum RTG temperature was about 620 K. At this temperature flow-field surveys were made downstream of the model at the wind-tunnel longitudinal station $x = 2.03$ m.

TEST PROCEDURE

In general, the flow-field surveys were made by running horizontal traverses at six vertical stations at a given longitudinal station in the tunnel. The locations of the survey stations are shown in figure 5. At a given longitudinal station (x) and the lowest vertical station, the probe was moved across the tunnel continuously from the $-y$ limit to the $+y$ limit. The probe was then raised to the next higher vertical station and was moved across the tunnel from the $+y$ limit to the $-y$ limit. These horizontal sweeps back and forth across the tunnel continued until all the vertical stations had been surveyed. The survey device was then moved to a new longitudinal station (x), and the horizontal sweeps were repeated. The rate of movement of the probe was about 10 cm/sec. The scan rate of the digital recording system (33 channels/sec) allowed each of the 36 data channels to be sampled about once per second. Thirty-six channels were required to record tunnel conditions as well as the five primary data measurements. The primary data channels were grouped together to minimize their time differentials. Survey stations at $x = 0$ m were omitted for $z < 2.37$ m so that the survey probe would not be inadvertently run into the model.

The surveys were first made with the wind tunnel empty to establish a reference for evaluating the effects of the model. The model was then installed in the wind tunnel with its center at the origin of the wind-tunnel coordinate system. Before and after each complete flow-field survey, the survey probe was moved upstream to the position $x = 4.06$ m, $y = 0$ m, and $z = 2.03$ m. At this position the model had little influence on the flow field, and the hot-film anemometers on the survey probe were calibrated by using the wind-tunnel velocity as a reference.

FLOW-FIELD-SURVEY DATA REDUCTION

A complete tunnel survey was made for both the low and high Reynolds number test conditions prior to the installation of the model. Figure 6 shows typical wind-tunnel center-line velocity profiles for both test conditions. The boundary layer on the wind-tunnel floor was about 0.30 meter thick (full scale) for both test conditions. Wind-speed data within the boundary layer were not repeatable since the velocity values were sampled and thus the average values could not be obtained at each position. Therefore the influence of the model on the flow within the boundary layer was not determined.

The wind-speed interference parameter (or velocity ratio) represents the ratio of the local velocity as measured by the hot-film anemometers on the survey probe to the wind-tunnel free-stream velocity. In figure 7 typical plots are presented of velocity ratio V_T/V_∞ as a function of the lateral tunnel coordinate y for the empty tunnel at the high Reynolds number test conditions. These plots show that the velocity ratio (and therefore the velocity) was uniform above the boundary layer in the empty tunnel. Therefore, interference effects with the model in the wind tunnel were determined directly from the model flow-field measurements. Any differences between the local flow velocity and the wind-tunnel free-stream velocity were attributed to the effect of the model.

One of the problems in measuring flow interference was the gradual change of the hot-film wind sensor calibrations during a test. Since the average of the pretest and post-test calibrations for the wind sensors was used in the data reduction, the value of the velocity ratio V_T/V_∞ in regions of undisturbed flow was generally not equal to 1.0. In addition, with the model in the tunnel there was an increase in the local velocity (and therefore velocity ratio) of about 5 percent at the model station and downstream due to tunnel blockage. In order to reduce these errors in the data reduction, regions of uniform velocity ratio far from the lander model were judged to be essentially unaffected by the presence of the model. The value of the velocity ratio in these areas was adopted as a reference (rather than 1.0) and the wind-speed interference in areas close to the model was determined relative to the far field or reference. The magnitude of the wind-speed interference was calculated with the following equation:

$$\text{Percent interference} = \frac{(V_T/V_\infty)_{\text{far field}} - (V_T/V_\infty)_{\text{local}}}{(V_T/V_\infty)_{\text{far field}}} \times 100$$

Table II presents an assessment of errors associated with the measurement of wind speed, wind direction, and ambient temperature by using the survey probe. Since the measured wind speed was divided by the free-stream wind-tunnel velocity, random errors and errors due to drift during a test are more serious than bias errors and wind-tunnel blockage effects. In addition to the errors noted in table II, wind-speed errors caused by radiation from the wind-tunnel lighting system were noted at the low Reynolds number test conditions. Wind-speed errors of up to 6 percent occurred whenever the sensor was surveying near the tunnel wall lights (but outside the wall boundary layer). Estimates for these errors do not appear in table II since their effect was very localized. These data were not used in determining flow interference.

The ambient temperature data includes a rather large error due to the slow response of the temperature sensor as it moved through the heated RTG wake. This response lag distorts the boundary of the thermal wake in the survey scan direction. However, since

surveys were made in both directions, this distortion does not seriously affect the determination of the thermal wake boundaries.

RESULTS AND DISCUSSION

The test results can be divided into three categories: effect of Reynolds number, effect of model configuration changes, and effect of wind direction. The reference used for evaluating these effects was the 5-percent wind-speed interference boundaries for model configuration 1 (table I) at the high Reynolds number test conditions and 0° wind azimuth shown in figure 8. This figure shows the regions where the influence of the model on the local wind speed is less than 5 percent. Values of the abscissa represent longitudinal wind-tunnel coordinates and values of the ordinate represent lateral wind-tunnel coordinates. All coordinates in this report have been adjusted to represent dimensions consistent with a full-scale lander. The symbols represent the points nearest the model where the influence of the model on the local wind speed is 5 percent. All points farther from the model at the same vertical coordinate z and same longitudinal coordinate x have less than 5 percent interference. The solid lines, called interference boundaries in this report, have been faired through the data points to indicate where the wind-speed interference is less than 5 percent for $z \geq 1.69$ m and $z \leq 1.02$ m.

The interference pattern shown in figure 8 is typical of blunt bodies (for example, ref. 2) and is characterized by areas of reduced velocity (velocity ratio less than 1.0) upstream of and in the wake of the model and areas of increased velocity (velocity ratio greater than 1.0) as the flow accelerates around and over the lander. Five-percent interference effects extend about 1 model length upstream and the wake is just wider than the maximum lander width.

For $z \geq 1.69$ m, wind-speed interference effects did not exceed 10 percent at any of the survey positions at which data were taken except in the wake of the tracking antenna. (See fig. 5 for survey stations.) Measurements nearer the lander are necessary to define the flow characteristics in the vicinity of the antenna.

Figure 9 shows the variation of wind-speed interference with distance from the model for $z = 0.34$ m. The 5-, 10-, and 20-percent interference boundaries are shown for model configuration 1. It should be noted that the 10- and 20-percent interference boundaries are faired through a very limited number of points since little data were taken near the model.

In figure 10 are plots of the velocity ratio (ratio of local velocity to free-stream wind-tunnel velocity) as a function of the lateral wind-tunnel coordinate y for each lon-

gitudinal survey station. These data were taken with model configuration 1 at the high Reynolds number test conditions and were used to prepare figures 8 and 9.

Figure 11 presents the results of wind direction measurements around the model for configuration 1. In figure 11, $\frac{\alpha - \beta}{2}$ is approximately equal to the local flow angle in the horizontal plane relative to the wind-tunnel center line, where α and β are the angles between the wind vector and the axes of wind sensors a and b respectively. In general, the flow-angle data include some bias errors since the flow angles are derived from the measured components of wind speed.

Reynolds Number

The effect of Reynolds number may be observed by comparing figure 12 ($N_{Re} = 4400$) and figure 8 ($N_{Re} = 97\ 600$). The differences in the 5-percent interference patterns are small and can be at least partially explained by the larger measurement errors at the low Reynolds number conditions. This suggests that strict Reynolds number simulation may not be necessary for interference studies on future Mars landers.

Lander Configuration Changes

The flow field around the lander model changed significantly when antenna pointing was simulated. Figure 13 shows the 5-percent wind-speed interference boundaries for model configuration 2 at the high Reynolds number test conditions. The dashed line represents the 5-percent wind-speed interference boundaries at the $z = 1.69$ m elevation for model configuration 1 which was shown in figure 8. There is little difference in the 5-percent interference boundaries at the lower elevations; therefore, only the $z = 1.69$ m and $z = 2.37$ m data are presented. Figure 13 shows that facing the antenna dish into the wind extends the 5-percent wind-speed interference boundary upstream about 0.6 m at the $z = 1.69$ m level. In addition, strong interference effects extend upward to the $z = 2.37$ m level. Figure 14 presents the wind-speed data from which figure 13 was prepared. Figure 15 shows the effect of changing the antenna azimuth from 0° to 45° on the 5-percent wind-speed interference boundary for model configuration 3. Interference effects greater than 5 percent at the $z = 2.37$ m level are not present for this configuration but the 5-percent wind-speed interference boundary at the $z = 1.69$ m level is altered significantly. It is possible that other combinations of antenna angles and wind azimuth might produce even larger disturbances in the flow field. In view of this possibility, extreme care should be exercised in making wind measurements unless the antenna dish is facing upward ($\delta = 90^\circ$). Figure 16 presents the wind-speed data from which figure 15 was prepared. Figure 17 presents flow-angle data in the horizontal plane for this configuration.

Figure 18 shows the effect of lander tilt (model configuration 4) on the 5-percent wind-speed interference boundaries. This test simulated a Mars landing in which the shock absorbing material in one leg is crushed more than in the other two or a landing where one leg rests in a crater, soft spot, etc. It did not simulate landing on a slope. The dashed line represents the 5-percent interference boundary for the $z = 1.69$ m elevation for model configuration 1. This interference boundary was shown in figure 8 and is shown again for comparison. The effect of tilt is significant in the region just upstream of the model. Figure 19 presents the wind-speed data from which figure 18 was prepared. Figure 20 presents flow-angle data for model configuration 4.

Effect of Wind Direction

Flow-field measurements were made for wind azimuths ϕ of 0° , 180° , 270° , and 315° . Wind-speed interference boundaries for the 0° wind azimuth are presented in figures 8 and 9. Figure 21 shows the 5-percent wind-speed interference boundaries for $z \leq 1.02$ m and $z \geq 1.69$ m for $\phi = 180^\circ$ (model configuration 5). Figure 22 shows 5-, 10-, and 15-percent interference boundaries at $z = 0.34$ m for $\phi = 180^\circ$. Interference effects at $z \geq 1.69$ m were less than about 10 percent for all survey positions except those in the wake of the antenna. Figure 23 presents the wind-speed data from which figures 21 and 22 were prepared. Figure 24 presents local flow angles for this wind direction.

Figure 25 shows the 5-percent wind-speed interference boundaries for $z \leq 1.02$ m and $z \geq 1.69$ m for $\phi = 270^\circ$ (model configuration 6). Figure 26 presents 5-, 10-, and 20-percent interference boundaries at $z = 0.34$ m for this wind direction. Interference effects for $z \geq 1.69$ m were generally less than 10 percent. Figure 27 presents the wind-speed data from which figures 25 and 26 were prepared.

Figure 28 shows the 5-percent interference boundaries for $z \leq 1.02$ m and $z \geq 1.69$ m for $\phi = 315^\circ$ (model configuration 7). Figure 29 shows the 5- and 10-percent interference boundaries at $z = 0.34$ m. Interference effects at $z \geq 1.69$ m were generally less than 10 percent. Figure 30 presents the wind-speed data from which figures 28 and 29 were prepared.

Thermal Interference

Temperature profiles measured in the wake of the RTG's are presented in figure 31. The response of the temperature sensor is evident as the thermal wake is stretched in the direction of the wake traverse. These data were taken at low Reynolds number test conditions and thus represent the worst interference conditions. It is noteworthy that the thermal wake falls within the aerodynamic wake so that by avoiding wind-speed interference effects, thermal interference is also avoided.

CONCLUDING REMARKS

The results of an investigation of the flow field around a model of a proposed Viking lander under simulated Mars surface conditions have been presented. The effects of the lander model on the measurements of local wind speed, wind direction, and ambient temperature were determined as a function of Reynolds number, wind direction, and model configuration.

The wind-speed data taken at Reynolds numbers of 4400 and 97 600 indicate that the flow field around the model is relatively insensitive to Reynolds number over the range of Reynolds number anticipated on Mars. This suggests that strict Reynolds number simulation may not be necessary for any future Mars lander flow-field studies.

The flow-field measurements at different wind directions and model configurations indicated consistently that interference effects decrease rapidly with distance from the model, except in the model wake. The wind-speed interference for heights of 1.69 meters (full scale) or higher was less than 10 percent for all survey positions except those in the wake of the dish-type antenna and possibly those directly over the model. Survey positions over the model at heights of 1.69 meters (full scale) or less were omitted so that the survey probe would not be inadvertently run into the model. Additional data are necessary to define the flow field above the model.

Langley Research Center,

National Aeronautics and Space Administration,

Hampton, Va., July 7, 1972.

APPENDIX A

WIND-TUNNEL VELOCITY MEASUREMENT

The free-stream wind-tunnel velocity was determined from measurements of stagnation chamber pressure p_t and temperature and the difference between the stagnation chamber and test-section static pressures $p_t - p_{st}$. A transducer with a range of absolute pressure from 0 to 6516 N/m² (0 to 50 torr) was used to measure p_t , and a transducer with a range of differential pressure from 0 to 1333 N/m² (0 to 10 torr) was used to measure $p_t - p_{st}$. These transducers were of the stretched-diaphragm, capacitance type and were installed in temperature controlled chambers. The wind tunnel was periodically stopped to check the differential pressure transducer for drift errors.

Wind-tunnel velocity was determined from calculations of the Mach number and speed of sound by using isentropic flow equations. The pressure ratio p_t/p_{st} may be expressed in terms of Mach number by

$$\frac{p_t}{p_{st}} = \left(1 + \frac{\gamma_g - 1}{2} M^2 \right)^{\gamma_g / (\gamma_g - 1)} \quad (A1)$$

Since velocity measurement at low Mach numbers can be very sensitive to pressure measurement errors, the following error assessment is presented. By differentiating and rearranging equation (A1), the error in Mach number can be expressed in terms of the error in the pressure ratio as

$$\frac{\partial M}{M} = \left(\frac{1 + \frac{\gamma_g - 1}{2} M^2}{\gamma_g M^2} \right) \frac{\partial(p_t/p_{st})}{p_t/p_{st}} \quad (A2)$$

For small Mach numbers, the expression within the parentheses becomes very large and the error in Mach number becomes extremely sensitive to errors in pressure ratio. However by measuring p_t and $p_t - p_{st}$, the ratio p_t/p_{st} can be determined very accurately. The error in Mach number can be expressed in terms of the errors in each pressure measurement as follows:

$$\frac{\partial M}{M} = \frac{1 + \frac{\gamma_g - 1}{2} M^2}{\gamma_g M^2} \left[1 - \left(1 + \frac{\gamma_g - 1}{2} M^2 \right)^{\gamma_g / (\gamma_g - 1)} \right] \left[\left| \frac{\partial p_t}{p_t} \right| + \left| \frac{\partial(p_t - p_{st})}{p_t - p_{st}} \right| \right] \quad (A3)$$

For $M = 0.03$ (approximately 10 m/sec), $\gamma_g = 1.4$ (air), and by assuming a 2-percent error in p_t and a 10-percent error in $p_t - p_{st}$, the resulting error in Mach number would be approximately 6 percent.

APPENDIX A

In addition to the primary measurement, an independent velocity measurement was made with a pitot-static tube in the test section. For the low Reynolds number test conditions for which the dynamic pressure q was only 0.6 N/m^2 , velocities measured by the two independent systems agreed within 5 percent without viscous corrections for the pitot-static measurement. Although this does not establish the absolute accuracy of the measurement it does show the capability of the two systems to consistently measure very low pressure levels with a reasonable degree of accuracy. Velocity measurements with the two systems at the high Reynolds number test conditions were within 1 percent of each other.

APPENDIX B

FLOW-FIELD MEASUREMENTS

Local wind speed, local wind direction, and local ambient temperatures were measured by sensors on the survey probe. Figure 4 shows the arrangement of the various sensors. The probe is arranged so that one of the wind sensors (sensor c) is vertical, perpendicular to the tunnel floor. The other sensors (sensors a and b) are in the horizontal plane, 45° to the X-axis. Although all three sensors are used to determine the local wind vector, this arrangement provides a good approximation of wind speed with only the sensor c data and a good approximation of wind direction in the horizontal plane with only the sensor a and b data. Note that associated with each wind sensor is a temperature reference sensor. Also an ambient temperature sensor is located behind the probe stem and parallel to the flow. The active portion of each sensor consists of a platinum film deposited on a cylindrical aluminum oxide substrate which is 0.064 cm in diameter and 0.97 cm long. A thin protective layer of quartz overcoats the film. The cold (room-temperature) resistances of the wind sensors and the ambient temperature sensor are approximately 13 ohms, whereas the resistance of temperature reference sensor are approximately 1000 ohms.

The ambient temperature sensor operates as a resistance thermometer and uses standard circuitry. Figure 32 shows the arrangement of the various sensors and a block diagram of sensor c. Dashed lines indicate the long leads between the sensor and the electronics. The wind sensors and their associated temperature reference sensors are operated in a bridge circuit. An operational amplifier senses the bridge unbalance and applies the proper amount of bridge voltage to heat the wind sensor, which raises its resistance to balance the bridge. Thus, as the sensor is convectively cooled by the wind, the amplifier-driven bridge voltage E becomes the wind-speed analog. The temperature reference sensor in the bridge is not heated significantly since its resistance is extremely large; therefore, it does not respond to the wind speed. It responds to the ambient temperature and provides temperature compensation in the bridge so that the wind sensor operates at a constant temperature difference above the ambient temperature.

The particular formulation used to describe the response of the mutually perpendicular wind-speed sensors was taken from reference 5 and consists of three types of equations. These equations and a description of their use are as follows:

(1) An equation which relates the voltage response E of each sensor to the component of the wind vector which is perpendicular to the wind sensor. Sensors are relatively insensitive to parallel wind components. For example,

$$E_a^2 = A_a + B_a \rho^{1/m} V_a^{1/n} \quad (B1)$$

APPENDIX B

Equations for sensors b and c have b or c in place of the subscript a. Since the overheat or temperature differential was maintained constant for these tests, it does not appear directly in the equation.

(2) An equation which combines the outputs of all three sensors to determine the total wind speed

$$V_T = \sqrt{\frac{V_a^2 + V_b^2 + V_c^2}{2 + k^2}} \quad (B2)$$

(3) Equations which define the angular response of each sensor

$$\left. \begin{aligned} V_a^2 &= V_T^2 (\sin^2 \alpha + k^2 \cos^2 \alpha) \\ V_b^2 &= V_T^2 (\sin^2 \beta + k^2 \cos^2 \beta) \\ V_c^2 &= V_T^2 (\sin^2 \gamma + k^2 \cos^2 \gamma) \end{aligned} \right\} \quad (B3)$$

Calibrations prior to the wind-tunnel tests showed that sensors of this type had a sufficient degree of uniformity to allow the use of the same values for $1/m$, $1/n$, and γ_g for all sensors. The values chosen on the basis of these calibrations were as follows:

$$1/m = 0.62$$

$$1/n = 0.53$$

$$k = 0.32$$

Any variation in sensors or any change of conditions that might affect sensor response was accounted for by making pretest and posttest calibrations in the wind tunnel from which the values of the constants A and B were determined for each sensor.

The usual equation for the output of a hot-film anemometer has the form

$$E^2 = (A + B N_{Re}^{1/n}) (\Delta T) \quad (B4)$$

where ΔT is the difference between the sensor temperature and ambient temperature and $n \approx 2$. However, since this test was made at very low pressure (1000 N/m^2), the following equation was used so that different exponents could be assigned to density and velocity:

APPENDIX B

$$E^2 = (A + B\rho^{1/m}V^{1/n}) \quad (B5)$$

Since ΔT was held constant it was included in the constants A and B . Since the value of A was large compared to the maximum output (due to the relatively low mass-flow range), it was necessary to use the method of Fabula (ref. 6) to determine the exponents. This method requires differentiating equation (B5) with ρ held constant to obtain

$$E^2 = A + nV(dE^2/dV) \quad (B6)$$

The exponent n was determined by plotting E^2 against $V(dE^2/dV)$ and fitting the best straight line, n being the slope of the line. In a similar manner the exponent m was determined by plotting E^2 against $\rho(dE^2/d\rho)$ at a constant velocity.

As a final check a plot was made of all precalibration points for sensor c , E_c^2 against $\rho^{0.62}V^{0.53}$. (See fig. 33.) Many authors indicate that A will be a function of ΔT , gas composition, etc., but not density. However, figure 33 indicates that A is a function of density. The same indication was obtained for all sensors. Since testing was done in a very low mass-flow region (A is large compared to the full-scale output), small changes in A are important. Many different formulations could be used to describe the nonlinear relationship between voltage and velocity, but all must account for the large initial offset. Thus, it is important that any hot-film anemometer that cannot be recalibrated periodically be calibrated over a range of density and velocity so any dependency of the constants on density can be determined.

Temperature Effect on Leads

As stated previously, the constants A and B were adjusted by pretest and post-test calibrations for each flow-field survey. If the same constants were used for all measurements at 4100 N/m^2 , errors of up to about 10 m/sec at 55 m/sec would result. This large shift in sensitivity could be caused by

- (1) Improper matching of the temperature compensation coefficient to the velocity sensor
- (2) Dirt and other accumulation on the probes
- (3) Temperature changes on bridge interconnecting cables which will cause a change in sensor overheat
- (4) Temperature changes on leads external to the bridge which will cause a change in voltage (IR) drop.

A visual inspection of the probes showed no accumulation of dirt. Although no direct checks were made, ambient temperature compensation should (except for time-constant

APPENDIX B

effects) be adequate since both the velocity sensor and the compensation sensor were platinum film. However, a close examination showed that all calibration shifts could be easily caused by temperature changes on the long leads.

The anemometer lead wires had resistances (at 295.4 K) of 3.05 ohms per lead for the preliminary tests and 5.0 ohms for the wind-tunnel tests. Figure 32 shows the relationship of the bridge and leads. The following equation holds when the bridge is at balance:

$$\frac{\text{Potentiometer resistance}}{\text{Temperature reference sensor} + \text{Cable resistance}} = \frac{10\Omega + \text{Cable resistance}}{\text{Velocity sensor resistance}}$$

The other resistance values (at 295.4 K) for probe c are given in the following table:

| | |
|--|--------|
| Velocity sensor | 12.781 |
| Reference sensor | 1130.2 |
| Potentiometer (preliminary test) | 1006.9 |
| Potentiometer (first test, wind-tunnel value) | 1006.9 |
| Potentiometer (other tests, wind-tunnel value) | 1180.5 |

A typical probe was calibrated, resistance plotted against temperature, and a temperature coefficient of 0.002572/K was determined. In the following table, the operating conditions are given for probe c with the long cables assumed to be at 295.4 K:

| Test | Velocity sensor resistance, ohms | R_h/R_c | Sensor ΔT , K |
|----------------------------|--|-----------|--------------------------|
| Preliminary | 14.424 | 1.129 | 50.0 |
| First (wind-tunnel values) | 16.911 | 1.323 | 126 |
| Other (wind-tunnel values) | 14.668 | 1.148 | 57.4 |

If the cable temperature changed 15 K, the resistance change of each cable lead would be approximately 0.28 ohm. A change in the lead resistance from 5.0 to 5.28 ohms will raise the overheat of the velocity sensor from 50.0 to 58.3 K. For a typical sensor this change in overheat would cause a voltage error of about 0.3 volt at the high Reynolds number test conditions. The error in indicated velocity with an error of 0.3 volt is about 20 m/sec under these conditions.

The typical temperature change of the wind sensor leads during tests at low Reynolds number test conditions was 2.22 K and at high Reynolds number test conditions was 1.67 K. The following errors were caused if the leads changed temperature with test section ambient during any one test and calibration being made only at the start of the test.

APPENDIX B

| Cable temperature change, K | Change in sensor overheat, K | Total voltage error, V | Error at wind off, m/sec | Error at full scale, m/sec |
|--------------------------------------|------------------------------|------------------------|--------------------------|----------------------------|
| High Reynolds number test conditions | | | | |
| 1.67 | 0.82 | 0.032 | <0.2 | 1.6 |
| 14.44 | 8.31 | .307 | .6 | 20 |
| Low Reynolds number test conditions | | | | |
| 2.22 | 1.18 | 0.030 | 0.2 | 1.3 |

Although the actual temperature changes are difficult to estimate since the cable was exposed to several different temperatures between the control room and the test section, the actual errors encountered due to cable resistance change were smaller than shown in the previous table since a pretest and posttest calibration was made.

The point is that large overheat errors can be caused by resistance changes in the leads. These errors can be reduced by

- (1) Completing bridge at sensor
- (2) Keeping leads balanced in each arm
- (3) Keeping leads short so that lead resistance is small compared to sensor resistance
- (4) Measuring bridge current (feedback current)

Recommendations

(1) Careful consideration should be given the effect of resistance changes in the cable between the electronics and the sensor for any anemometer designed to work in a Mars atmosphere and where periodic recalibration is not possible. The bridge should be completed at sensor for smallest lead errors.

(2) Bench and calibration checks should include exposing the leads and electronics as well as the sensor to the actual temperature, density, and velocity environment.

(3) Calibration should include several different densities so that the dependency of constants on density can be determined.

REFERENCES

1. Moses, Harry; and Daubek, Hugh G.: Errors in Wind Measurements Associated With Tower-Mounted Anemometers. *Bull. Amer. Meteorol. Soc.*, vol. 42, no. 3, Mar. 1961, pp. 190-194.
2. Thornthwaite, C. W.; Superior, W. J.; and Field, R. T.: Disturbance of Airflow Around Argus Island Tower Near Bermuda. *J. Geophys. Res.*, vol. 70, no. 24, Dec. 15, 1965, pp. 6047-6052.
3. Cermak, J. E.; and Horn, J. D.: Tower Shadow Effect. *J. Geophys. Res.*, vol. 73, no. 6, Mar. 15, 1968, pp. 1869-1876.
4. Schaefer, William T., Jr.: Characteristics of Major Active Wind Tunnels at the Langley Research Center. NASA TM X-1130, 1965.
5. Champagne, F. H.; Sleicher, C. A.; and Wehrmann, O. H.: Turbulence Measurements With Inclined Hot-Wires. Pt. 1. Heat Transfer Experiments With Inclined Hot-Wire. *J. Fluid Mech.*, vol. 28, pt. 1, Apr. 12, 1967, pp. 153-175.
6. Fabula, A. G.: Operating Characteristics of Some Hot Film Velocity Sensors in Water. *Advances in Hot-Wire Anemometry*, W. L. Melnik and J. R. Weske, eds., AFOSR No. 68-1492, U.S. Air Force, July 1968, pp. 167-193. (Available from DDC as AD 676 019.)

TABLE I. - WIND-TUNNEL TEST PROGRAM

| Type of test | Nominal wind-tunnel conditions (a) | Model configuration | Model angles, deg | | Antenna angles, deg | | RTG temperature, K |
|----------------------------------|---|------------------------|----------------------|-----------------------|------------------------|-----------------------|--------------------------|
| | | | Roll, ϕ | Attack, α_L | Elevation, δ | Azimuth, β_a | |
| Empty tunnel | H | --- | --- | --- | --- | --- | ----- |
| | L | --- | --- | --- | --- | --- | ----- |
| Effect of Reynolds number | H | 1 | 0 | 0 | 90 | 90 | Ambient |
| | L | 1 | | | | | |
| Effect of antenna orientation | H | 2 | 0 | 0 | 0 | 90 | Ambient |
| | | 3 | 0 | 0 | 0 | 45 | |
| Effect of lander tilt | H | 4 | 0 | 10 | 90 | 45 | Ambient |
| Effect of wind direction | H | 5 | 180 | 0 | 90 | 90 | Ambient |
| | | 6 | 270 | 0 | 90 | 90 | |
| | | 7 | 315 | 0 | 90 | 90 | |
| Effect of RTG operation | L | 8 | 0 | 0 | 90 | 90 | 620 |

a H denotes high Reynolds number test conditions which are $NRe = 97\ 600$, $V = 55\ m/sec$, $p_{st} = 4100\ N/m^2$;
L denotes low Reynolds number test conditions which are $NRe = 4400$, $V = 10\ m/sec$, $p_{st} = 1000\ N/m^2$.

TABLE II. - SURVEY-MEASUREMENT-ERROR ASSESSMENT

| Measurand | Error type | Error magnitude (a) | Error estimation | Error sources unique to test |
|--------------------------------------|-------------------------------------|---|---|---|
| Wind speed (steady state) | Random | 2% (1 σ) for H 3% (1 σ) for L | Standard deviation of fluctuations during pretest and posttest calibrations | Sampling errors associated with low frequency fluctuations in tunnel |
| | Drift (during a test) | Usually <2% but may approach 3% for H Usually <3% but may approach 10% for L | Based on comparing pretest and posttest calibrations and adding 0.5% for error associated with reference pressure gage (pressure gage was zeroed before calibrations and several other times during a test) | Pressure transducer drift Temperature effect on leads Foreign material (e.g., oil) on sensors Density error via faulty stagnation temperature measurements |
| | Bias (excluding tunnel blockage) | Usually <±1% but varies with test up to ±3% for H Same with variations up to ±4% for L | Based on pretest calibrations with velocity determined from pressure measurements as a standard | Test to check drift not completely accounted for by calibration constants used for reducing data of individual tests Velocity interference from lander at calibration position Pressure and stagnation temperature errors |
| | Tunnel blockage | 5% for H and L | | |
| Wind direction (horizontal plane) | Random | <1° (1 σ) for H | Based on errors in measuring individual velocity components | Same error sources as for velocity since angles are calculated from velocity components Error in angle calculation formula and in value of k chosen |
| | Drift (during a test) | Usually <2° for H | | |
| | Bias | Usually ±2° but varies with test up to ±6° for H | | |
| Temperature (ambient) | Random | <1° | Eyeball | Drift error caused by temperature effect on leads Slow time response |
| | Drift | <1° | Based on lead resistance change with temperature ±0.7° margin | |
| | Bias Lag | <5° <4° | Based on comparison with thermocouple | |

^a H denotes high Reynolds number test conditions which are $N_{Re} = 97\,600$, $V = 55\text{ m/sec}$, $p_{st} = 4100\text{ N/m}^2$; L denotes low Reynolds number test conditions which are $N_{Re} = 4400$, $V = 10\text{ m/sec}$, $p_{st} = 1000\text{ N/m}^2$.

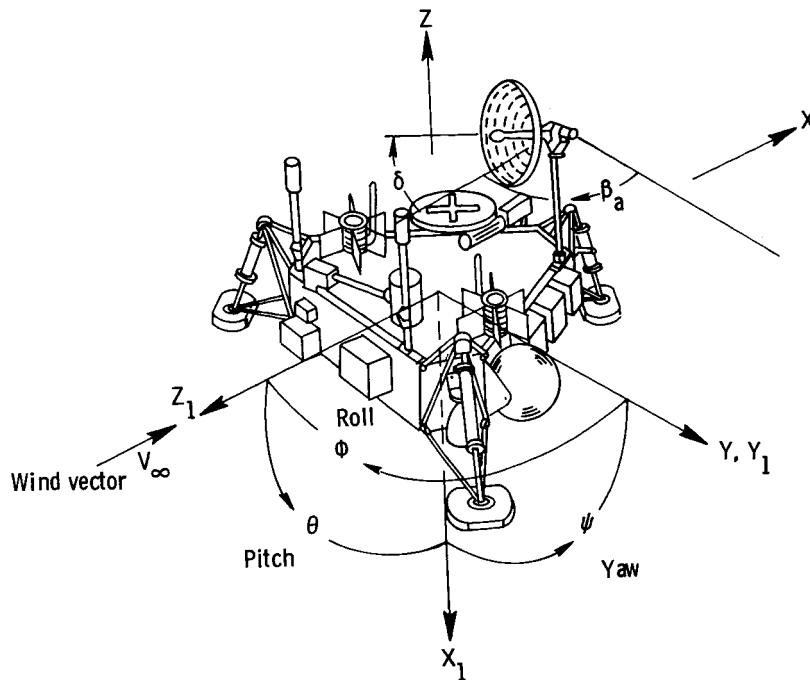


Figure 1.- Axis designations. Positive directions are shown; roll angle is 0° as shown.

- 1 Antenna
- 2 Camera
- 3 UHF antenna
- 4 RTG 2
- 5 RTG 1
- 6 Meteorological boom (stowed)
- 7 Soil sampler
- 8 Terminal propellant tank
- 9 Terminal engine

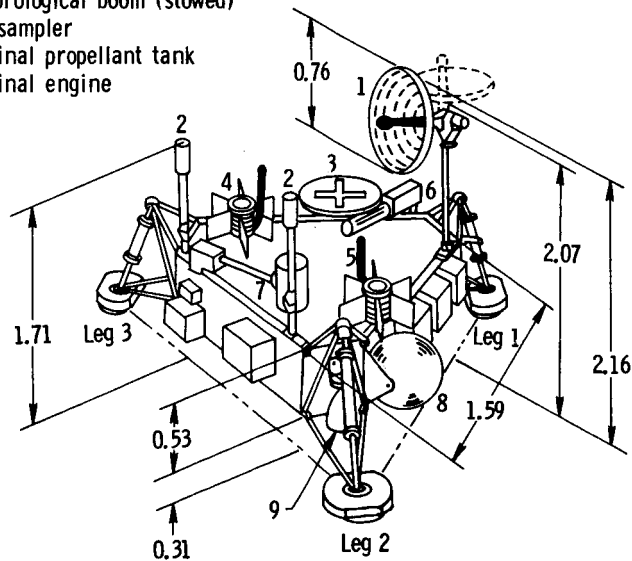


Figure 2.- Proposed Viking lander dimensions and identification of components. All dimensions are given in meters.



Figure 3.- Model installation in wind tunnel.

L-70-7351.1

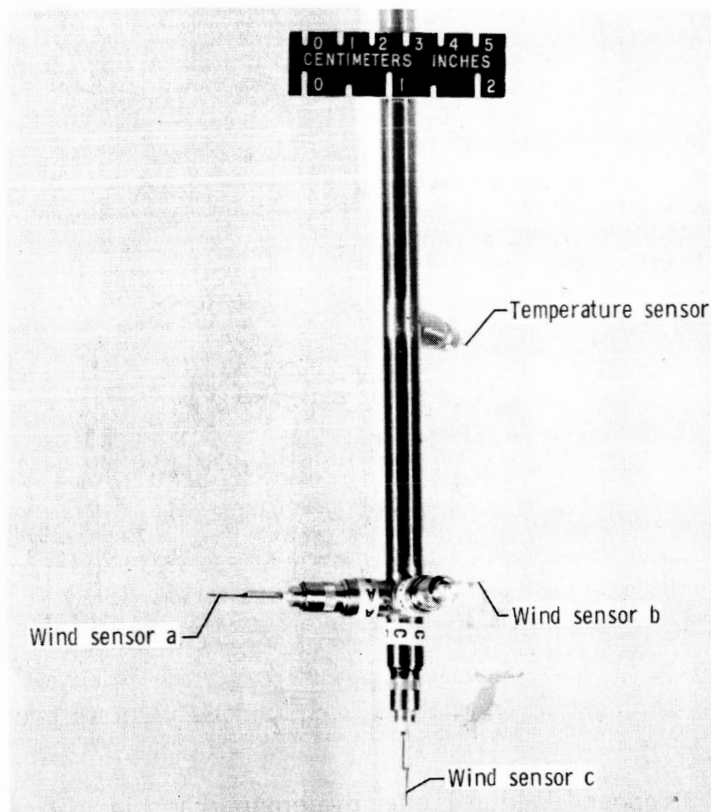


Figure 4.- Survey probe.

L-71-5159.1

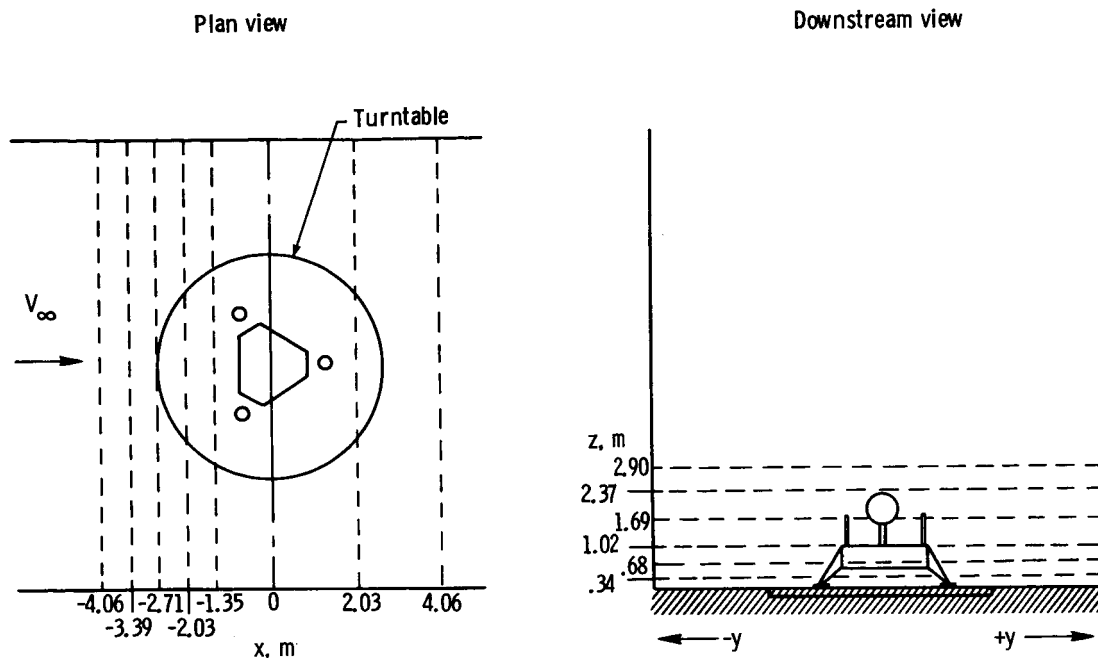


Figure 5.- Survey stations.

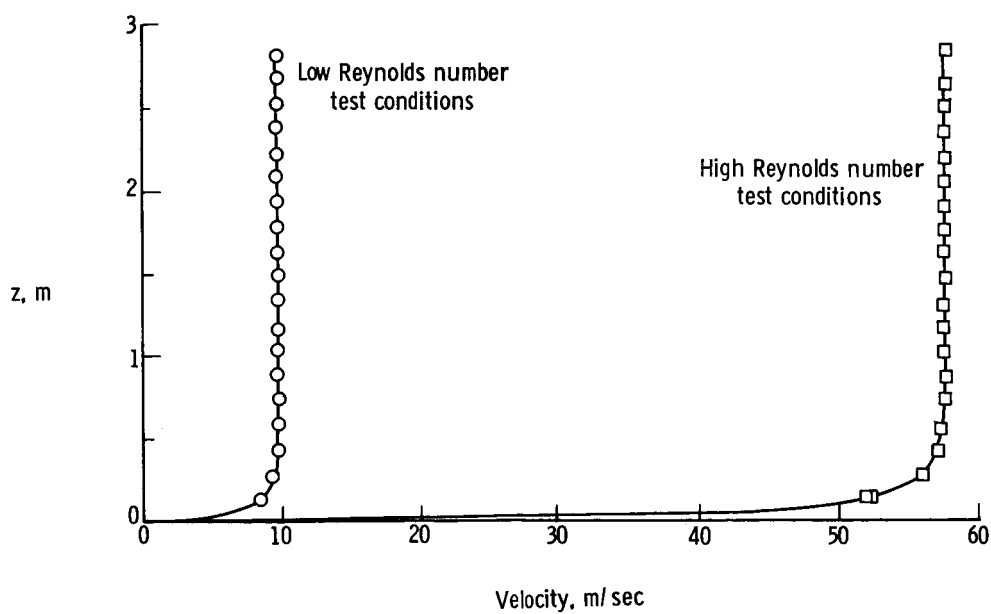
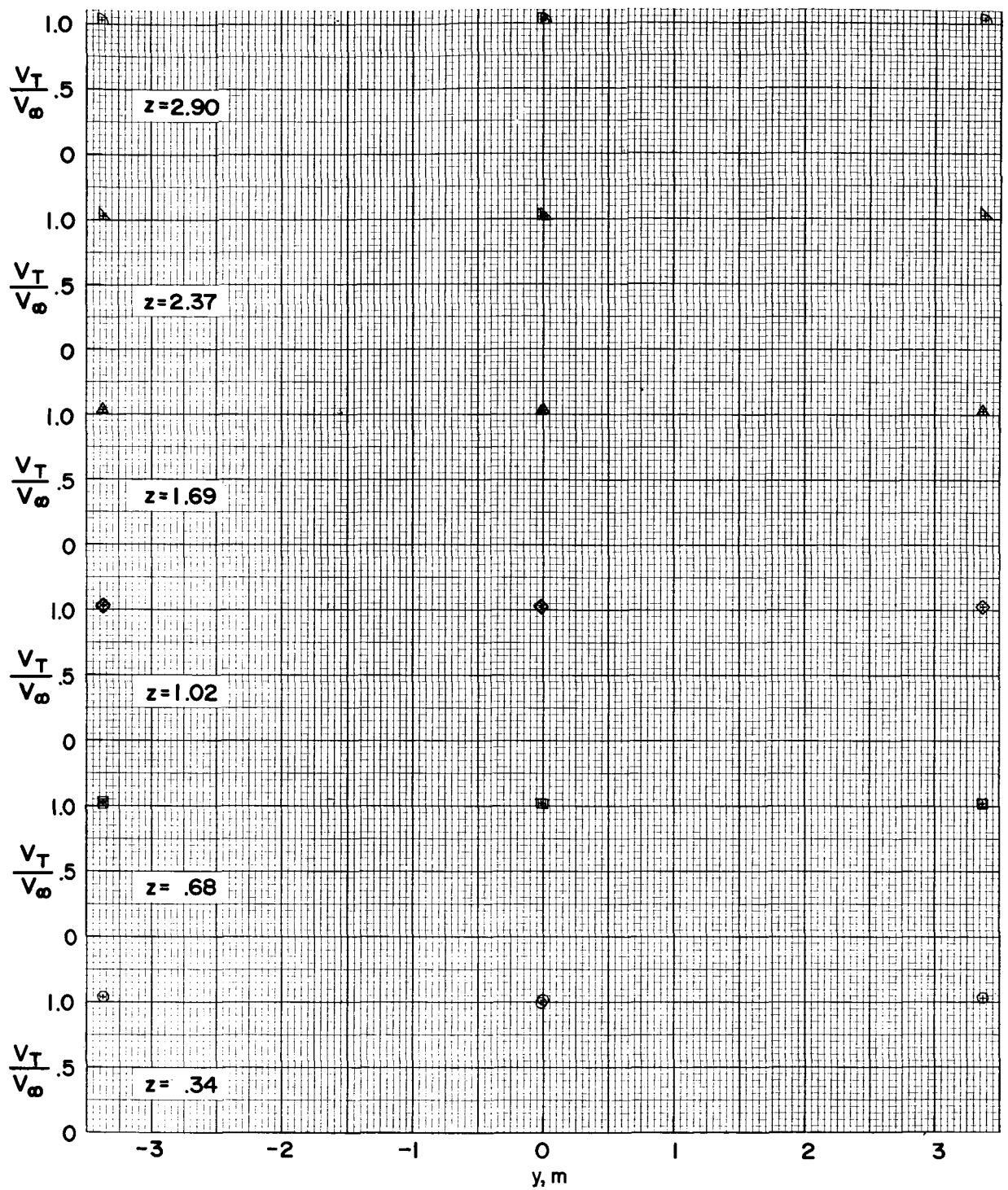
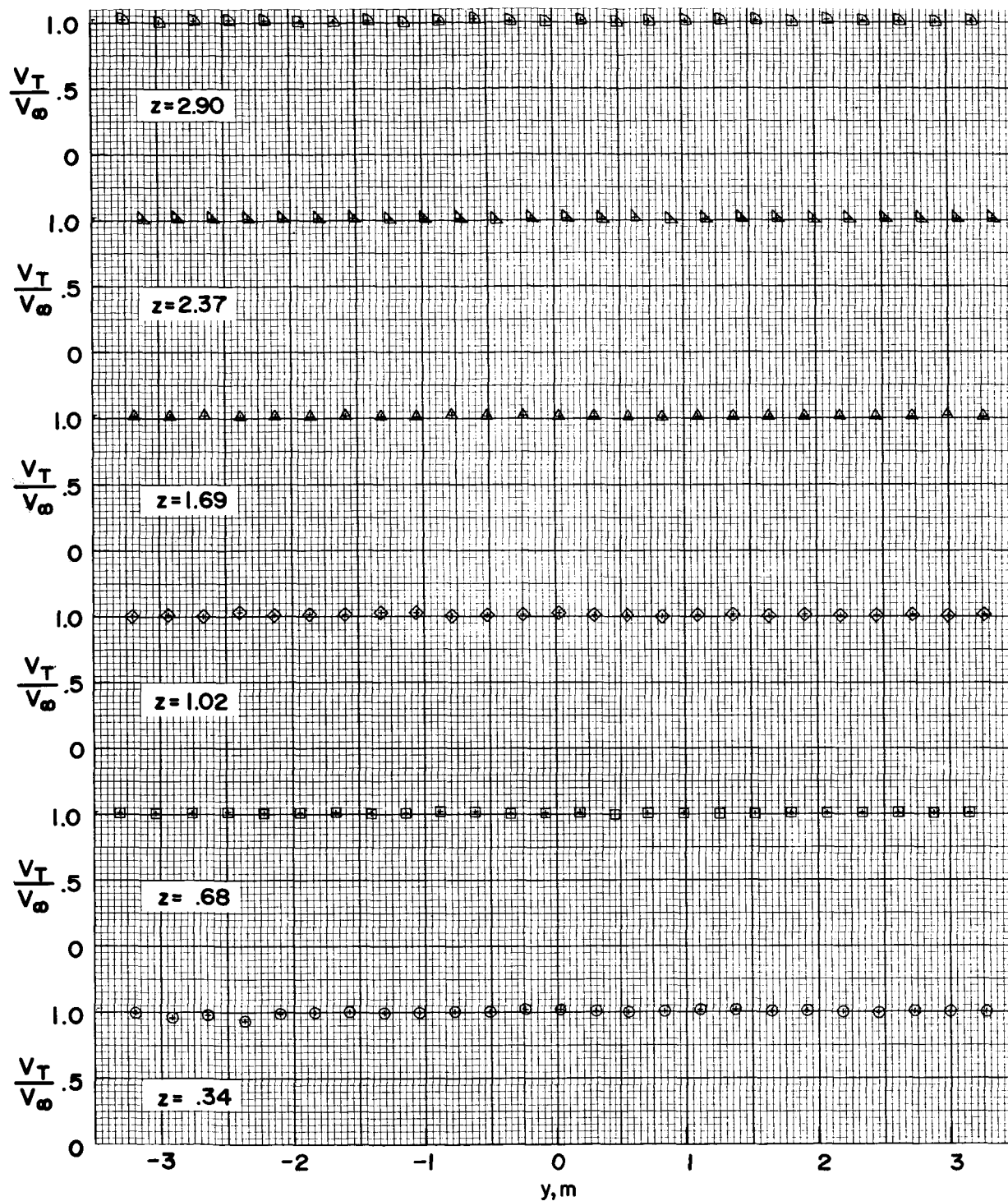


Figure 6.- Typical wind-tunnel center-line velocity profiles.



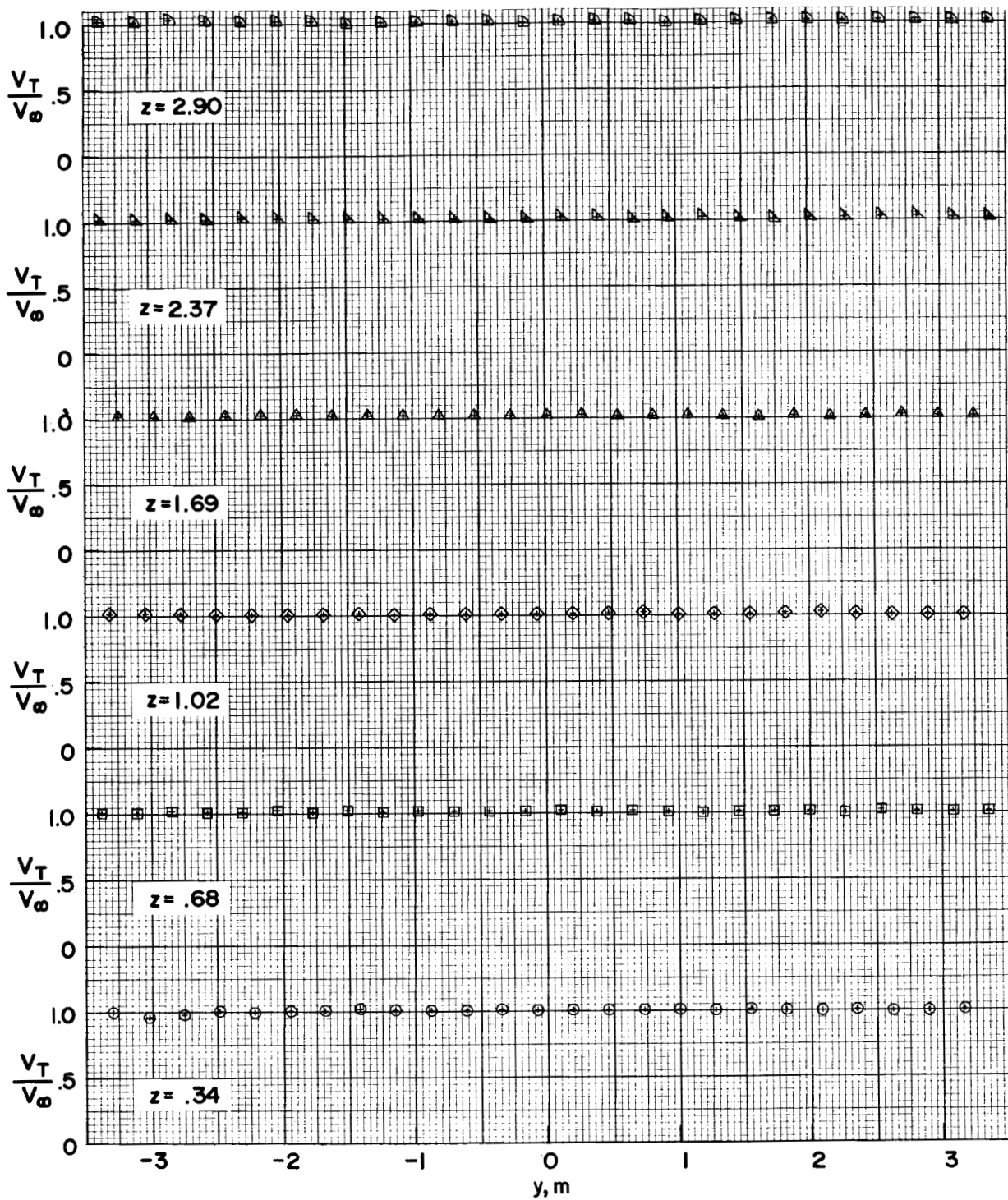
(a) $x = -4.06$ m.

Figure 7.- Velocity ratio, V_T/V_∞ as a function of lateral position y for empty tunnel.



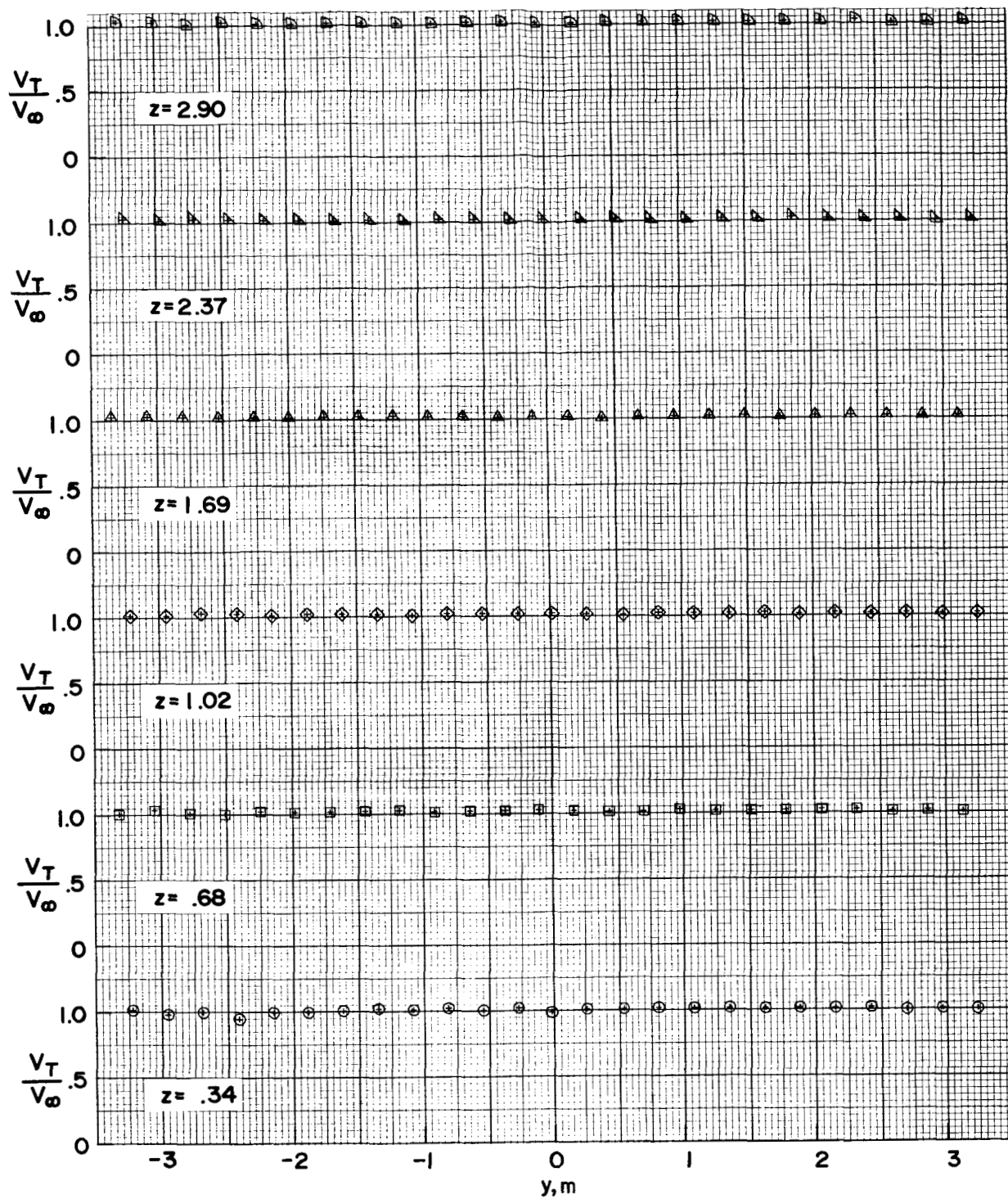
(b) $x = -3.39$ m.

Figure 7.- Continued.



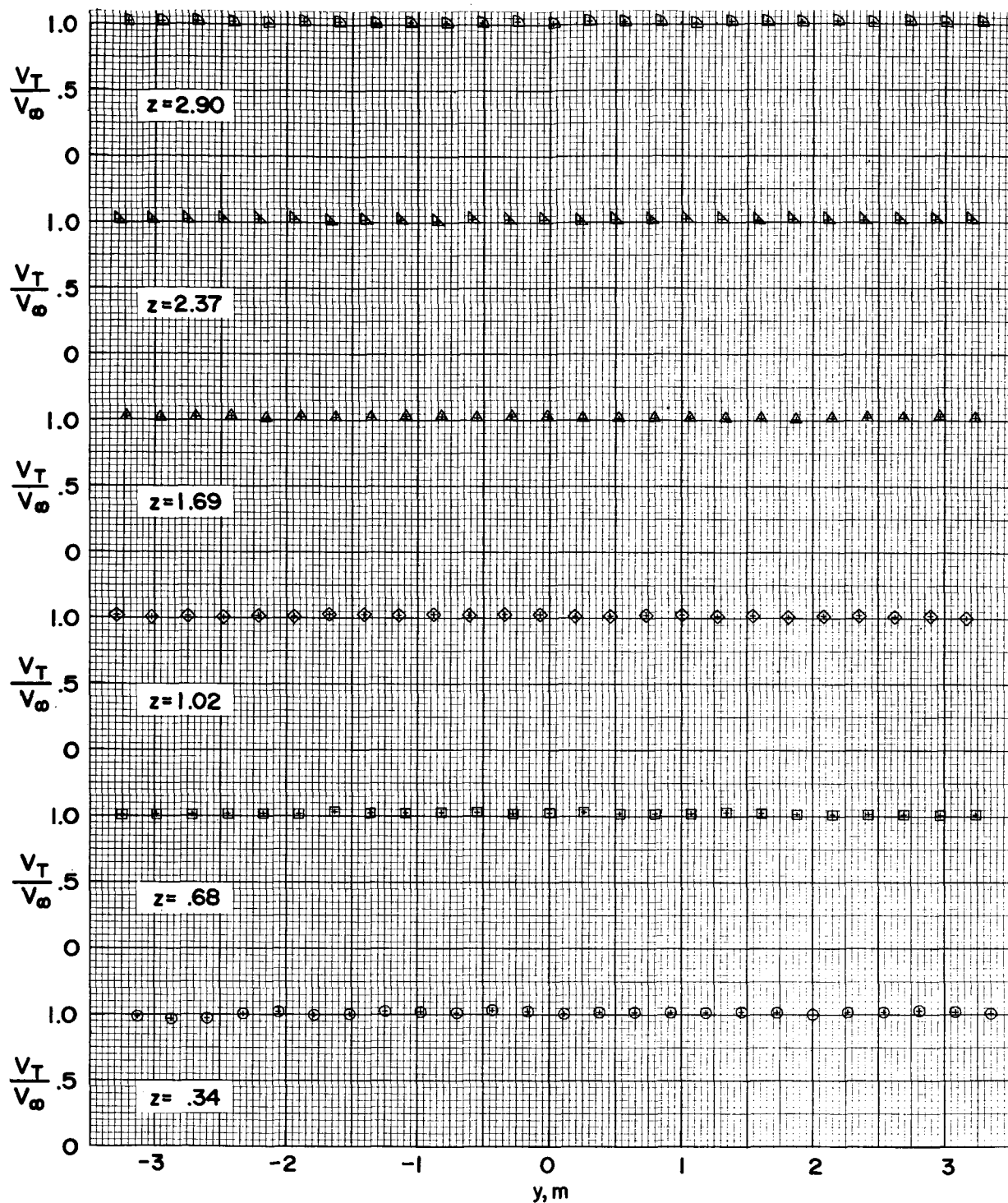
(c) $x = -2.71$ m.

Figure 7.- Continued.



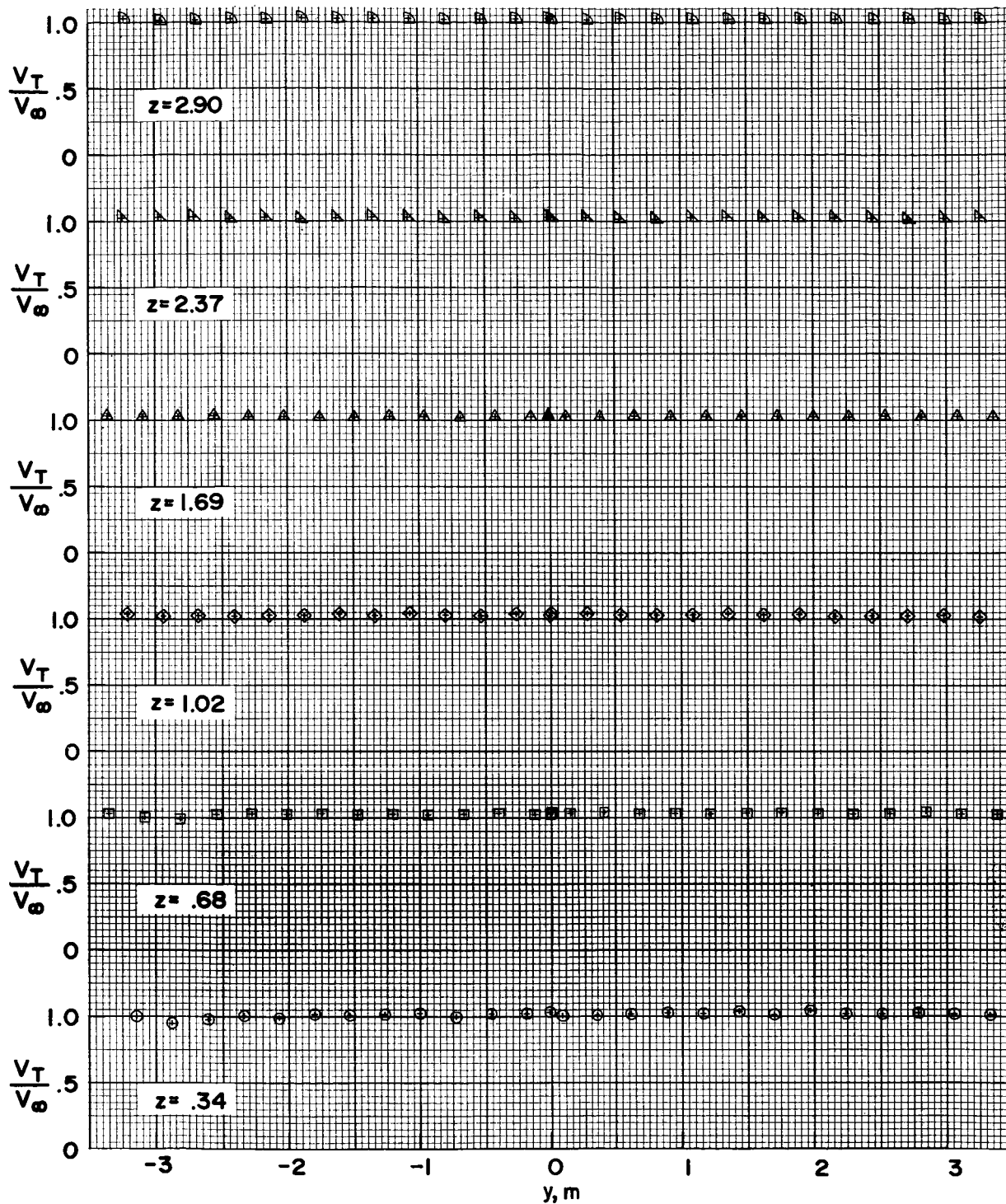
(d) $x = -2.03$ m.

Figure 7. - Continued.



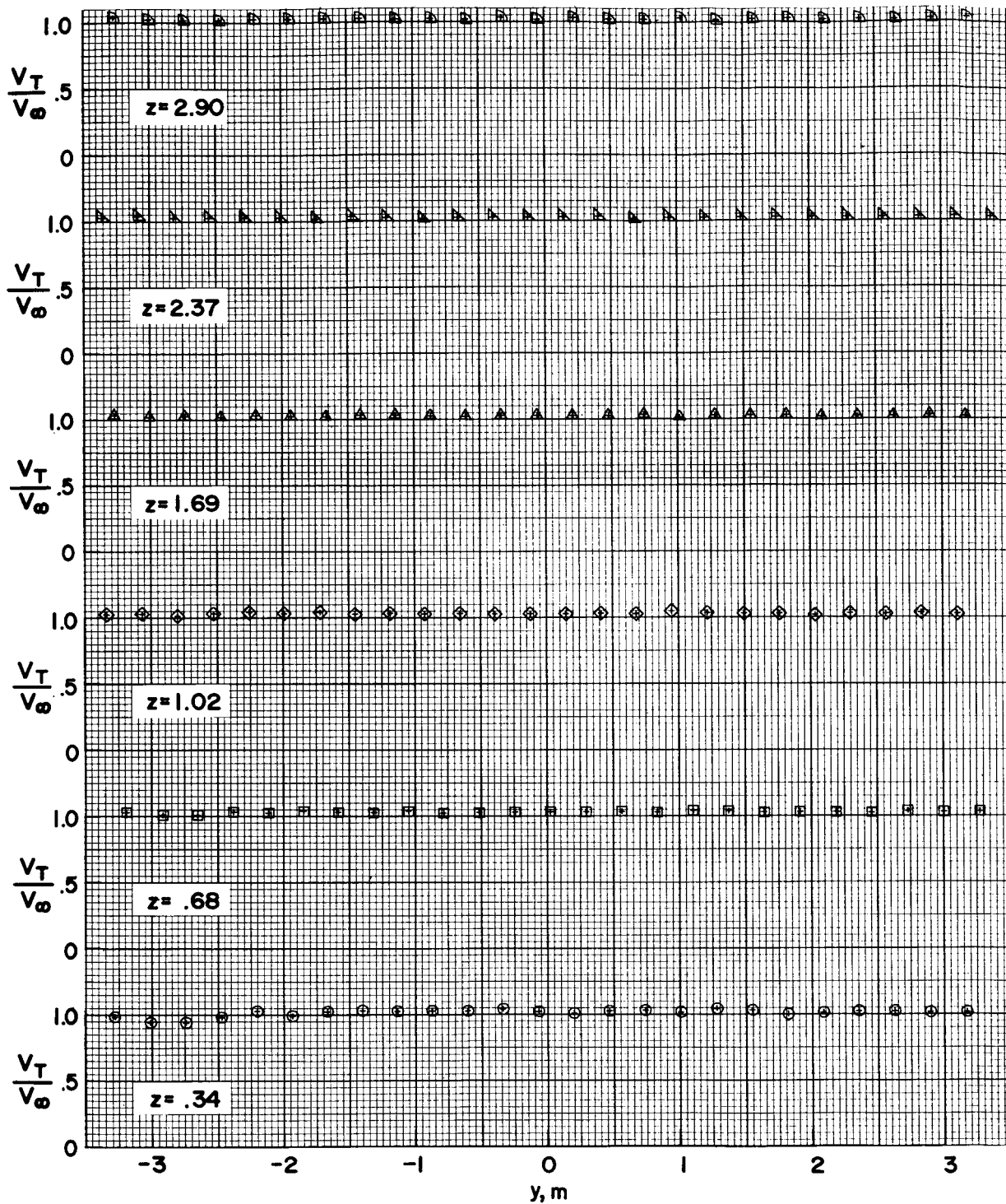
(e) $x = -1.35$ m.

Figure 7.- Continued.



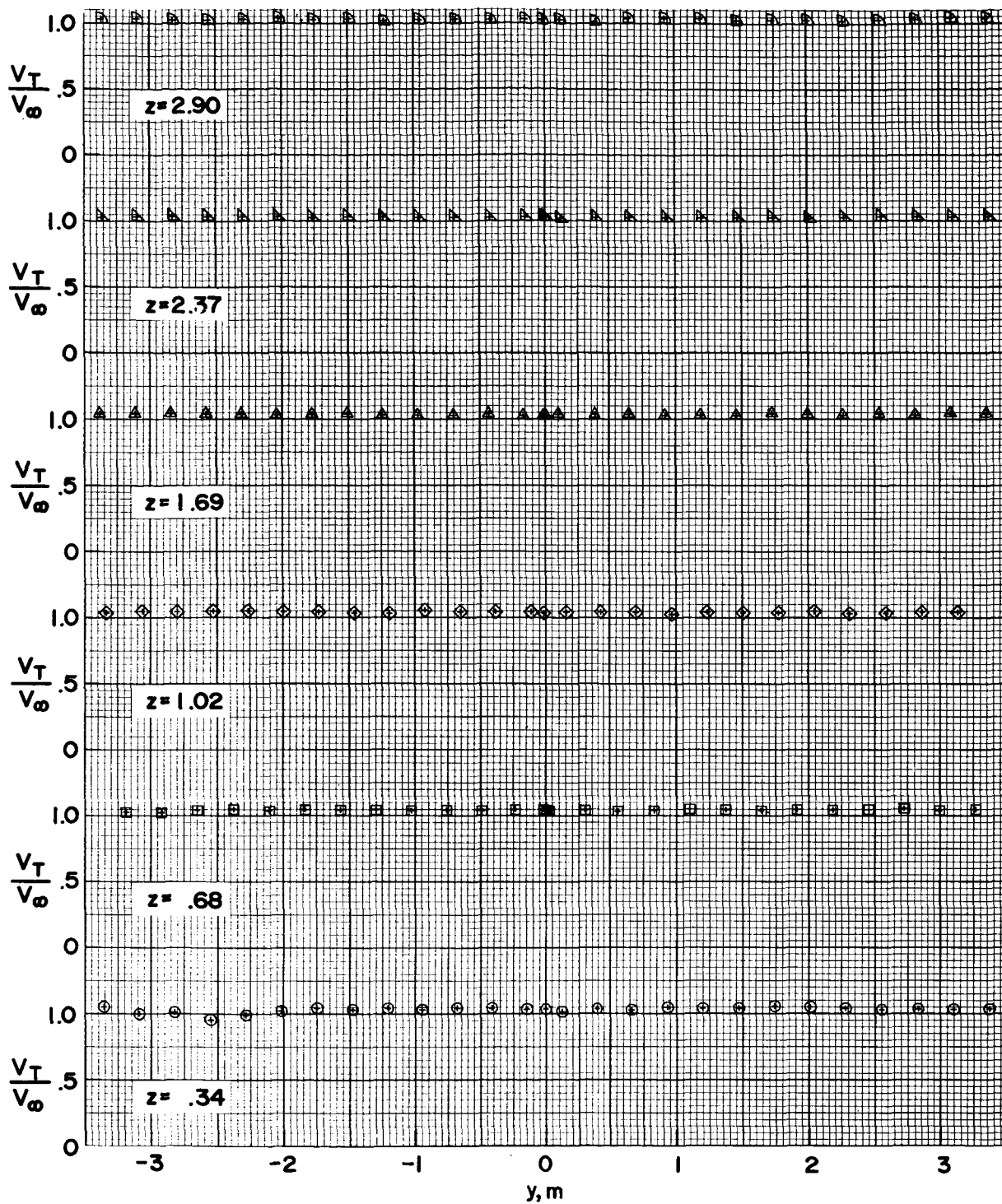
(f) $x = 0$ m.

Figure 7.- Continued.



(g) $x = 2.03$ m.

Figure 7.- Continued.



(h) $x = 4.06$ m.

Figure 7. - Concluded.

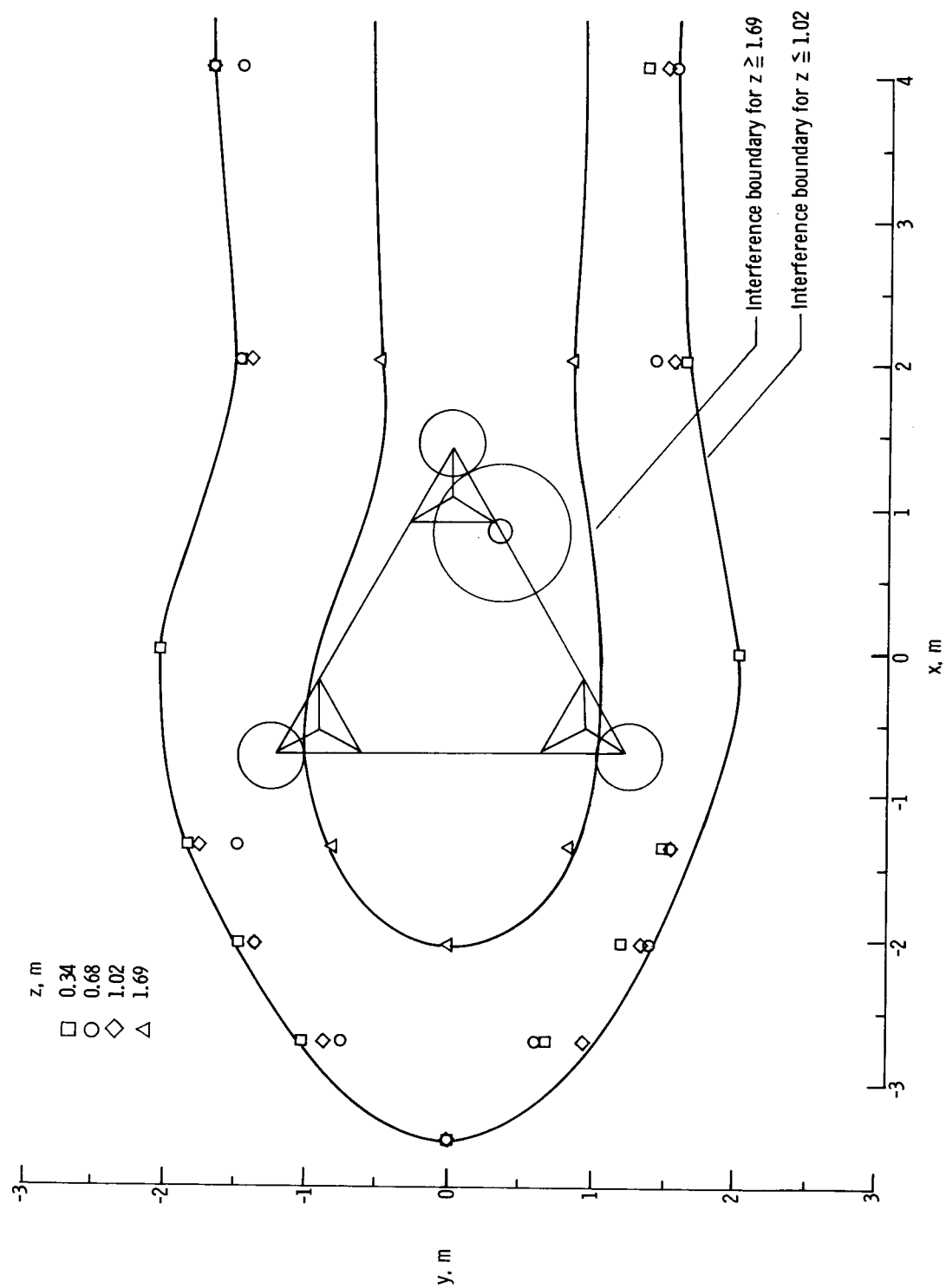


Figure 8.- The 5-percent wind-speed interference boundaries for model configuration 1 at $N_{Re} = 97\,600$.

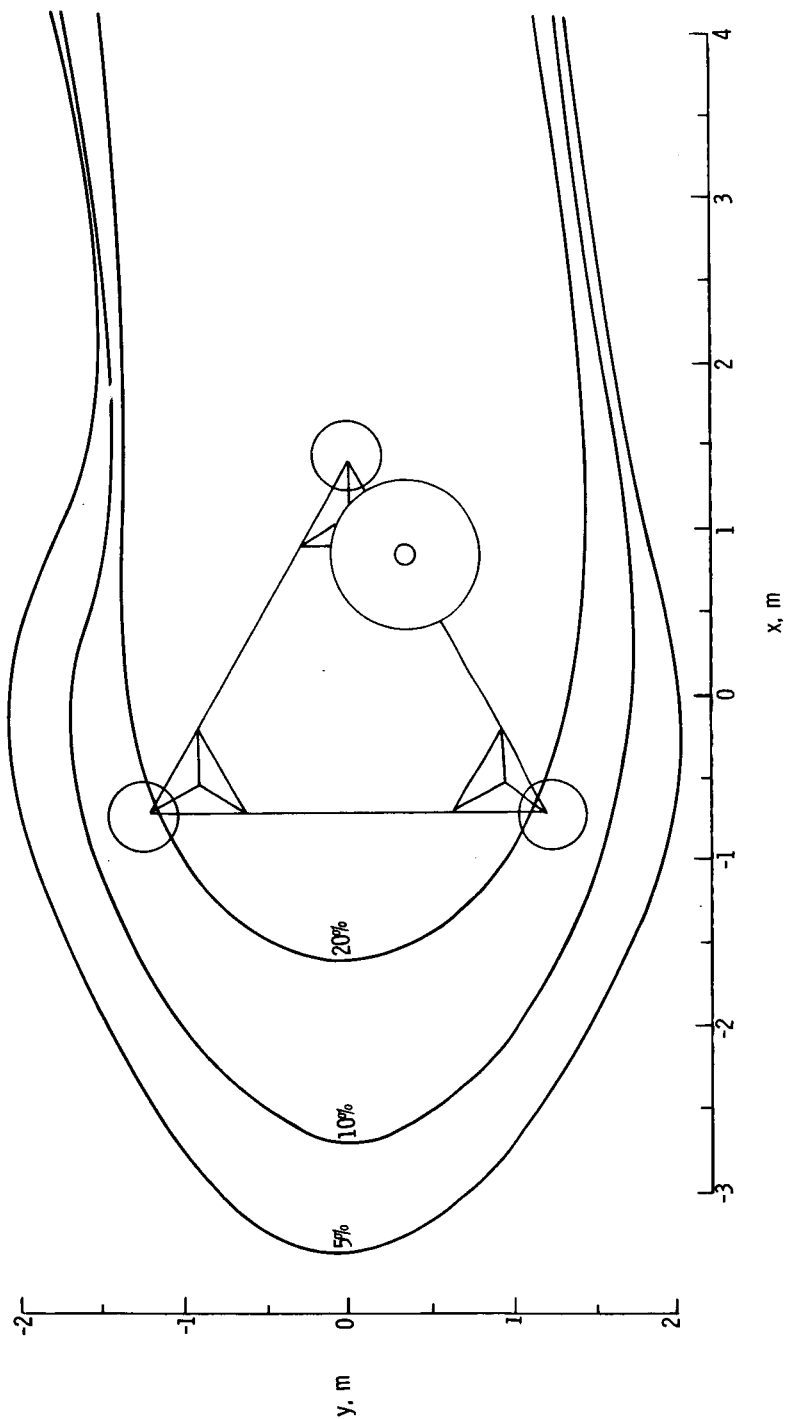
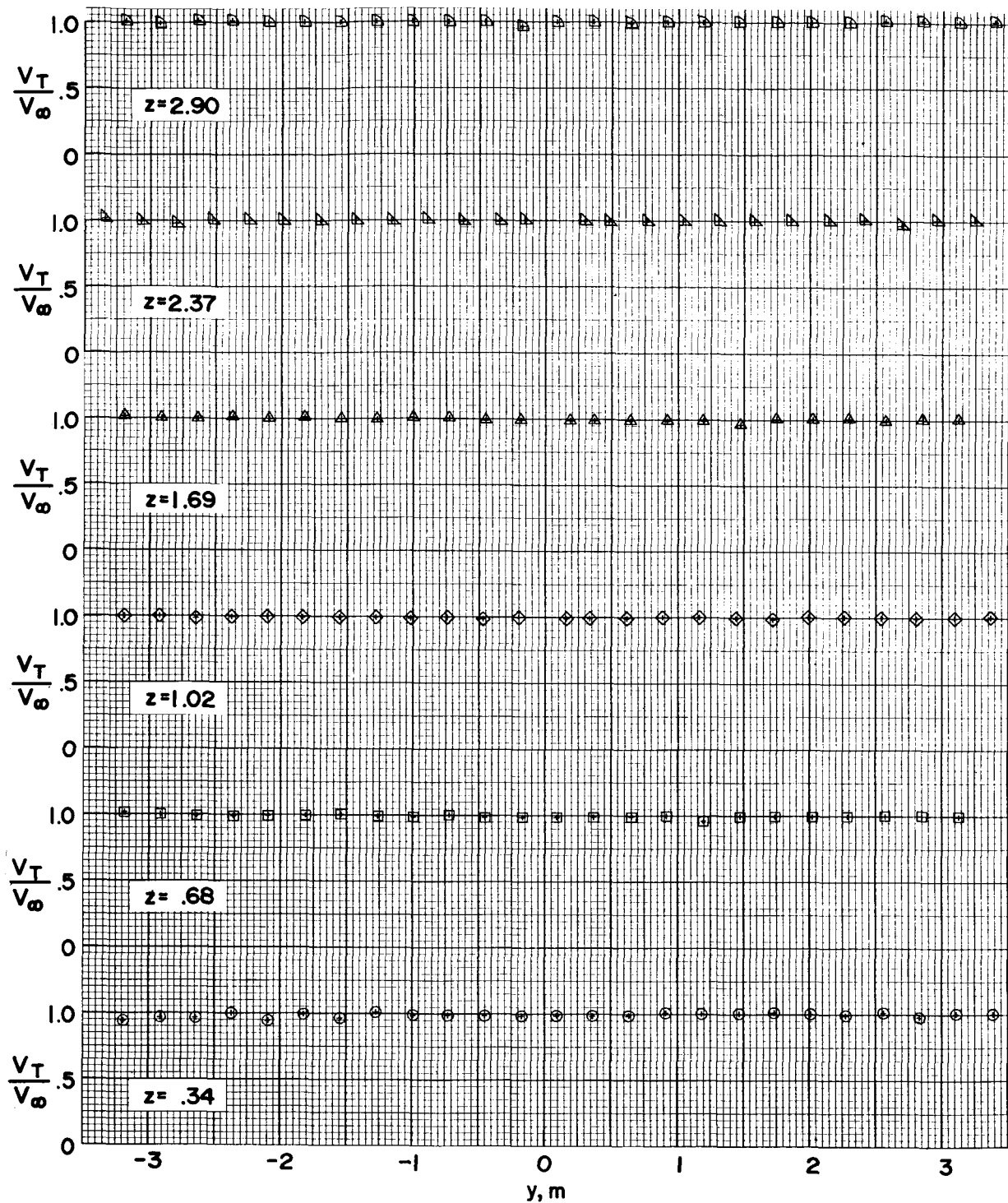
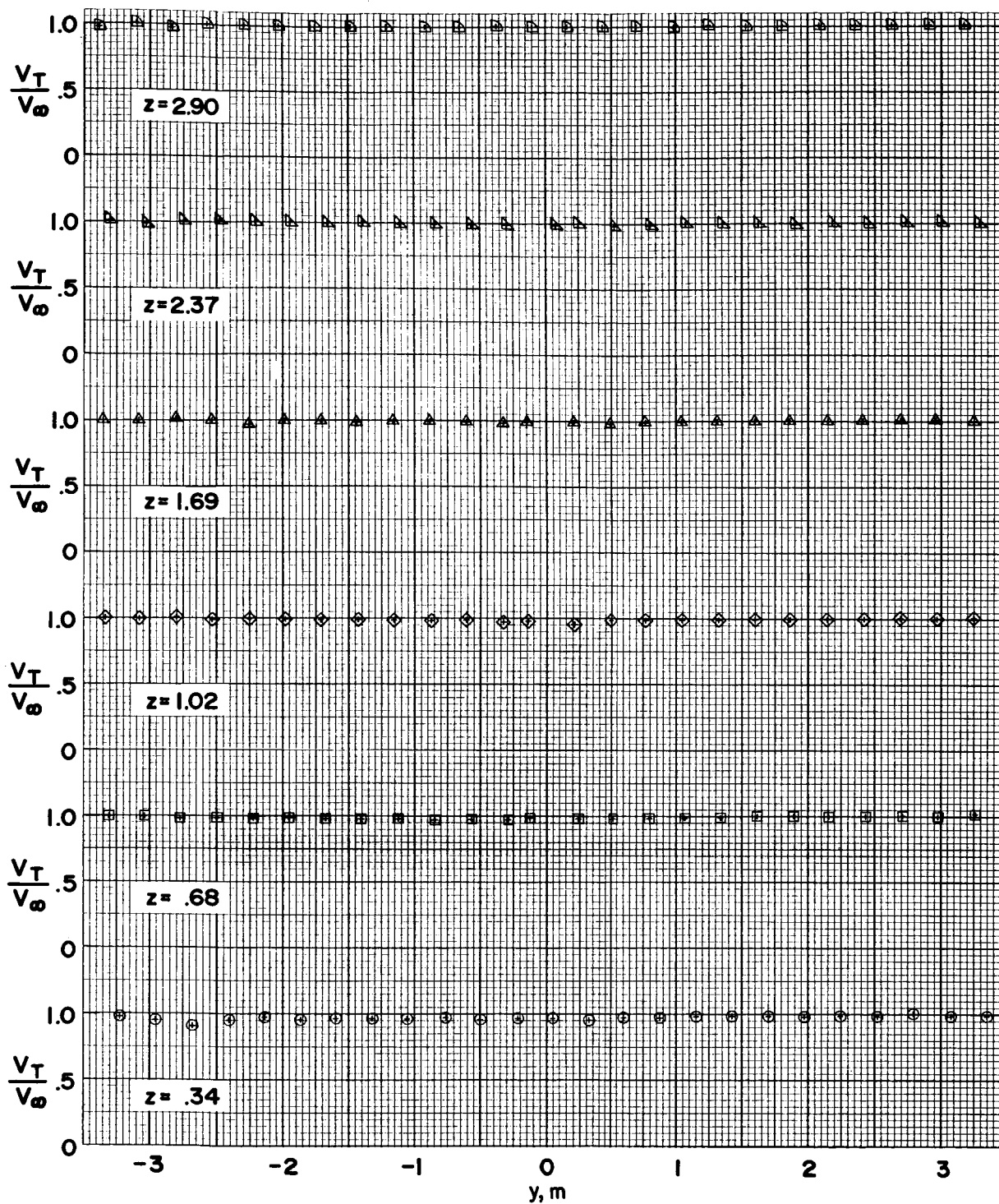


Figure 9. - The 5-, 10-, and 20-percent wind-speed interference boundaries for model configuration 1. $z = 0.34$ m.



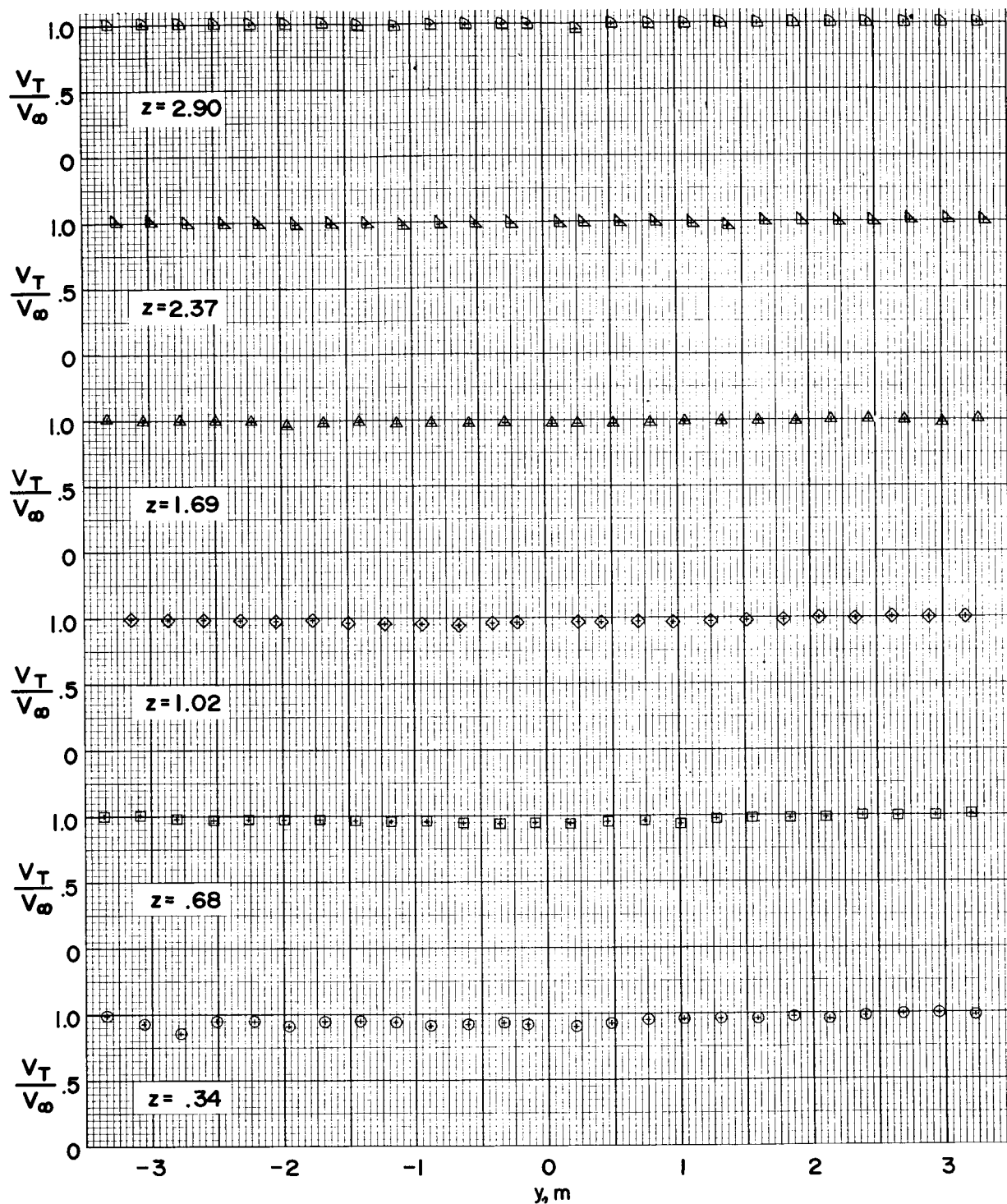
(a) $x = -4.06$ m.

Figure 10.- Velocity ratio V_T/V_∞ as a function of lateral position y for model configuration 1.



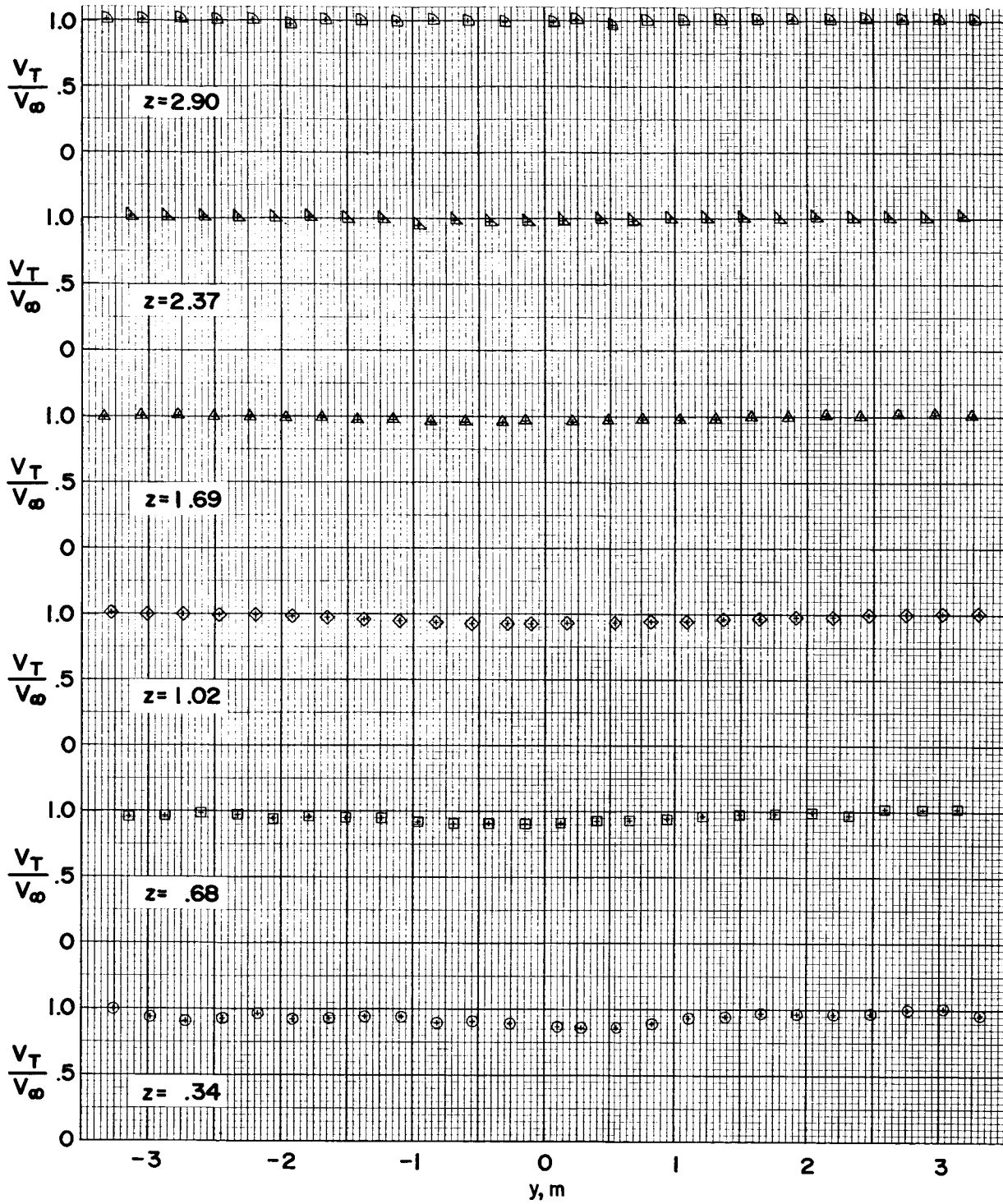
(b) $x = -3.39$ m.

Figure 10.- Continued.



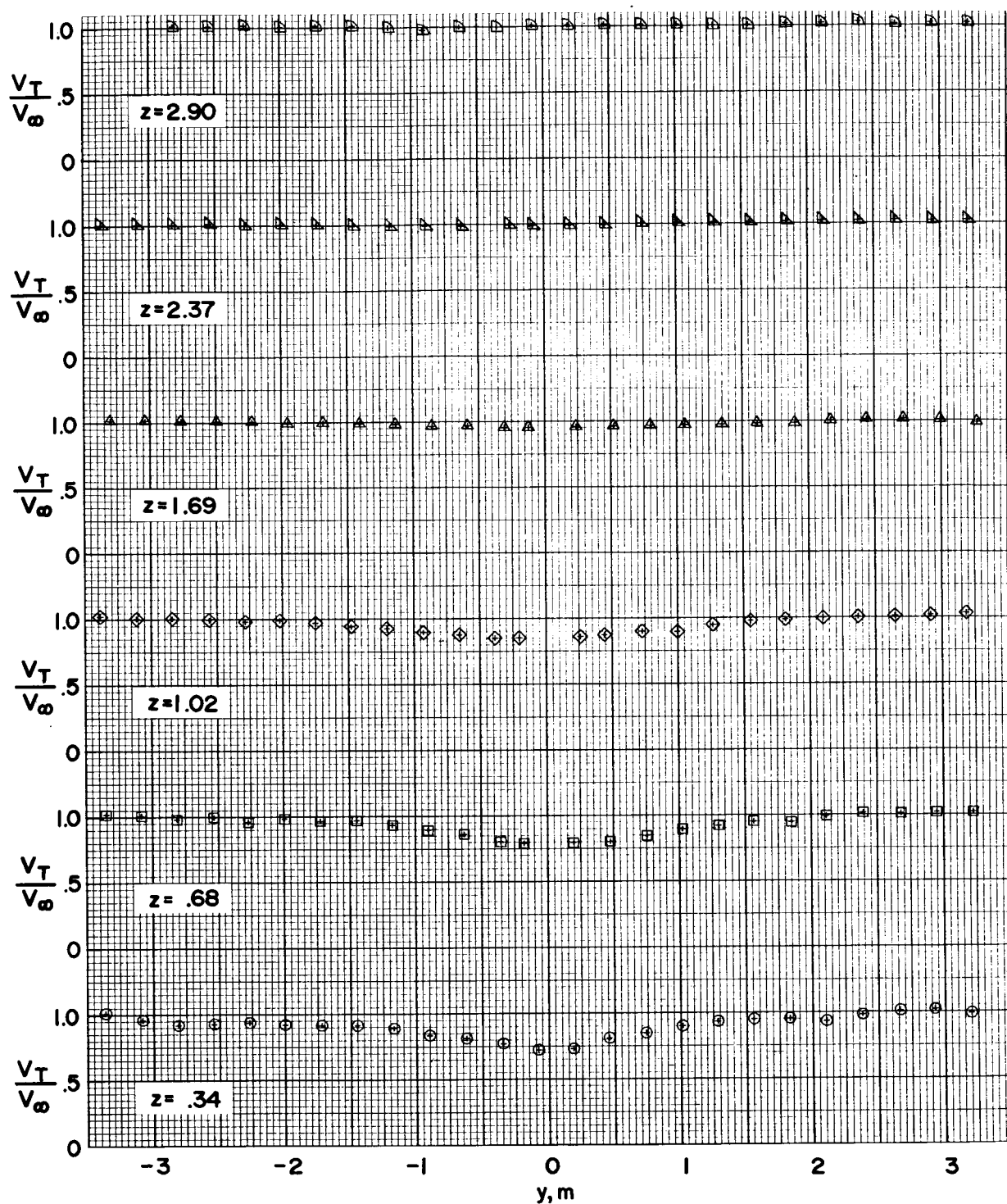
(c) $x = -2.71$ m.

Figure 10.- Continued.



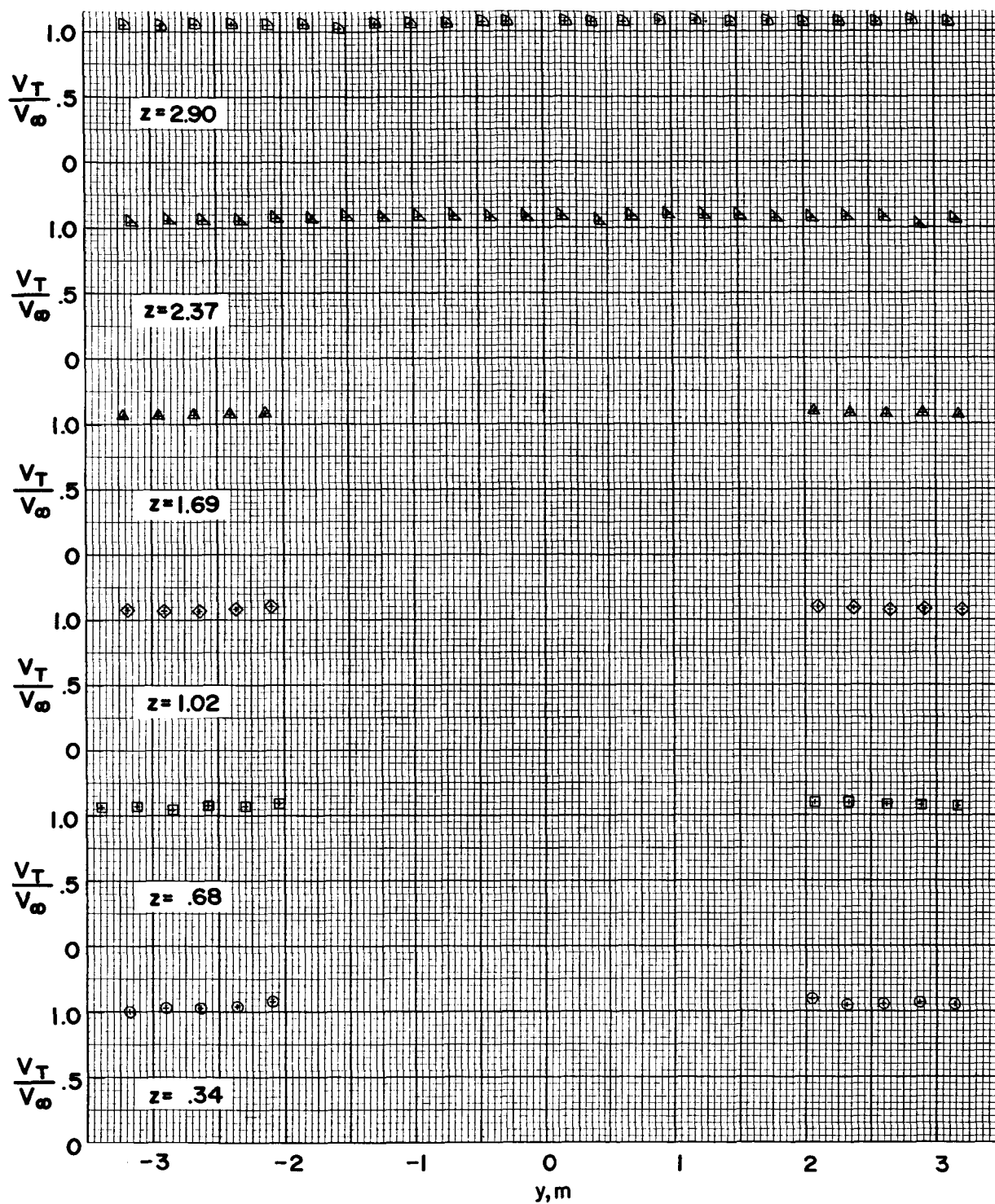
(d) $x = -2.03$ m.

Figure 10.- Continued.



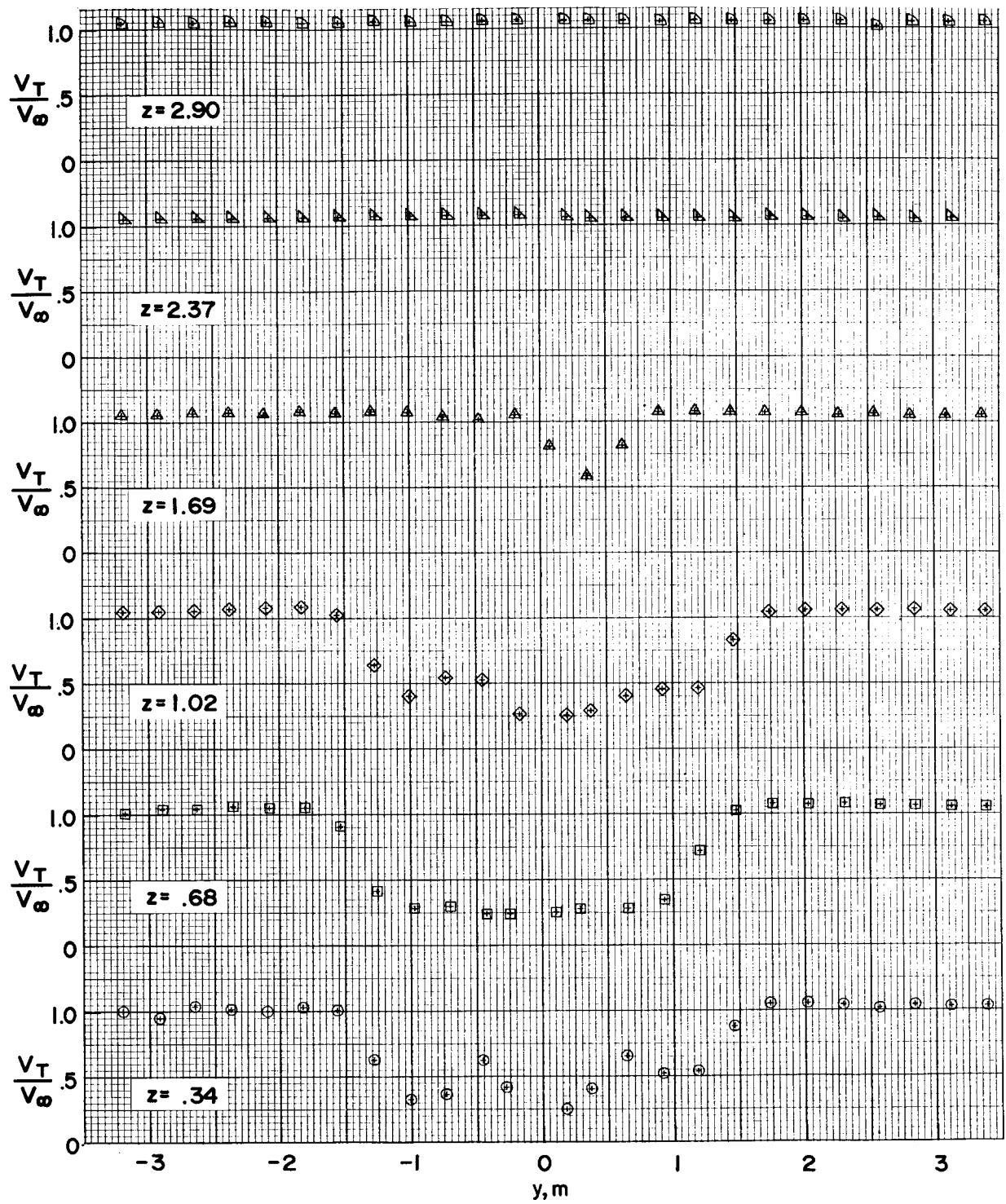
(e) $x = -1.35$ m.

Figure 10.- Continued.



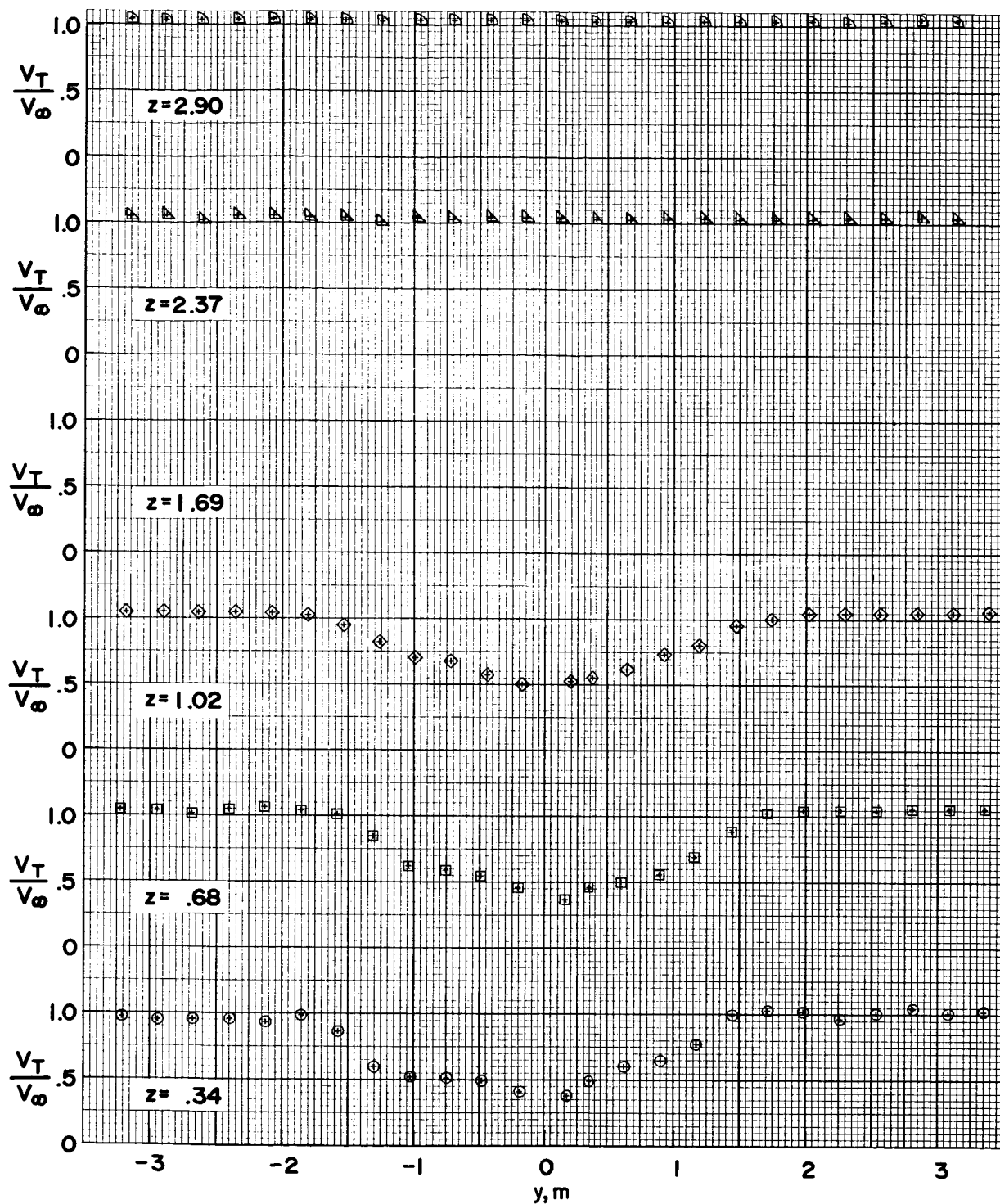
(f) $x = 0$ m.

Figure 10.- Continued.



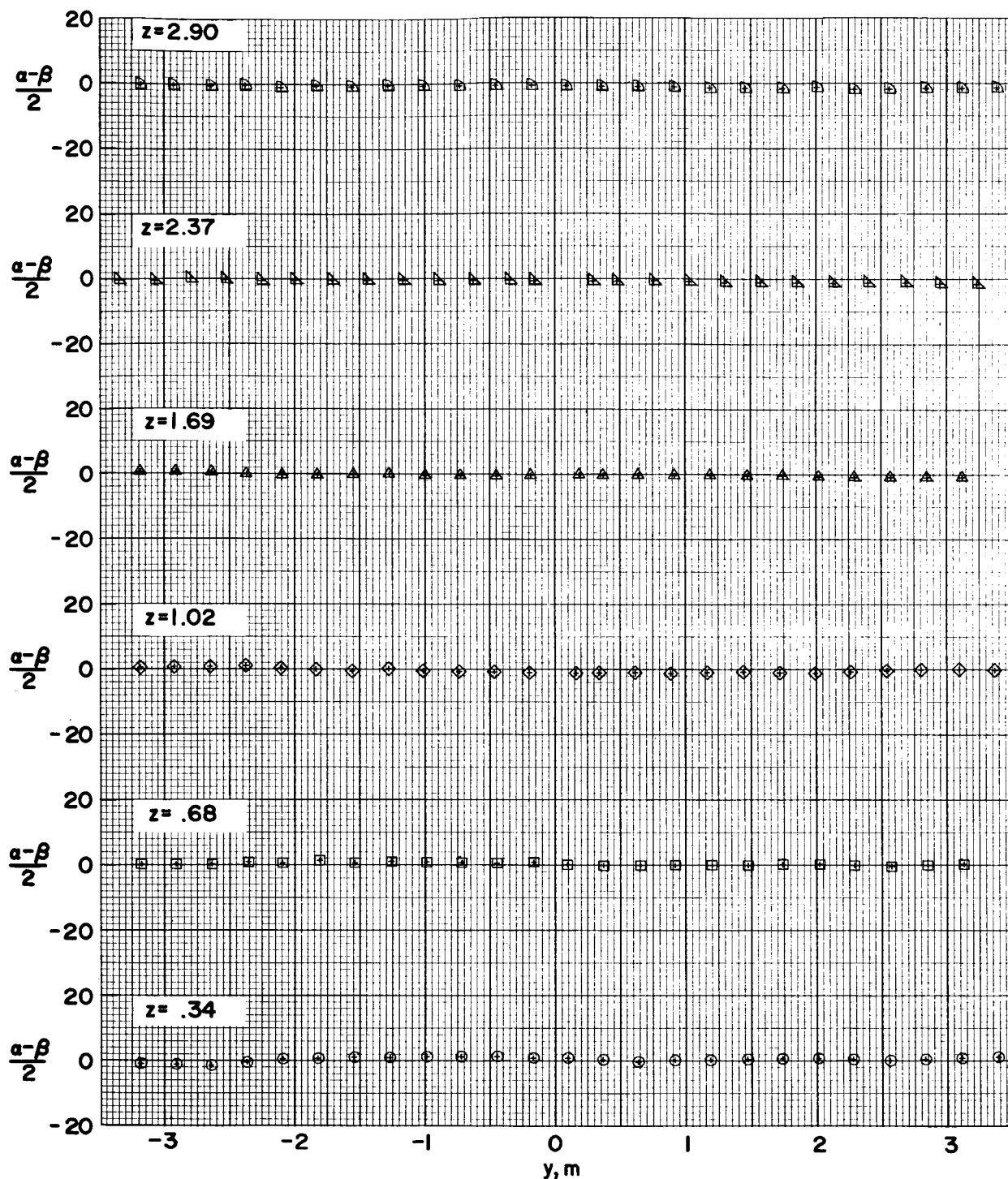
(g) $x = 2.03$ m.

Figure 10.- Continued.



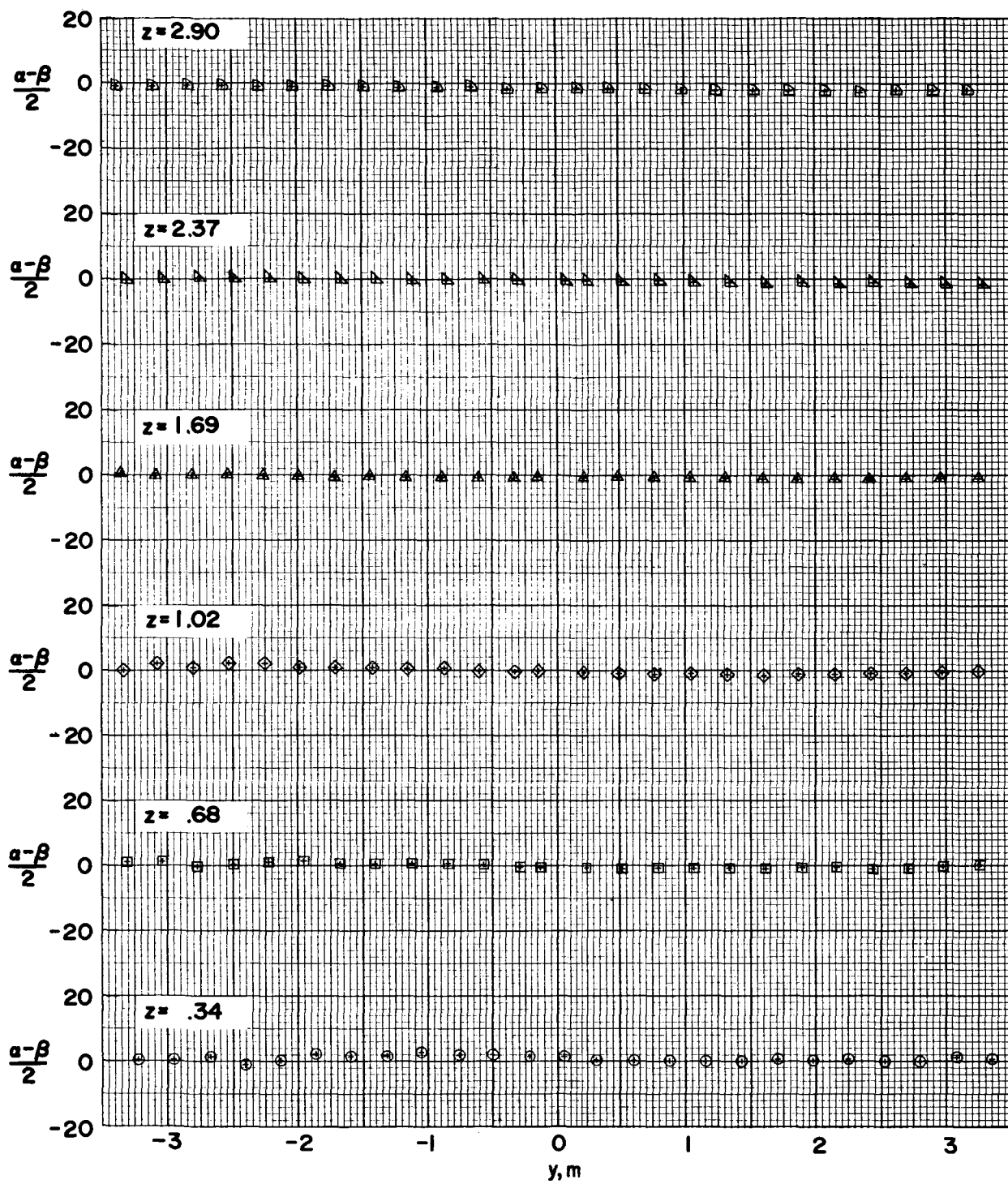
(h) $x = 4.06$ m.

Figure 10. - Concluded.



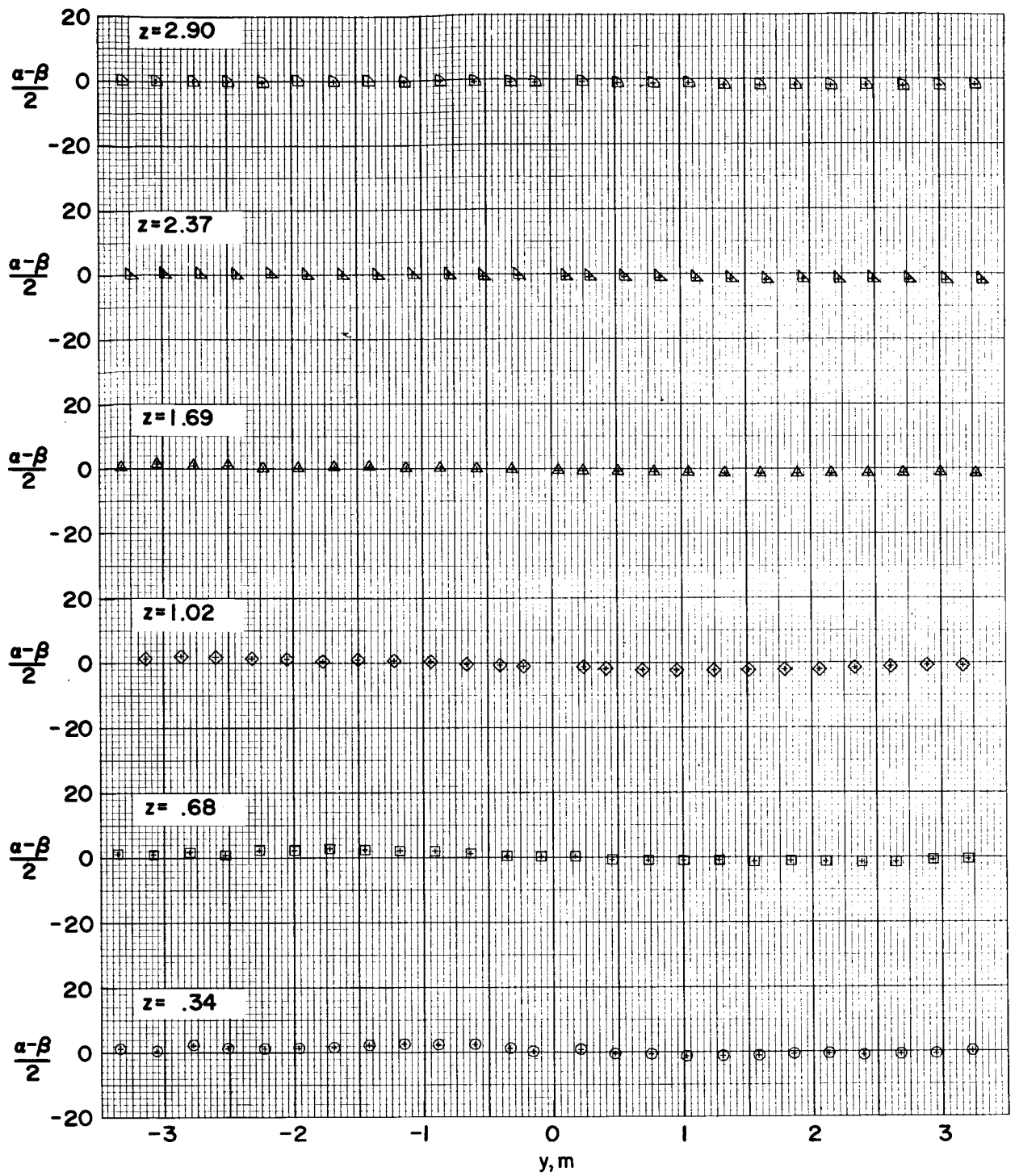
(a) $x = -4.06$ m.

Figure 11.- Local flow angle $\frac{\alpha - \beta}{2}$ as a function of lateral position y for model configuration 1.



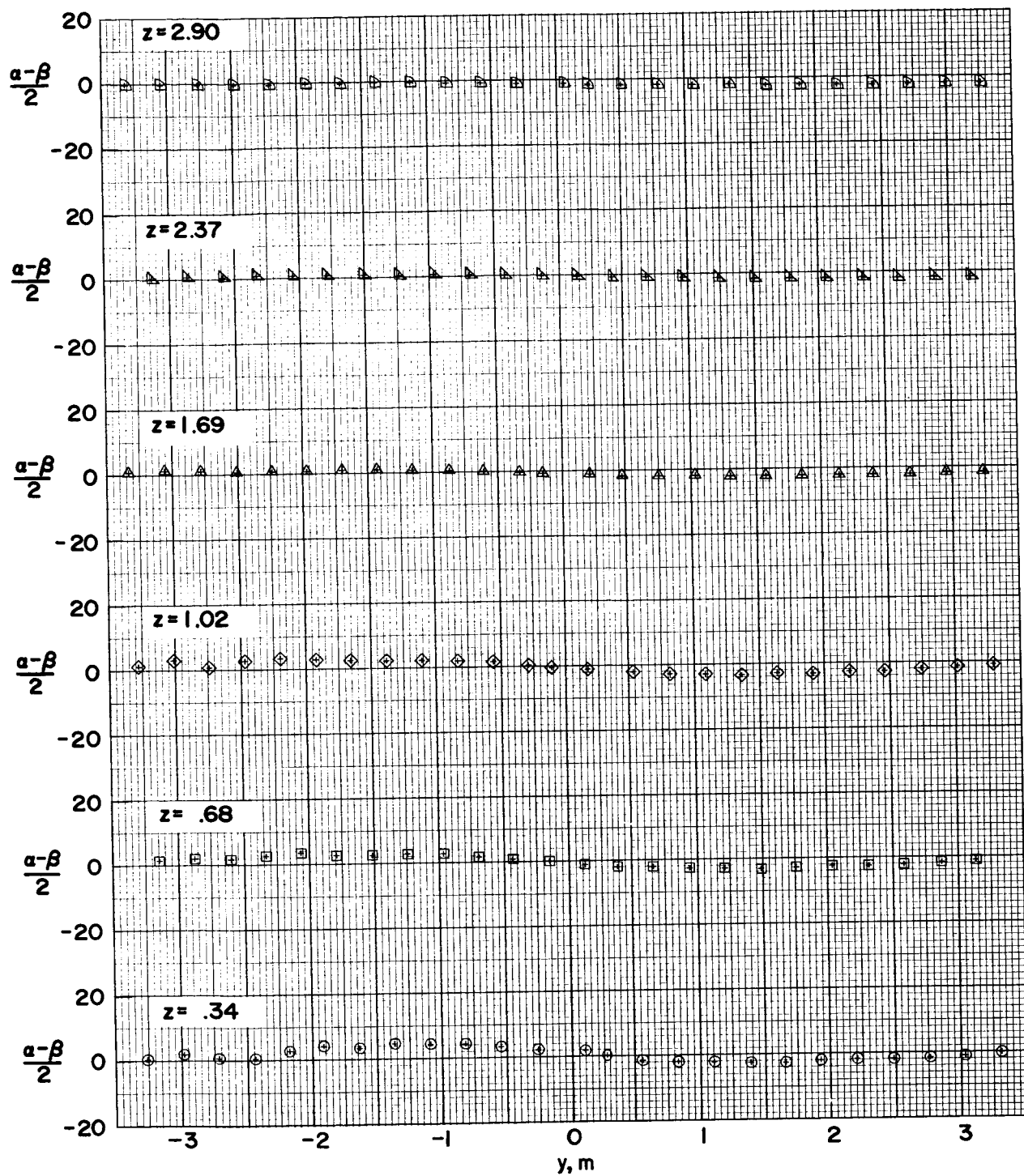
(b) $x = -3.39$ m.

Figure 11.- Continued.



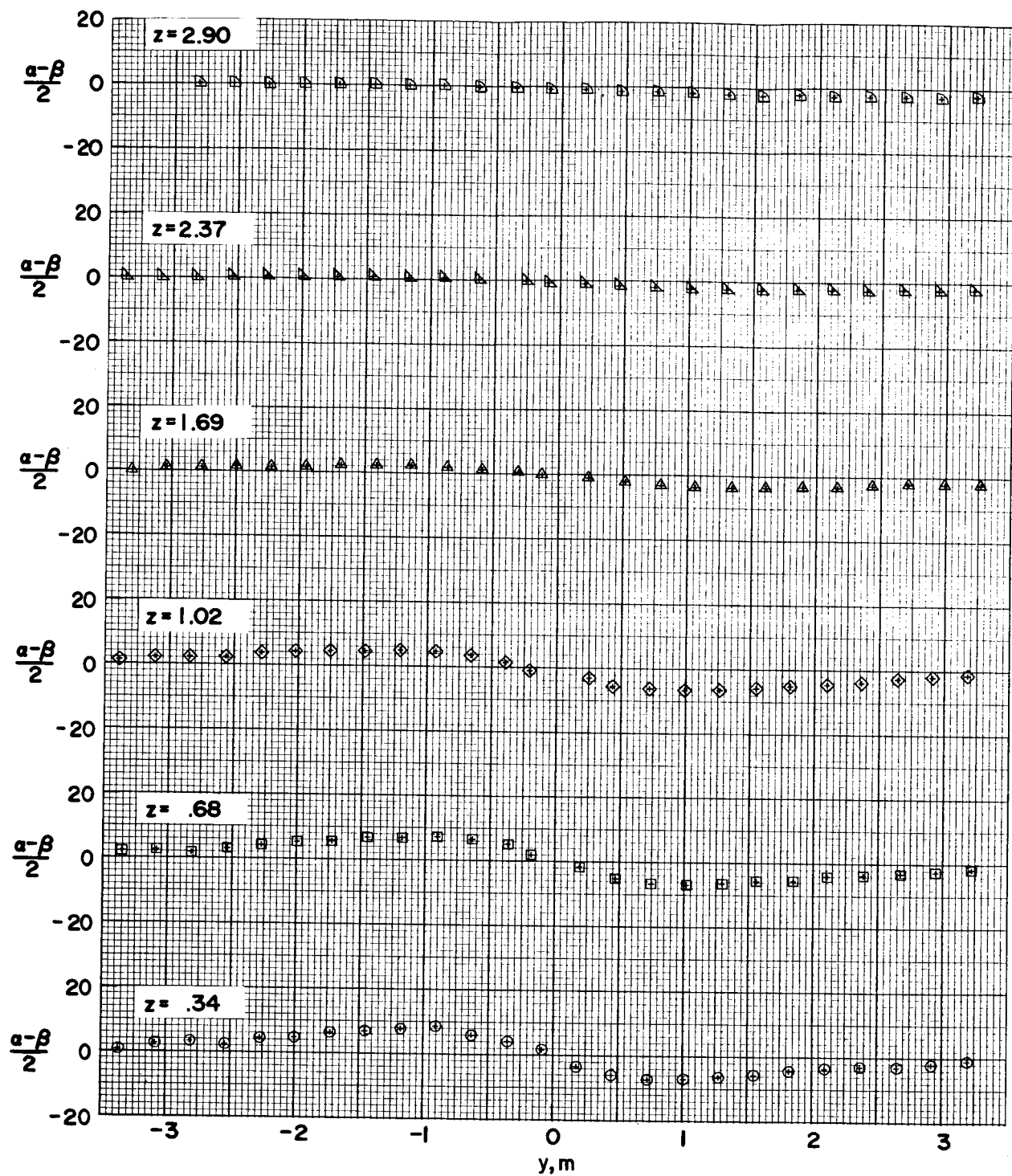
(c) $x = -2.71$ m.

Figure 11.- Continued.



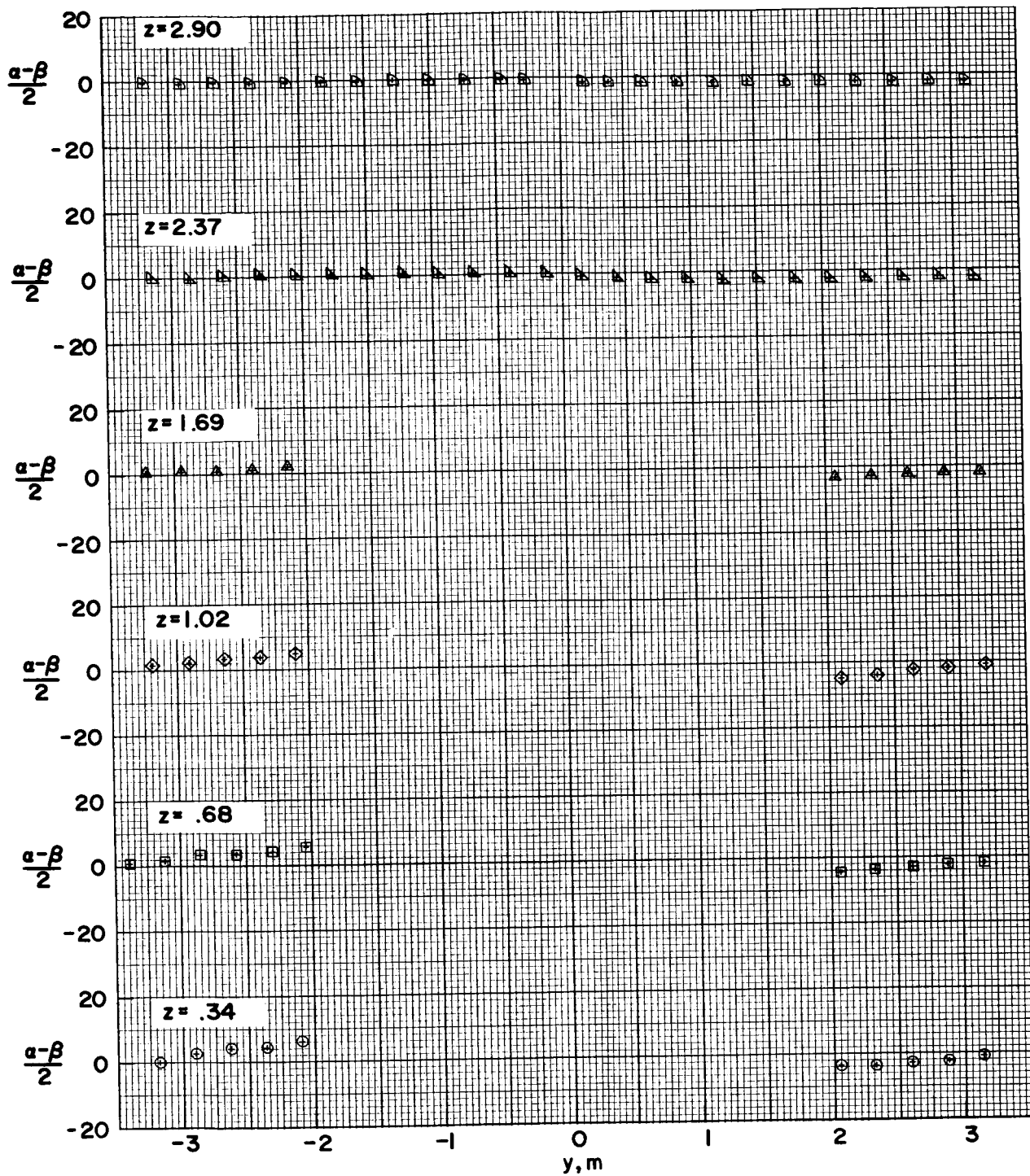
(d) $x = -2.03$ m.

Figure 11. - Continued.



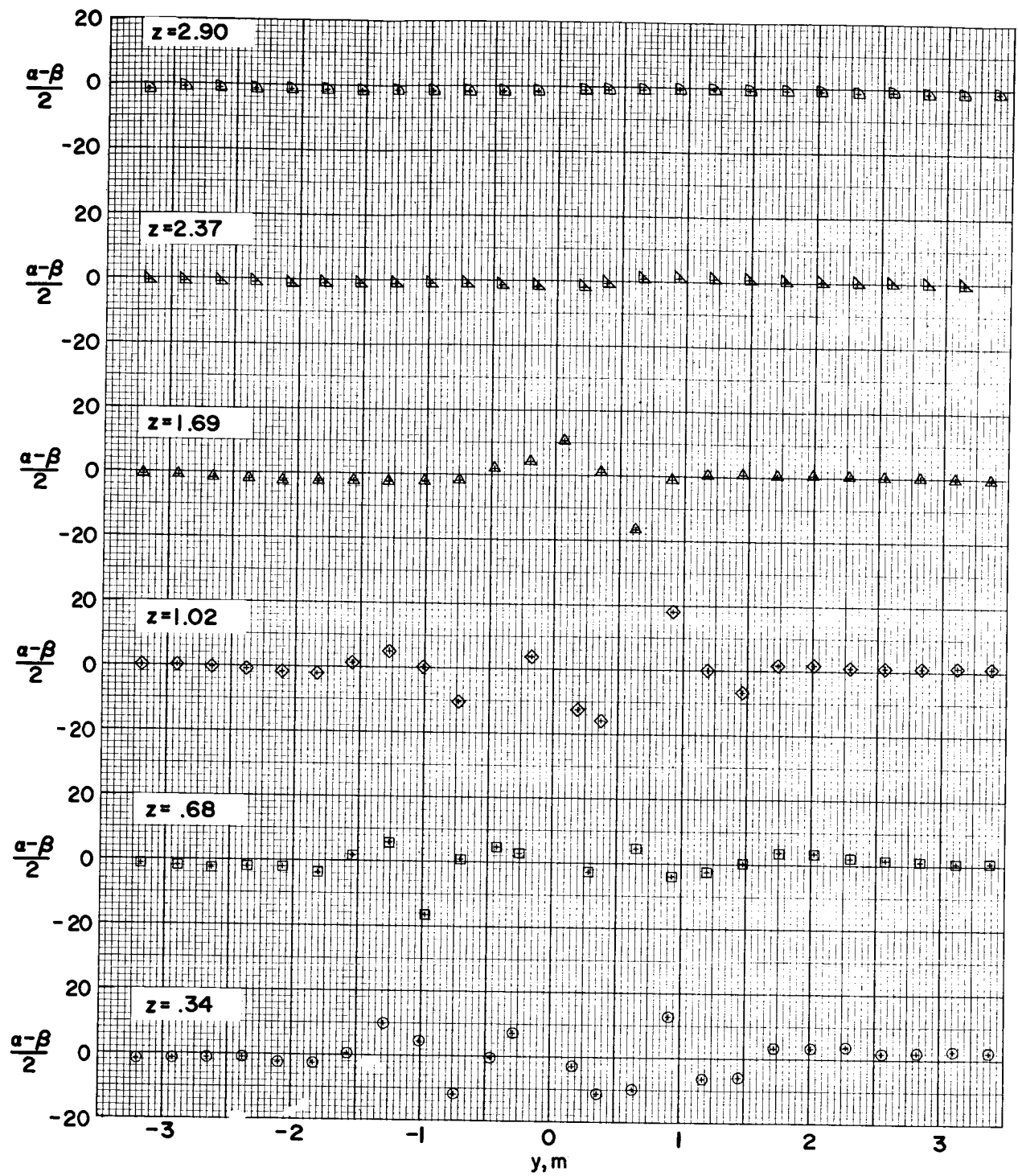
(e) $x = -1.35$ m.

Figure 11. - Continued.



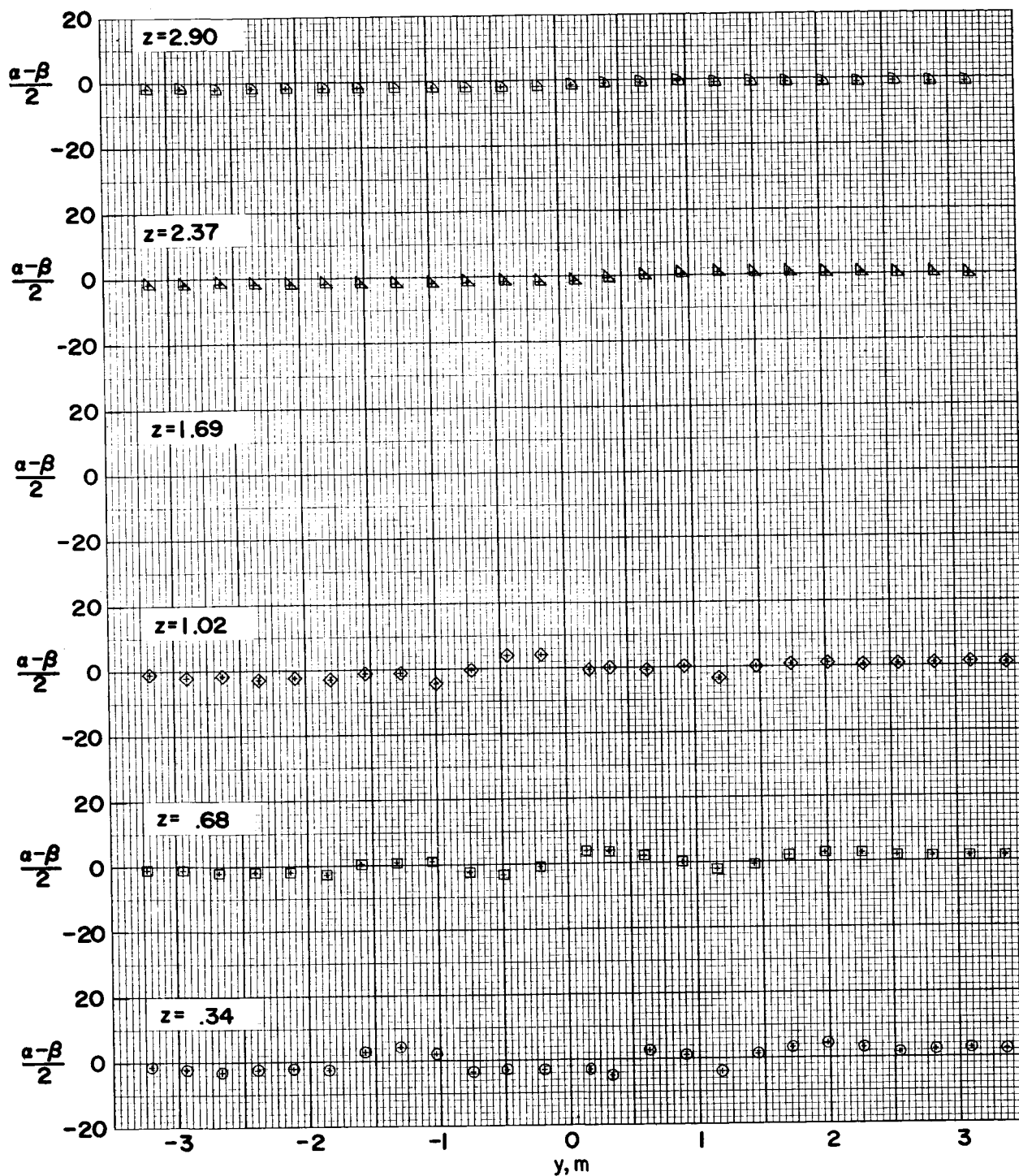
(f) $x = 0$ m.

Figure 11.- Continued.



(g) $x = 2.03$ m.

Figure 11. - Continued.



(h) $x = 4.06$ m.

Figure 11. - Concluded.

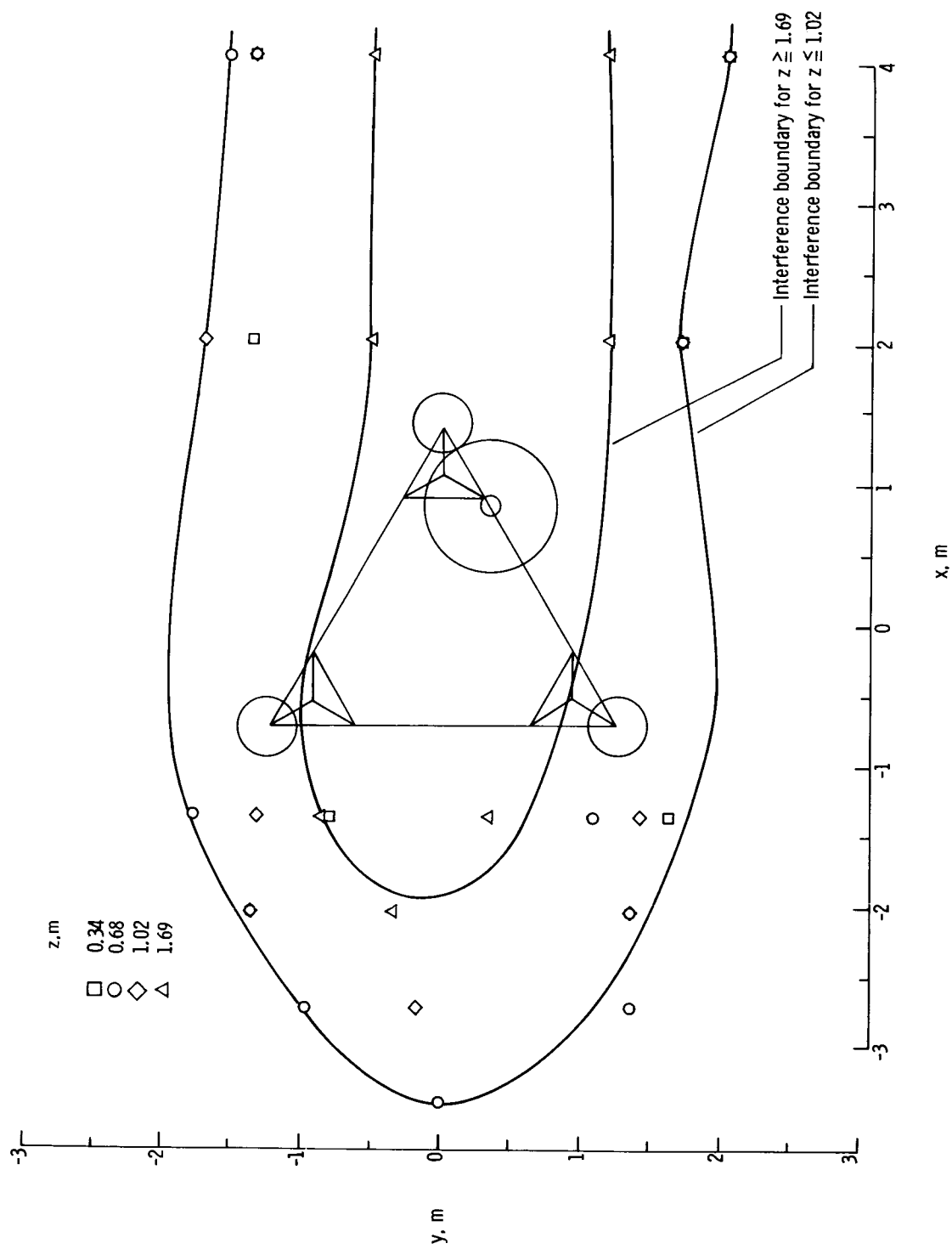


Figure 12.- The 5-percent wind-speed interference boundaries for model configuration 1 at $N_{Re} = 4400$.

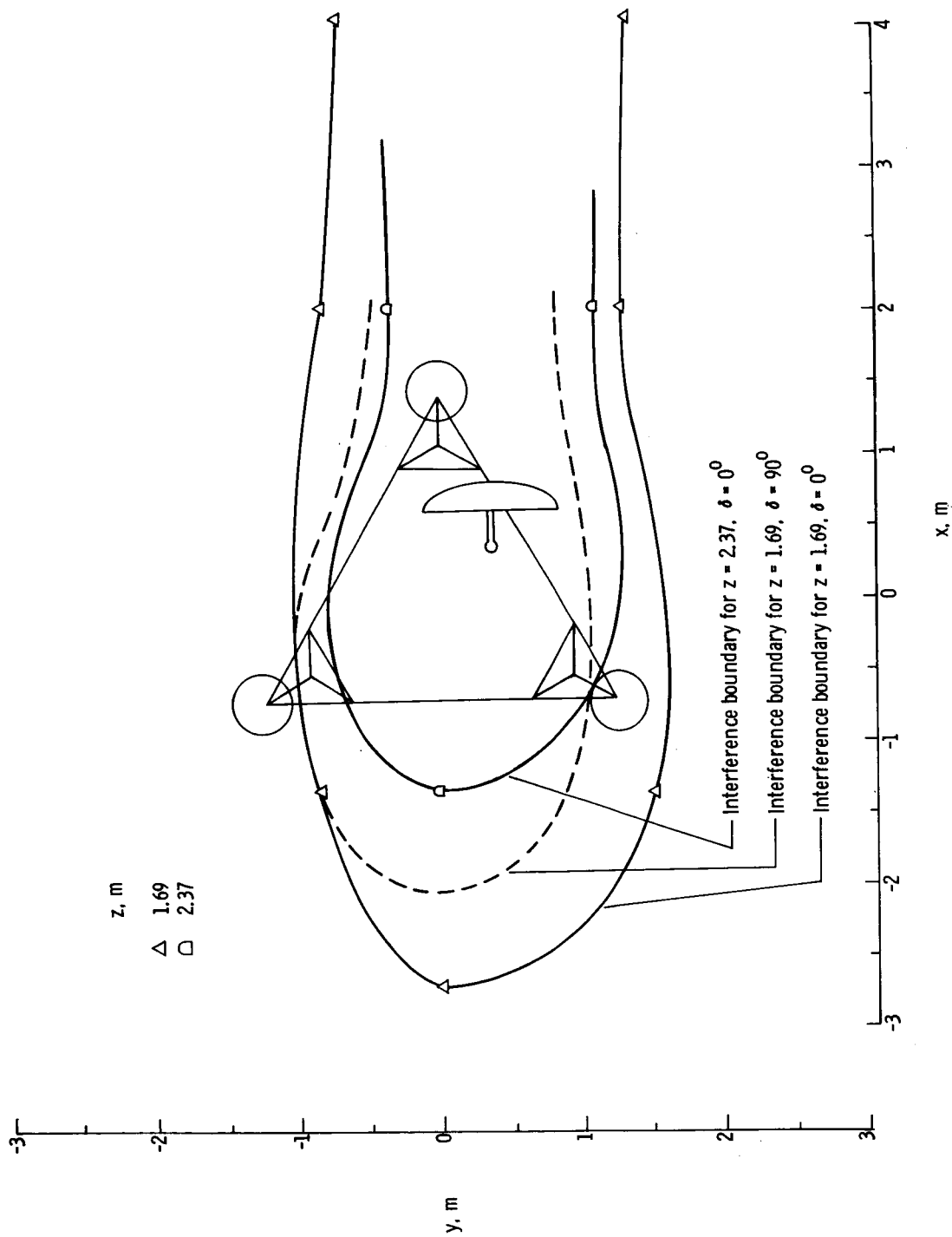
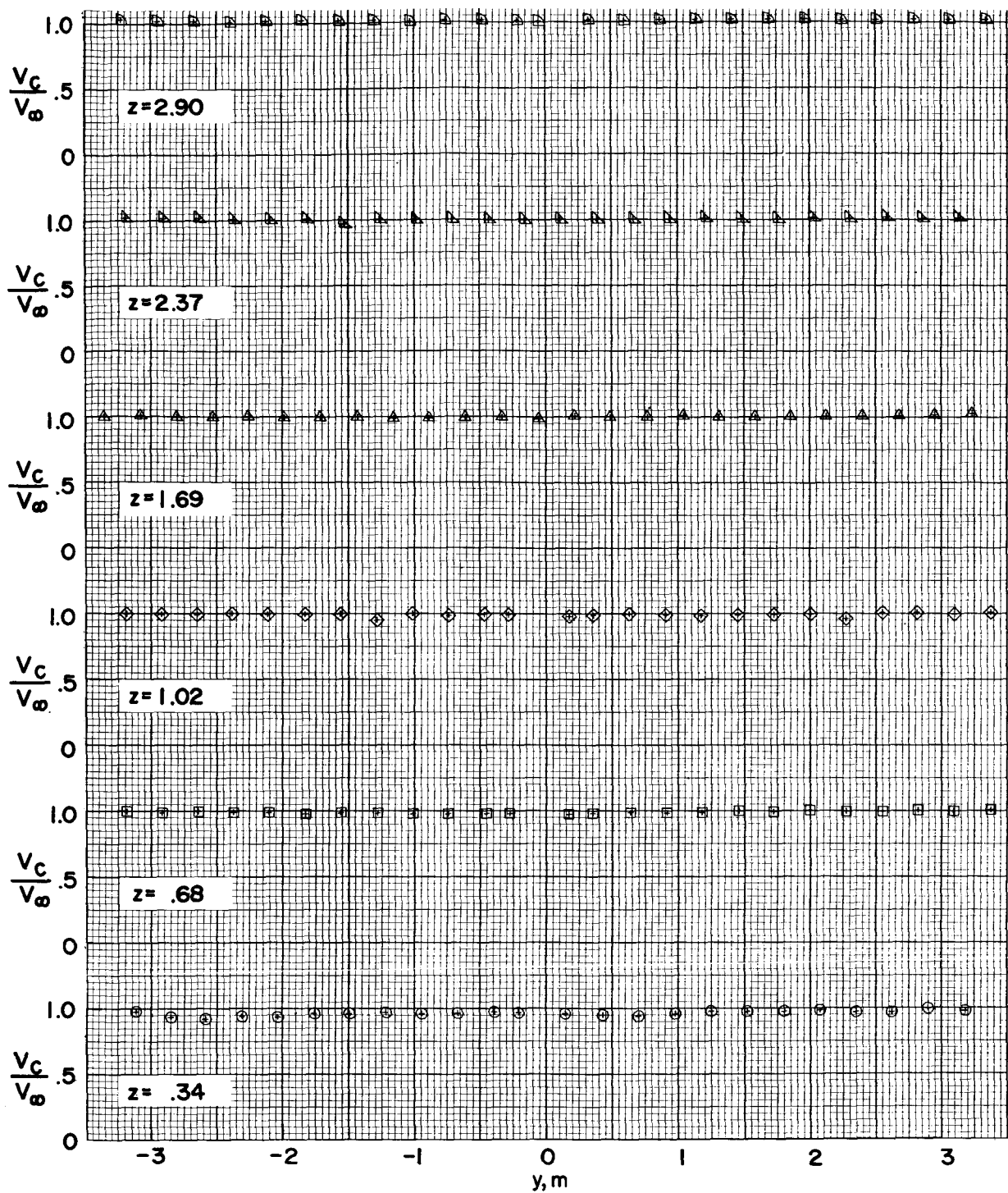
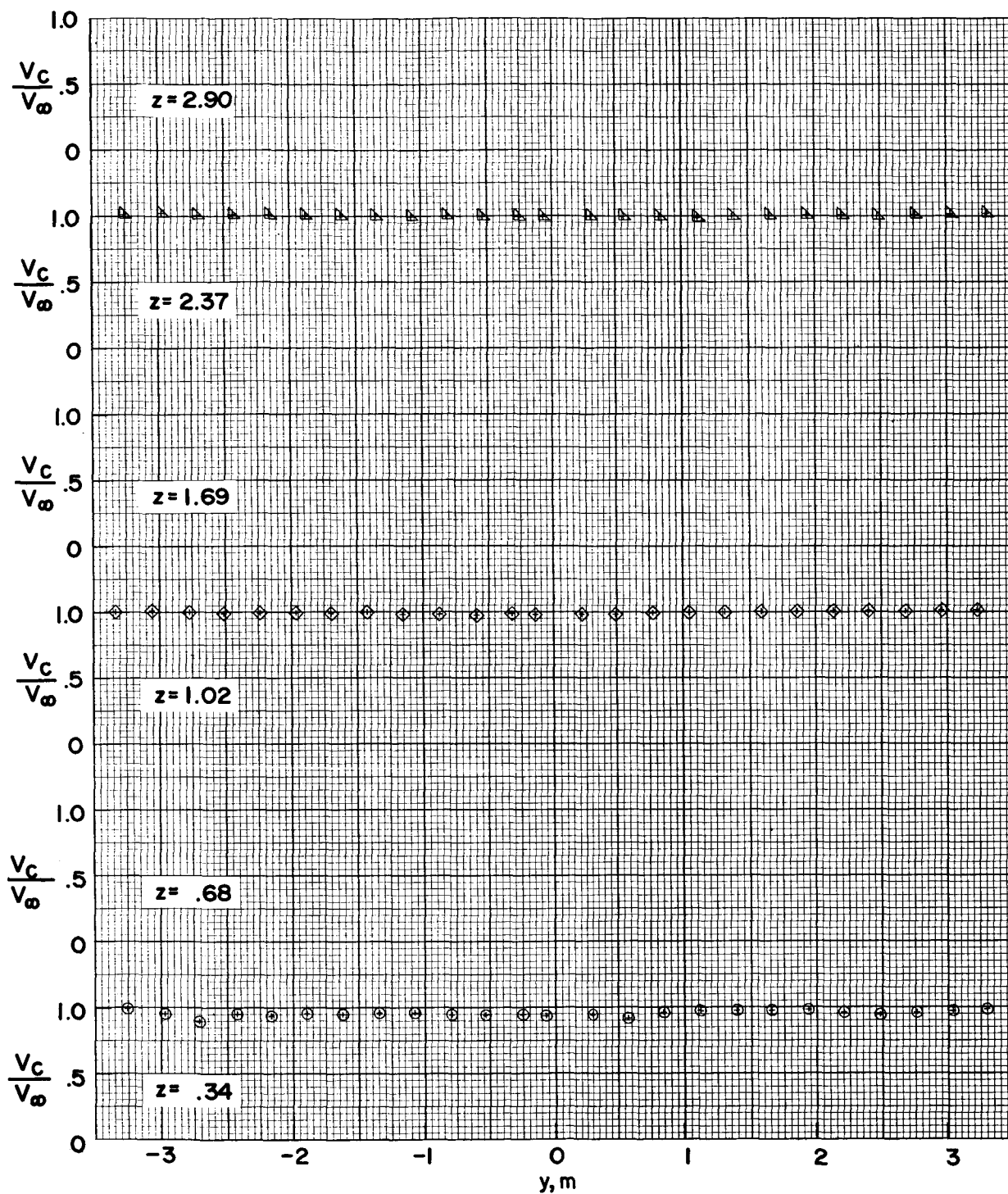


Figure 13. - Effect of antenna elevation on 5-percent wind-speed interference boundaries for model configuration 2.



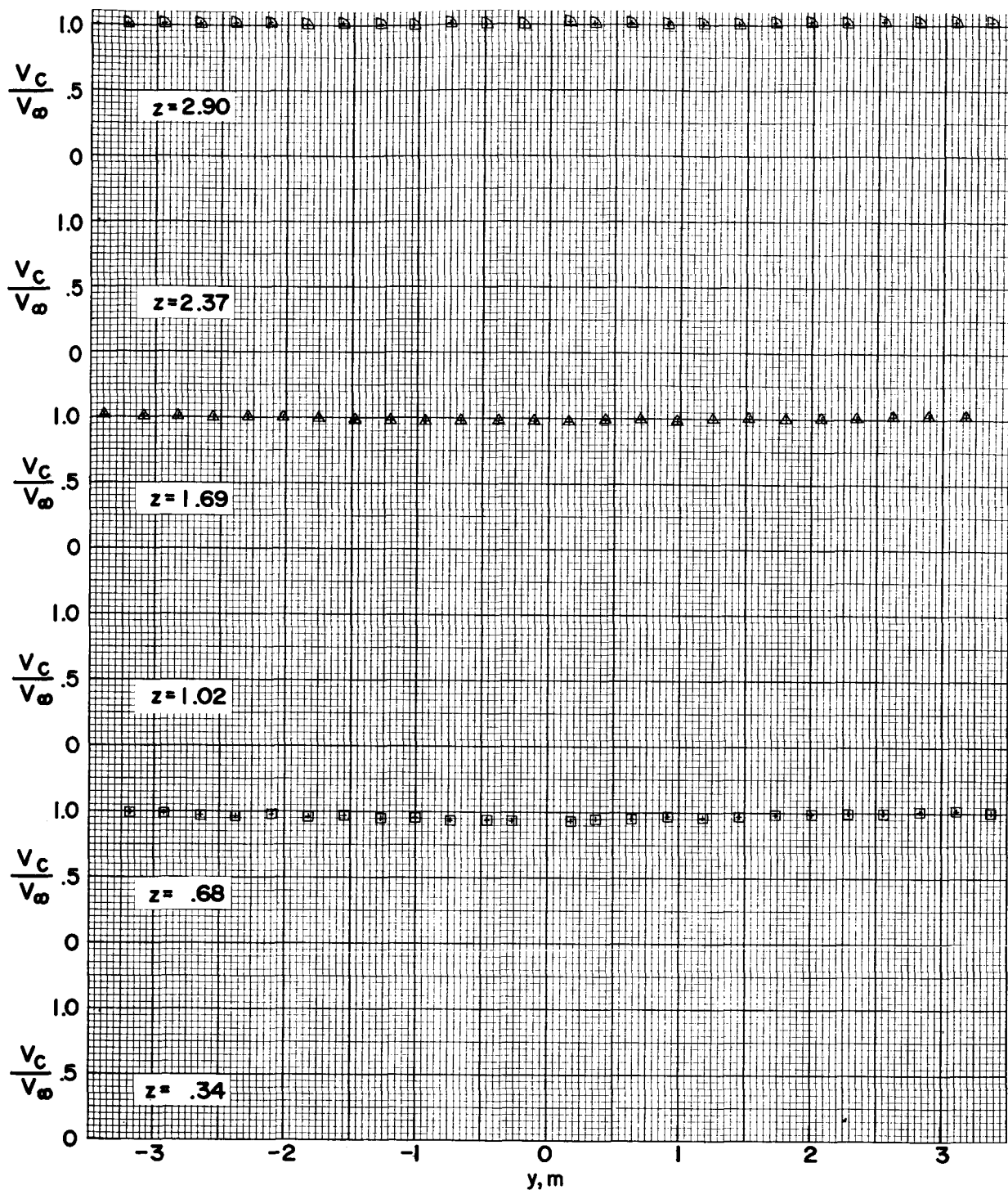
(a) $x = -4.06$ m.

Figure 14.- Velocity ratio V_c/V_∞ as a function of lateral position y for model configuration 2.



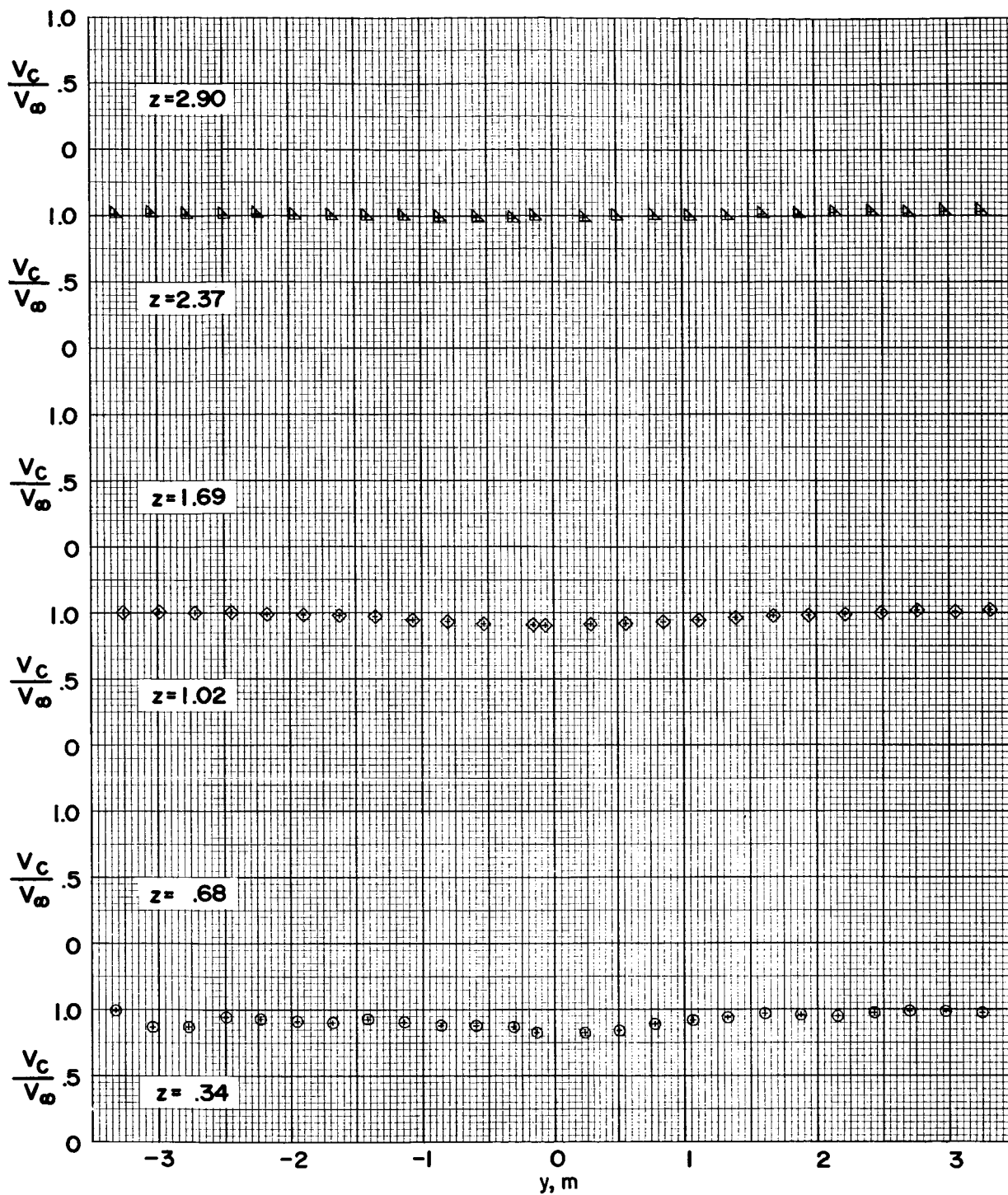
(b) $x = -3.39$ m.

Figure 14.- Continued.



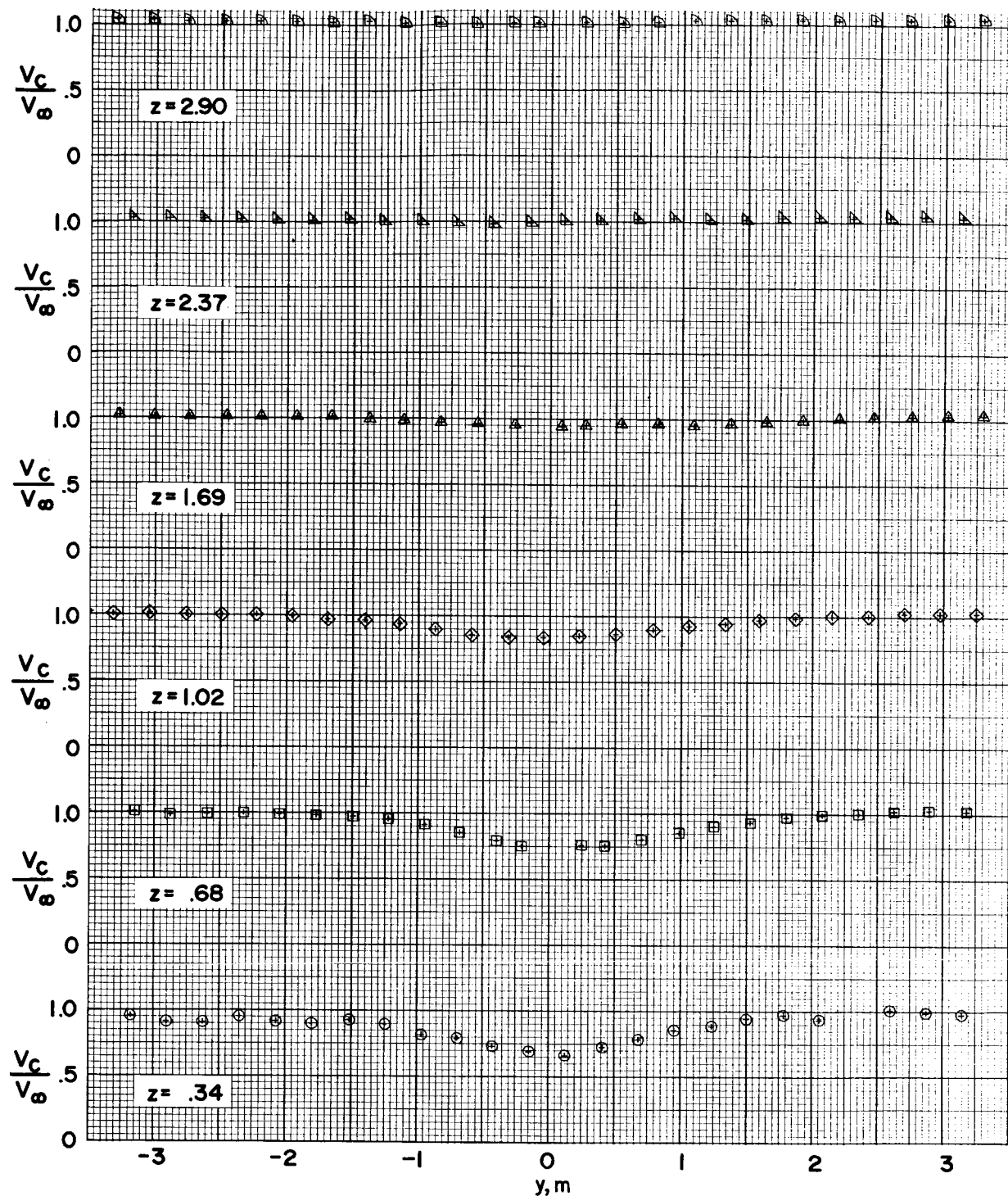
(c) $x = -2.71$ m.

Figure 14.- Continued.



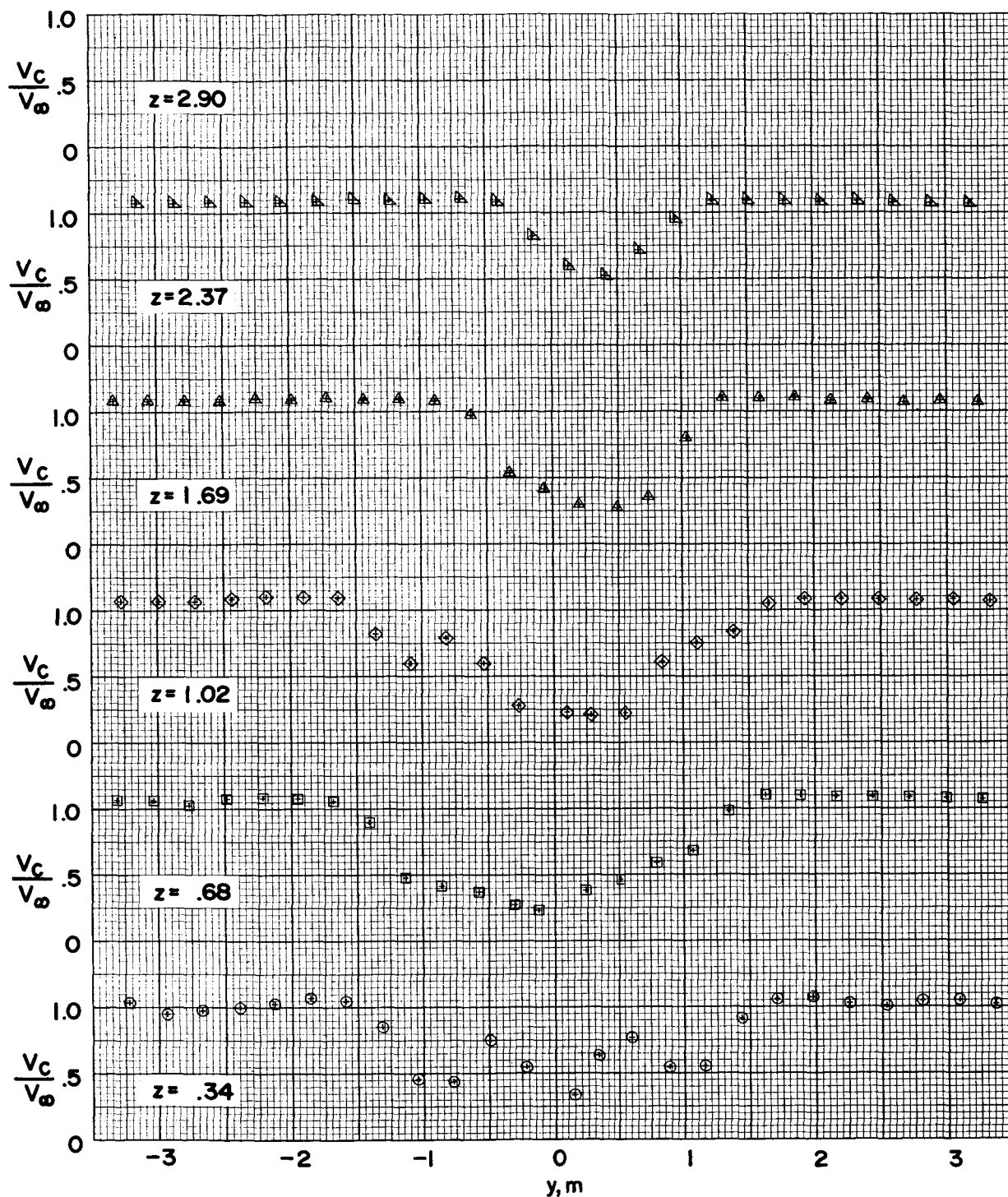
(d) $x = -2.03$ m.

Figure 14. - Continued.



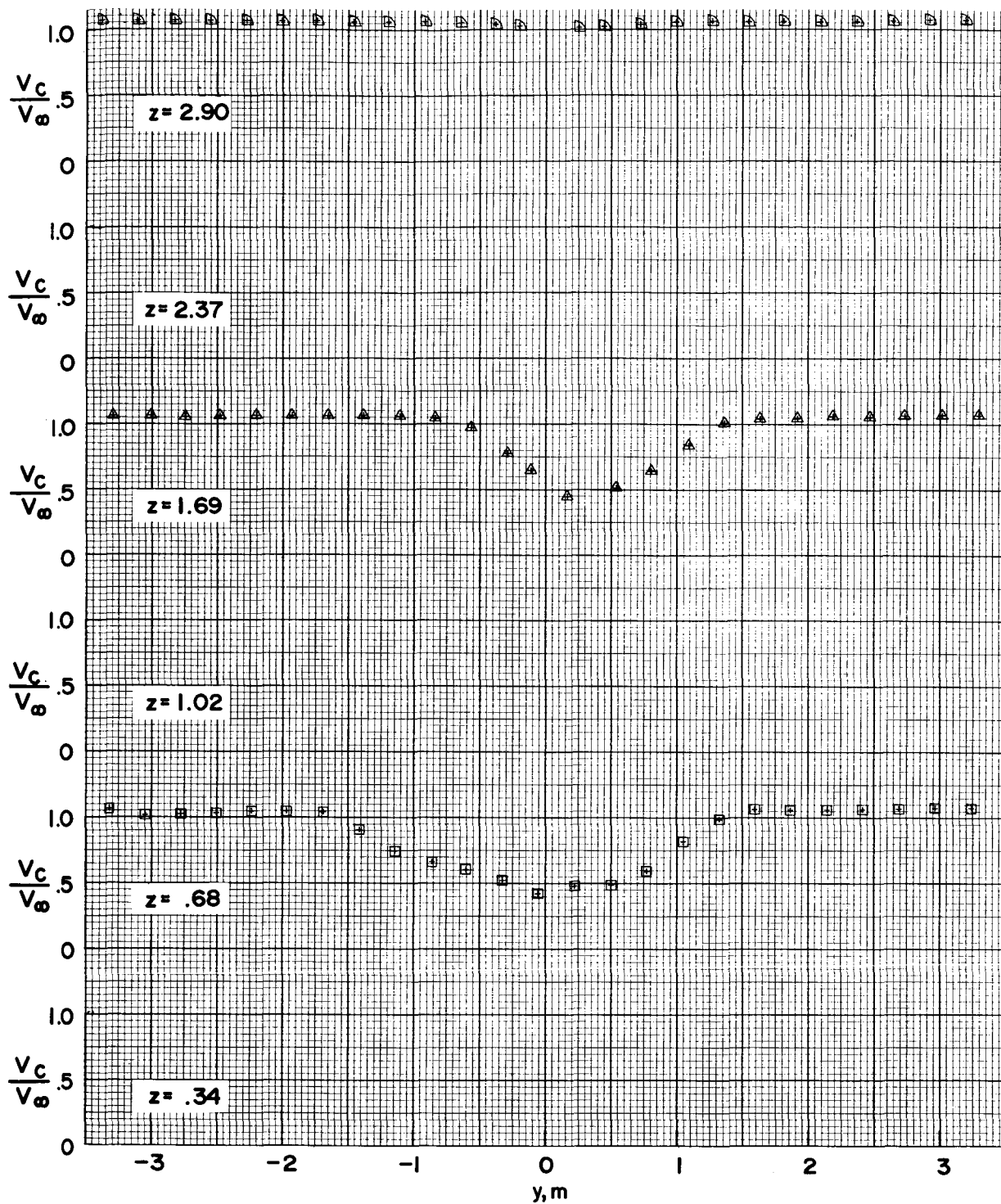
(e) $x = -1.35$ m.

Figure 14.- Continued.



(f) $x = 2.03$ m.

Figure 14.- Continued.



(g) $x = 4.06$ m.

Figure 14. - Concluded.

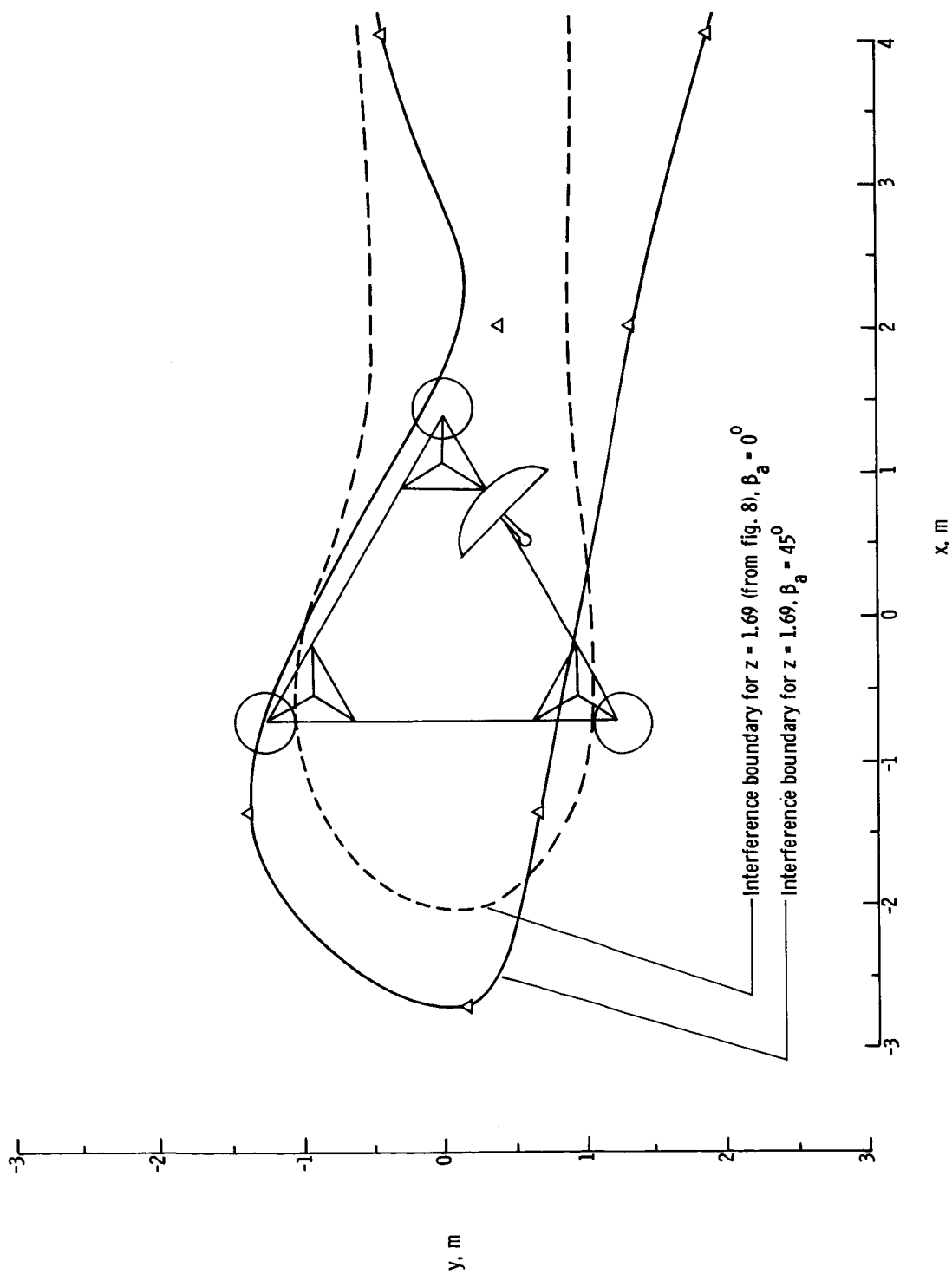
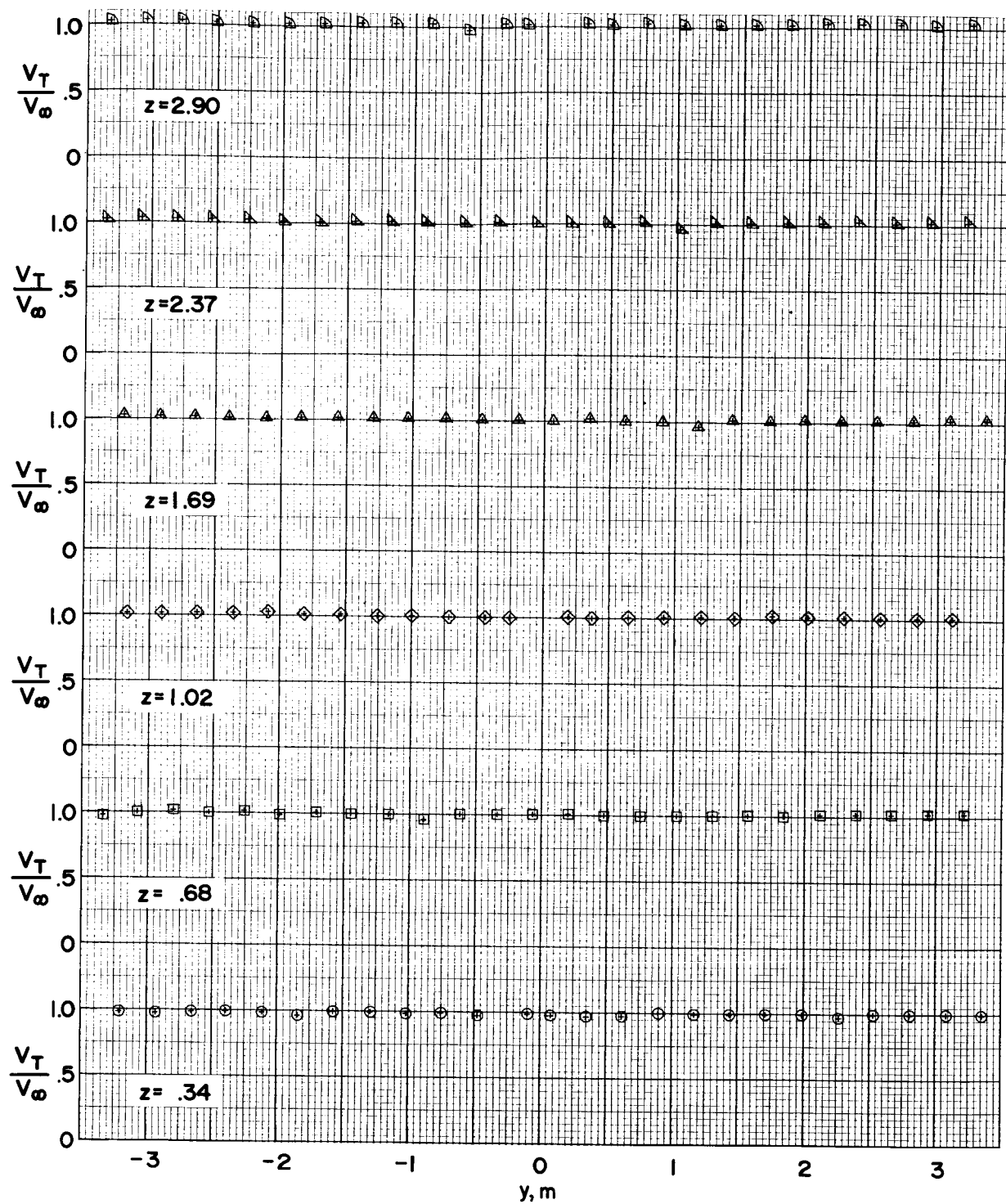
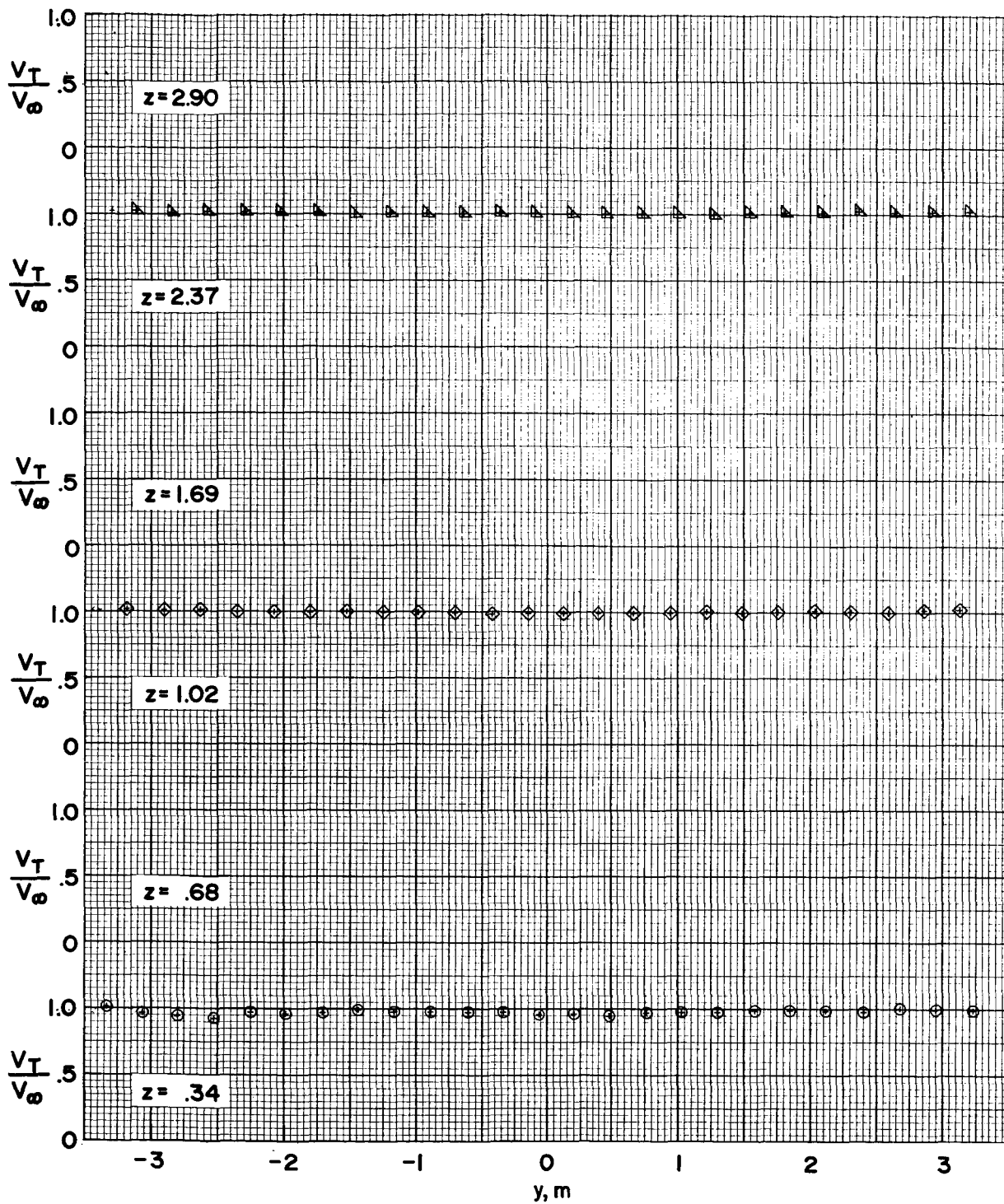


Figure 15. - Effect of antenna azimuth on 5-percent wind-speed interference boundaries
for model configuration 3.



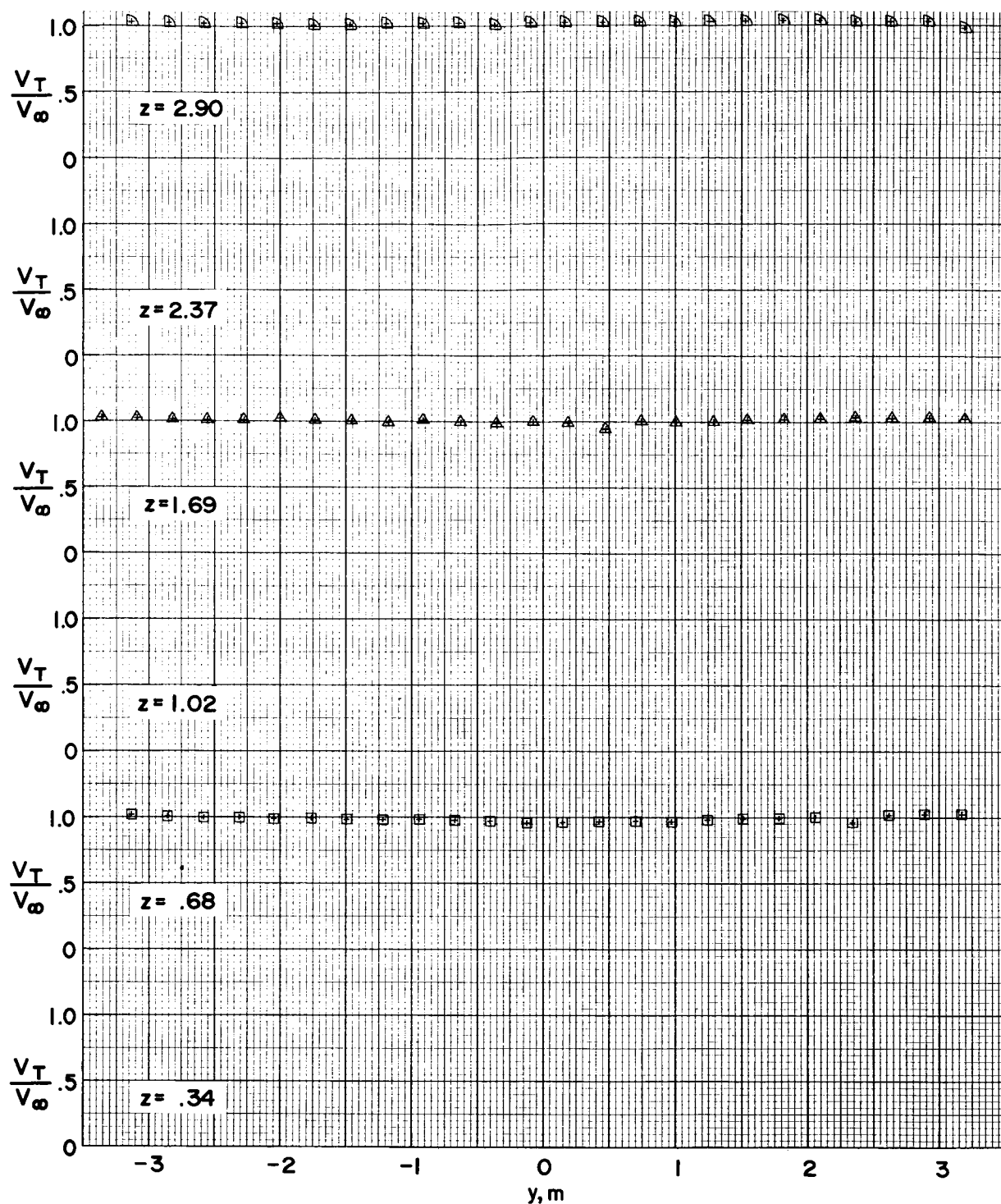
(a) $x = -4.06$ m.

Figure 16.- Velocity ratio V_T/V_∞ as a function of lateral position y for model configuration 3.



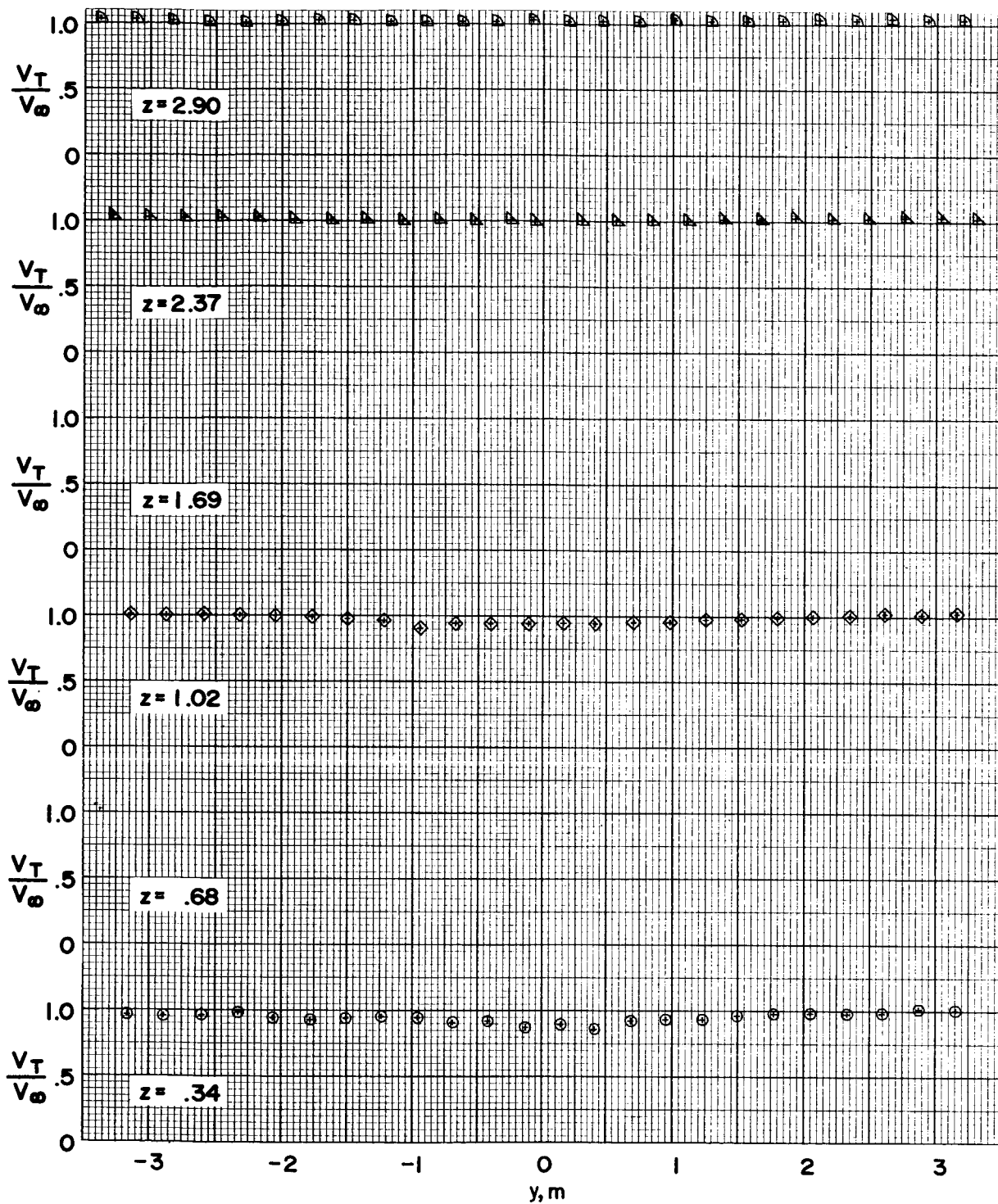
(b) $x = -3.39$ m.

Figure 16.- Continued.



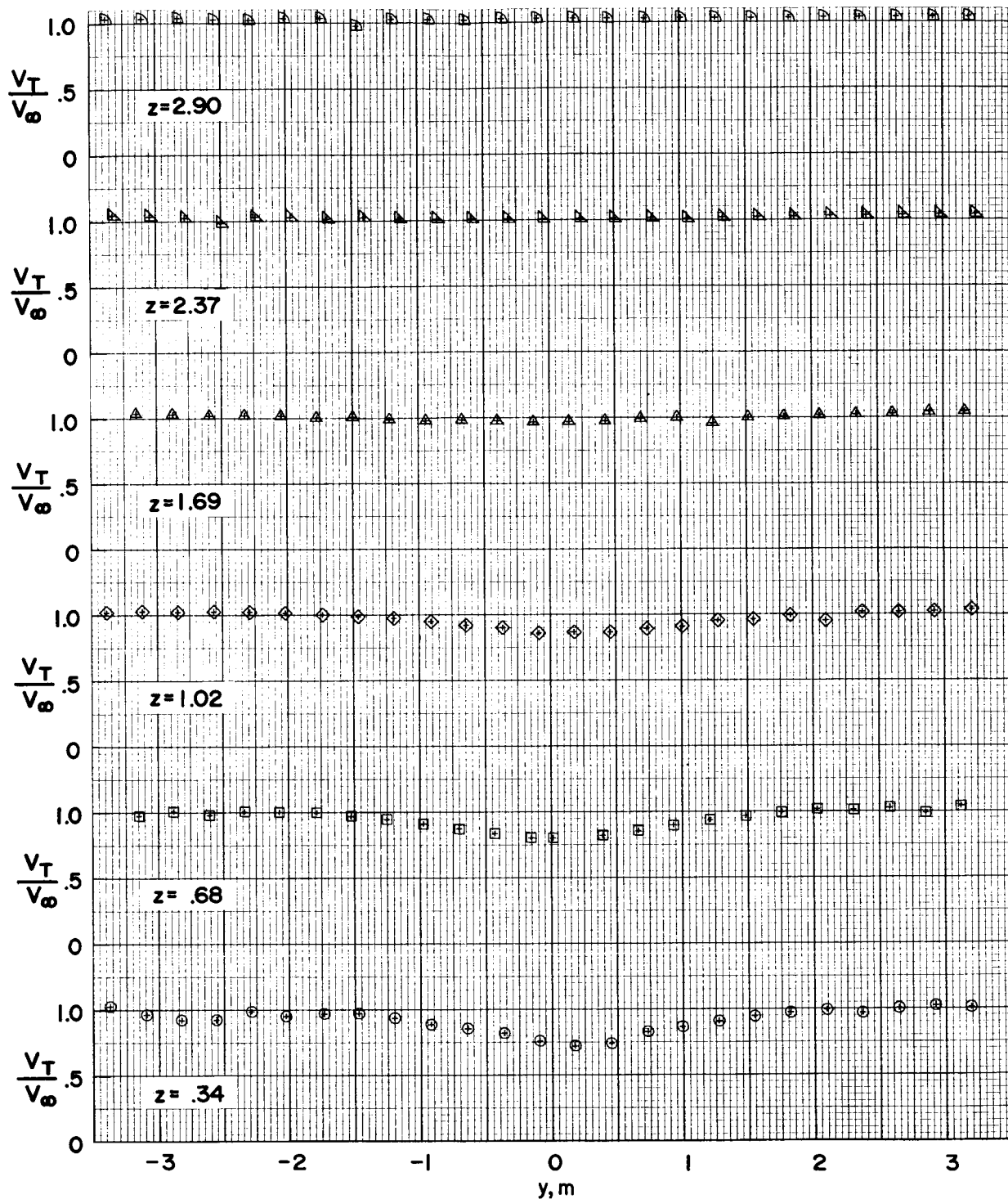
(c) $x = -2.71$ m.

Figure 16.- Continued.



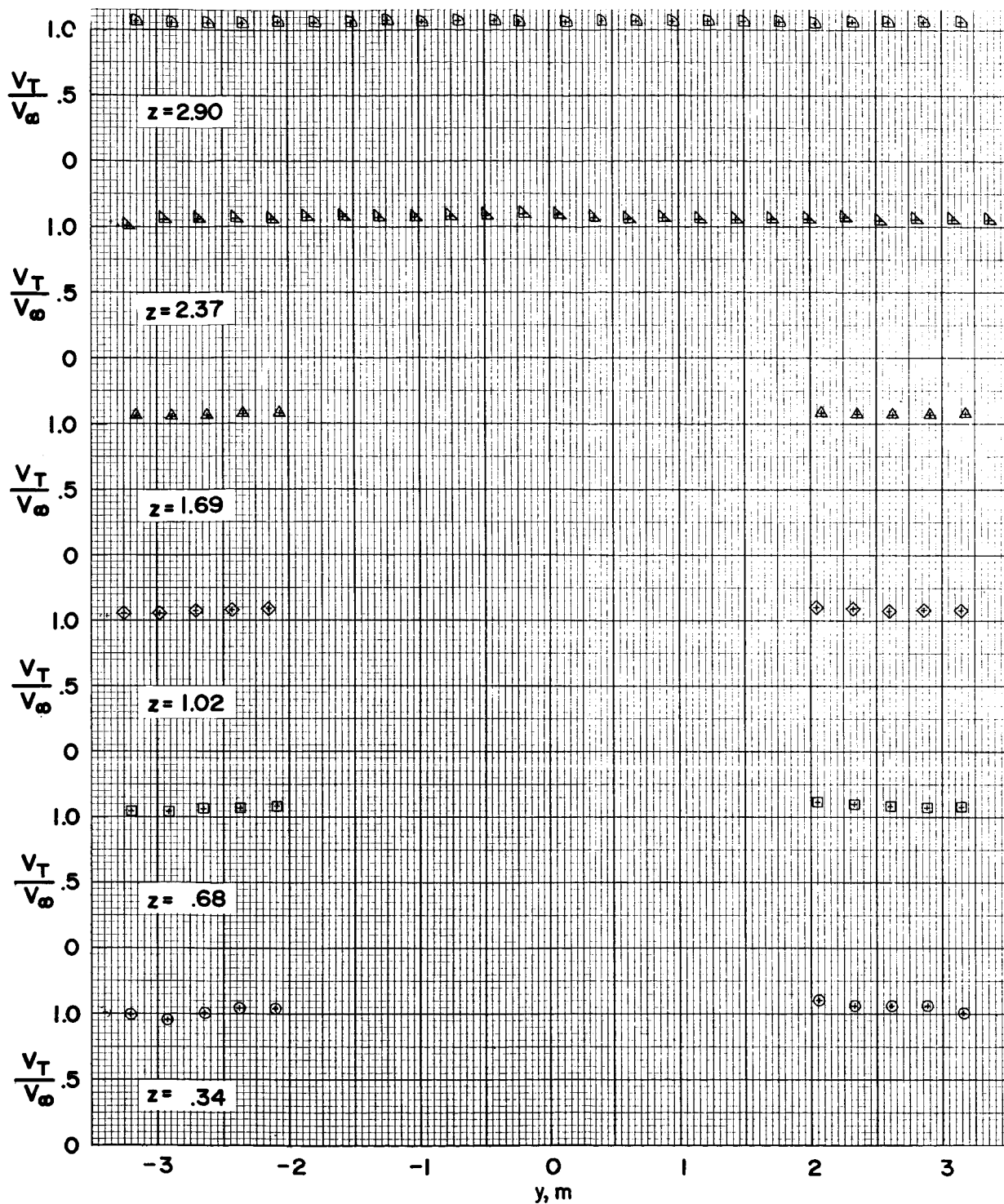
(d) $x = -2.03$ m.

Figure 16.- Continued.



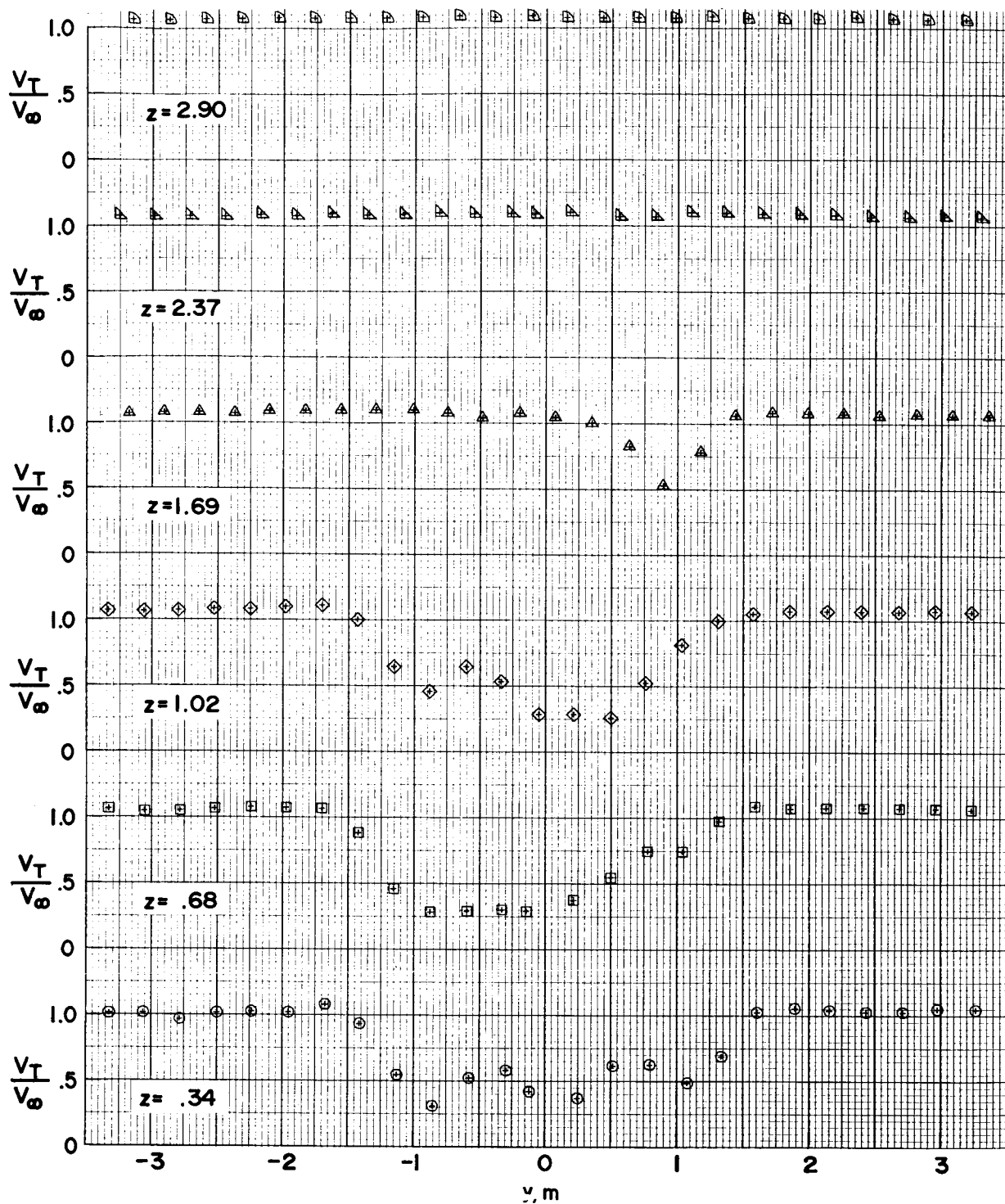
(e) $x = -1.35$ m.

Figure 16.- Continued.



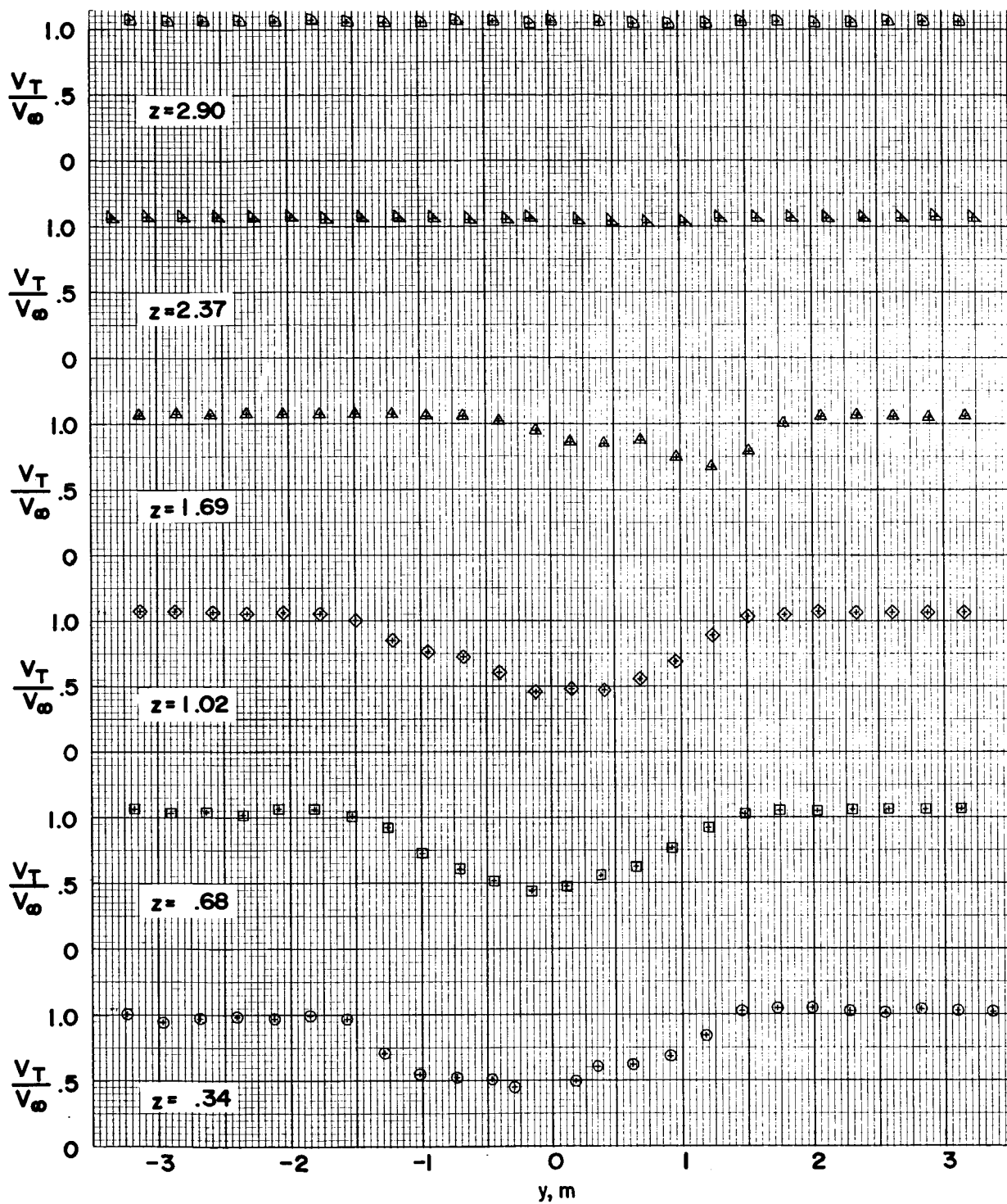
(f) $x = 0$ m.

Figure 16.- Continued.



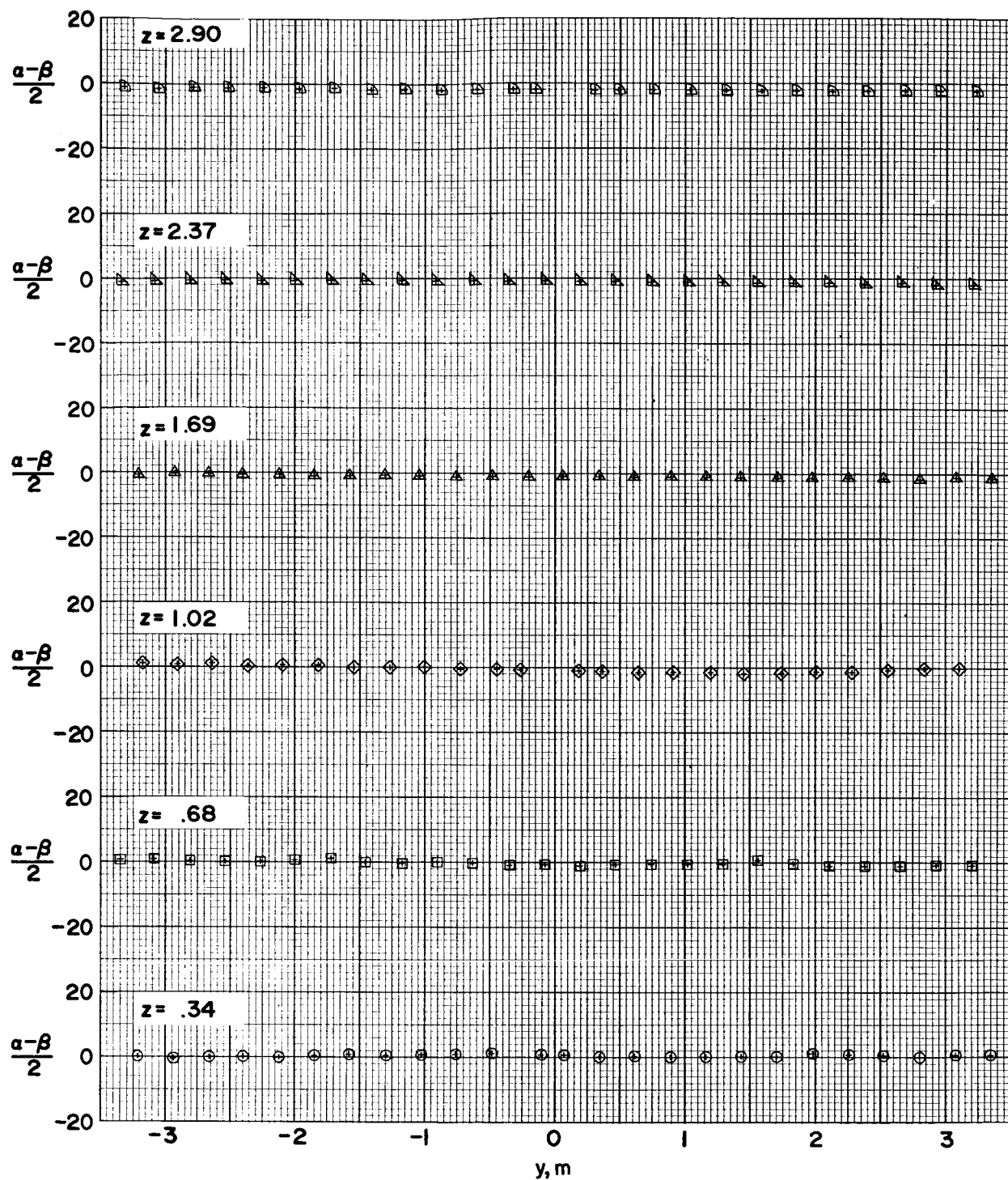
(g) $x = 2.03$ m.

Figure 16.- Continued.



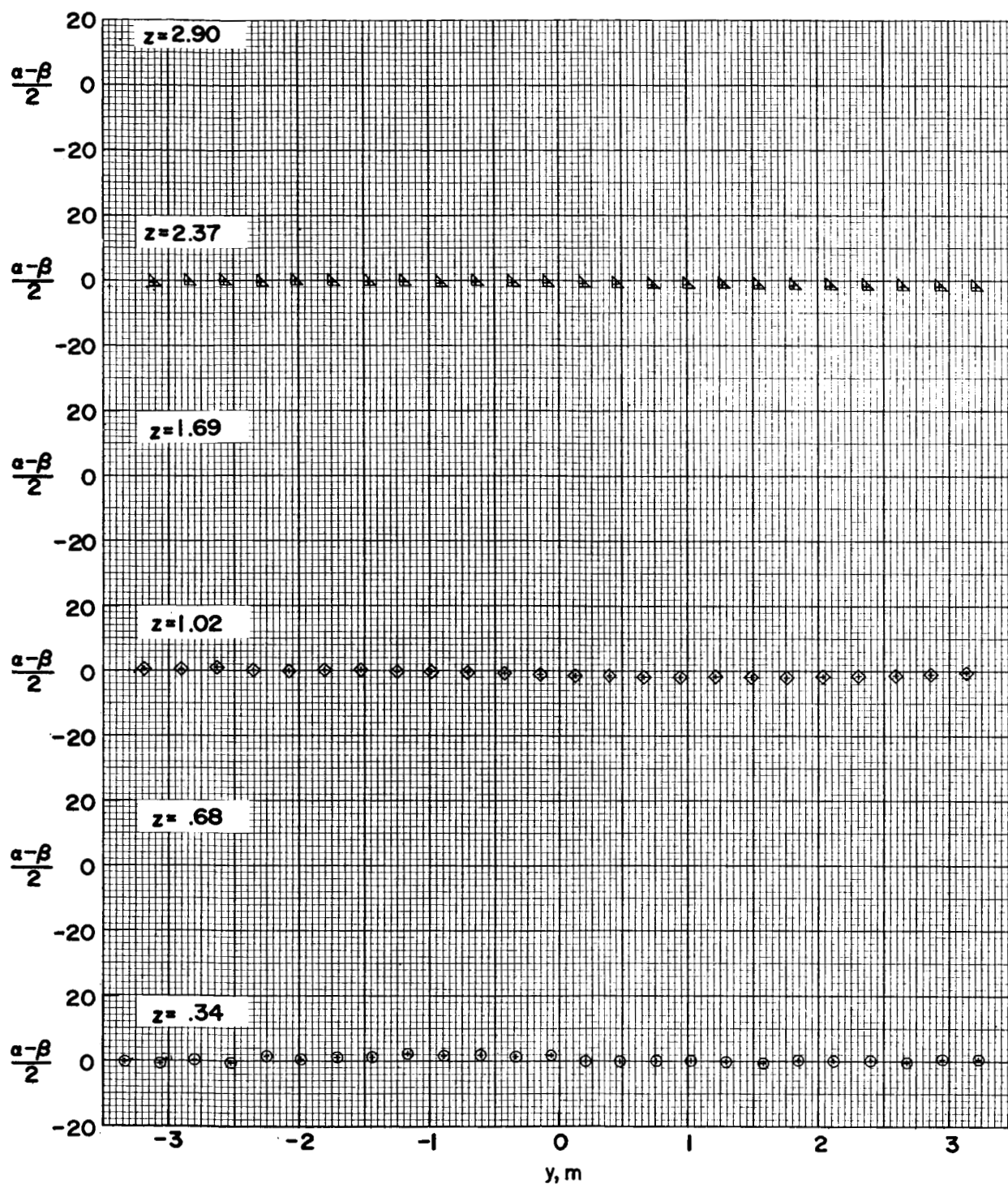
(h) $x = 4.06$ m.

Figure 16. - Concluded.



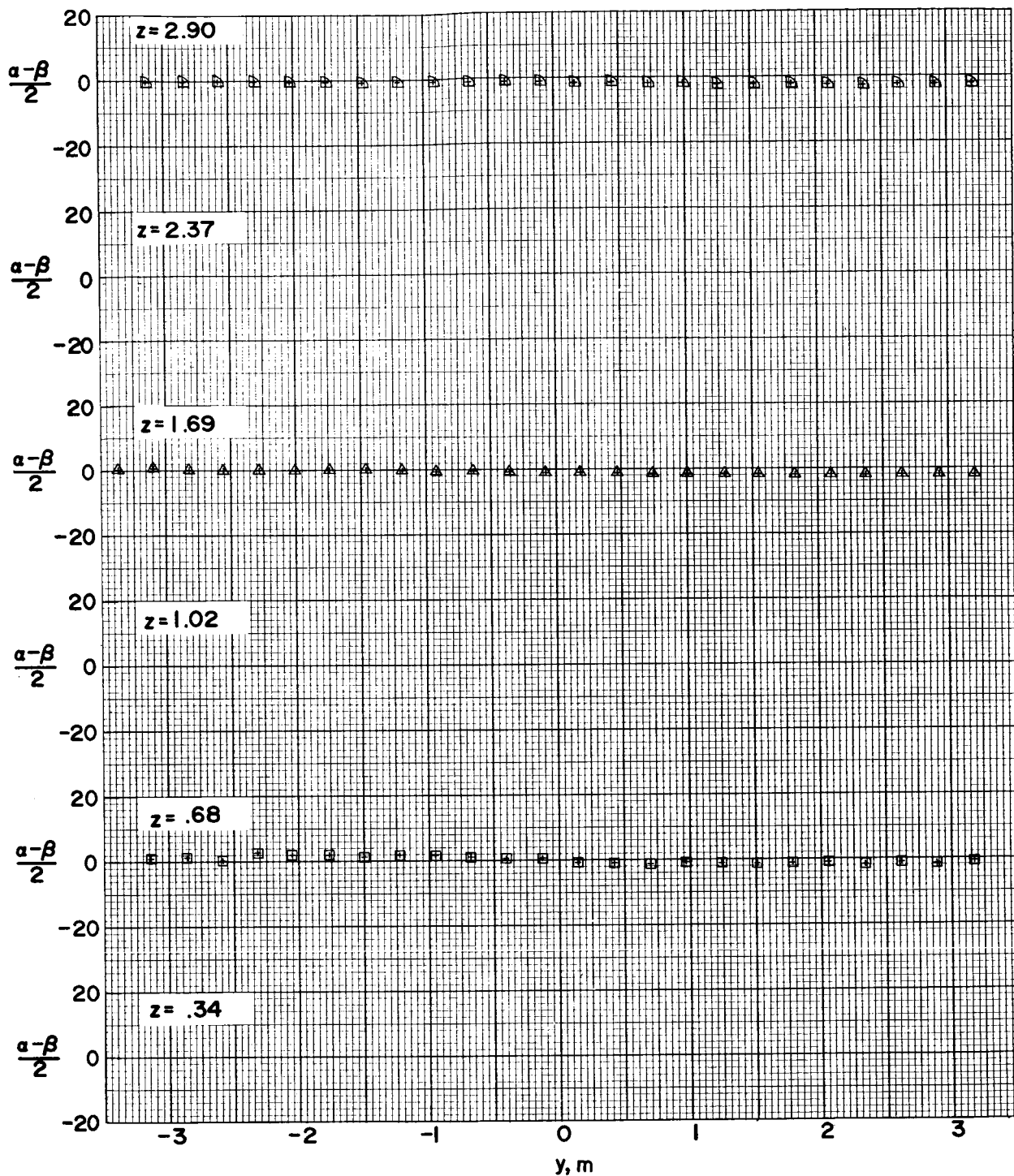
(a) $x = -4.06$ m.

Figure 17.- Local flow angle $\frac{\alpha - \beta}{2}$ as a function of lateral position y for model configuration 3.



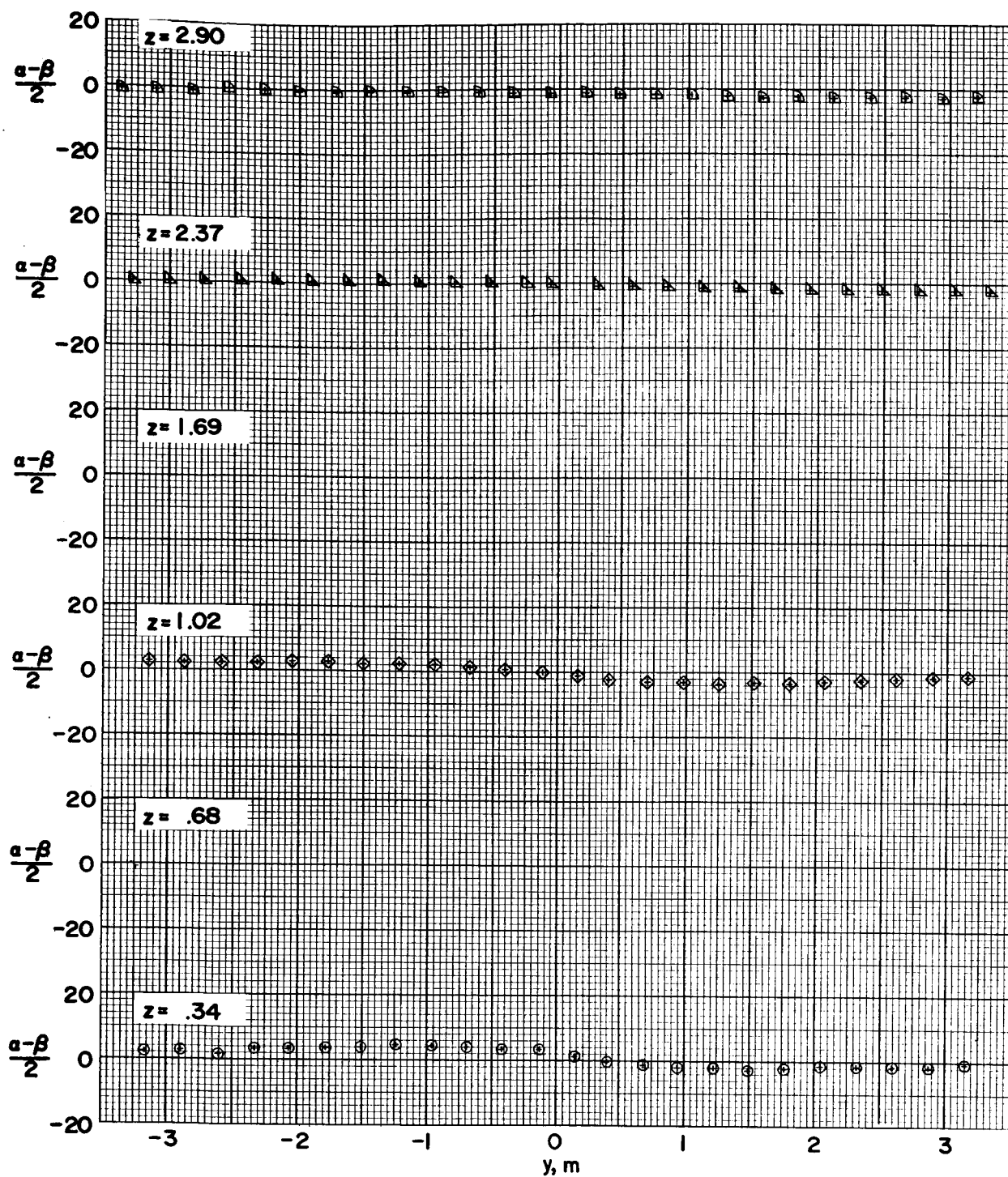
(b) $x = -3.39$ m.

Figure 17.- Continued.



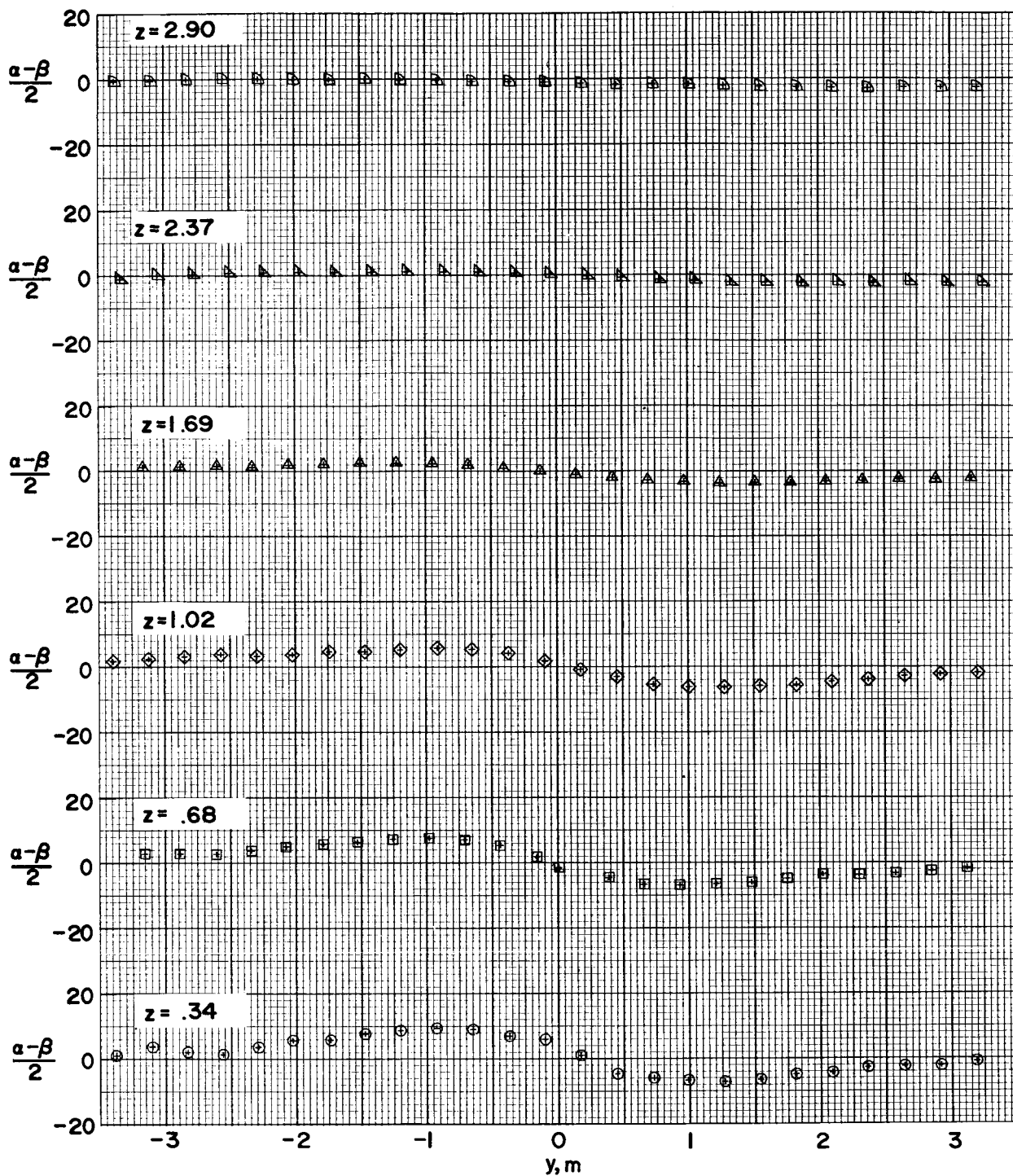
(c) $x = -2.71$ m.

Figure 17.- Continued.



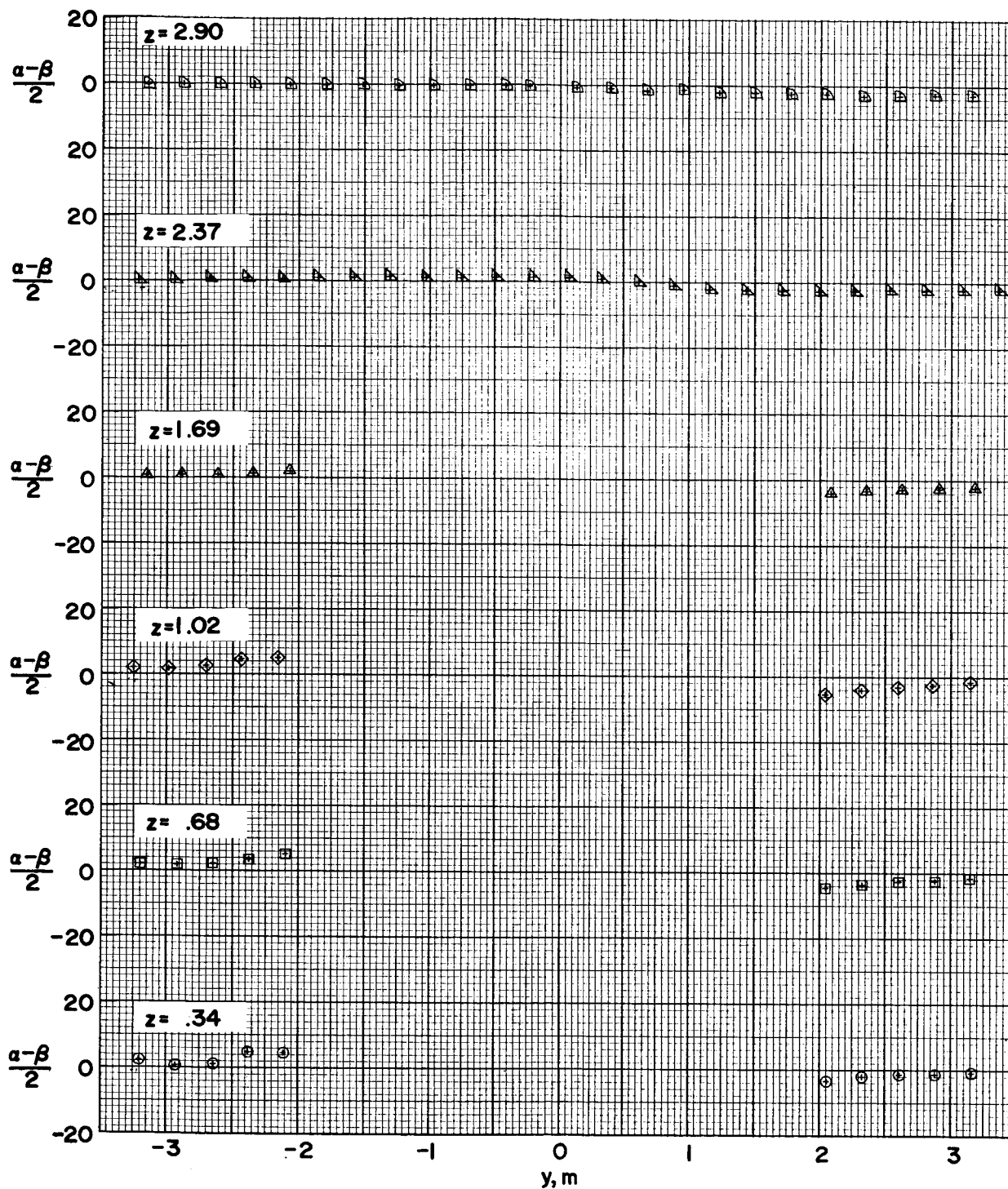
(d) $x = -2.03$ m.

Figure 17.- Continued.



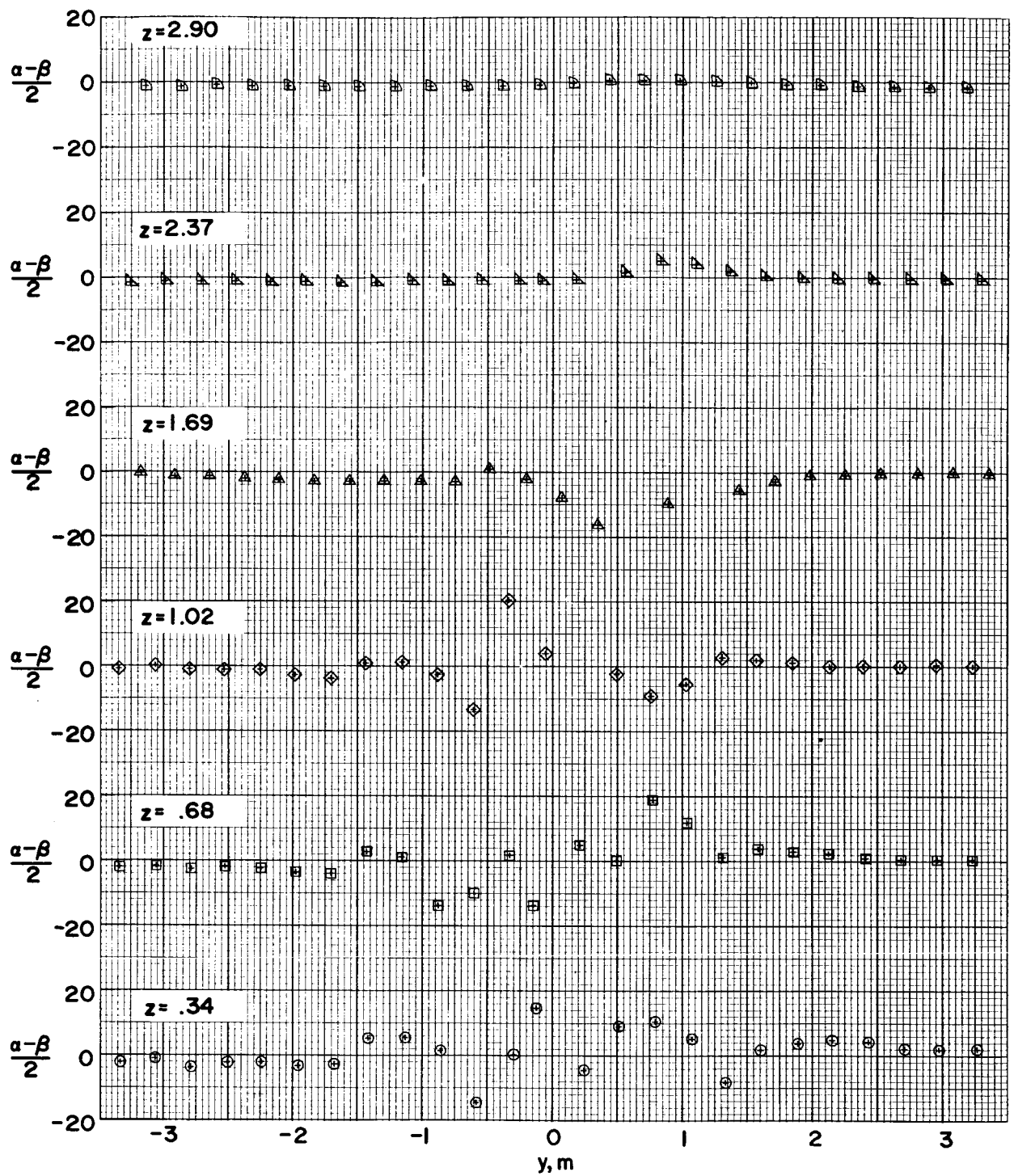
(e) $x = -1.35$ m.

Figure 17.- Continued.



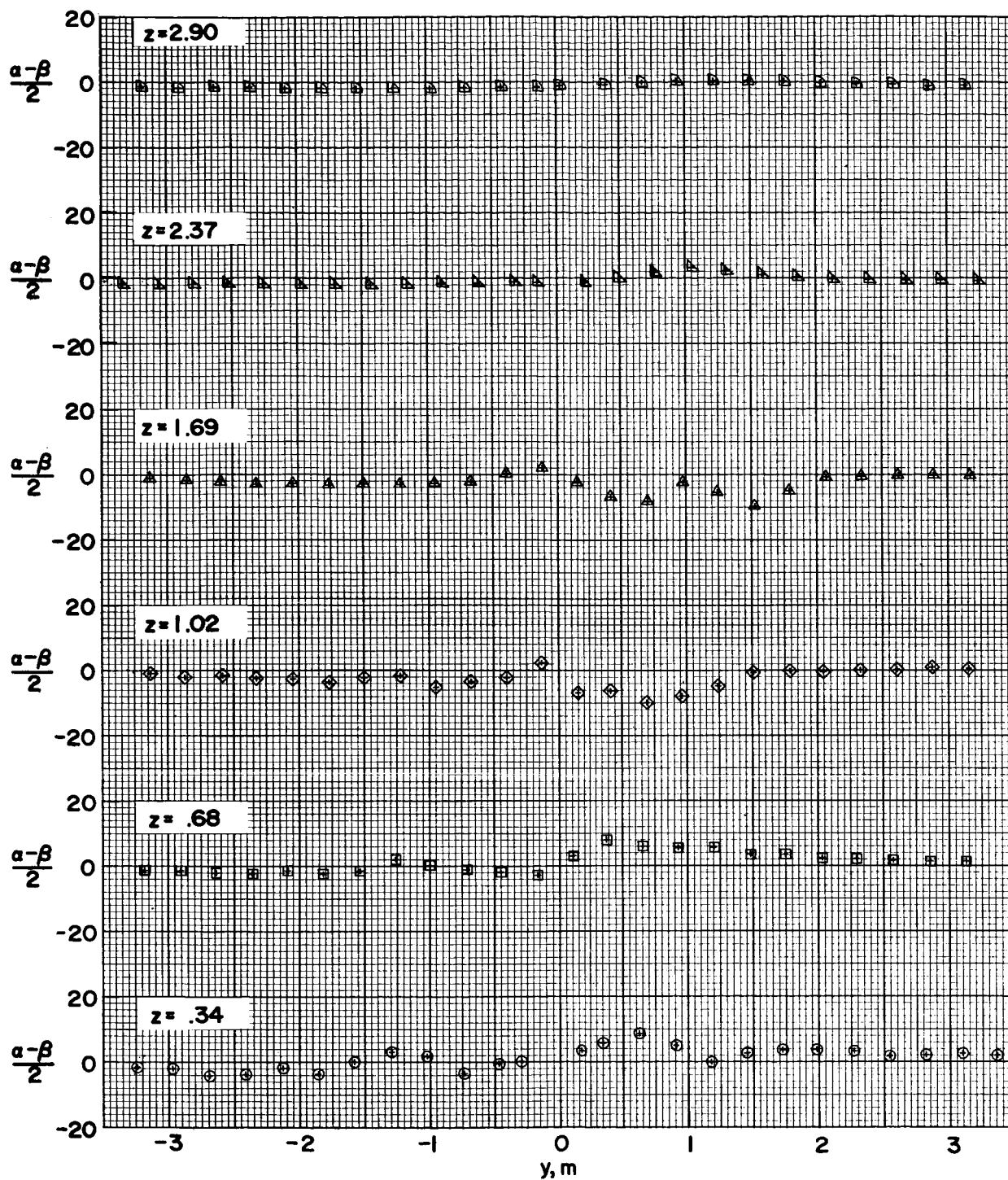
(f) $x = 0$ m.

Figure 17.- Continued.



(g) $x = 2.03$ m.

Figure 17.- Continued.



(h) $x = 4.06$ m.

Figure 17. - Concluded.

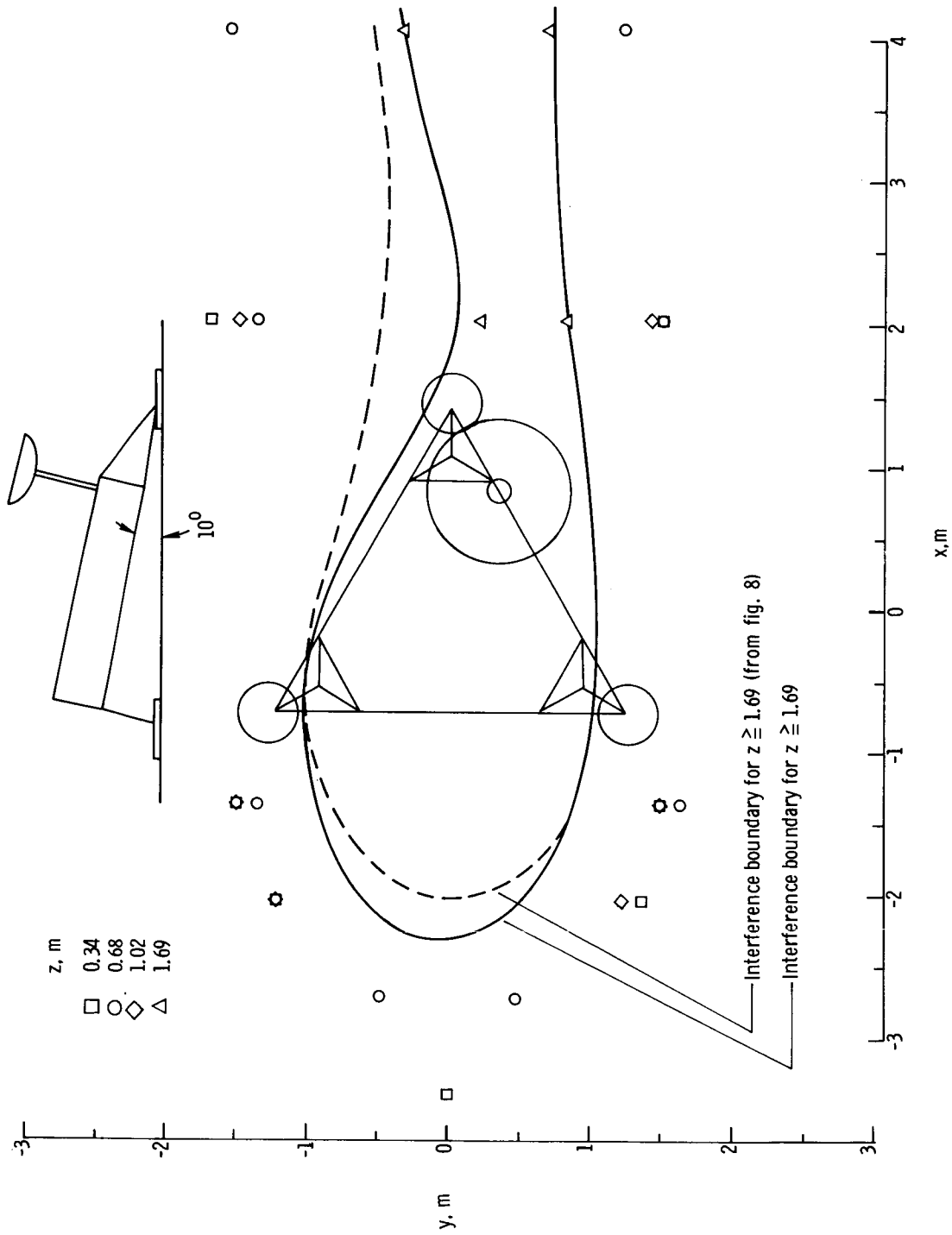
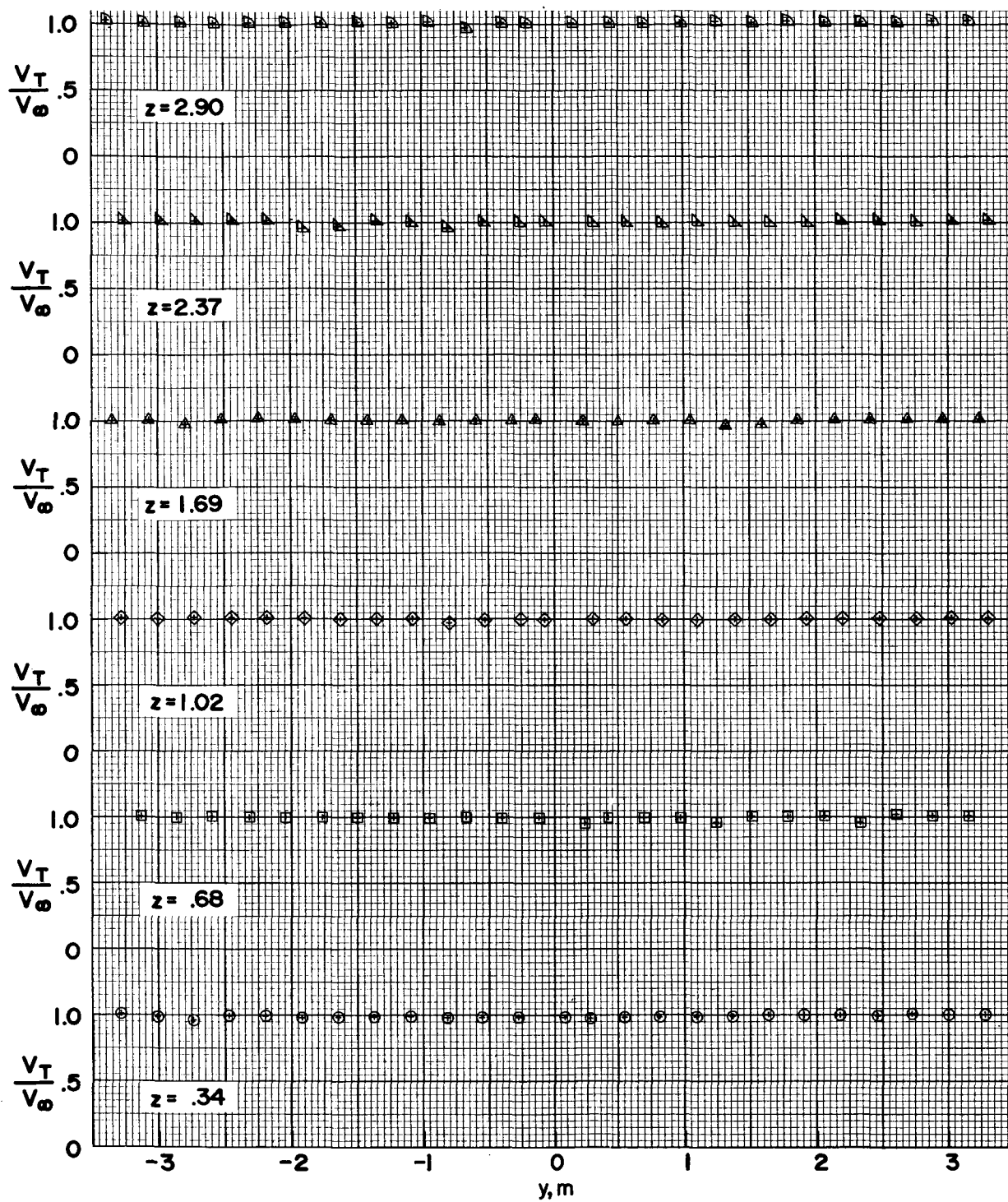
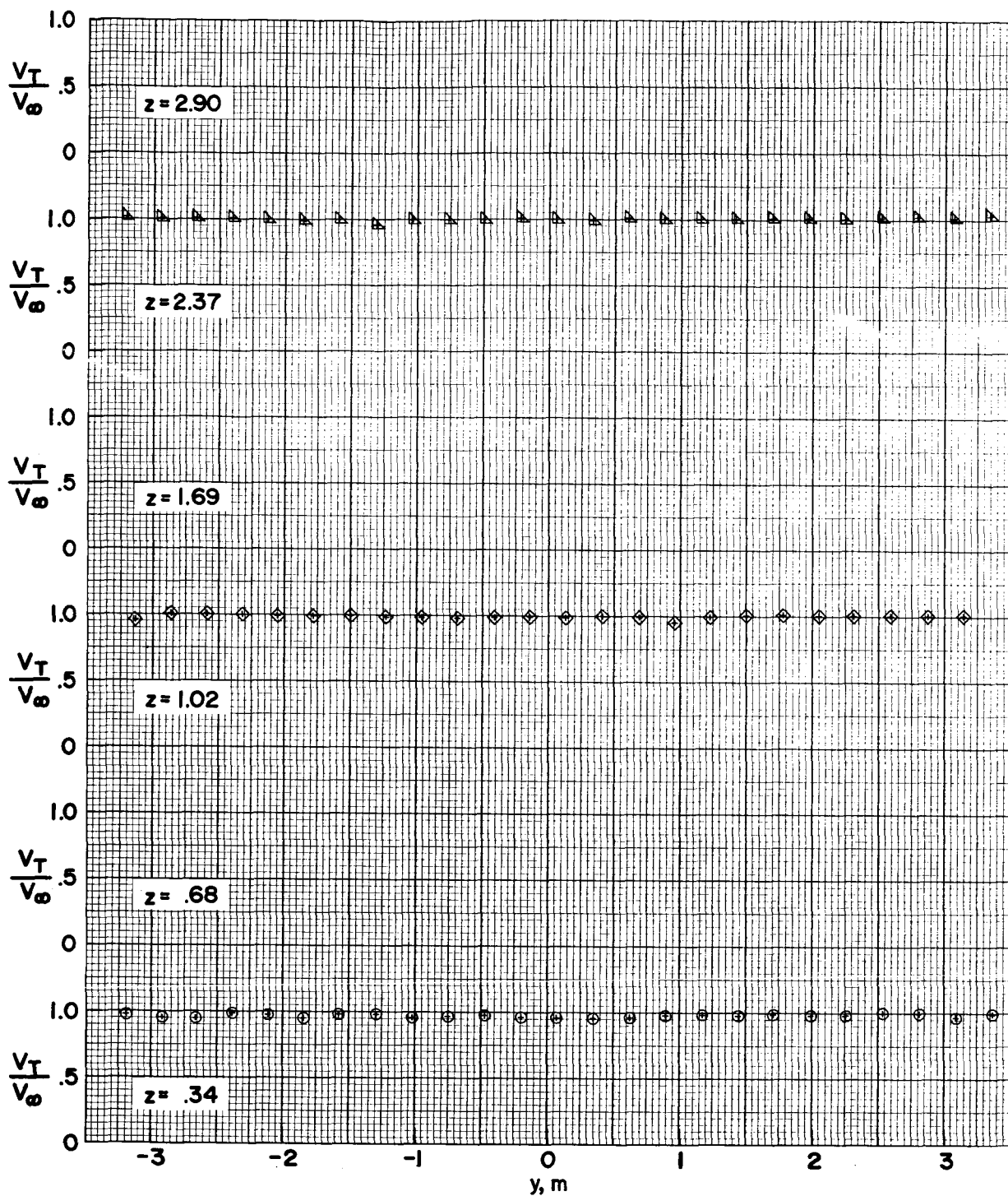


Figure 18.- Effect of lander tilt on 5-percent wind-speed interference boundaries for model configuration 4.



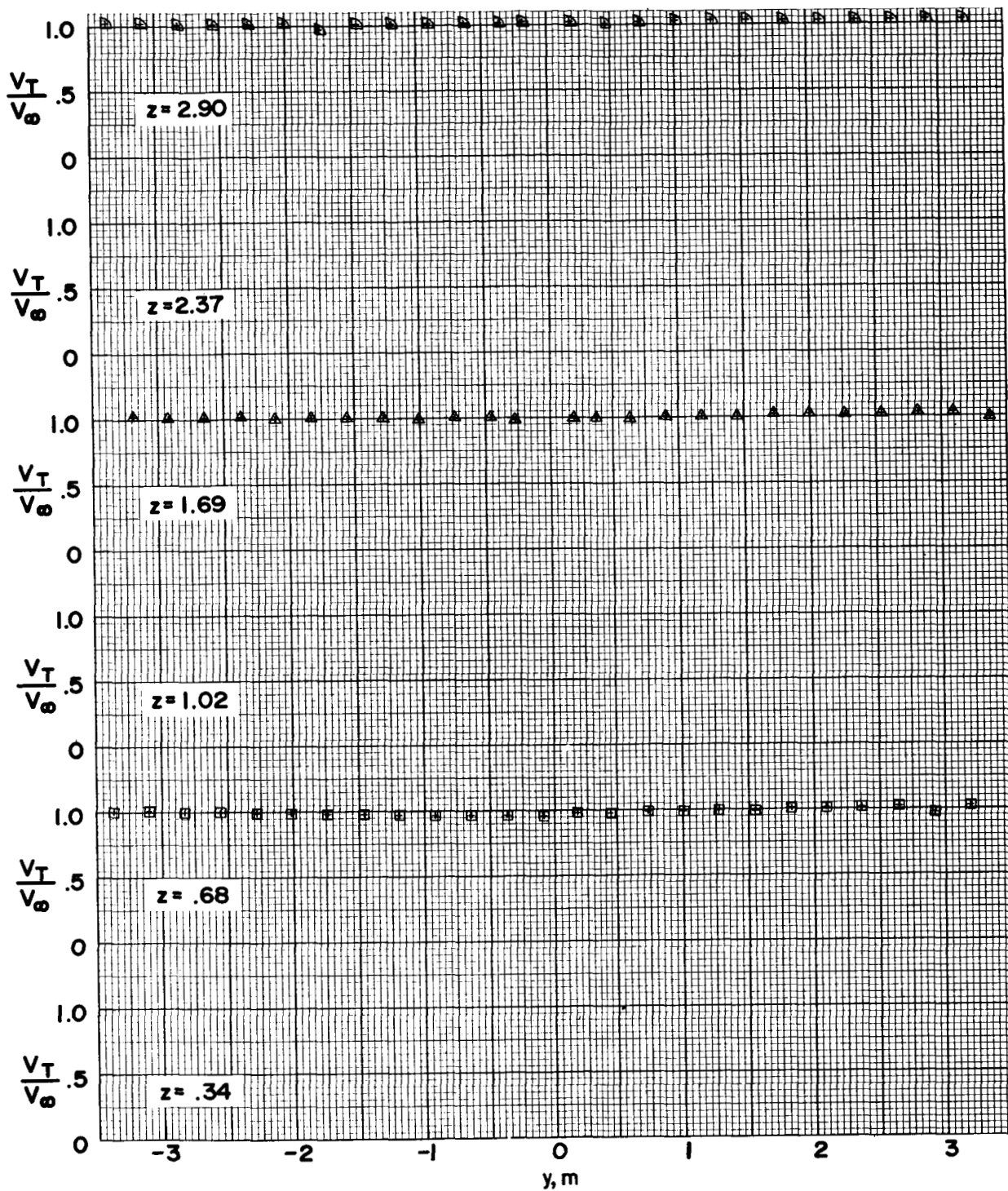
(a) $x = -4.06$ m.

Figure 19.- Velocity ratio V_T/V_∞ as a function of lateral position y for model configuration 4.



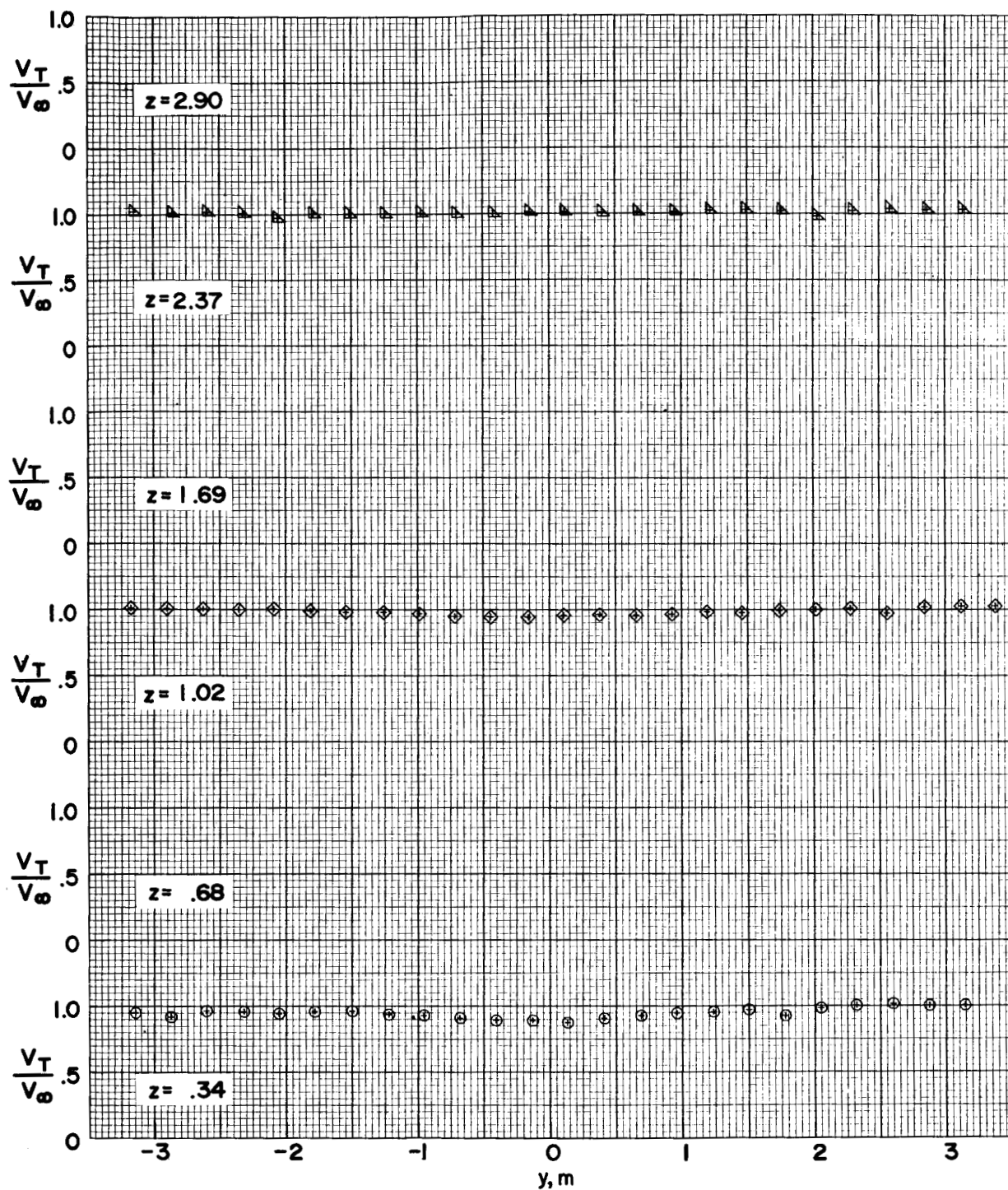
(b) $x = -3.39$ m.

Figure 19.- Continued.



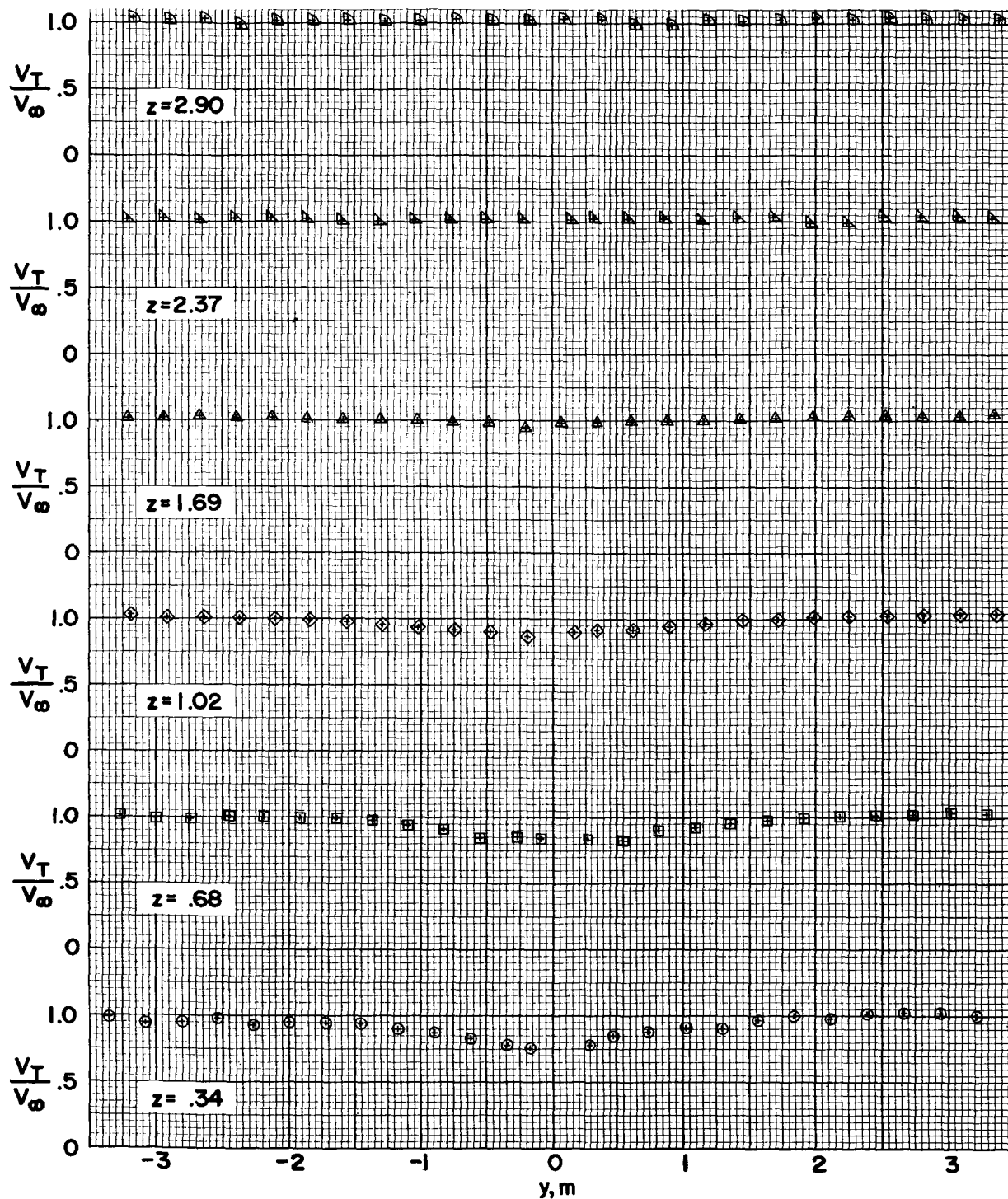
(c) $x = -2.71$ m.

Figure 19.- Continued.



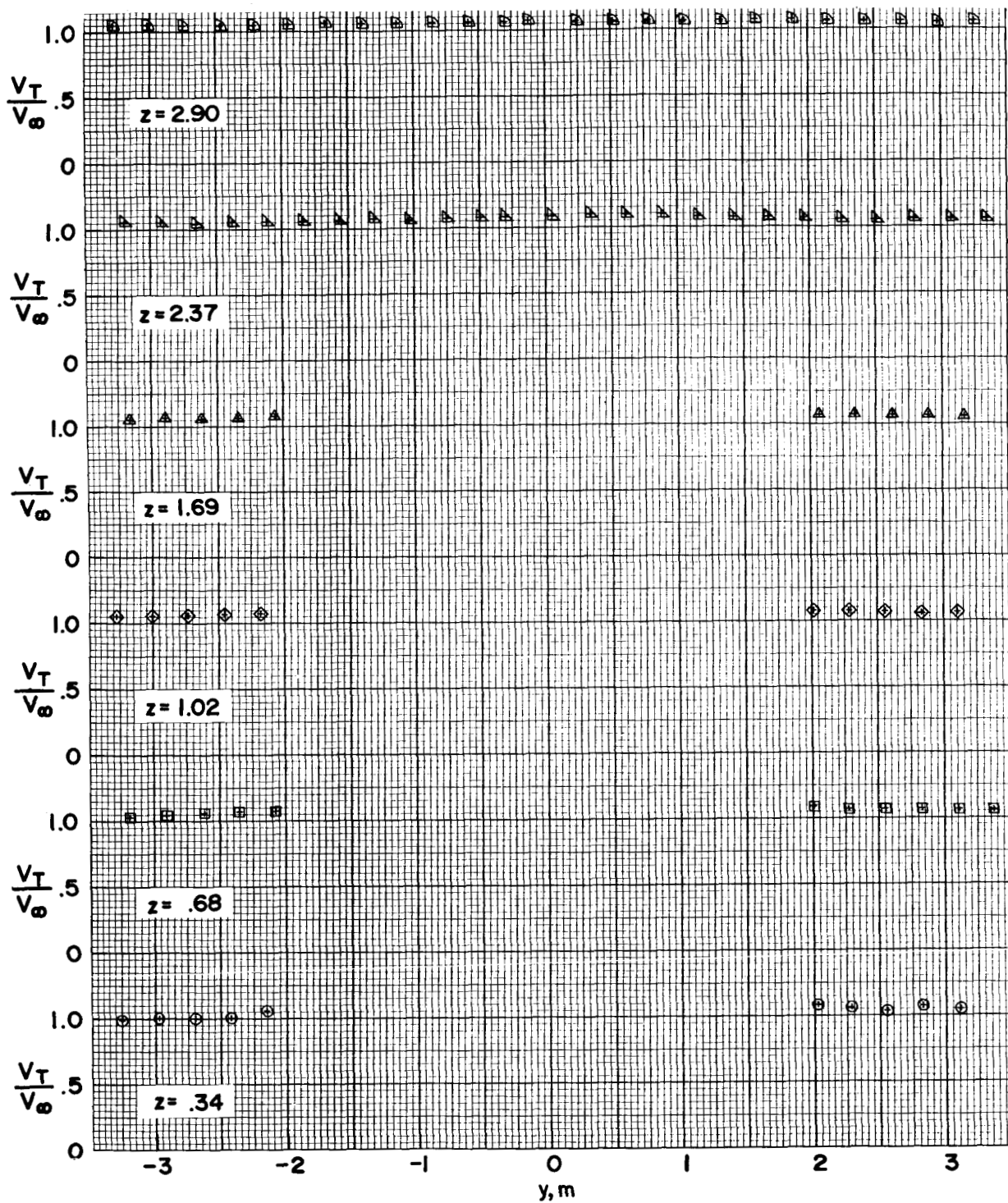
(d) $x = -2.03$ m.

Figure 19.- Continued.



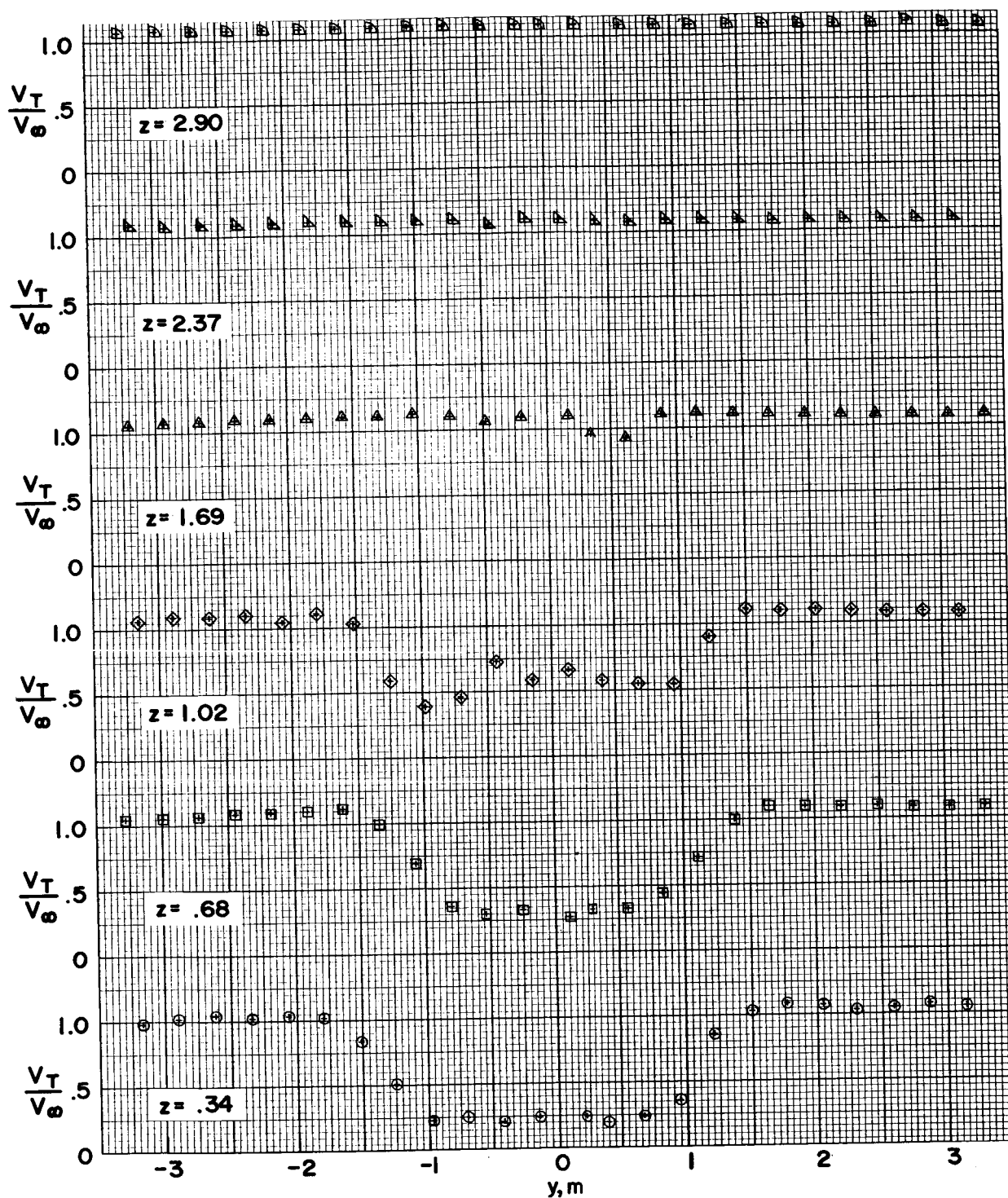
(e) $x = -1.35$ m.

Figure 19. - Continued.



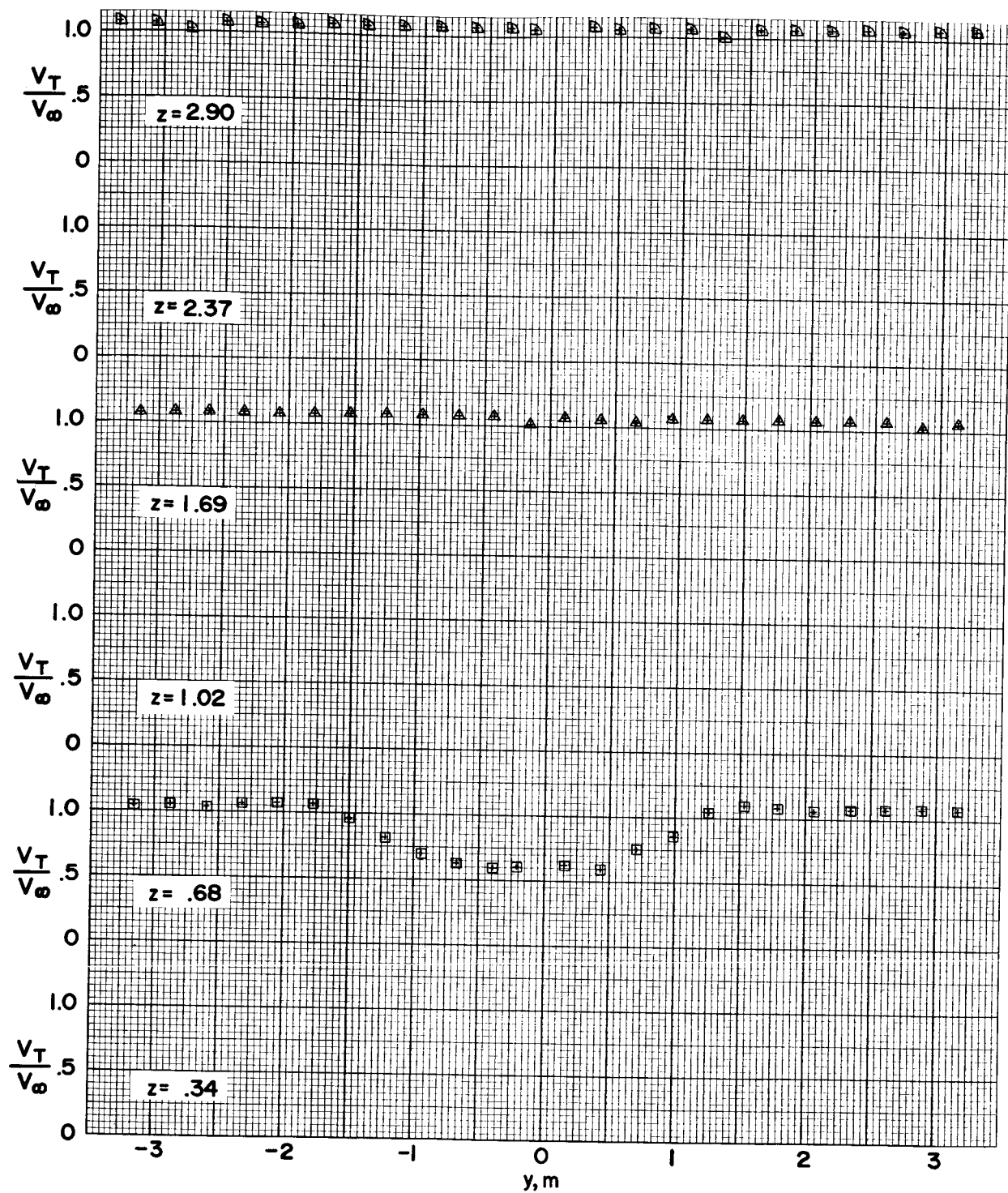
(f) $x = 0$ m.

Figure 19. - Continued.



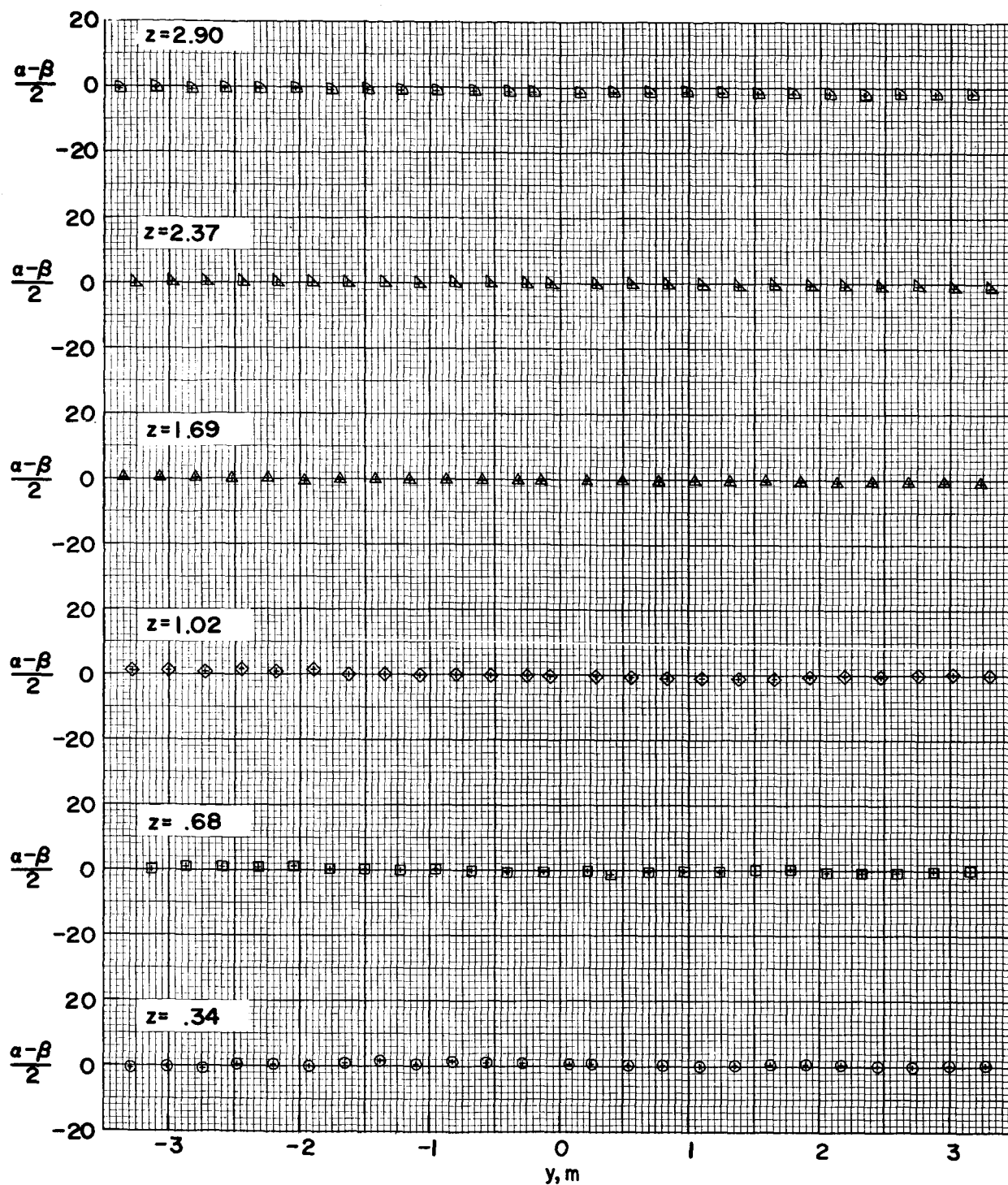
(g) $x = 2.03$ m.

Figure 19. - Continued.



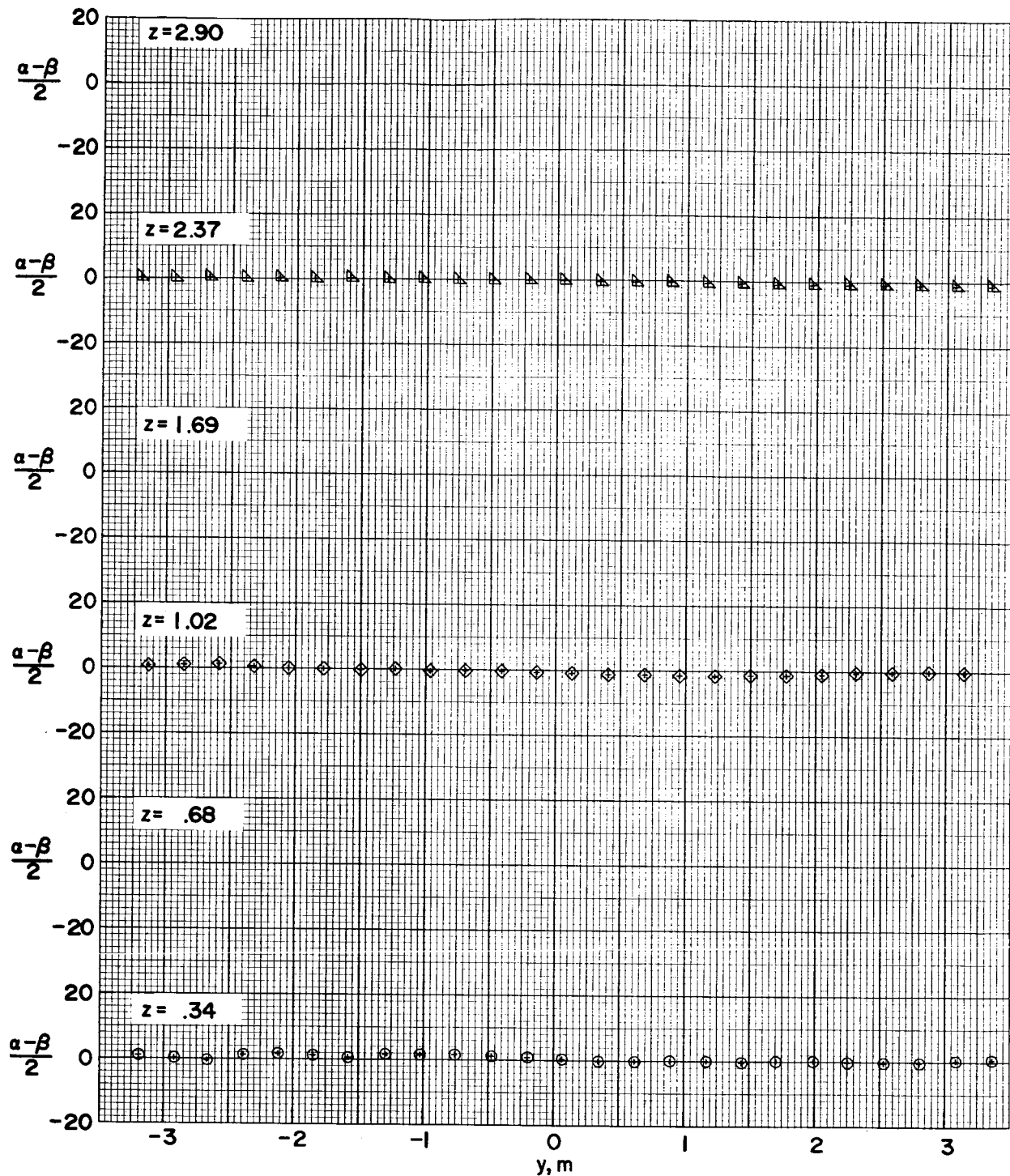
(h) $x = 4.06$ m.

Figure 19. - Concluded.



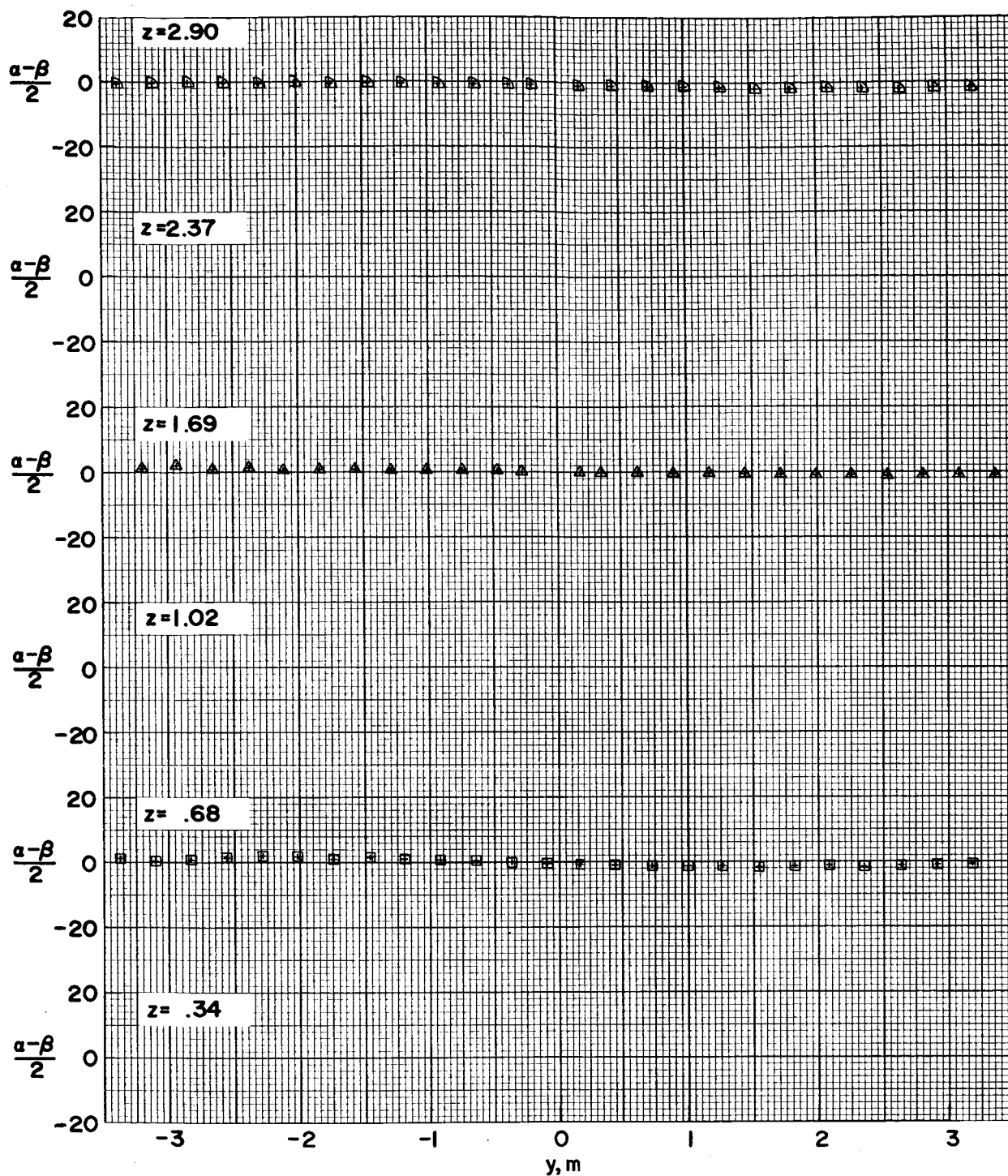
(a) $x = -4.06$ m.

Figure 20.- Local flow angle $\frac{\alpha - \beta}{2}$ as a function of lateral position y for model configuration 4.



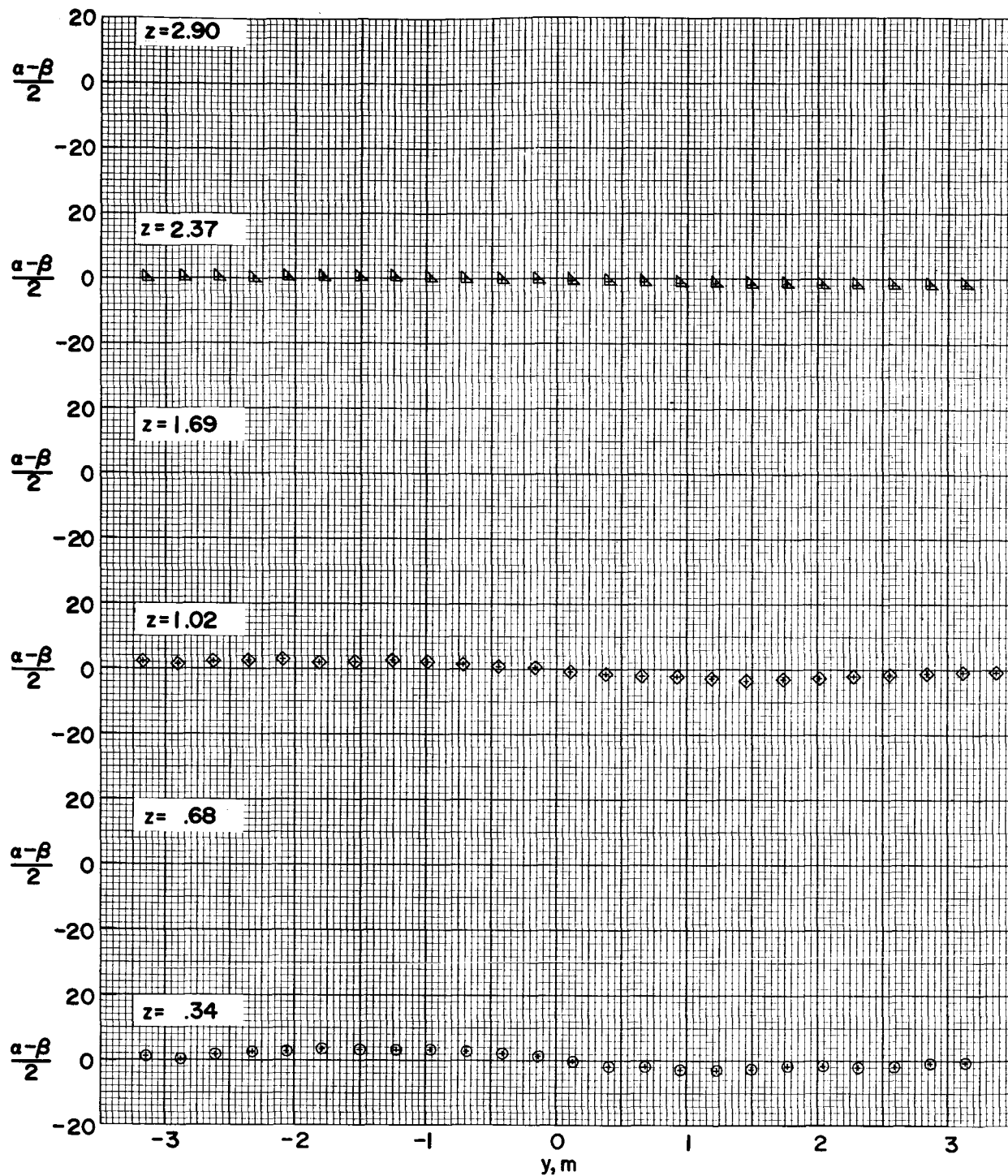
(b) $x = -3.39$ m.

Figure 20. - Continued.



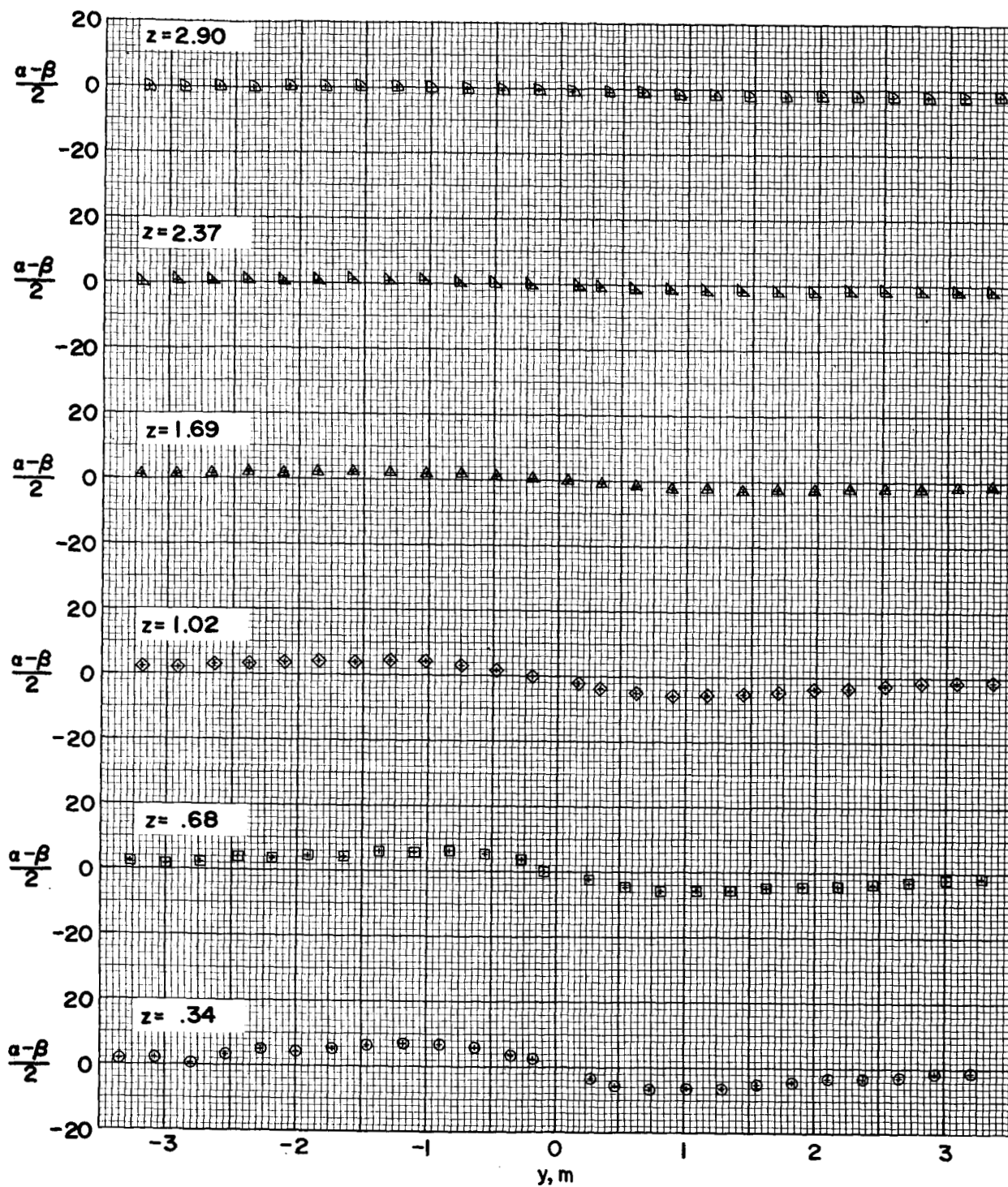
(c) $x = -2.71$ m.

Figure 20. - Continued.



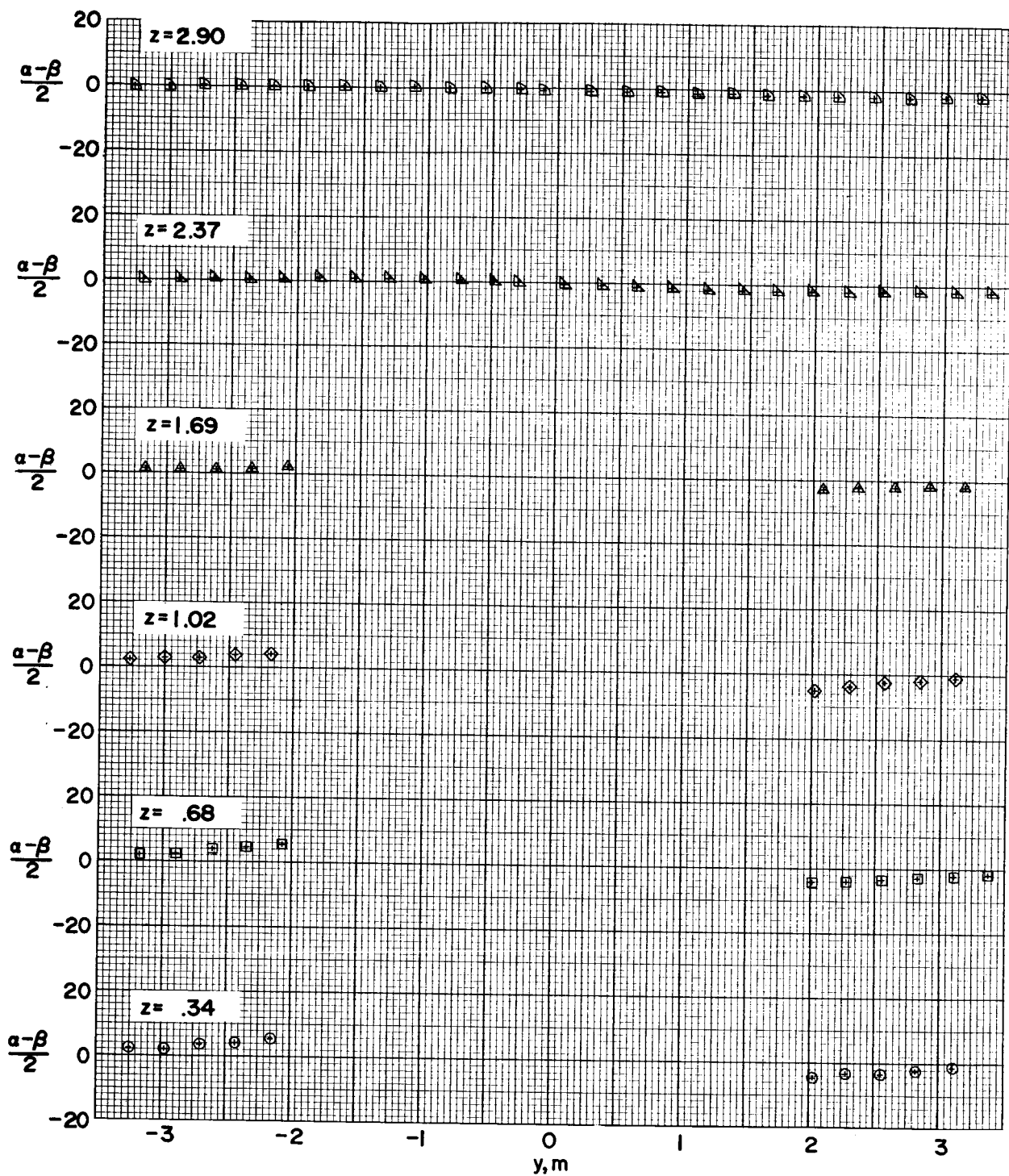
(d) $x = -2.03$ m.

Figure 20.- Continued.



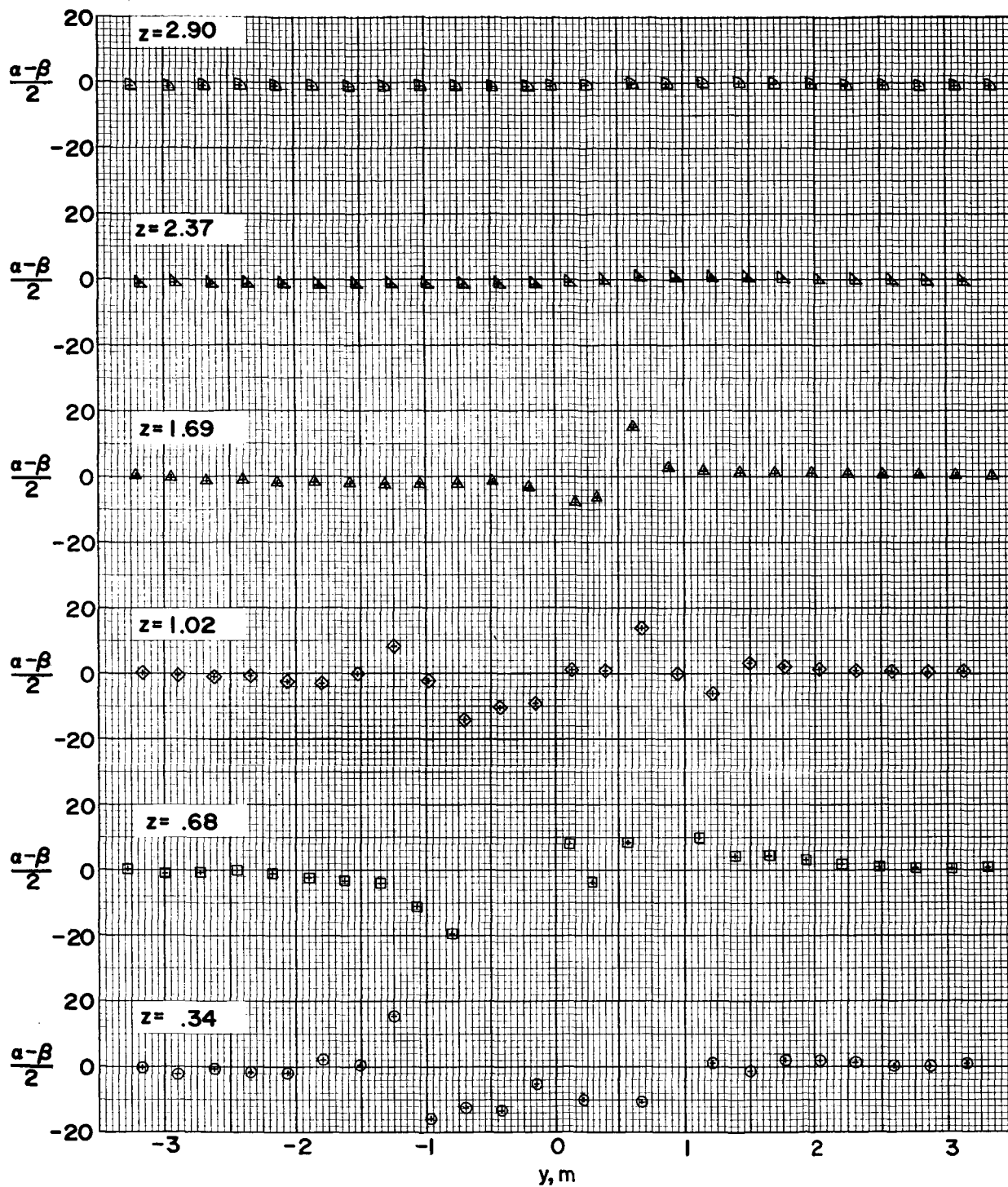
(e) $x = -1.35$ m.

Figure 20. - Continued.



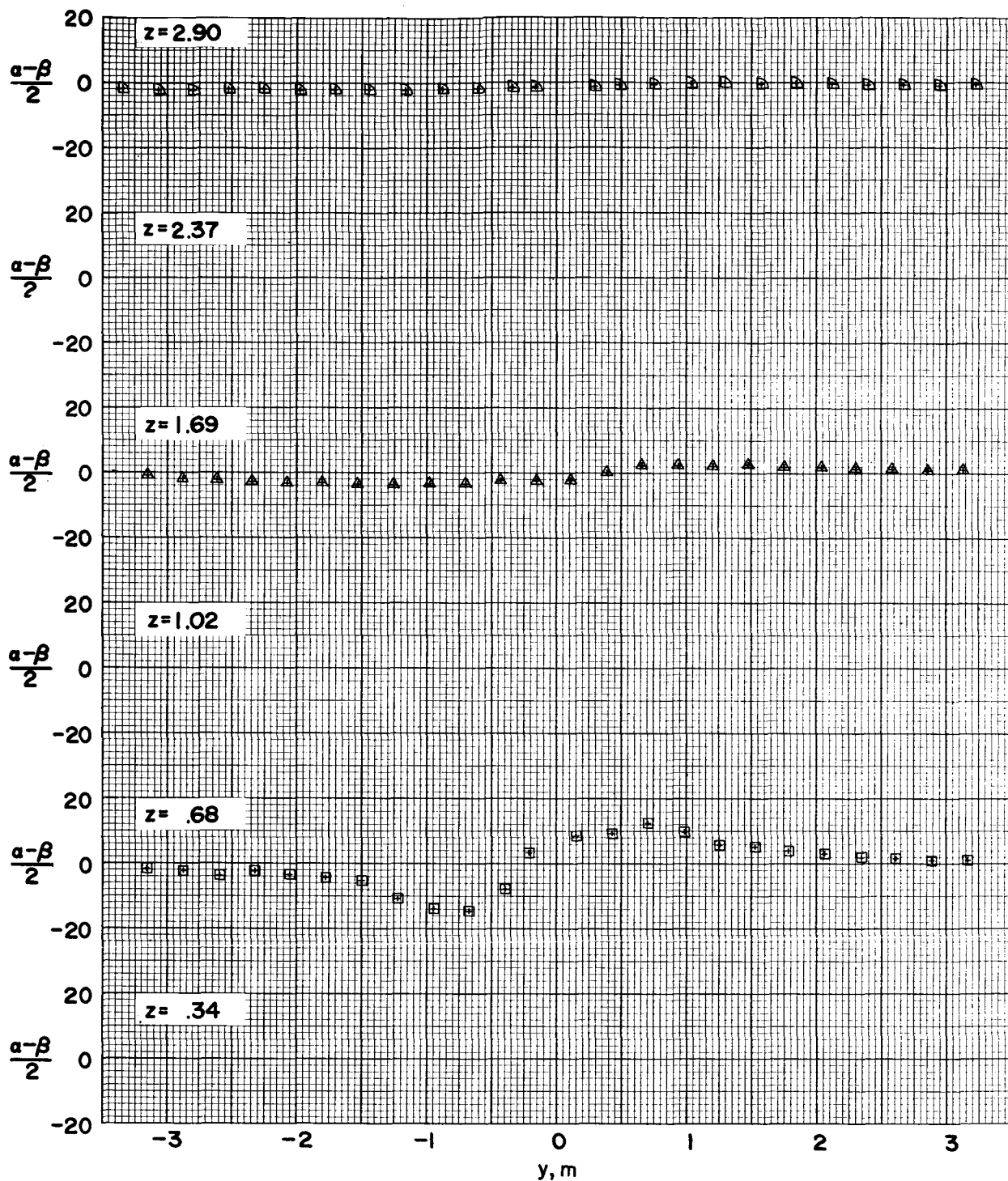
(f) $x = 0$ m.

Figure 20.- Continued.



(g) $x = 2.03$ m.

Figure 20. - Continued.



(h) $x = 4.06$ m.

Figure 20. - Concluded.

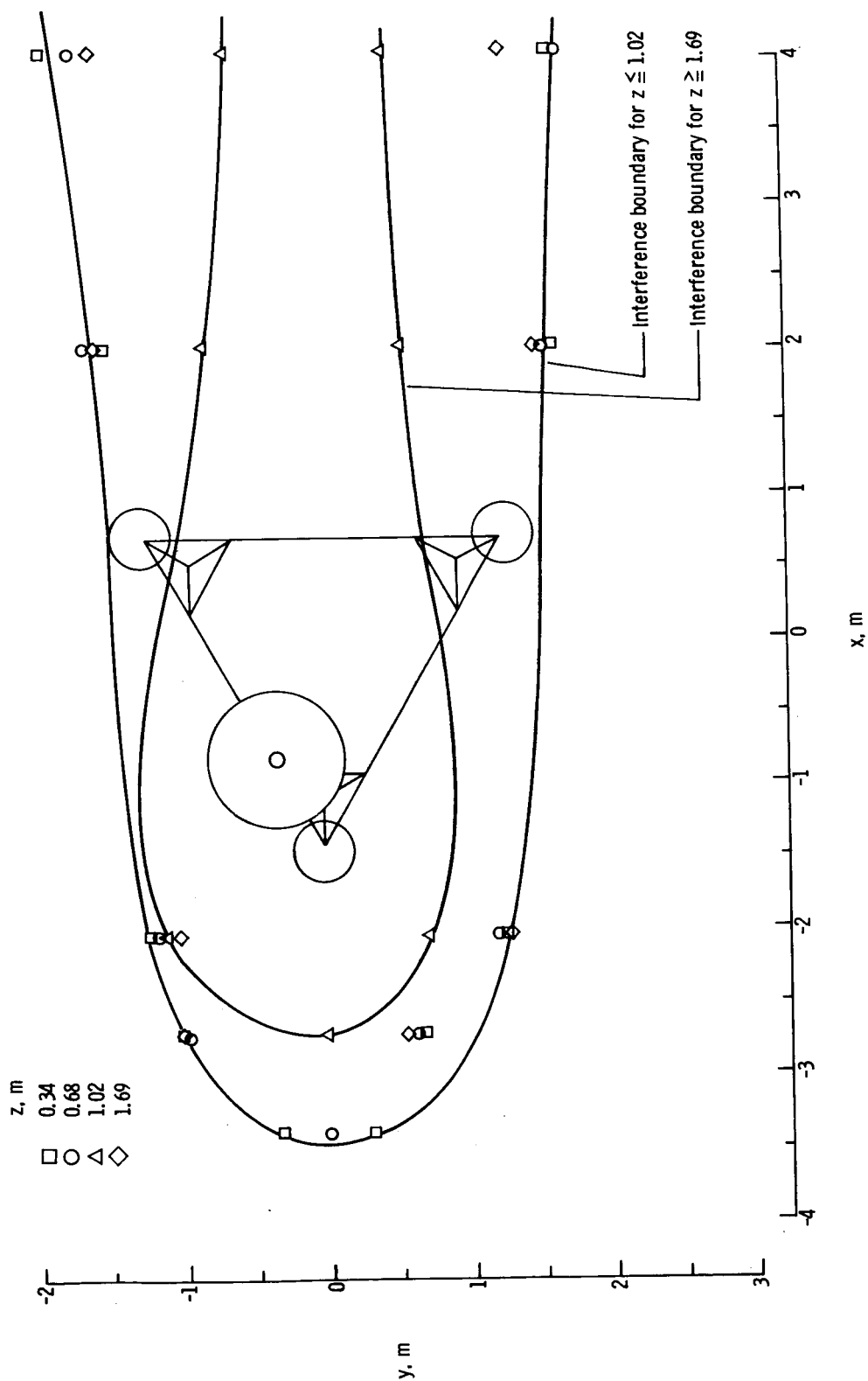


Figure 21.- Effect of wind direction on 5-percent wind-speed interference boundaries
for model configuration 5. $\phi = 180^\circ$.

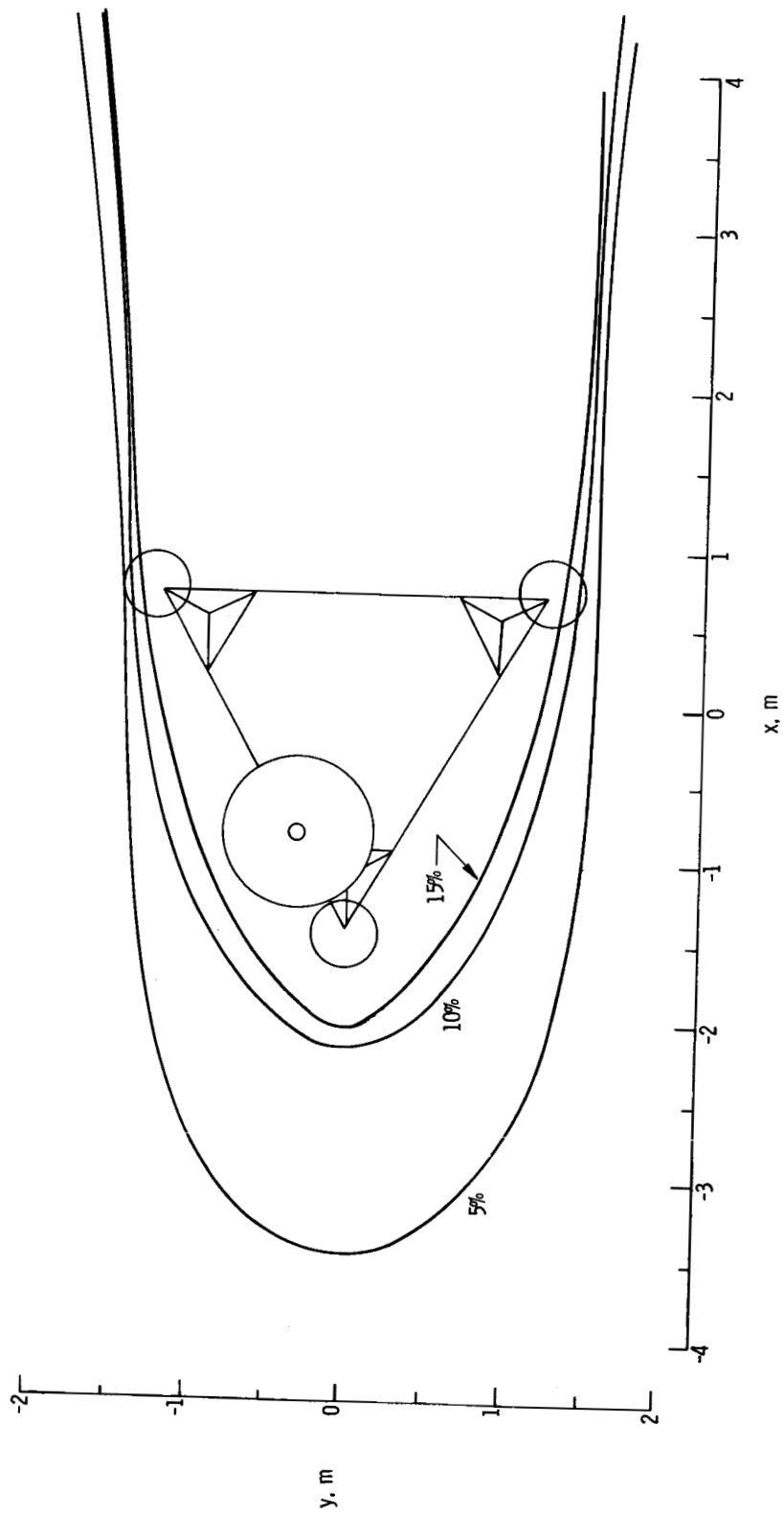
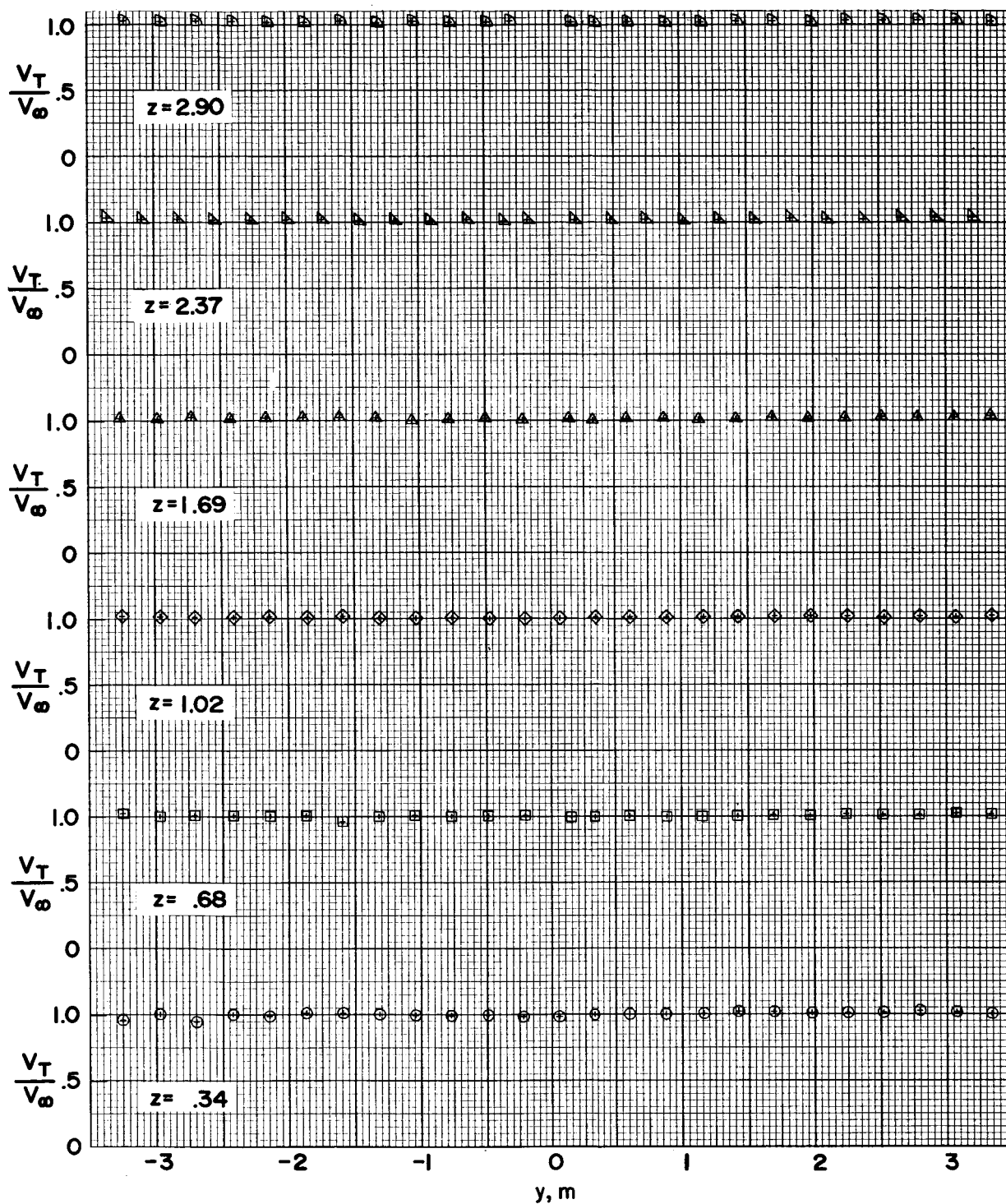
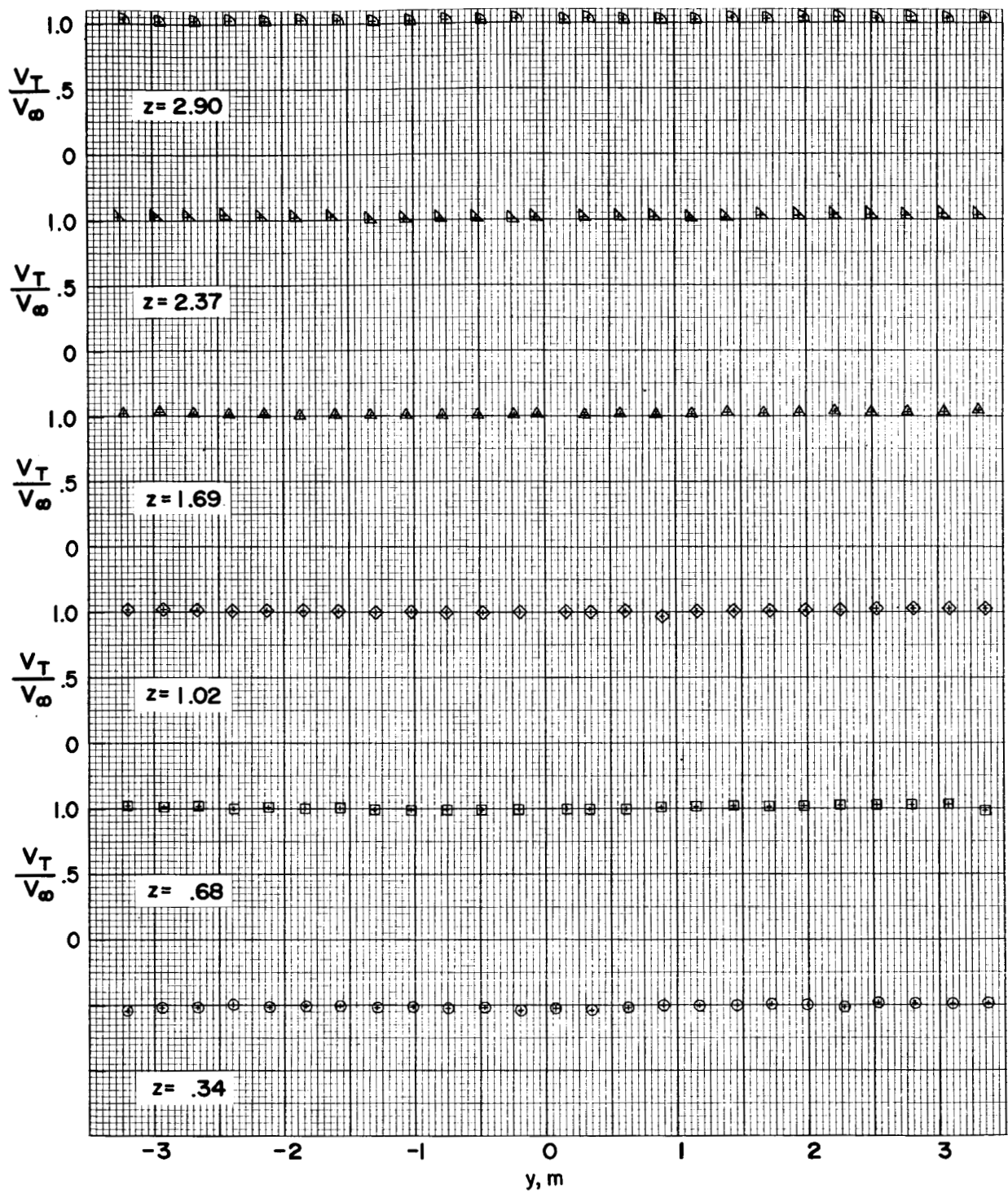


Figure 22.- The 5-, 10-, and 15-percent wind-speed interference boundaries for model configuration 5. $z = 0.34$ m.



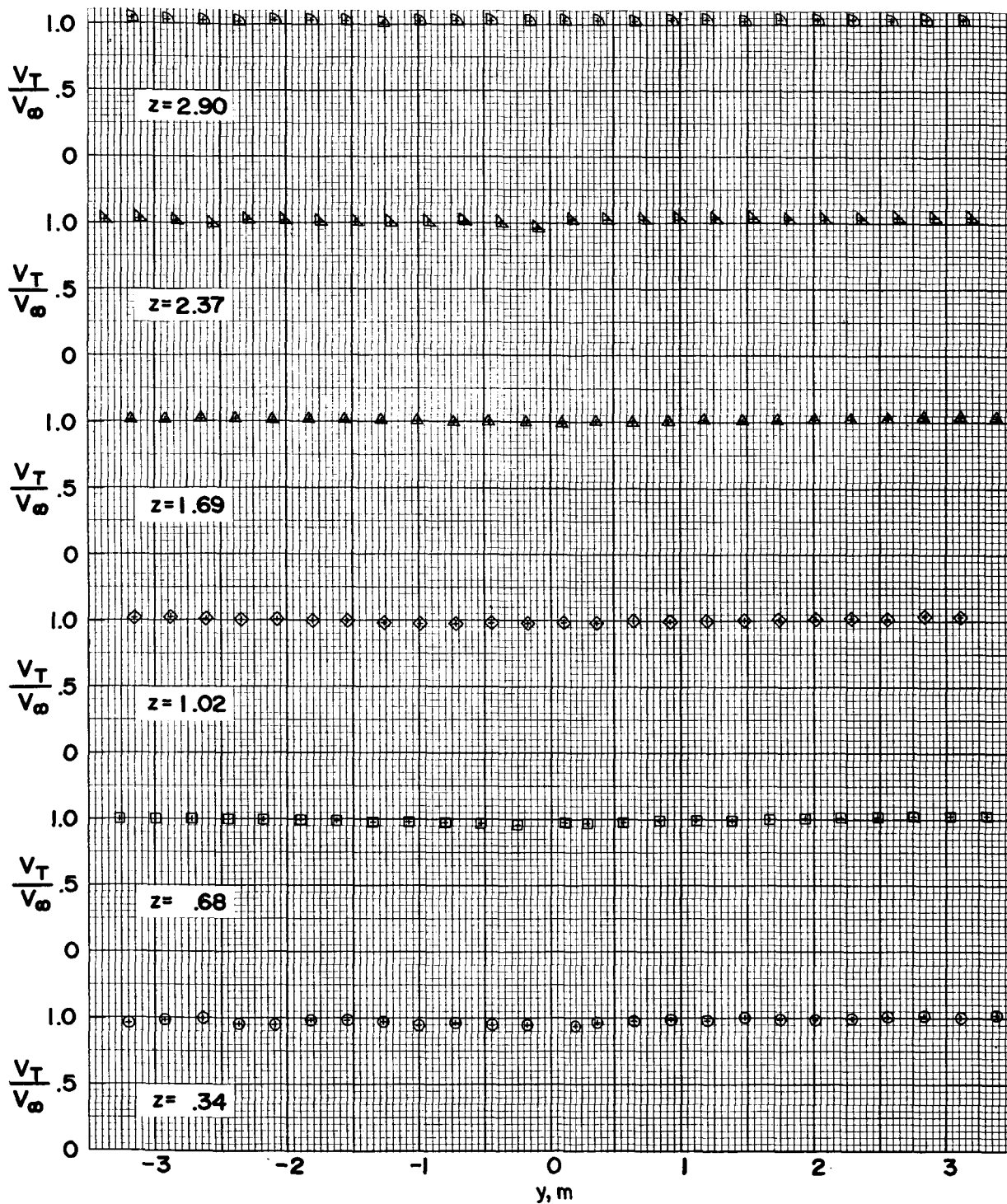
(a) $x = -4.06$ m.

Figure 23.- Velocity ratio V_T/V_∞ as a function of lateral position y for model configuration 5.



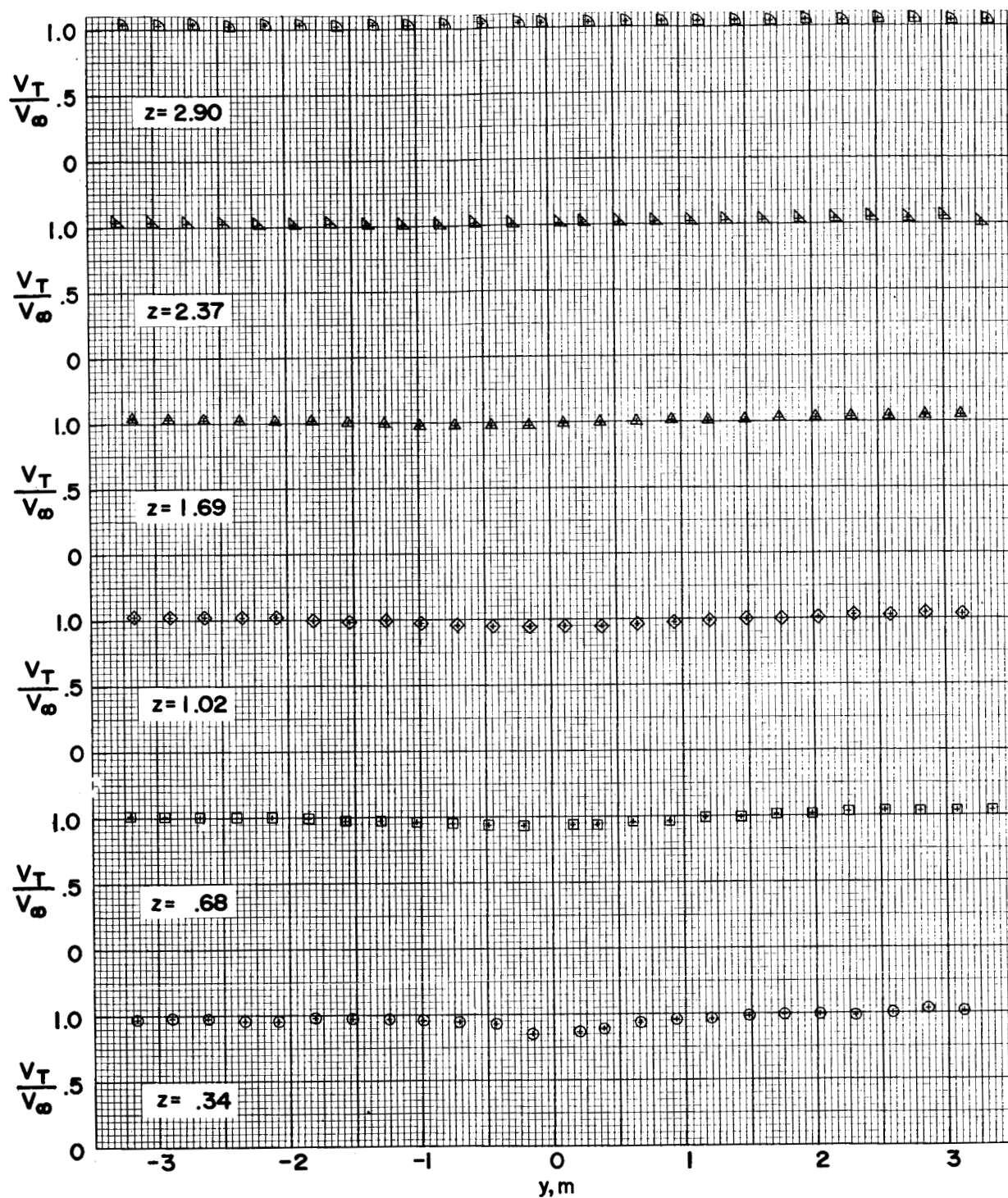
(b) $x = -3.39$ m.

Figure 23.- Continued.



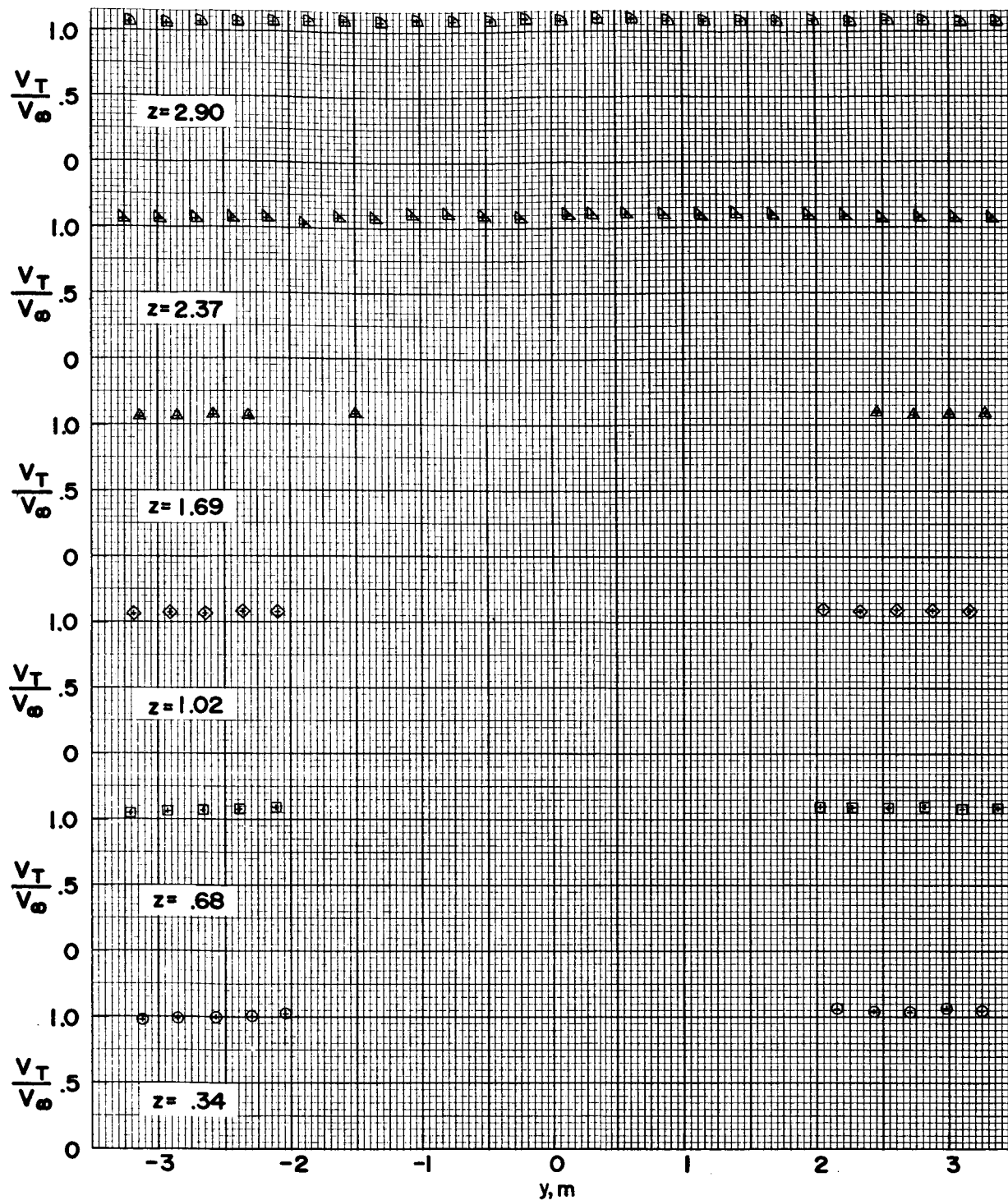
(c) $x = -2.71$ m.

Figure 23. - Continued.



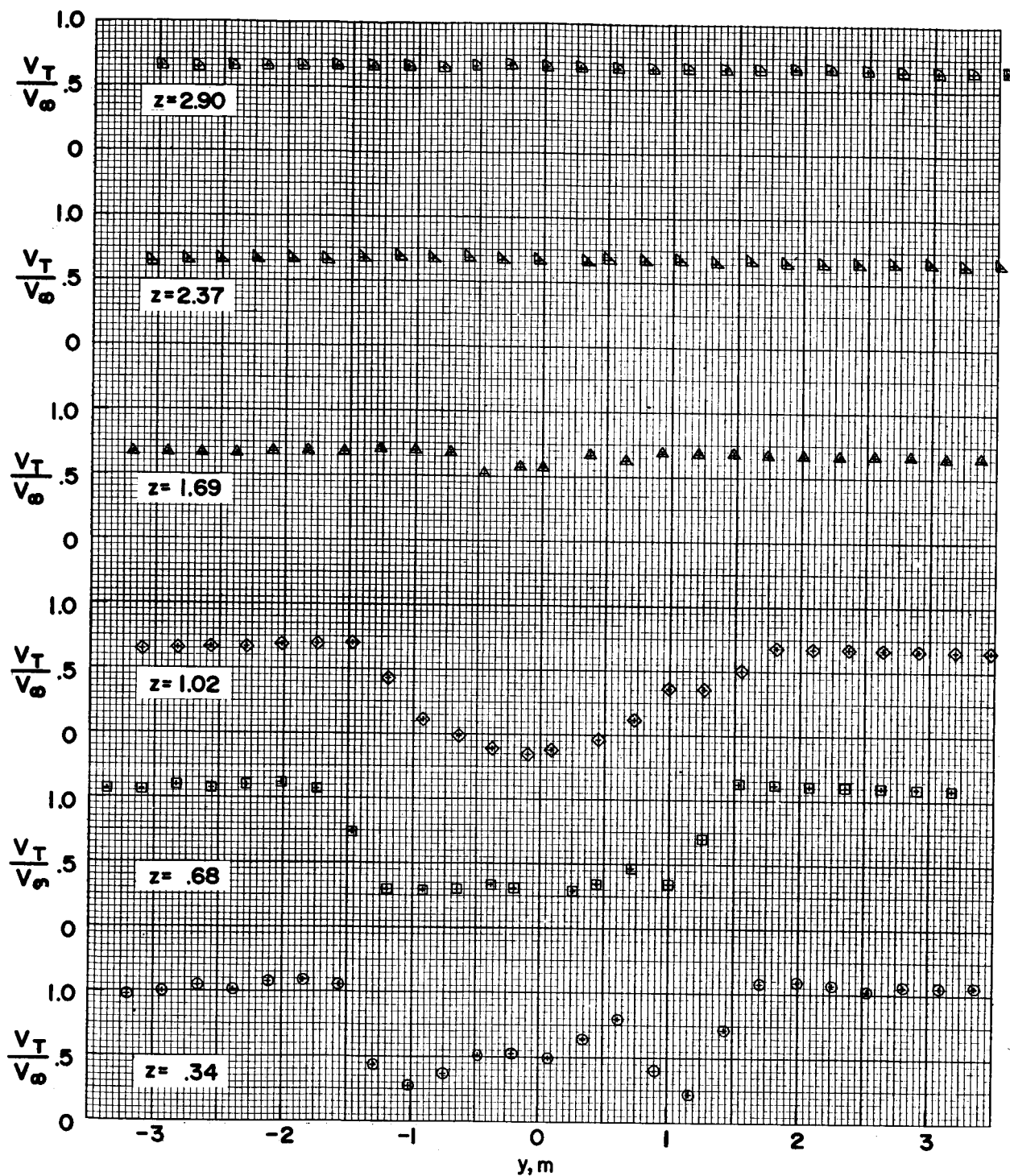
(d) $x = -2.03$ m.

Figure 23.- Continued.



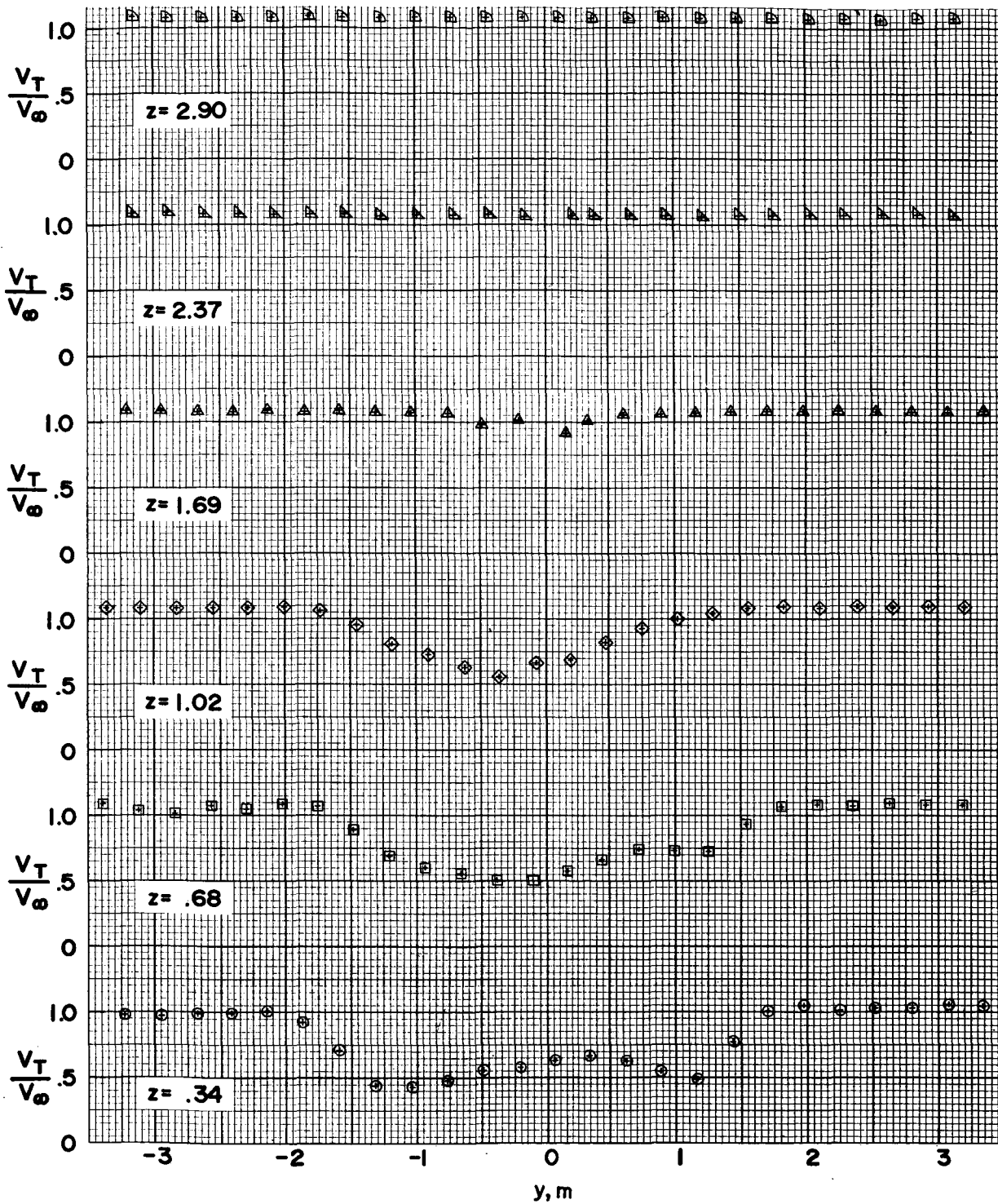
(e) $x = 0$ m.

Figure 23. - Continued.



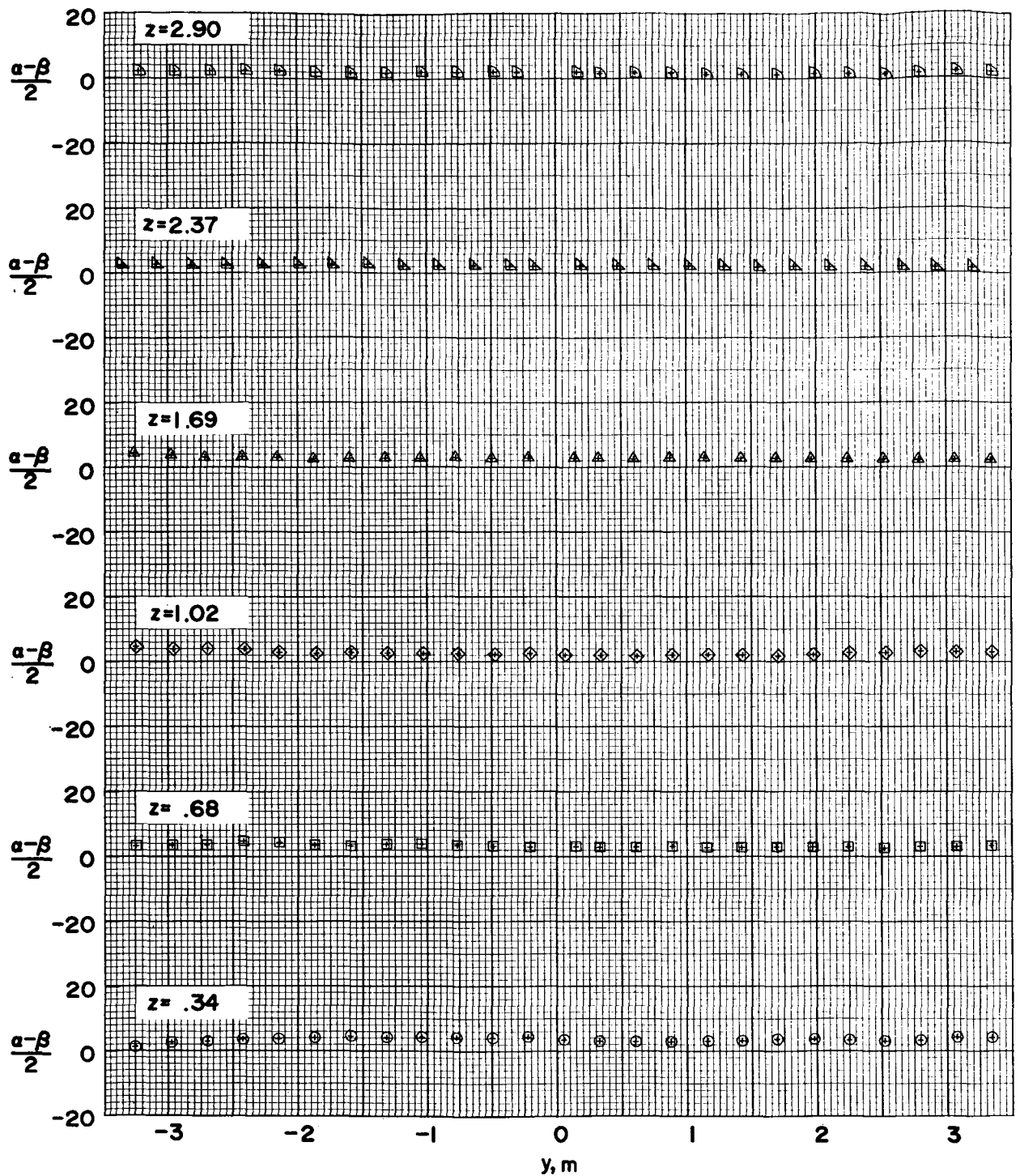
(f) $x = 2.03$ m.

Figure 23.- Continued.



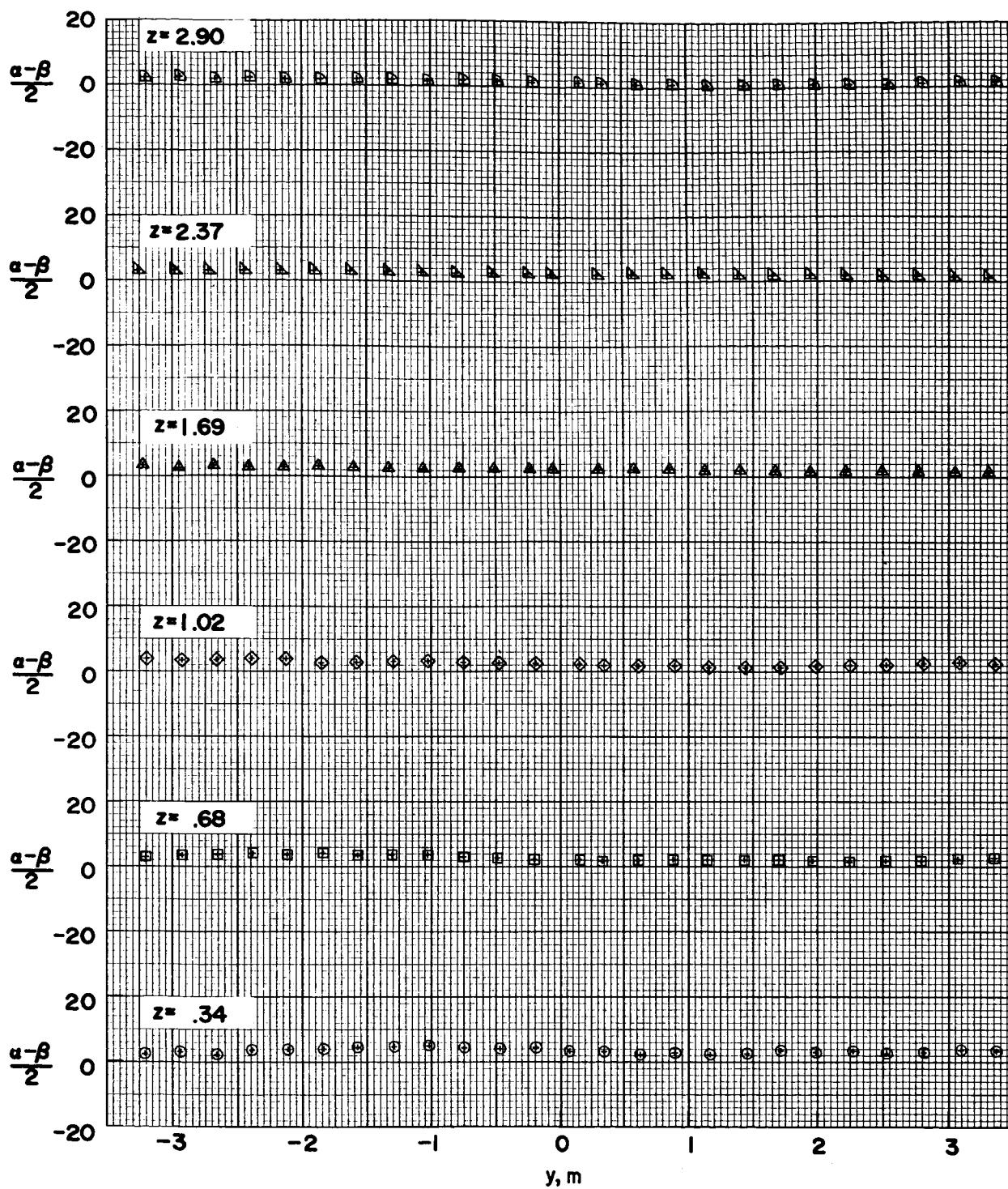
(g) $x = 4.06$ m.

Figure 23.- Concluded.



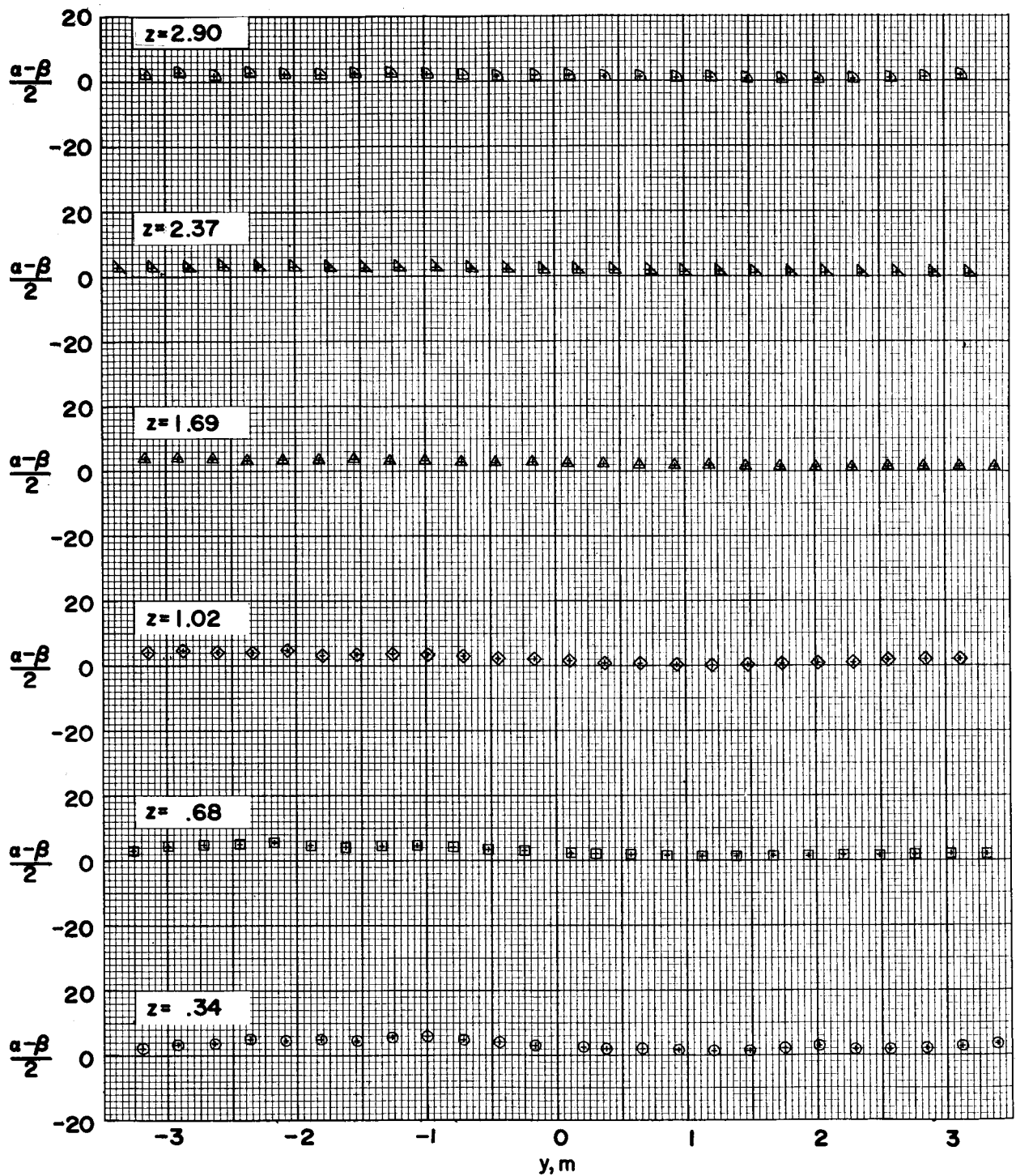
(a) $x = -4.06$ m.

Figure 24.- Local flow angle $\frac{\alpha - \beta}{2}$ as a function of lateral position y for model configuration 5.



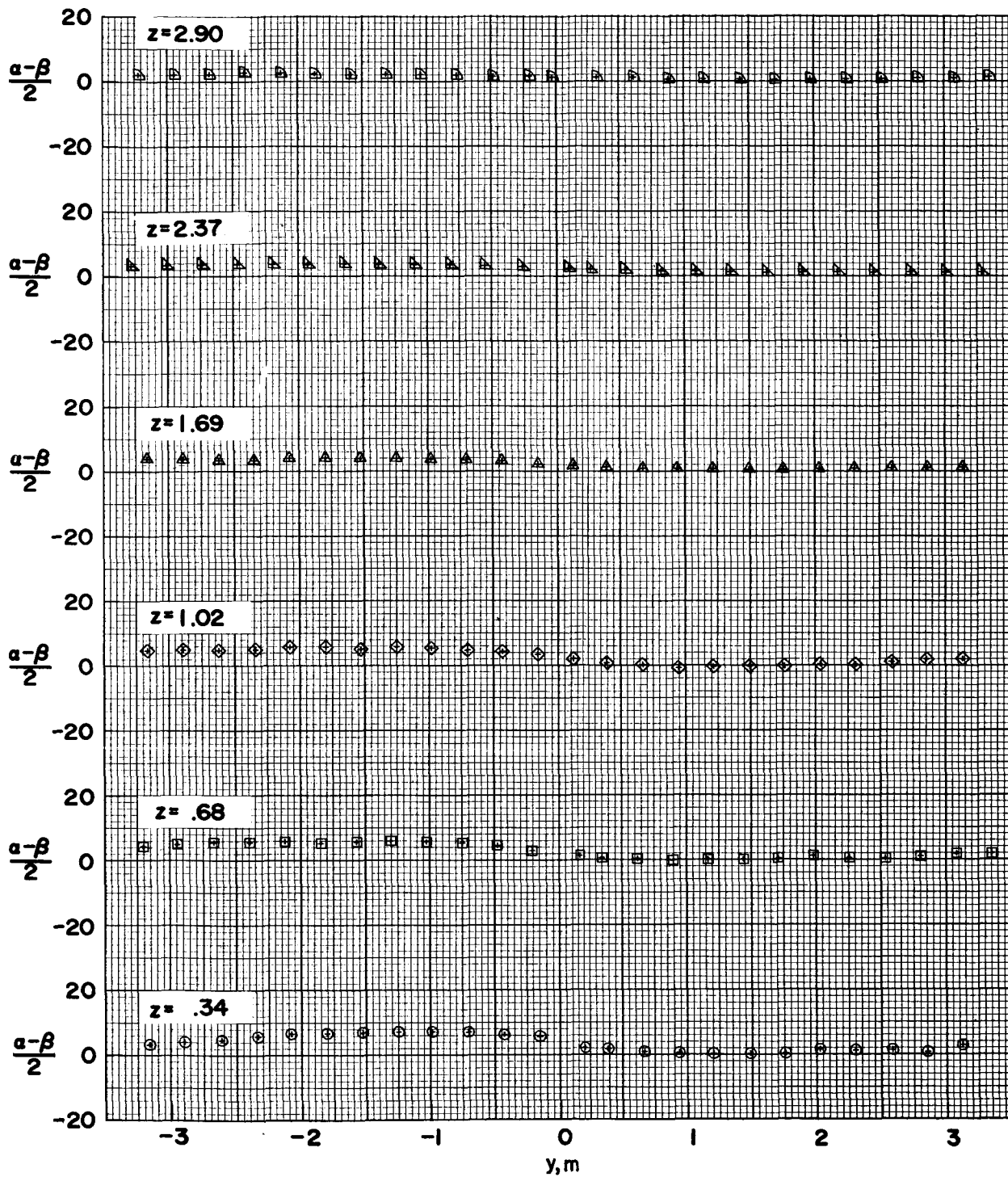
(b) $x = -3.39$ m.

Figure 24. - Continued.



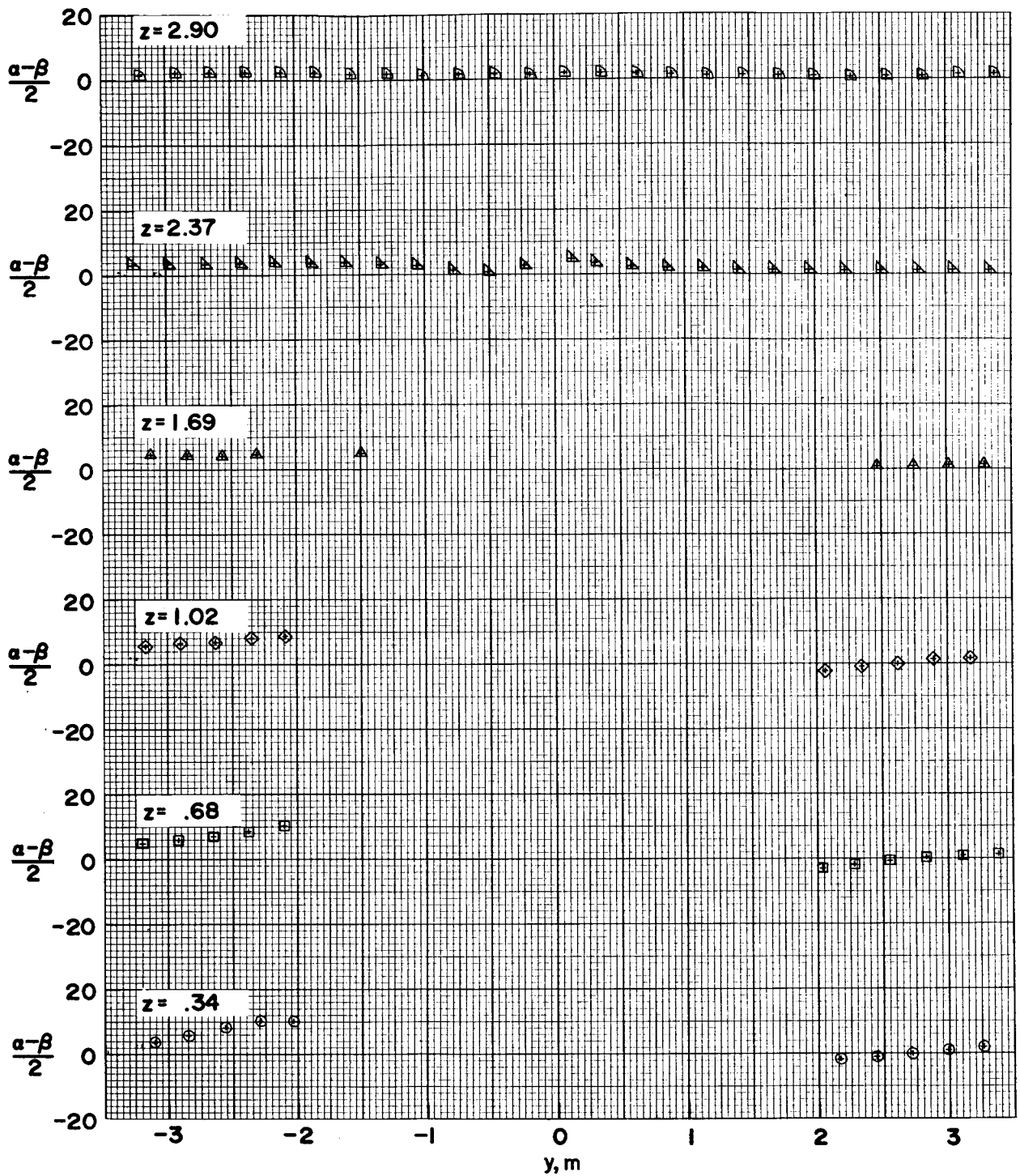
(c) $x = -2.71$ m.

Figure 24.- Continued.



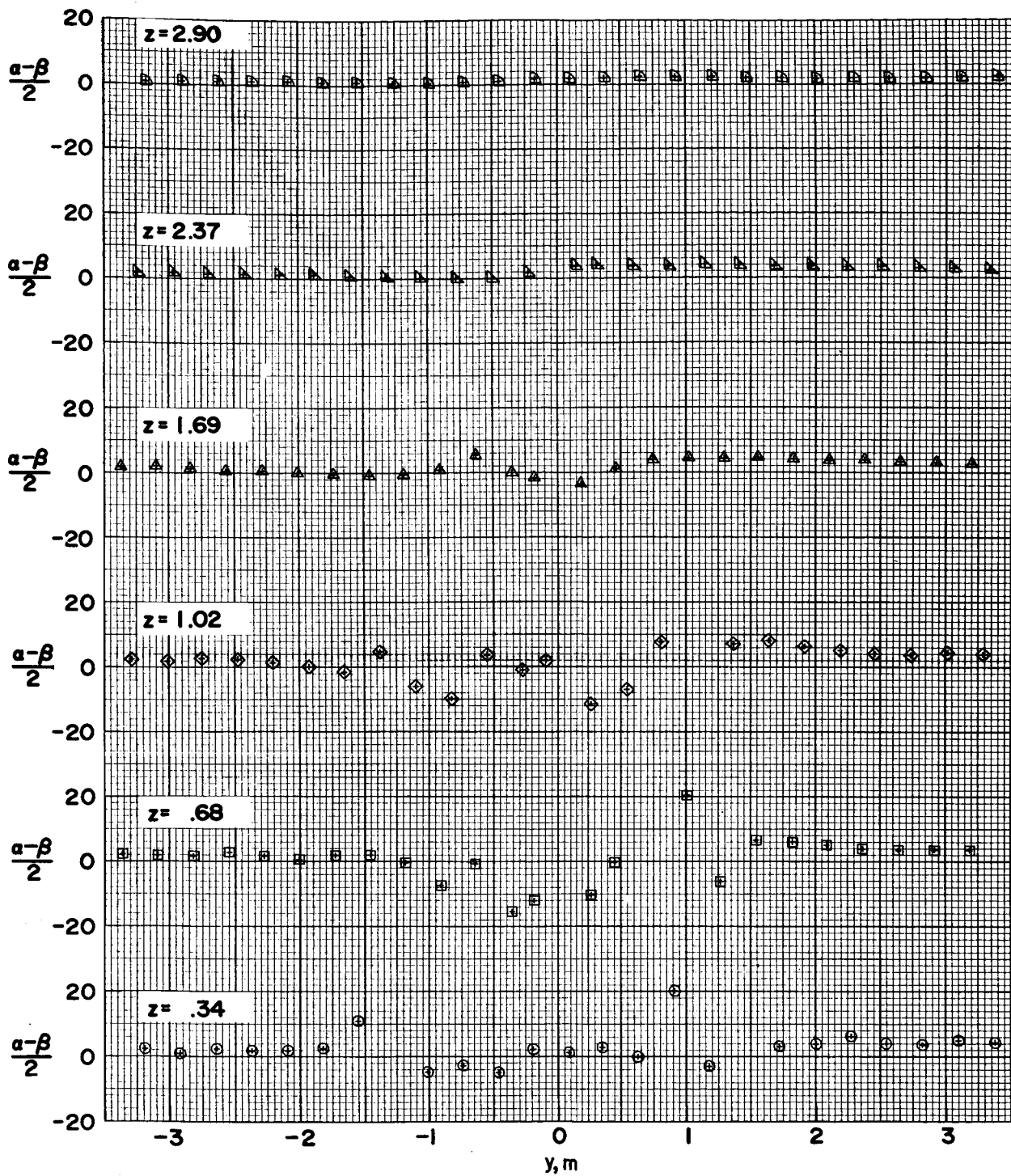
(d) $x = -2.03$ m.

Figure 24. - Continued.



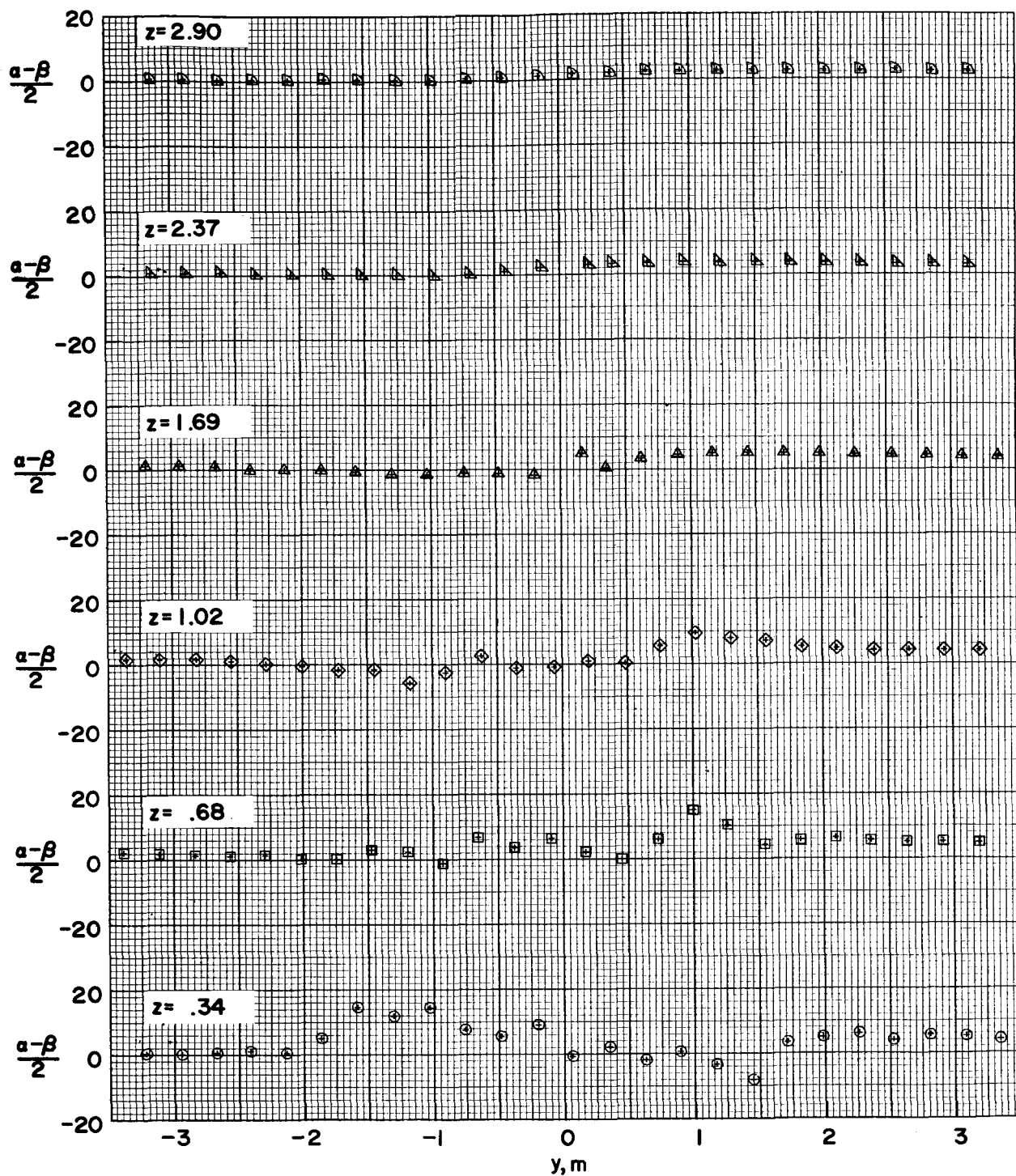
(e) $x = 0$ m.

Figure 24.- Continued.



(f) $x = 2.03$ m.

Figure 24. - Continued.



(g) $x = 4.06$ m.

Figure 24.- Concluded.

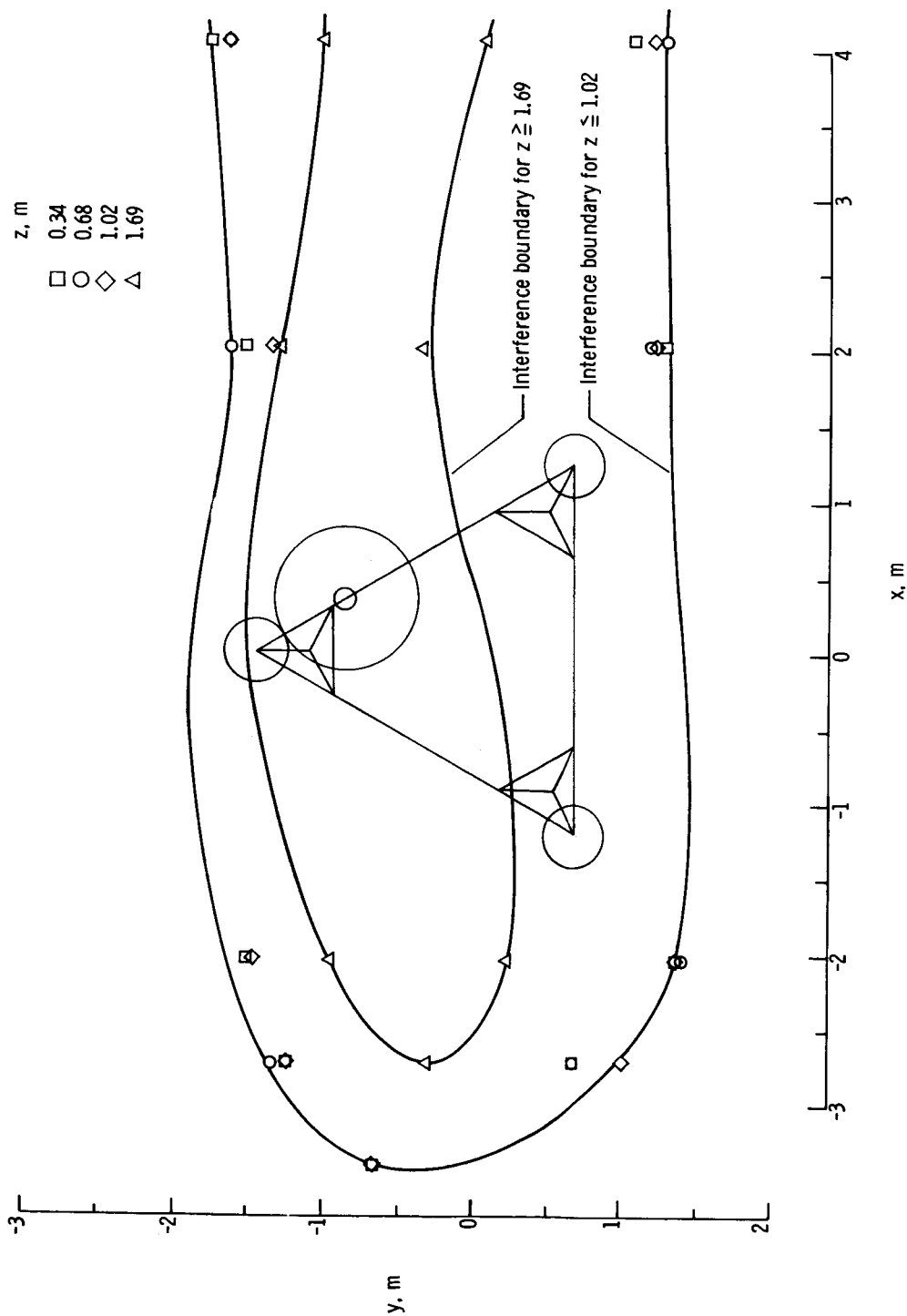


Figure 25.- Effect of wind direction on 5-percent wind-speed interference boundaries
for model configuration 6. $\phi = 270^\circ$.

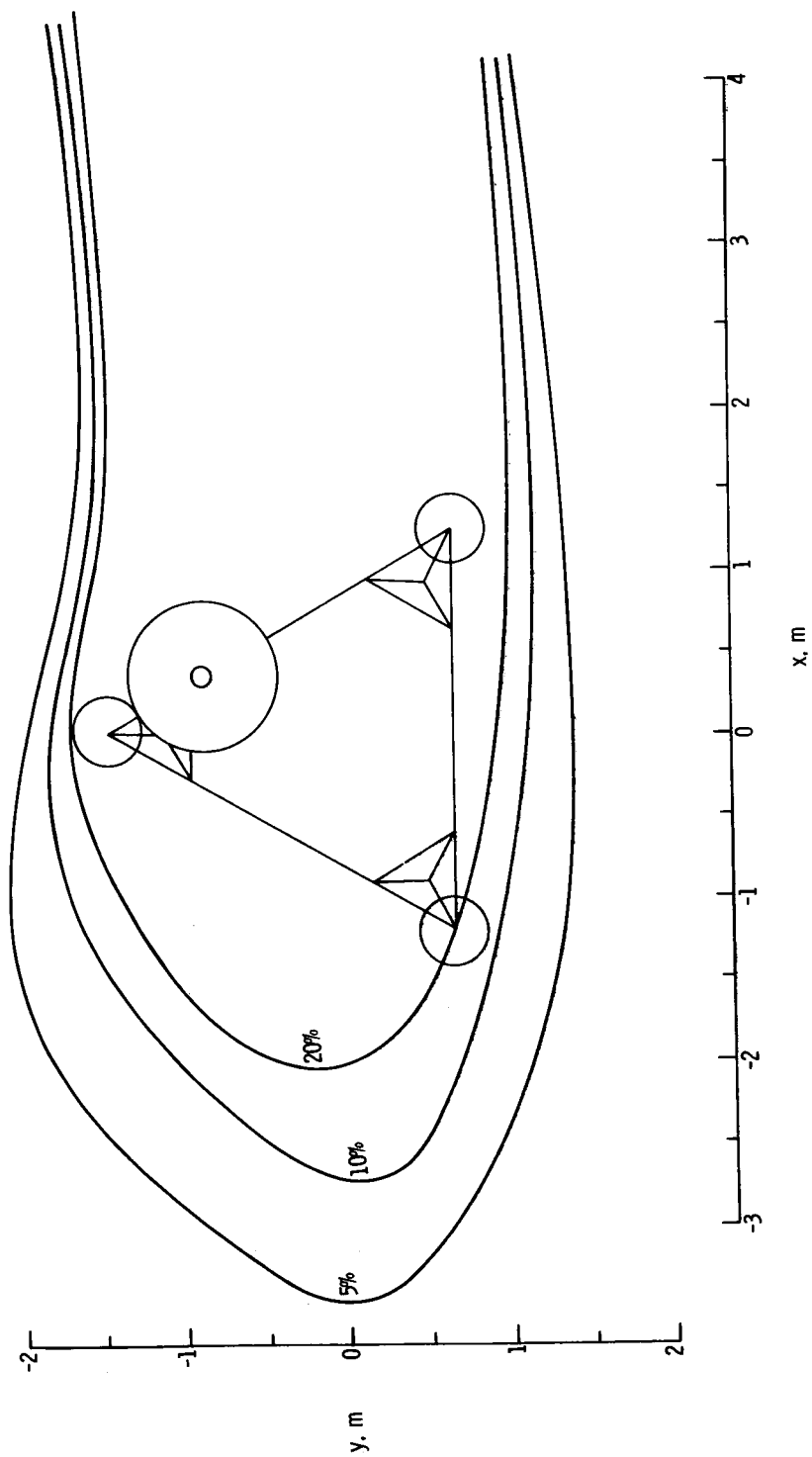
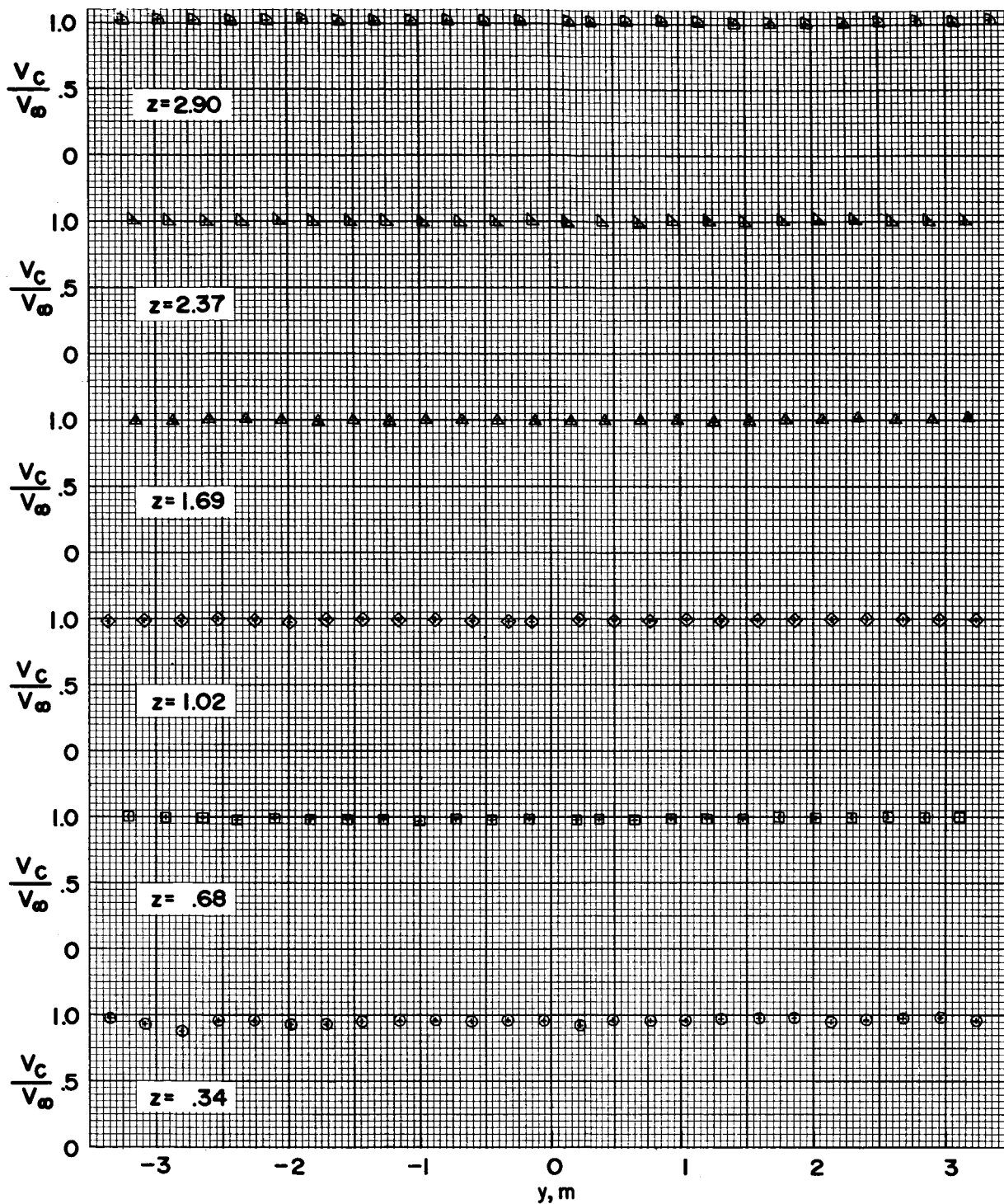
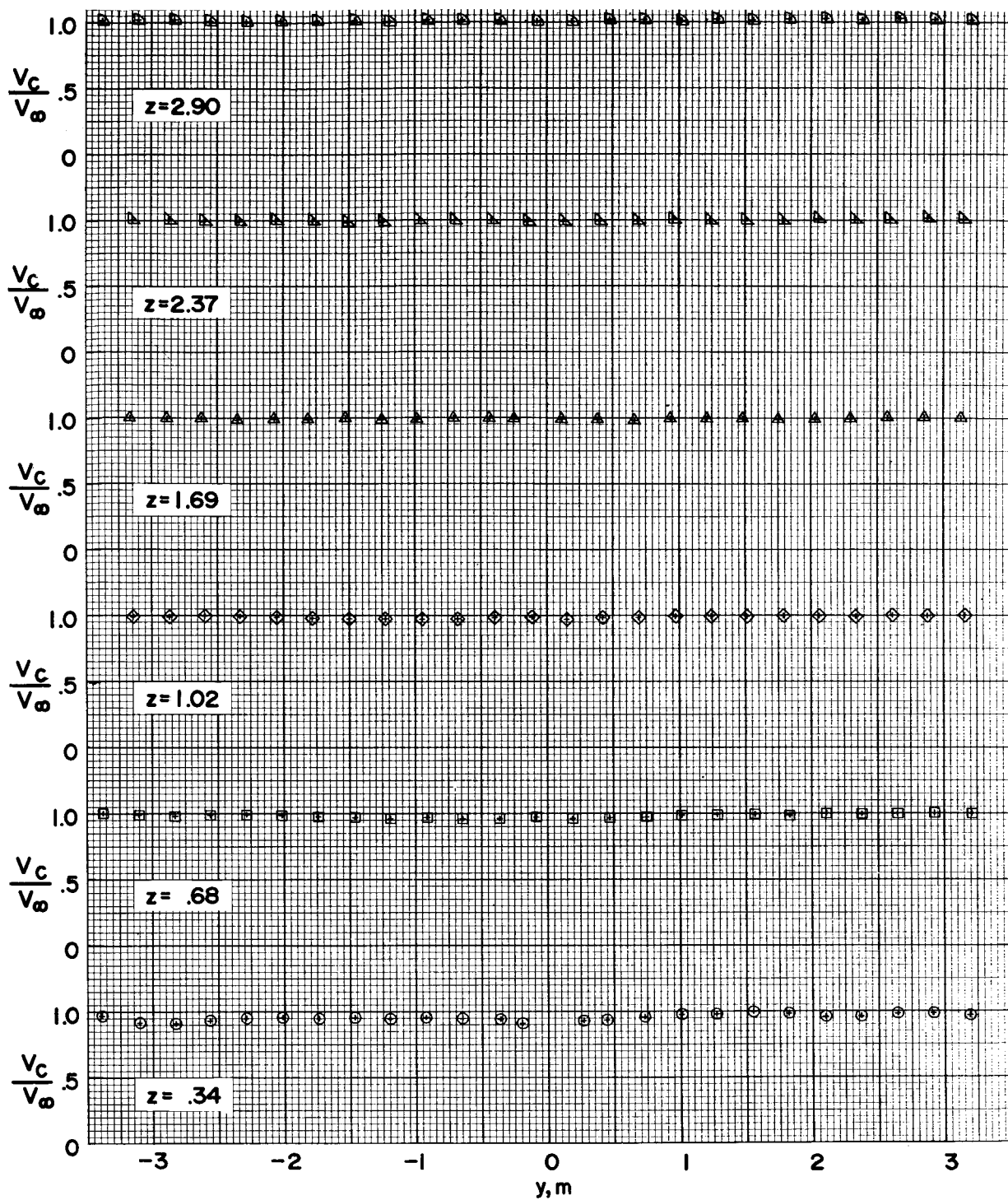


Figure 26.- The 5-, 10-, and 20-percent wind-speed interference boundaries for model configuration 6. $z = 0.34$ m.



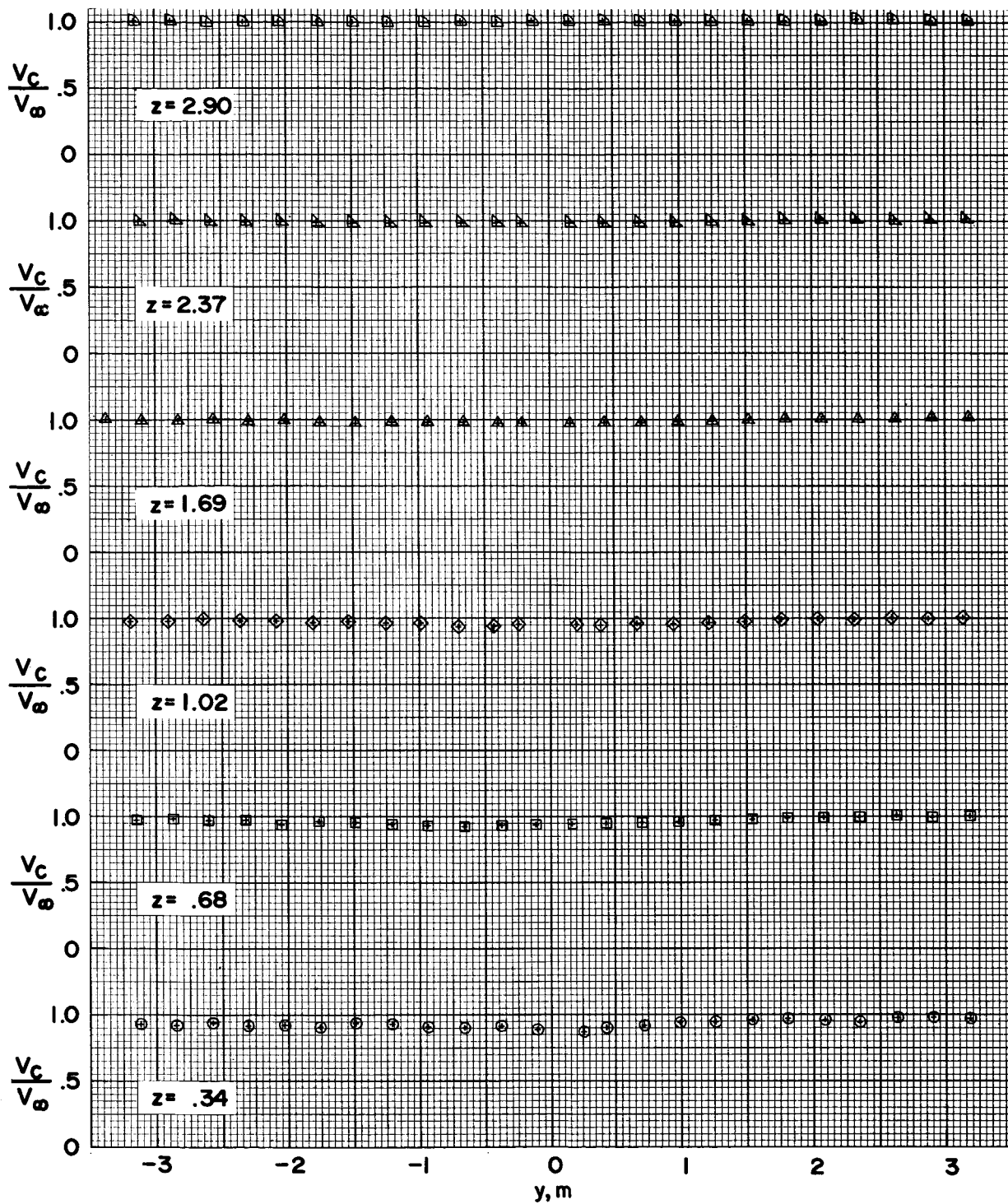
(a) $x = -4.06$ m.

Figure 27.- Velocity ratio V_c/V_∞ as a function of lateral position y for model configuration 6.



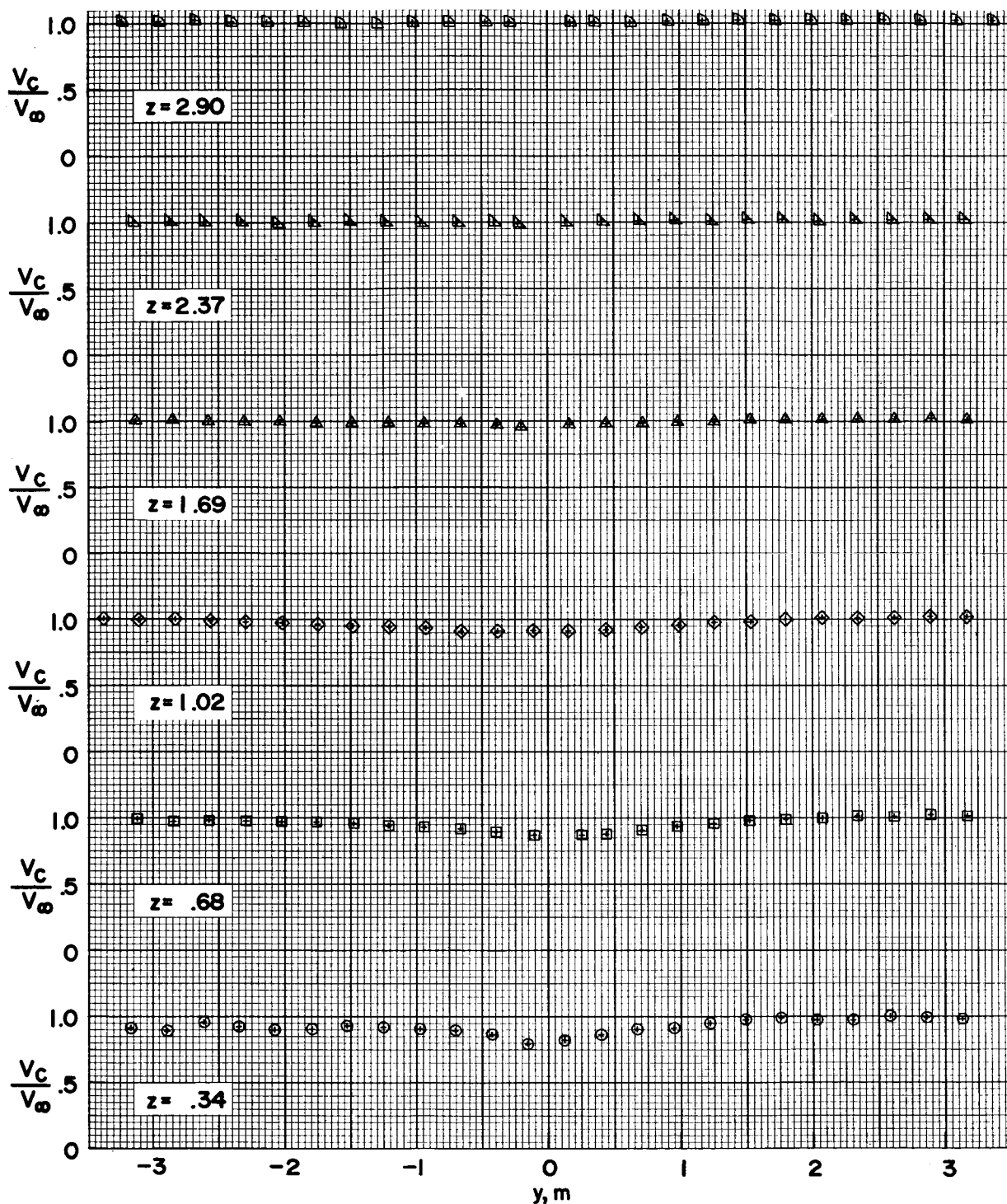
(b) $x = -3.39$ m.

Figure 27.- Continued.



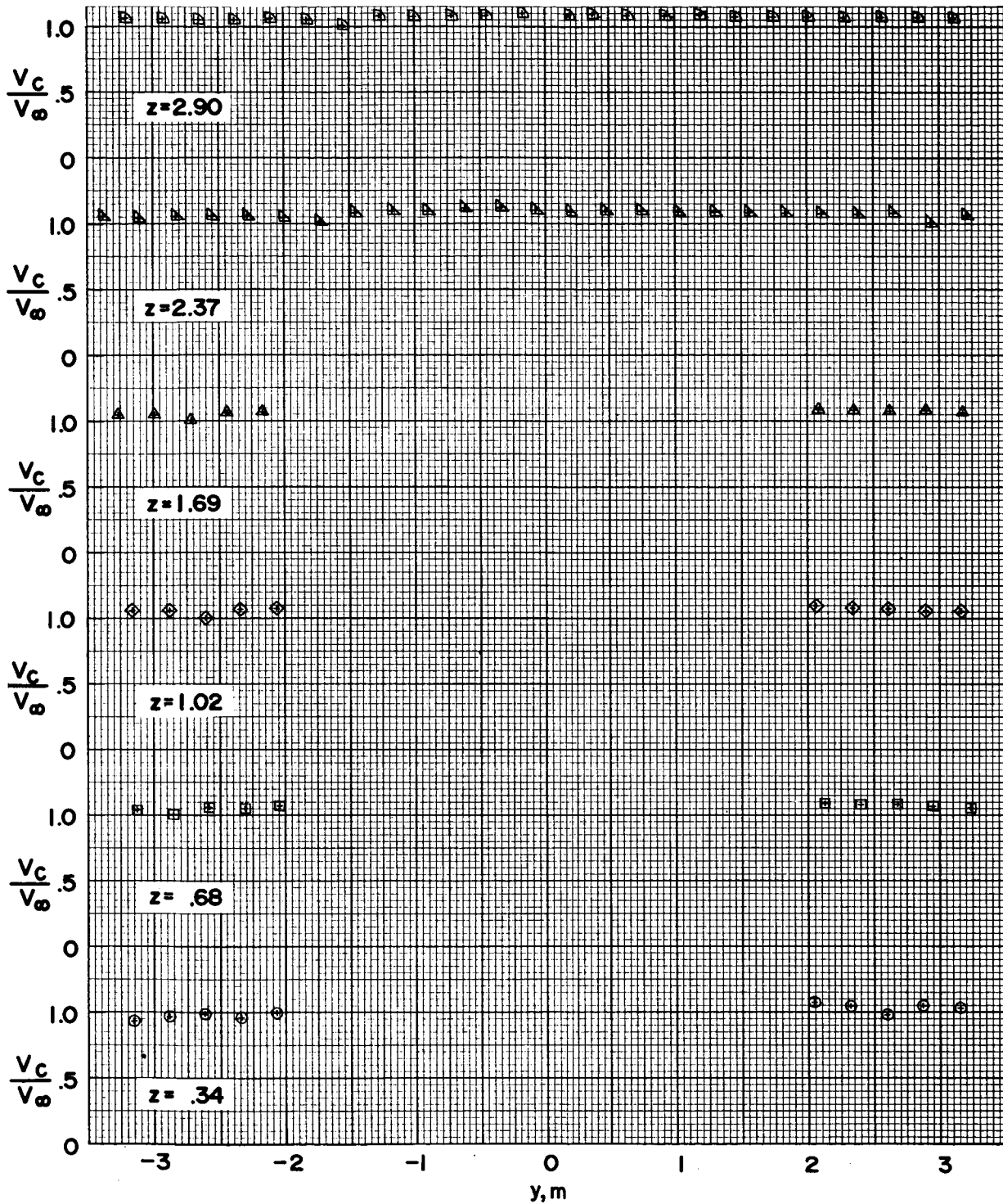
(c) $x = -2.71$ m.

Figure 27.- Continued.



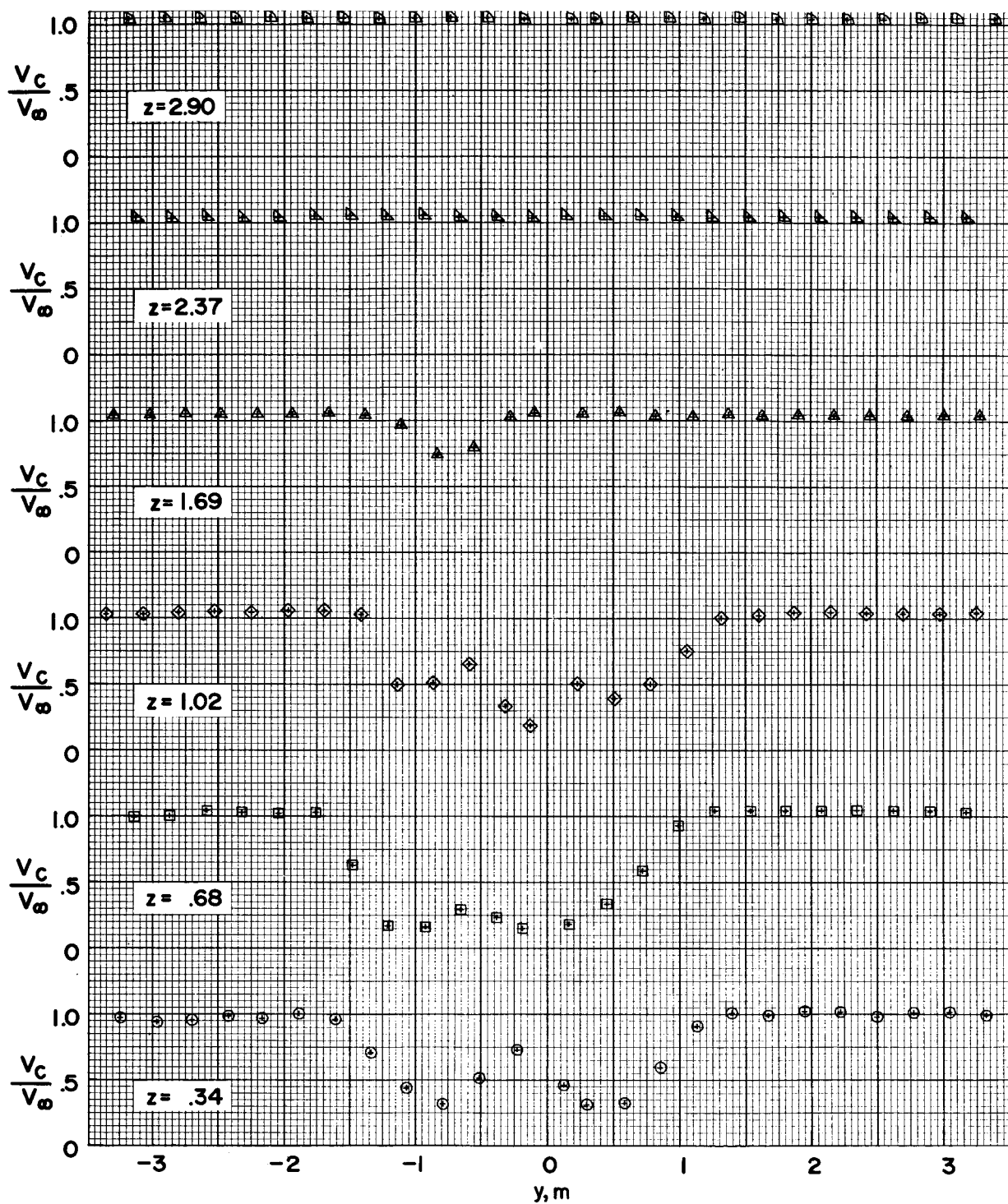
(d) $x = -2.03$ m.

Figure 27. - Continued.



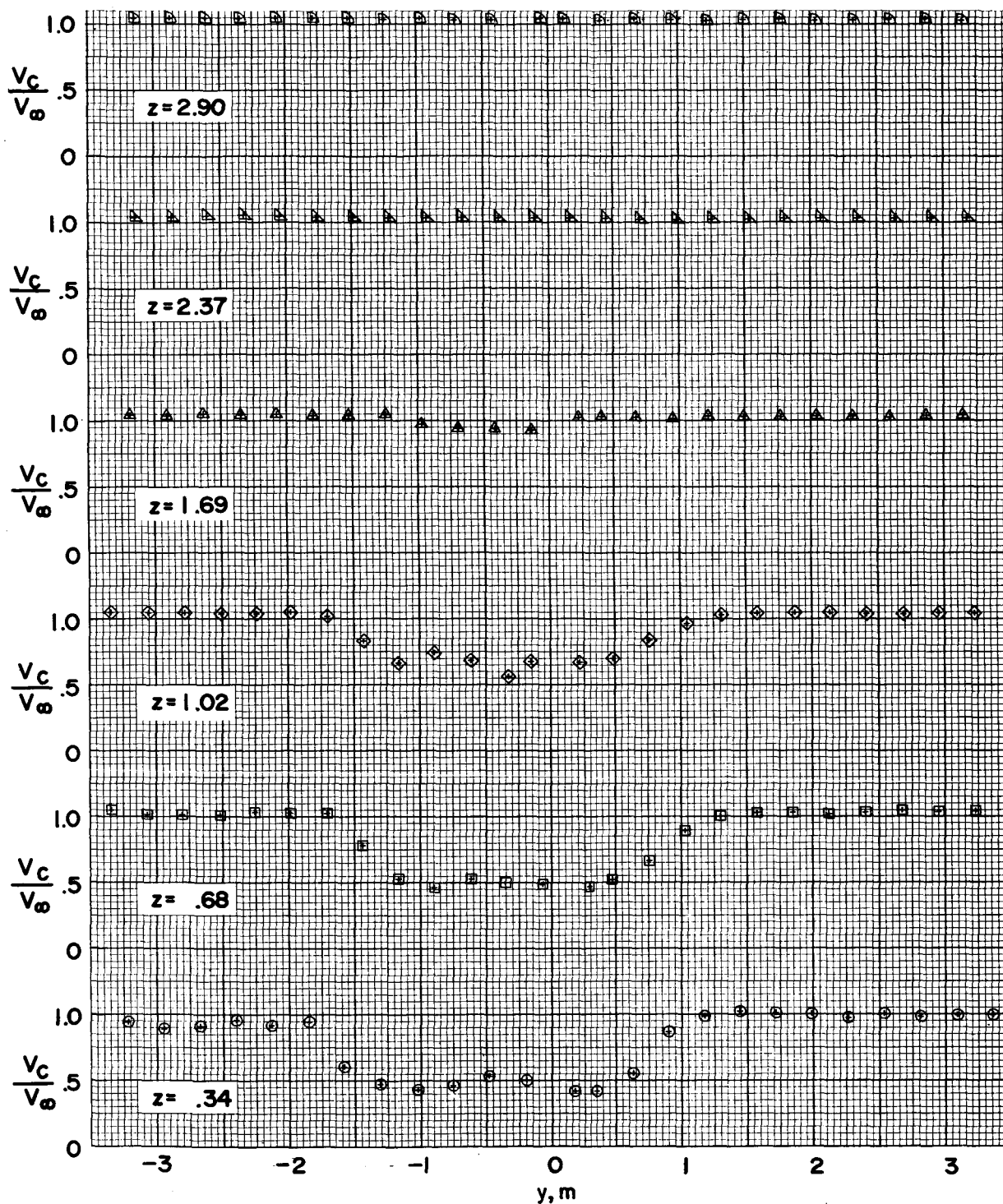
(e) $x = 0$ m.

Figure 27. - Continued.



(f) $x = 2.03$ m.

Figure 27.- Continued.



(g) $x = 4.06$ m.

Figure 27.- Concluded.

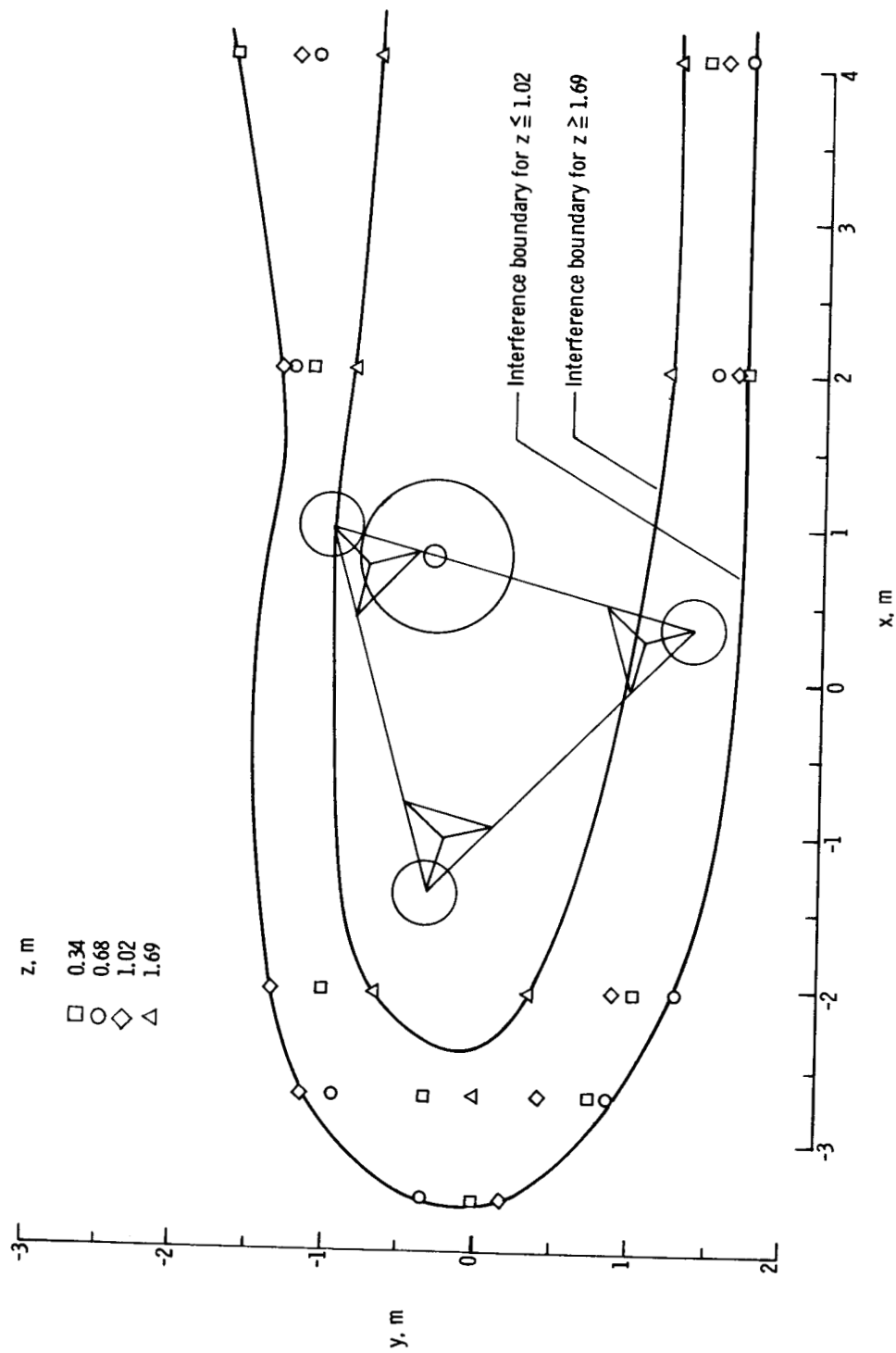


Figure 28.- Effect of wind direction on 5-percent wind-speed interference boundaries
for model configuration 7. $\phi = 315^\circ$.

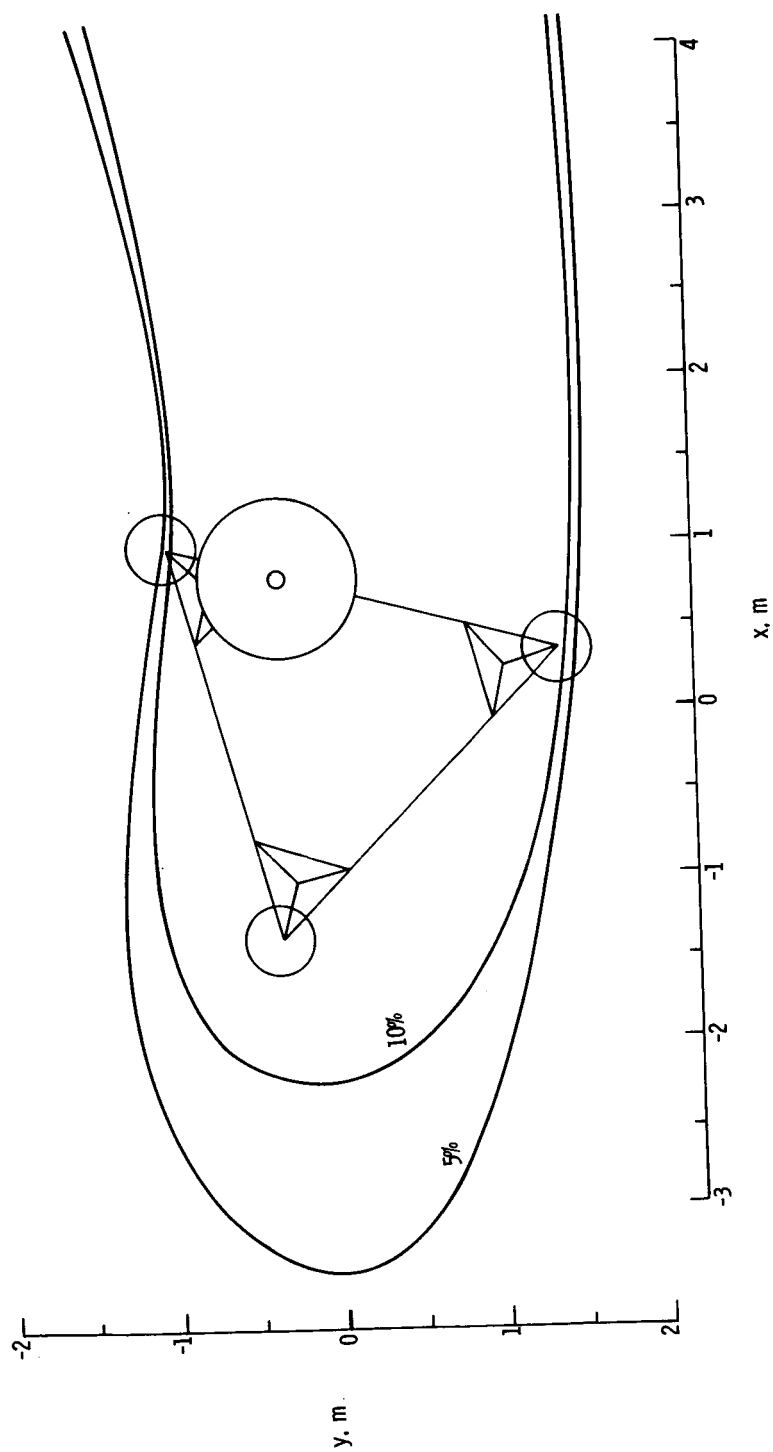
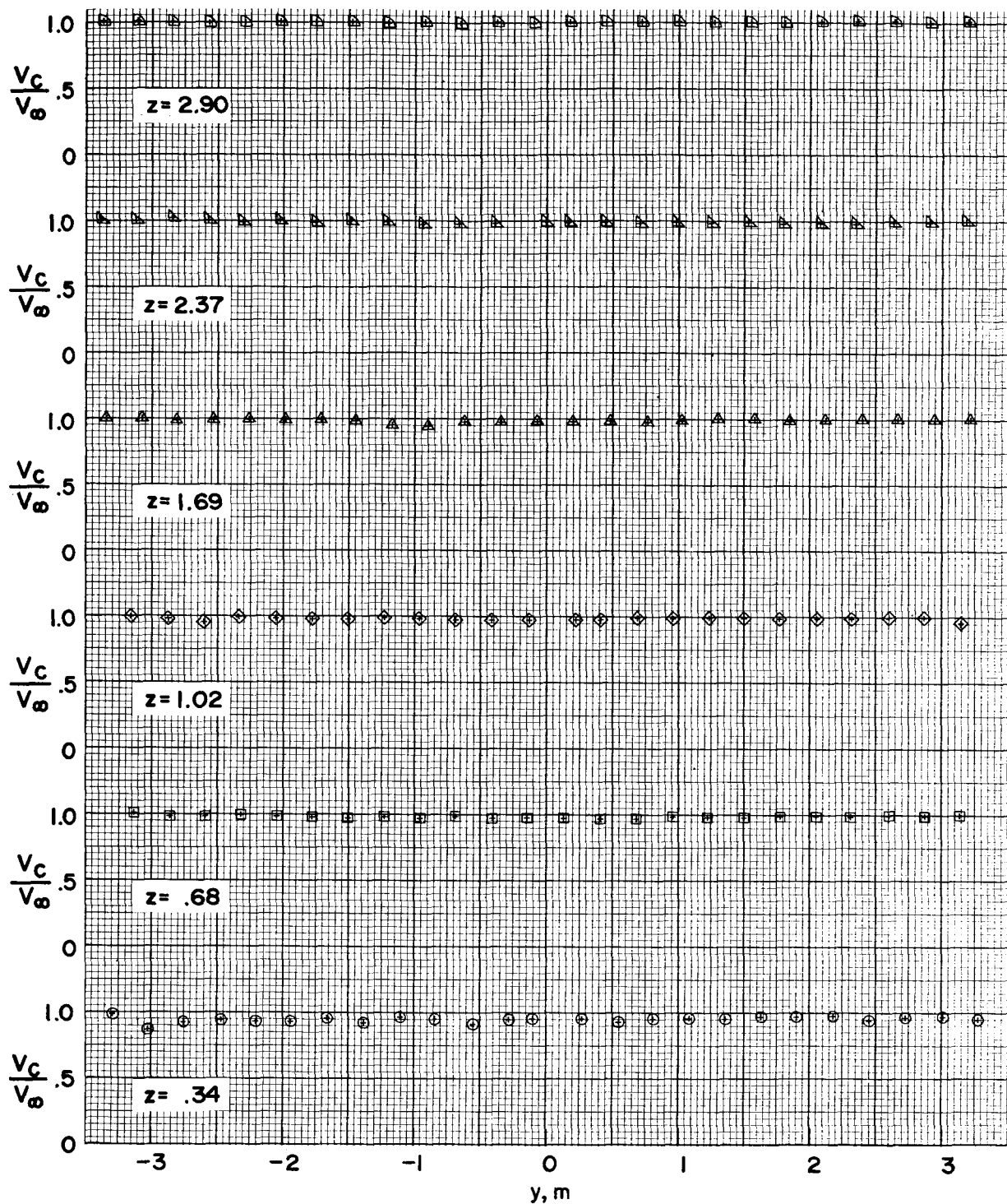
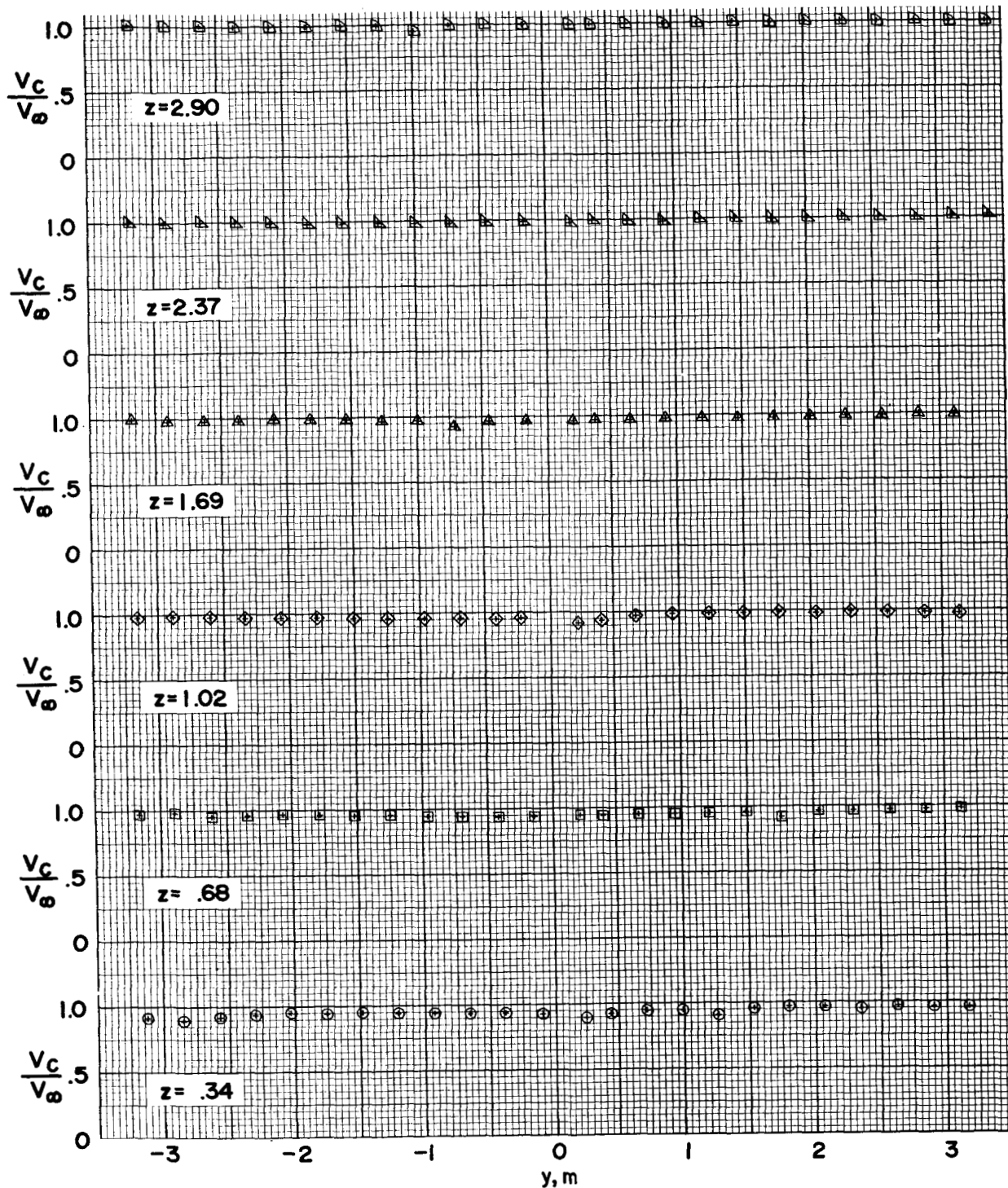


Figure 29. - The 5- and 10-percent wind-speed interference boundaries for model configuration 7. $z = 0.34$ m.



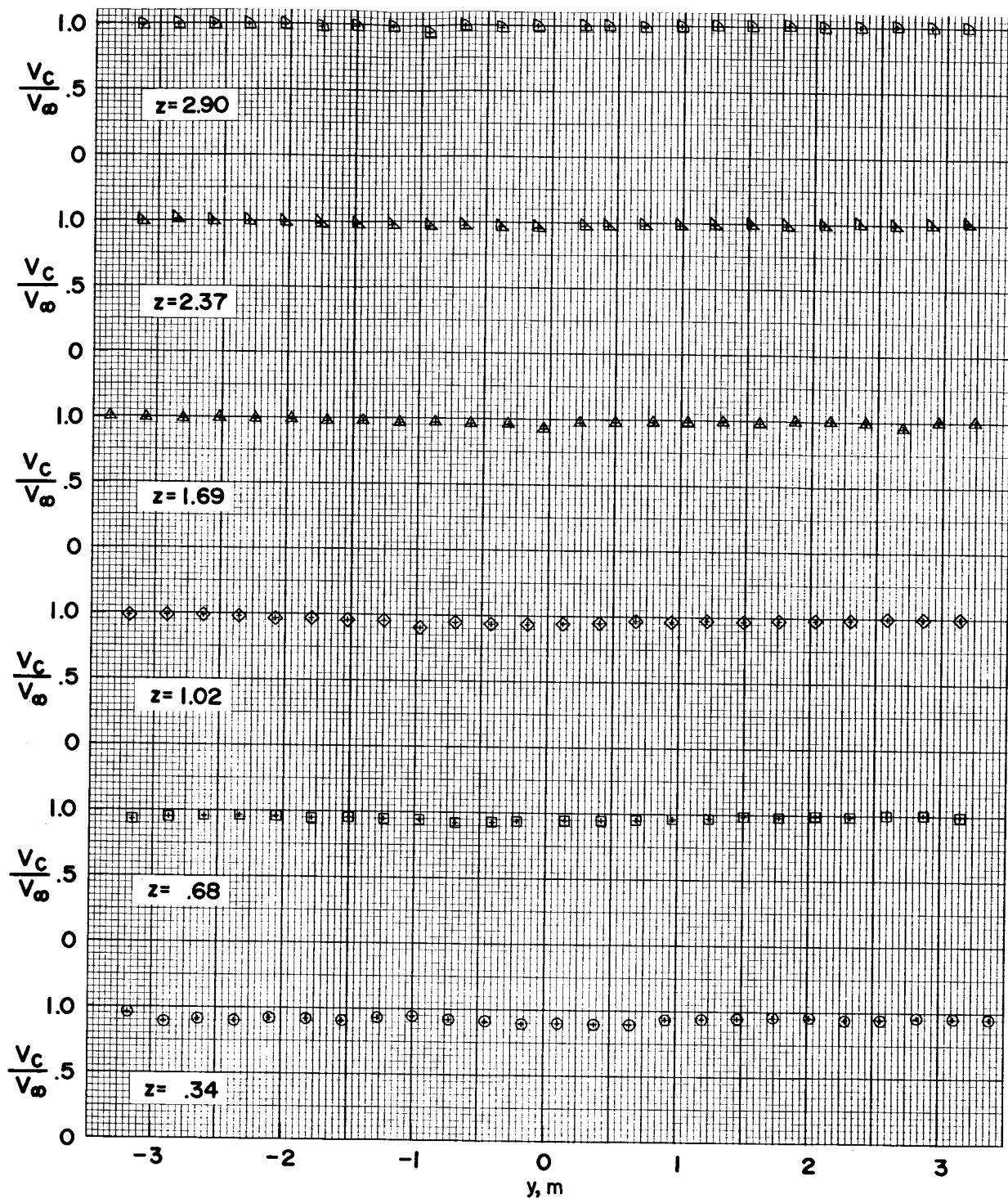
(a) $x = -4.06$ m.

Figure 30.- Velocity ratio V_c/V_∞ as a function of lateral position y for model configuration 7.



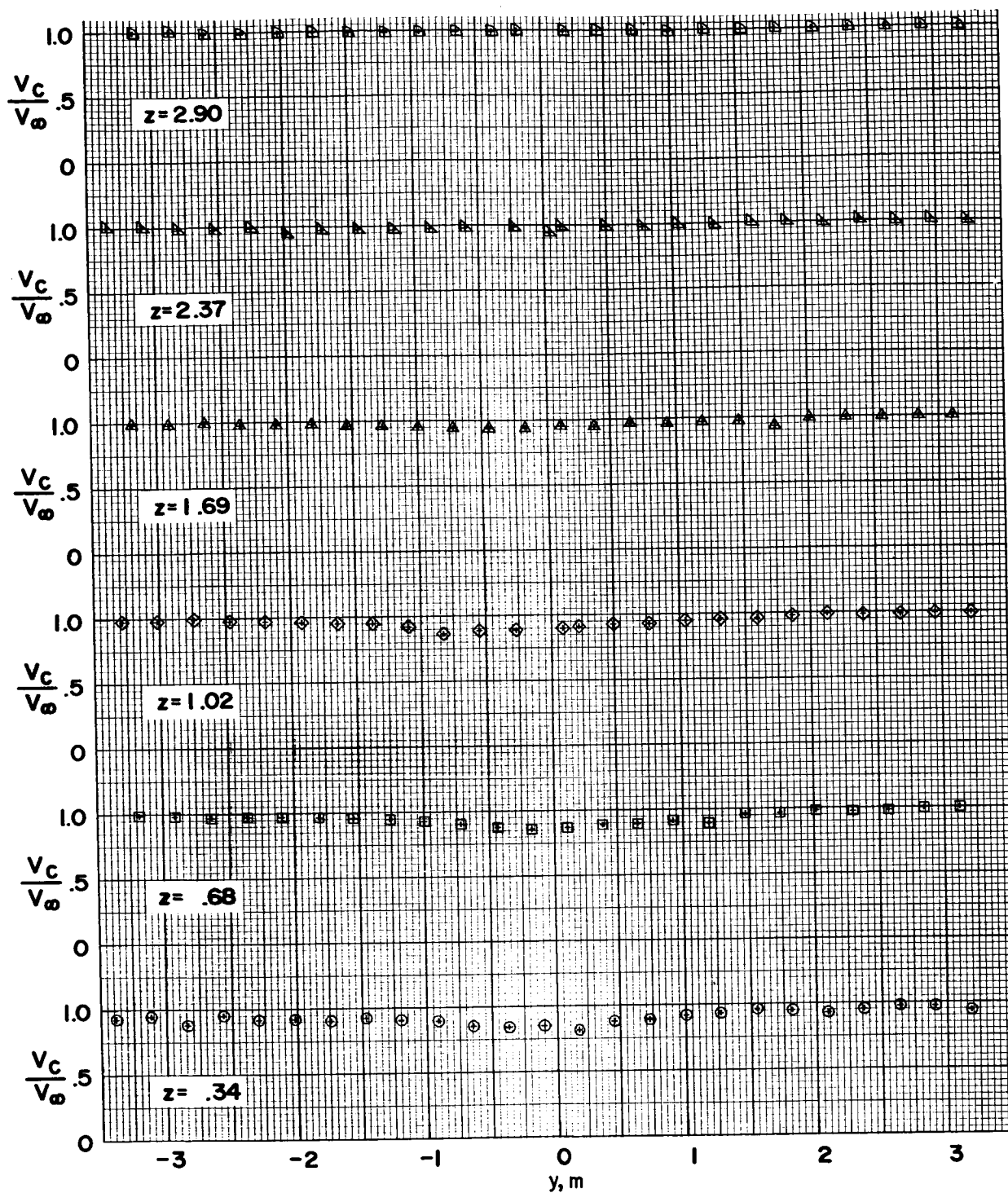
(b) $x = -3.39$ m.

Figure 30.- Continued.



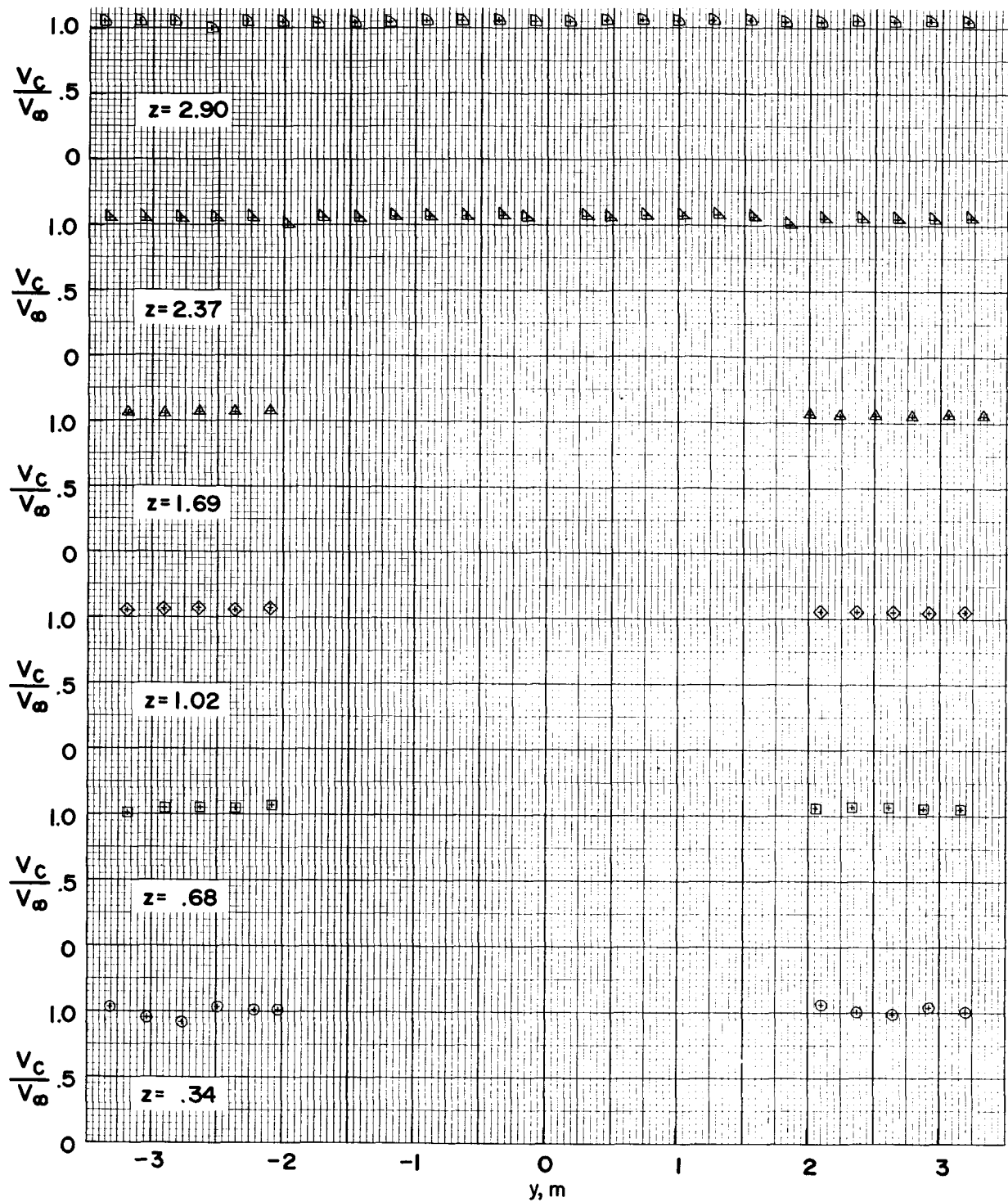
(c) $x = -2.71$ m.

Figure 30.- Continued.



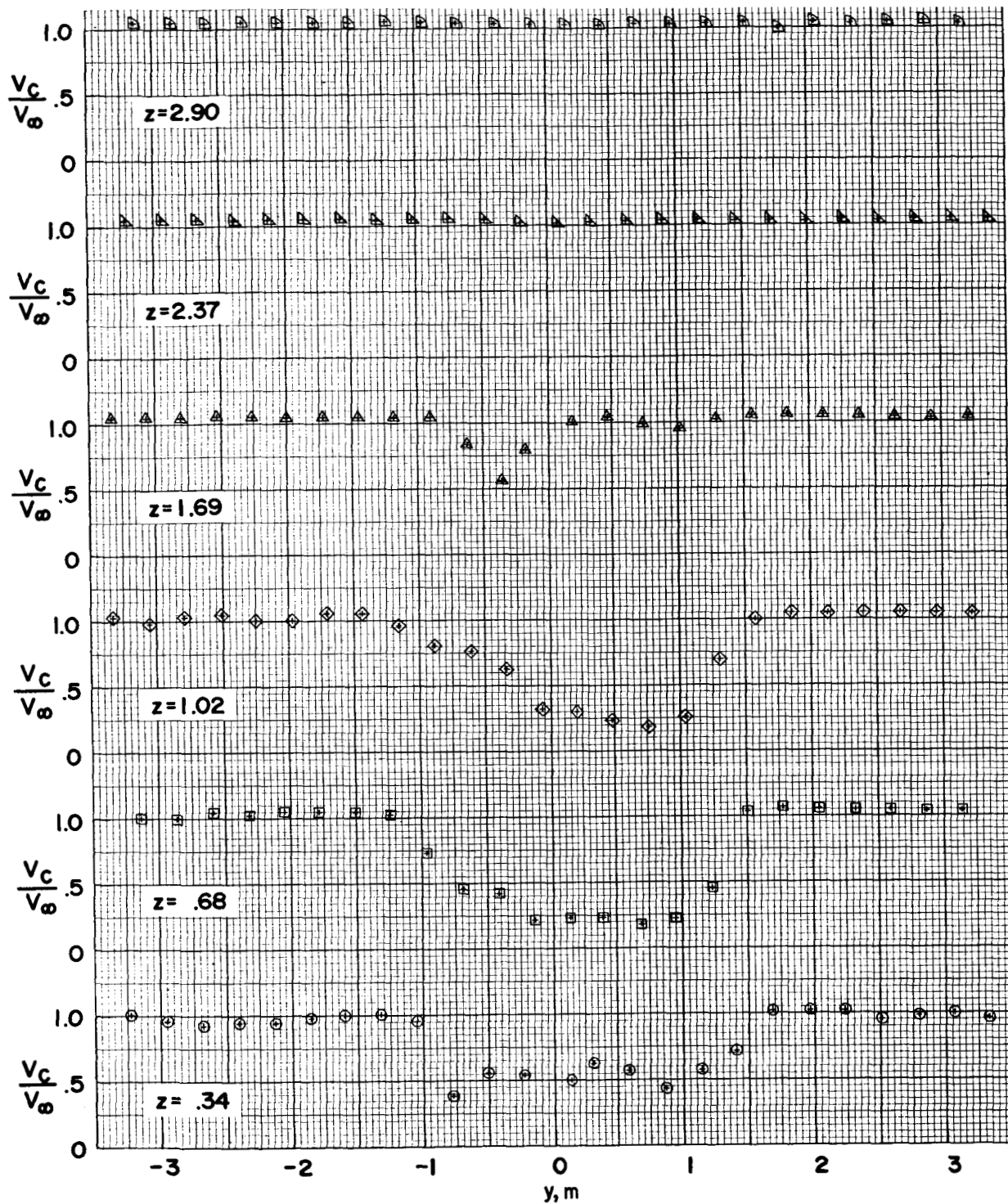
(d) $x = -2.03$ m.

Figure 30.- Continued.



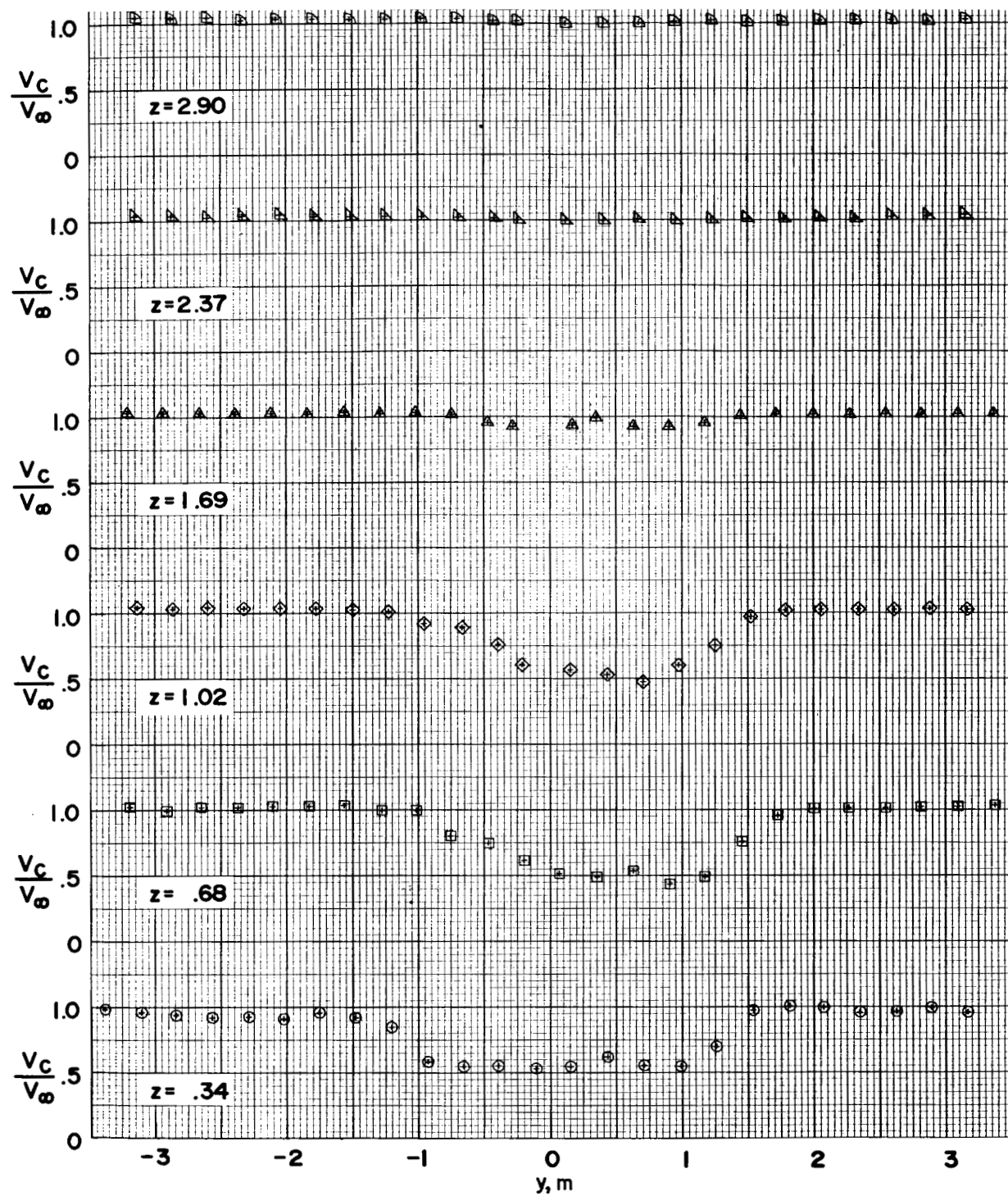
(e) $x = 0$ m.

Figure 30. - Continued.



(f) $x = 2.03$ m.

Figure 30. - Continued.



(g) $x = 4.06$ m.

Figure 30.- Concluded.

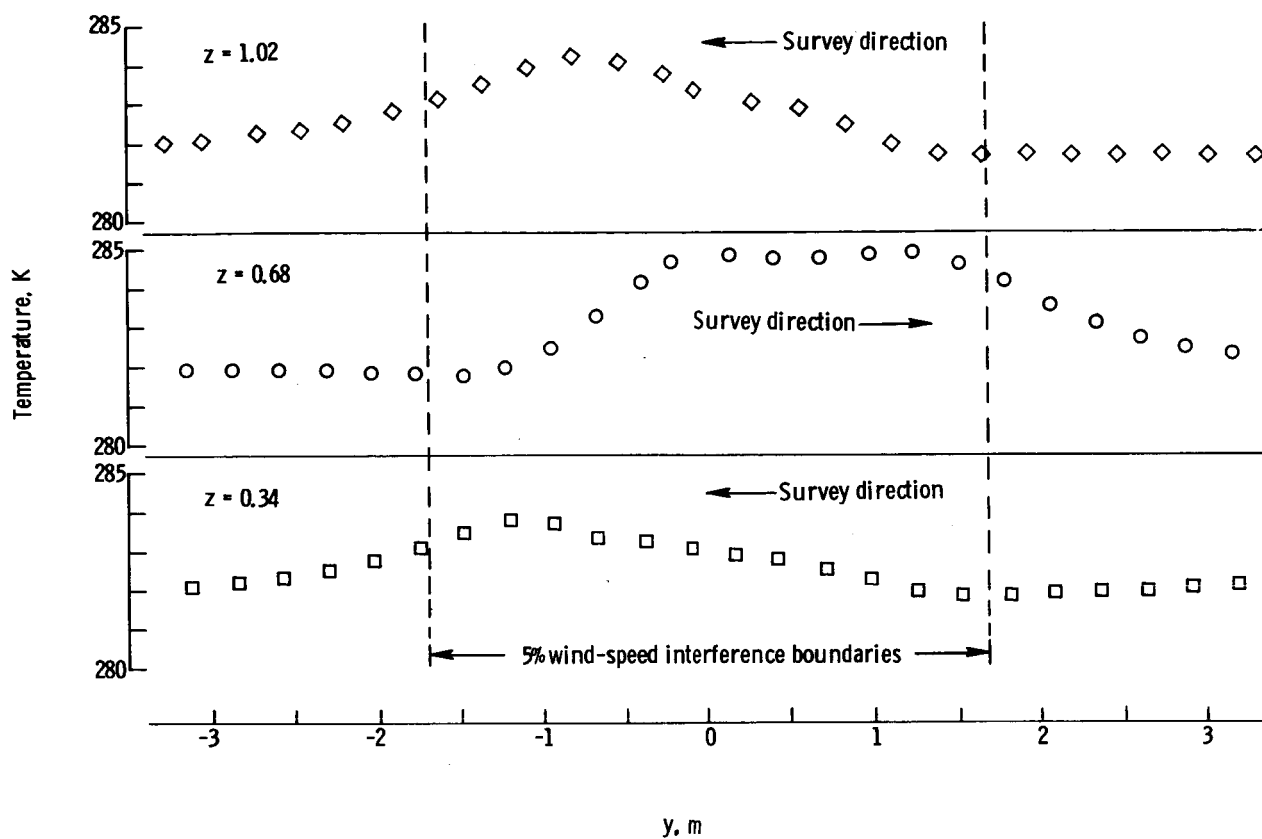


Figure 31.- Temperature profiles in the RTG thermal wake at $N_{Re} = 4400$.

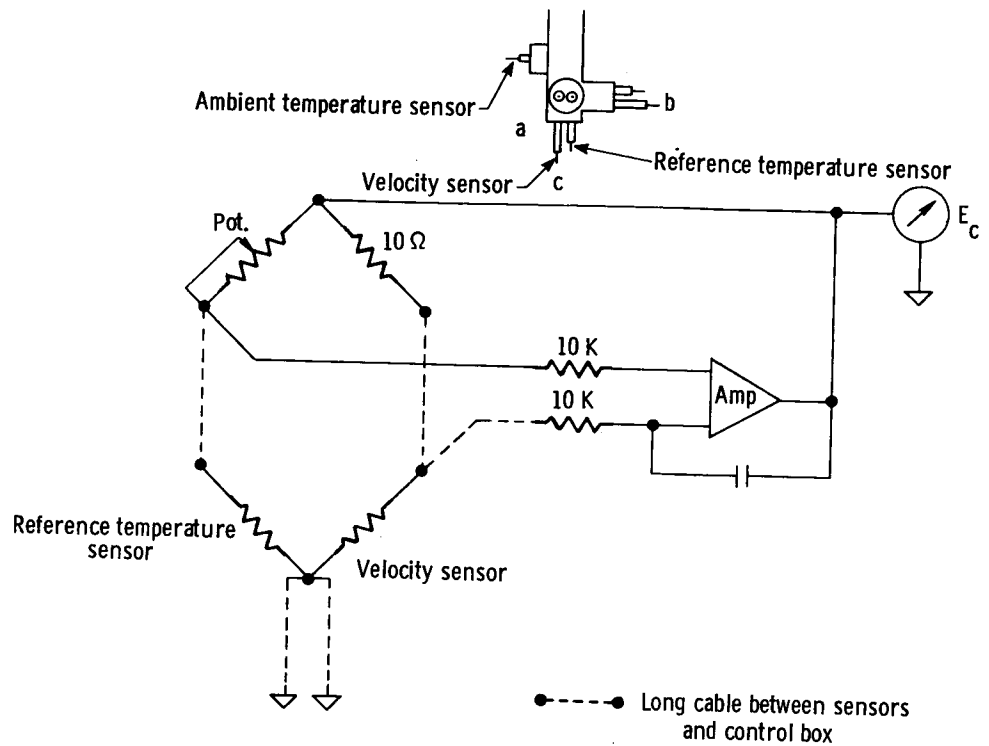


Figure 32.- Three-axis wind-sensor arrangement and equivalent circuit for wind sensor c.

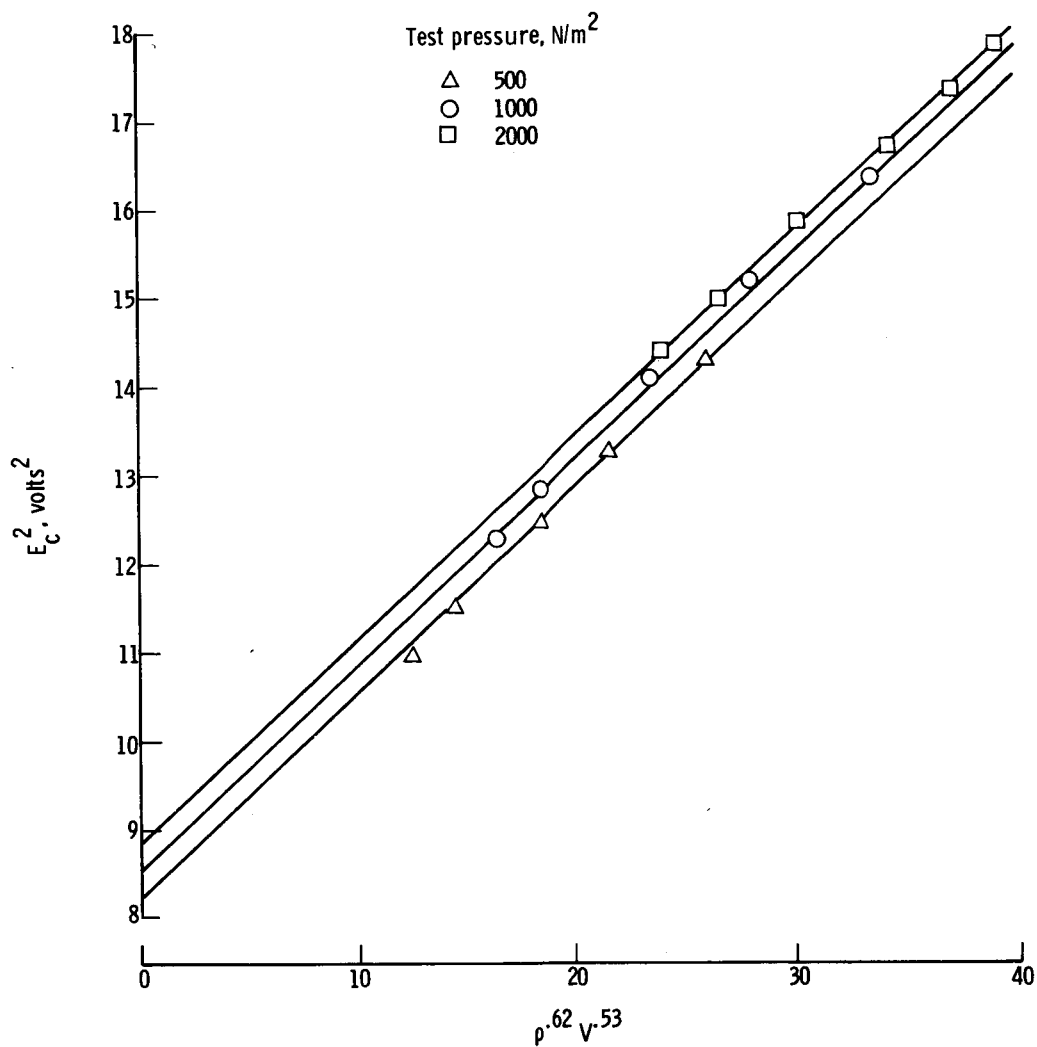


Figure 33.- Calibration curves for wind sensor c.